Validation of Phase Contrast Flow Quantification and Relaxometry for Cardiovascular Magnetic Resonance Imaging

Bidhult, Sebastian

2018

Document Version:
Publisher's PDF, also known as Version of record

Link to publication

Citation for published version (APA):
Bidhult, S. (2018). *Validation of Phase Contrast Flow Quantification and Relaxometry for Cardiovascular Magnetic Resonance Imaging*. Department of Biomedical Engineering, Lund university.

Total number of authors:
1

LUND UNIVERSITY

PO Box 117
221 00 Lund
+46 46-222 00 00

Validation of Phase Contrast Flow Quantification and Relaxometry for Cardiovascular Magnetic Resonance Imaging

Validation of Phase Contrast Flow Quantification and Relaxometry for Cardiovascular Magnetic Resonance Imaging

Sebastian Bidhult

LUND
UNIVERSITY

Dissertation for the degree of Doctor of Philosophy
Dissertation advisors: Assoc. Prof. Einar Heiberg,
Assoc Prof. Erik Hedström, Prof. Anthony H. Aletras
Faculty opponent: Prof. Sebastian Kozerke

To be defended, with the permission of the Faculty of Engineering of Lund University, in the GK lecture hall (BMC) at the Biomedical Centre on Friday, 17th of August 2018 at 09:00.

Organization
LUND UNIVERSITY

Document name
DOCTORAL DISSERTATION

Date of issue

Sponsoring organization

Author(s)

Title and subtitle

Abstract

Key words:

Classification system and/or index termes (if any):

Supplementary bibliographical information:

Language

ISSN and key title:

ISBN

Recipient's notes

Number of pages

Price

Security classification

DOKUMENTDATABLAD enl SIS 61 41 21

Distribution by (name and address)
I, the undersigned, being the copyright owner of the abstract of the above-mentioned dissertation, hereby grant to all reference sources permission to publish and disseminate the abstract of the above-mentioned dissertation.

Signature_____________________________________ Date_______________________

Validation of Phase Contrast Flow Quantification and Relaxometry for Cardiovascular Magnetic Resonance Imaging

Sebastian Bidhult

LUND
UNIVERSITY

Faculty Opponent
Prof. Sebastian Kozerke
ETH Zurich
Zurich, Switzerland

Evaluation Committee
Assoc. Prof.
Kerstin Lagerstrand
University of Gothenburg
Gothenburg, Sweden

Assoc. Prof.
Tomas Bjerner
Uppsala University
Uppsala, Sweden

Assoc. Prof.
Per Thunberg
Örebro University
Örebro, Sweden

Deputy Committee
Assoc. Prof.
Elin Trädgårdh
Lund University
Malmö, Sweden

Faculty of Engineering , Department of Biomedical Engineering
ISBN: 978-91-7753-742-7 (print)
ISBN: 978-91-7753-743-4 (electronic)
Printed in Sweden by E-husets tryckeri, Lund University, Lund 2018

Contents

I Research context

II Research Papers

List of publications

This dissertation is based on the following studies:

I. *Bidhult S*, Xanthis CG, Liljekvist LL, Greil G, Nagel E, Aletras AH, Heiberg E, Hedström E: **Validation of a new T2* algorithm and its uncertainty value for cardiac and liver iron load determination from MRI magnitude images.** *Magnetic Resonance in Medicine* 2016, 75(4):1717-29

II. *Bidhult S*, Kantasis G, Aletras AH, Arheden H, Heiberg E, Hedström E: **Validation of T1 and T2 algorithms for quantitative MRI: Performance by a vendor-independent software.** *BMC Medical Imaging* 2016, 16(1):46

III. Xanthis CG, *Bidhult S*, Kantasis G, Heiberg E, Arheden H, Aletras AH: **Parallel simulations for QUAntifying RElaxation magnetic resonance constants(SQUAREMR): An example towards accurate MOLLI T1 measurements.** *Journal of Cardiovascular Magnetic Resonance* 2015, 17:104

IV. *Bidhult S*, Hedström E, Carlsson M, Töger J, Steding-Ehrenborg K, Arheden H, Aletras AH, Heiberg E: **Validation of a new vessel segmentation algorithm with data driven shape constraints for robust noninvasive blood flow quantification from phase contrast magnetic resonance images.** *Manuscript*

V. *Bidhult S*, Töger J, Heiberg E, Carlsson M, Arheden H, Aletras AH, Hedström E: **Independent validation of Metric Optimized Gating for fetal cardiovascular phase-contrast flow imaging.** *Accepted manuscript Magnetic Resonance in Medicine 2018*

Author contributions

Study I
I participated in the design of the introduced T2* algorithm, the design of numerical simulations and the design of phantom validation experiments. I participated in data collection of phantom data, and analyzed data from the phantom experiments. I wrote and revised the manuscript.

Study II
I participated in the design of the new software tool and the design of the phantom validation study. I participated in data collection, analyzed data from the phantom experiments and wrote and revised the manuscript.

Study III
I prepared and measured the gel-phantoms used in the phantom experiments and I participated in data collection and analysis of phantom data. I assisted with writing parts of the methods section of the manuscript.

Study IV
I participated in the design of the new segmentation algorithm and I implemented the method. I participated in the design of algorithm training and evaluation procedures, and I contributed to the design and data collection of the phantom validation experiment. I performed data analysis of the phantom experiment and participated in data analysis for the invivo flow measurements. I wrote and revised the manuscript.

Study V
I contributed to: the design of the phantom validation experiment, data collection and analysis of the phantom experiment, and data collection for the invivo study. I wrote and revised the manuscript.

Popular summary

Quantitative imaging, where every pixel of an image represents a physical quantity (e.g. time or velocity) is being increasingly used in the field of diagnostic radiology and has potential to enhance medical diagnosis. Quantitative methods for Magnetic Resonance Imaging (MRI) enables measurements of velocity and flow using a technique called Phase Contrast Magnetic Resonance (PC-MR), and different time constants of the magnetic resonance signal can be measured to characterize different tissue types such as muscle and fat in MR images using a technique called magnetic resonance relaxometry.

One of the first clinical applications of MR relaxometry was to estimate iron load in different organs noninvasively by measuring the time constant called T2*. Patients suffering from iron load disease are at risk of developing organ failure due to iron overload. Iron chelate therapy has been shown to reduce chronic iron overload but it is toxic and has been linked to renal failure at high doses. MRI T2* measurements can be used to effectively tailor chelate therapy for patients with iron load disease, thereby reducing mortality of the disease. Several methods for calculating T2* from MRI images are currently being used, each with its own advantages and disadvantages. Different MRI vendors generally use slightly different methods. Further, some methods are mainly suitable for cases with moderate to normal iron load while other methods are more suitable for cases with severe iron load.

For other clinical applications of MR relaxometry the MR time constants called T1 and T2 are measured. For example, T1 measurements before and after administration of a certain MRI contrast agent makes it possible to determine the extracellular volume in different parts of the heart muscle which can be used to examine damages to the heart muscle after a heart attack. T2 measurements can for example be used to detect edema in the heart muscle and to determine blood oxygen saturation noninvasively. Several methods exist for T1 and T2 calculation from MRI images and software tools that can be used to calculate T1 and T2 values could be of help to standardize methodology in the clinics. A previous software for T1 and T2 analysis exist but it is designed to be used for research only.

The latest MR relaxometry methods often use computer simulations of MR physics together with MR images to enable measurement of several MR time constants at the same time or to increase the accuracy of each measurement. These techniques show great promise in advancing the research field of MRI but current methods require state of the art measurement techniques which can only be implemented on high-end MRI scanners, limiting wide clinical use.

Phase Contrast Magnetic Resonance (PC-MR) can be used to measure velocity in each pixel of an MRI image and have been used for many years as the reference standard for noninvasive measurements of blood flow. In order to measure the total net flow in a blood vessel over a heartbeat, the vessel of interest has to be delineated in a time-resolved PC-MR image series usually containing 15-35 images. Manual vessel delineation in these images is time consuming and requires user experience for accurate results. Semi-automatic delineation methods based on image analysis have reduced the amount of required user input and the total time of analysis for PC-MR flow measurements. However, currently existing semi-automatic methods often need manual corrections from the user.

Non-invasive flow and blood velocity measurements in the fetal cardiovascular system by MRI is a promising alternative to doppler ultrasound for diagnosing disease such as congenital heart defects and intra-uterine growth restriction. Conventional PC-MR flow measurements require an ECG-recording during the MRI scan which is used to sort the collected MRI data to form a time-resolved video over a heartbeat, a process called retrospective image gating. The lack of a usable ECG by surface electrodes for fetal imaging requires alternative image gating techniques. Metric Optimized Gating (MOG) is a previously published image gating technique which does not require a fetal ECG recording. MOG together with PC-MR flow measurements (MOG PC-MR) has demonstrated reproducibility for fetal imaging in studies from one research center. However, MOG PC-MR flow measurements have not been validated for a range of flow rates or a range of peak velocity. This dissertation investigates existing and newly developed MR relaxometry and PC-MR measurement methods with the purpose of evaluating clinical applicability.

In **Study I** a new vendor-independent T2* calculation method was validated over the range of clinically relevant T2* values in phantom experiments. Invivo T2* measurements using the proposed method were in good agreement with T2* measurements using a vendor-specific T2* method in the heart and liver of patients with known or suspected iron load disease.

In **Study II** a vendor-independent software for T1 and T2 analysis was validated in phantom experiments.

In **Study III** a new MR-relaxometry method called SQUAREMR, which was applied to a previously introduced and widely available T1 measurement technique (MOLLI), was shown to provide improved T1 measurement accuracy in phantom experiments.

In **Study IV** a new semi-automatic delineation method for PC-MR flow measurements which uses a database of manual vessel delineations to control the shape of the delineation was validated in a pulsatile flow phantom experiment and showed good agreement with manual delineations in invivo PC-MR images of the ascending aorta and main pulmonary artery.

Finally, in **Study V** MOG PC-MR showed good agreement with conventional PC-MR in a pulsatile flow phantom experiment except for cases with low Velocity to Noise Ratio (VNR), which resulted in underestimation of peak velocity and overestimation of flow which warrants optimization of the PC-MR measurement to individual fetal vessels for accurate MOG PC-

MR fetal flow measurements.

Acknowledgements

I would like to express my gratitude to everyone who have supported me during my time as a Phd student.

My main supervisor Einar Heiberg: Thank you for excellent supervision, all your help and support over the years and for a solution focused way of working and reasoning.

My co-supervisor Anthony Aletras. Thank you for excellent supervision, for welcoming me as a hang-around student during scanner experiments and for introducing me to the field of MR physics.

My co-supervisor Erik Hedström. Thank you for excellent supervision, support and cooperation over the years.

Håkan Arheden. Thank you for creating, and letting me be apart of, the Cardiac MR Group during these past years, for your leadership, and for sharing your thoughts on professional and personal development.

Christos Xanthis. Thank you for great cooperation and friendship over the years.

Johannes Töger. Thank you for all the years of great collaboration and for teaching me about flow phantoms, laser experiments and everything in between.

The EAG group: For a excellent teamwork over the years.

All of my colleagues in the cardiac MR Group: Thank you very much for all your support, friendship, and great discussions over the years.

Lastly, to Agneta, Lars and Inger: Thank you for all your love and support over the years, and for giving me a great start in life.

The studies in this dissertation were supported by grants from the Swedish Heart and Lung Foundation, Swedish Research Council, the Medical Faculty at Lund University, Region of Skåne, the Greek General Secretariat for Research and Development, the Swedish Medical Society, Skane University Hospital, the Swedish Society of Medicine Radiology and Cardiology and the European Commission.

Part I

Research context

Chapter 1

Background

1.1 Introductory cardiovascular physiology

The cardiovascular system provides oxygen and nutrients to the organ systems of the body and removes metabolic waste products. This exchange takes place in the capillaries, which contains approximately 5% of the total blood volume [1]. The cardiovascular system is composed of blood vessels, the blood and the heart, and is divided into two circuits which both begin and end in the heart: the systemic and the pulmonary circulation. The heart contains four chambers (shown in Figure 1.1): the right atrium (RA), the right ventricle (RV), the left atrium (LA) and the left ventricle (LV). The ventricles are separated by a part of the cardiac muscle wall called the **interventricular septum**, while atria and ventricles are separated by the **atrioventricular plane (AV-plane)**, a fibrous structure containing the four heart valves. On the right side of the heart, blood flows from the atrium to the ventricle through the tricuspid valve and exits the ventricle through the pulmonary valve and into the main pulmonary artery. On the left side of the heart, blood flows from the atrium to the ventricle through the mitral valve and exits the left ventricle through the aortic valve and into the aorta. No blood flow exists between atria or between ventricles in healthy hearts of adults. Abnormal blood flow connections between atria or between ventricles are called **cardiac shunts**, which are caused by some forms of congenital heart defects such as atrial septal defects (ASD) and ventricular septal defects (VSD).

The tip of the heart is called the **apex**, and the **base** of the heart is located on the opposite side of the heart.

In the pulmonary circulation, deoxygenated blood is pumped from the RV into the lungs through the main pulmonary artery. Oxygen rich blood is transported from the lungs to the LA and continues to the LV.

In the systemic circulation, oxygen rich blood is pumped from the LV through the aorta and into the arterioles which branch into the microcirculation, including the capillaries. deoxygenated blood continues to the veins and is transported back to the RA through the su-

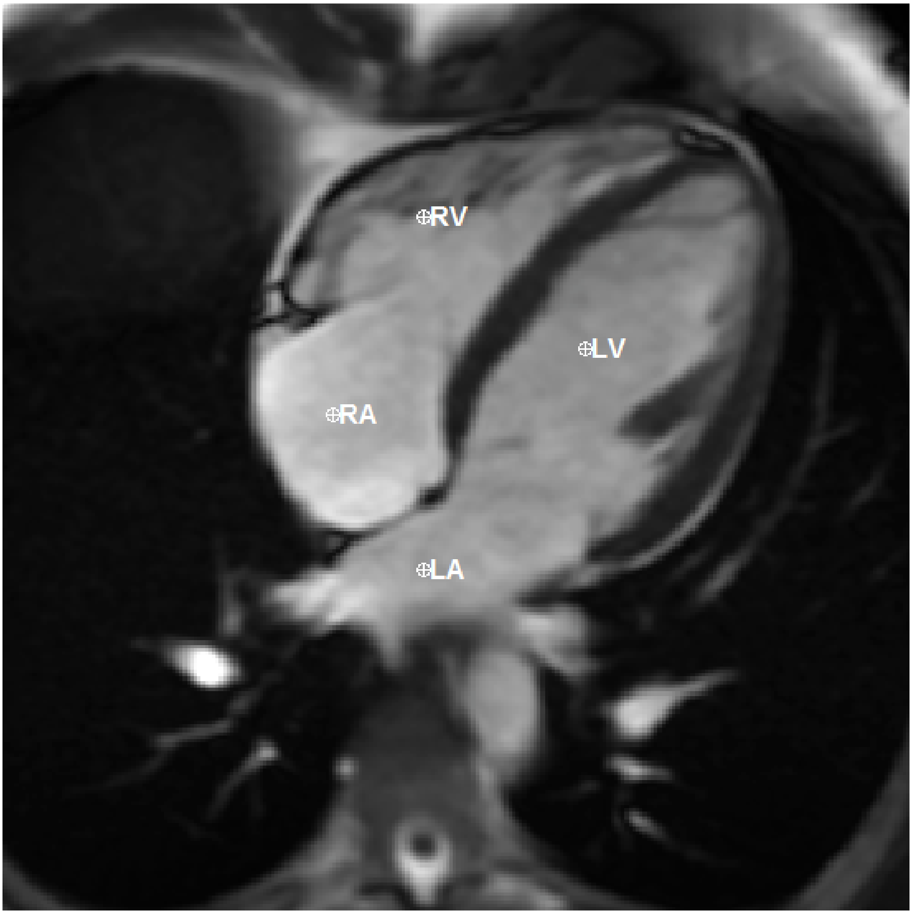

Figure 1.1 An MR image showing the four chambers of the heart: the right atrium (RA), the right ventricle (RV), the left atrium (LA) and the left ventricle (LV).

perior and inferior vena cava.

The activity of the heart is periodic/cyclic and the heart cycle consist of two phases: **systole**, the contraction phase, and **diastole**, the relaxation phase. Immediately before the onset of contraction the aortic and pulmonary valves are closed and the mitral and tricuspid valves are open. During ventricular systole, the muscle tissue of the heart, known as the **myocardium**, starts to contract, which exerts a force on the AV-plane, dragging it down towards the apex. A buildup of pressure occurs in the ventricles and the tricuspid and mitral valves close. At first, ventricular pressures will increase without an associated change in ventricular volume, known as the isovolumetric contraction phase. The aortic and pulmonary valves open when ventricular pressures exceed the pressure in the aorta and in the main pulmonary artery, respectively. At that point in time, ventricular volumes start to decrease and blood is ejected from the ventricles. Eventually, ventricular pressures start to decrease and the pressure differences between ventricles and arteries change direction. The reversed direction of pressure differences will lead to reversed blood flow after a time delay due to the momentum of blood flow. When blood flow is reversed, the aortic and pulmonary valves close. At this stage, known as **end-systole**, all heart valves are closed. The majority of blood ejection from the ventricles during systole is caused by longitudinal pumping due to AV-plane motion towards the apex [2]. Radial pumping due to thickening and inward motion of the myocardium is responsible for the remaining blood ejection. During the systolic AV-plane motion, blood is sucked from the veins to the atria[3].

Relaxation of the heart muscle initially occurs in an isovolumetric manner, leading to decreased ventricular pressures while ventricular volumes are unchanged. This phase is followed by the rapid filling phase, in which the AV-plane moves towards the base of the heart while the mitral and tricuspid valves open. After a short time period during which the heart is approximately stationary, called the diastasis, the atria starts to contract. Atrial contraction leads to additional filling of the ventricles and the time point after atrial contraction is called **end-diastole**.

The volume of blood in a ventricle that is ejected during systole is called **stroke volume** (**SV**) and can be calculated as the difference between the **end-diastolic volume** (EDV) and the **end-systolic volume** (ESV) of the ventricle $(EDV - ESV)$. The percentage of ejected blood volume is called the **ejection fraction** (**EF**) and can be calculated as:

$$EF = \frac{SV}{EDV} = \frac{EDV - ESV}{EDV}$$

In healthy adults, the duration of the heart cycle is on average 860ms, corresponding to a heart rate (HR) of 70 beats per minut (bpm). The duration of diastasis, the time phase where the heart is approximately stationary, varies with heart rate and disappears completely for heart rates above approximately 80bpm[4].

The product of heart rate and stroke volume gives the delivered blood volume per minute, known as **cardiac output** (**CO**).

1.2 Nuclear Magnetic Resonance (NMR)

The nuclear magnetic resonance (NMR) method for measuring nuclear magnetic moments was formulated in the late 1930s [5] and is used as basis for signal detection in magnetic resonance imaging (MRI) and magnetic resonance spectroscopy (MRS). The following sections describe the NMR signal and how it is detected in a pulsed NMR experiment, which is the most commonly used NMR method for MRI and MRS applications today.

1.2.1 Nuclear spin

Atomic nuclei have an intrinsic property called nuclear spin, which is a form of angular momentum. The nuclear spin is described by the angular momentum quantum number I which can have a positive or negative integer or half-integer value in increments of 1/2 (e.g. -1, -1/2, 0, 1/2, 1, etc).

Atomic nuclei with $I \neq 0$ have an associated non-zero magnetic moment. When placed in a strong external magnetic field, multiple distinct nuclear spin energy levels, or spin states, are formed due to the Zeeman effect [6]. The energy difference between adjacent spin states is proportional to the strength of the external magnetic field B_0 which is measured in Tesla (T). The following discussion on NMR will refer to experiments on atomic nuclei with $I = 1/2$, for example the hydrogen nucleus (proton), with negligible mutual spin interactions.

For a sample in thermal equilibrium, the relative population among different spin states will be slightly disproportionate, with a small overrepresentation in low-energy states. This population difference between spin states is a prerequisite for NMR measurements and results in a net magnetization along the B_0 magnetic field, called longitudinal magnetization. Further, the magnitude of population differences partly determines the maximum signal strength in an NMR experiment, and increases with increasing B_0 and decreases with increasing sample temperature. In addition, the maximum NMR signal strength is proportional to the spin density (ρ) of the sample.

1.2.2 Spin precession and resonance

The external magnetic field (the B_0-field) causes spin orientations of nuclei to precess around the z-axis, at a precession frequency called the Larmor frequency (ω_0). The Larmor frequency is given by the product of the external magnetic field strength B_0 and the gyromagnetic ratio γ which is a nuclei-specific constant: $\omega_0 = \gamma B_0$ and it is proportional to the energy difference between spin states. Since the external magnetic field cannot be calibrated to have a perfectly homogeneous field strength over a volume, a range of Larmor frequencies will exist in a sample surrounding the Larmor frequency corresponding to the main field strength (B_0). Further, the Larmor frequency of a given nucleus, for example hydrogen, can be shifted due to the local molecular environment, an effect known as chemical shift.

Spin precession results in a rotating magnetic field component in a plane perpendicular to the external magnetic field direction, called the xy-plane or transverse plane. Such a rotating magnetic field can induce a current in a receiver coil with its symmetry axis perpendicular to the z-axis. However, in thermal equilibrium the spin orientations of nuclei do not precess in phase with one another which causes them to add destructively and therefore, a signal cannot be detected.

If an oscillating magnetic field, denoted as the B_1-field, is applied on-resonance with the spin precession ($\omega_1 = \omega_0$) and with an orientation perpendicular to the static magnetic field, the longitudinal magnetization is gradually converted into a rotating magnetization component in the xy-plane at a rate [γB_1] (Figure 1.2). Spin orientations of nuclei now starts to precess in phase with one another, creating phase coherence, and the rotating magnetic field in the xy-plane, called transverse magnetization, induces an alternating current in the receiver coil, which is the measured signal in an NMR experiment.

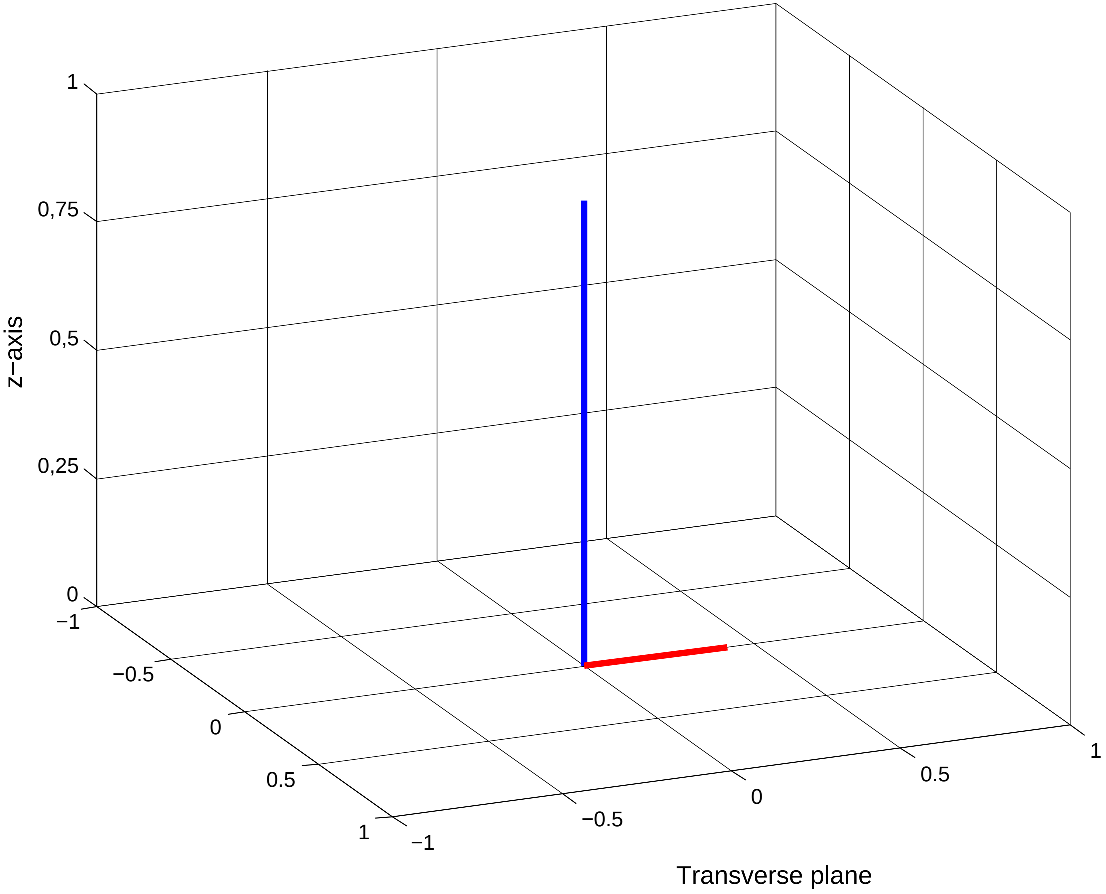

Figure 1.2 An example of longitudinal (blue) and transverse (red) NMR magnetization shown in a 3D-coordinate system. During the application of an oscillating B_1-field on-resonance with the spin precession, the net magnetization is periodically converted at a rate $[\gamma B_1]$ between a longitudinal component along the static B_0 magnetic field (z-axis), and a rotating transverse component. The total net magnetization is normalized to 1.0 in this plot.

1.2.3 Properties of the NMR signal

Since the NMR signal originates from a rotating magnetic field, every signal sample has an associated magnitude and phase. Measurement of both the magnitude and phase is performed by quadrature detection, where two orthogonal signal components separated by a 90° phase shift are sampled concurrently. The two signal components are usually represented as the real and imaginary parts of a complex number. The measured NMR signal will oscillate at the Larmor frequency, its carrier frequency, and is often demodulated by the receiver circuit such that only the envelope of the oscillating signal remains.

1.2.4 The pulsed NMR experiment

In a pulsed NMR experiment, the signal is detected after a short on-resonance $B1$-pulse. The duration of the B_1-pulse is in an order of just a few milliseconds, resulting in a wide frequency bandwidth in an order of kHz. The wide pulse bandwidth makes it possible to excite nuclei with different Larmor frequencies simultaneously, over the entire Larmor frequency spectrum of a sample. Since the Larmor frequency is in the radio frequency (RF) range, an electromagnetic RF-pulse can be used to generate the NMR signal. For many NMR applications, the RF-pulse is shaped by a modulation function over time in order to modify its excitation spectrum. Gaussian or sinc shapes of the RF-pulse are commonly used.

The NMR signal amplitude immediately after the B_1-pulse depends on the flip angle (α) which is given by the product of the gyromagnetic ratio and the time integral of the B_1 amplitude: $\alpha = \gamma \int_0^{t_p} B_1(t)dt$, where t_p is the total duration of the B_1-pulse. The flip angle is related to the proportion of transverse magnetization M_{xy} relative to the longitudinal magnetization M_z by: $tan(\alpha) = \frac{M_{xy}}{M_z}$. A flip angle of 90° corresponds to zero longitudinal magnetization and the maximum achievable transverse magnetization; a flip angle of 180° corresponds to zero transverse magnetization and maximum longitudinal magnetization with opposite polarity compared to the B_0-field; and a flip angle of 0° corresponds to zero transverse magnetization and maximum longitudinal magnetization along the B_0 field, similar to thermal equilibrium. A flip angle of 90° results in the maximum NMR signal amplitude since the entire net magnetization is converted into the xy-plane.

An illustration of the real component of an NMR signal response from hydrogen nuclei of water immediately after the application of a B_1-pulse is shown in Figure 1.3. The signal is oscillating at the Larmor frequency and is decaying at an exponential rate. This signal response is called the free induction decay (FID) and was first observed by Hahn [7].

For samples containing several different chemical structures, for example a mix of water and fat, the NMR spectrum may be composed of several distinct frequency peaks due to the chemical shift effect. If this is the case, the FID signal will have more than one oscillating component.

The NMR frequency spectrum of a sample can be obtained by performing a mathematical operation called Fourier transformation (FT) on the measured FID signal[8]. The Fourier transform operation is used extensively for both magnetic resonance spectroscopy (MRS) and magnetic resonance imaging (MRI).

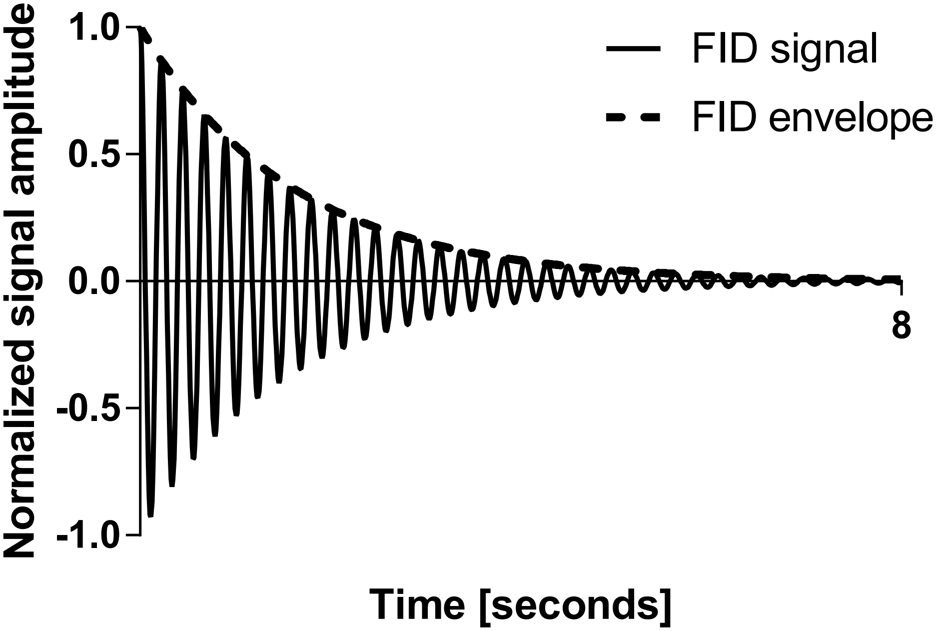

Figure 1.3 An example of the real component of a NMR free induction decay complex signal (FID) from hydrogen nuclei of water in a homogeneous static magnetic field (solid line), together with its decay envelope (dashed lines). The FID oscillation frequency equals the Larmor frequency but it has been reduced in this figure for better visualization.

1.2.5 Relaxation effects

NMR relaxation is the process in which an excited spin system is returned to thermal equilibrium. The measured transverse magnetization will decay to zero and the longitudinal magnetization will regrow to its maximum amplitude along the B_0 field. Both of these aspects of relaxation will be described separately, starting with the recovery of longitudinal magnetization.

Of note, the exponential equations used to describe NMR relaxation in this section are approximations which are reasonably accurate for rapidly tumbling molecules, such as most molecules in the liquid state, but breaks down for slow molecular motion. Therefore the discussion is limited to NMR measurement of molecules in the liquid state.

Longitudinal relaxation

After the application of a B_1-pulse, the spin system will eventually be restored to thermal equilibrium and the net longitudinal magnetization M_z will be recovered. During this process energy is exchanged between the spin system and its molecular environment.

The rate of longitudinal relaxation depends on the difference between the current state of longitudinal magnetization and the thermal equilibrium state according to:

$$\frac{dMz}{dt} = -(M_z(t) - M_0)/T_1$$

Here, M_0 is the longitudinal magnetization at thermal equilibrium and T_1 is a time constant known as the longitudinal relaxation time.

Longitudinal relaxation over time is described by the solution to the differential equation above:

$$M_z(t) = M_0 - (M_0 - M_z(0))e^{-t/T_1}$$

Here, $M_z(0)$ is the longitudinal magnetization immediately after the $B1$-pulse.

T_1 increases with increasing static magnetic field strength B_0 and decreases in the presence of paramagnetic ions. T_1 is also highly sensitive to the temperature and the molecular composition of a sample. For example, at clinically used magnetic field strengths, T_1 of water is several seconds while T_1 of fat is in the order of hundreds of milliseconds.

The free induction decay and the effect of off-resonance

Immediately after a B_1-pulse, the FID signal decays due to loss of phase coherence between precessing spins, also called **dephasing.** The FID decay rate depends on two factors: 1) magnetic field strength inhomogeneity of the B_0 magnetic field over the sample volume and 2) an irreversible process called transverse relaxation.

Magnetic field strength inhomogeneity results in a widening of the NMR frequency spectrum in the sample, which gives rise to off-resonance frequencies ($\Delta\omega$) surrounding the center frequency. In this setting, the net rotating magnetization in the xy-plane will be composed of a combination of frequencies which will dephase over time, leading to destructive interference and decay of the net NMR signal.

In addition to imperfections of the static B_0 field, local magnetic field inhomogeneity can also be caused by regions containing ferromagnetic materials in the sample volume, leading to an increased signal decay rate.

By assuming that the width of the NMR spectrum due to off-resonance frequencies is much smaller than the center frequency of the spectrum, the NMR signal decay over time can be described as[7]:

$$M_{xy}(t) \approx M_{xy}(0)e^{-t/T_2^*}$$

Here, $M_{xy}(0)$ is the magnitude of transverse magnetization immediately after the B_1-pulse, T_2^* is a time constant describing the decay rate and t is the time from the end of the B_1-pulse to signal measurement. By definition, T_2^* is the time for which the signal has decayed to 37% of its original value and is described by the following formula[7]:

$$\frac{1}{T_2^*} = \frac{1}{T_2} + \frac{(\Delta\omega)_{1/2}}{2}$$

Here, $(\Delta\omega)_{1/2}$ is the width at half maximum of the NMR frequency spectrum due to off-resonance and T_2 is a time constant describing irreversible transverse relaxation. Since magnetic field inhomogeneity over a volume is not a random process and is approximately constant during the NMR experiment, the decay component due to off-resonance can be reversed by using a specific combination of B_1-pulses before signal measurement. This technique is called spin echo and will be described further in section 1.2.7.

Transverse relaxation

Transverse relaxation refers to the process in which spin precession of nuclei dephase due to energy exchange between spins. This results in irreversible loss of transverse magnetization over time according to:

$$M_{xy}(t) = M_{xy}(0)e^{-t/T_2}$$

Here, $M_{xy}(0)$ is the transverse magnetization immediately after the application of a $B1$-pulse and T_2 is a time constant which describes the rate of signal decay due to transverse relaxation. t is the time delay between the end of the $B1$-pulse and the NMR signal measurement.

T_2 is always shorter than T_1, since the regrowth of longitudinal magnetization inherently results in loss of transverse magnetization. Thus, any phenomena causing T_1 relaxation also causes T_2 relaxation. However, T_2 relaxation can occur without T_1 relaxation. For example, T_2 is sensitive to the molecular composition of the sample[9].

1.2.6 The Bloch equations

If mutual spin interactions are negligible, the spin motion of atomic nuclei with $I = 1/2$ in the presence of external magnetic fields can be completely described by a precessing net magnetization vector[10] according to:

$$\frac{d\mathbf{M}}{dt} = \gamma\mathbf{M} \times \mathbf{B}$$

Here, **M** is the net magnetization 3D-vector and **B** is a 3D-vector composed of the sum of all active external magnetic fields. Since the transverse components of both **M** and **B** in an NMR experiment are rotating around the z-axis at the Larmor frequency, it is convenient to redefine the x- and y-axes of the coordinate system as two orthogonal axes in the transverse plane which are rotating at the Larmor frequency, also called the rotating frame of reference. In this coordinate system, both the transverse magnetization components (M_x and M_y) and the B_1-field are stationary if precessing on-resonance. One advantage with this frame of reference is that two B_1-pulses which are out of phase with one another can be described with simple subscripts. For example, one B_1-pulse with flip angle 60° and one pulse with flip angle 180° which are 90° out of phase can be written as 60_x and 180_y, respectively. Further, two pulses with, for example, flip angles 90°, which are 180° out of phase with each other can be written: 90°_x and 90°_{-x}. In practice, signal measurements in the rotating frame of reference can be achieved by demodulation of the NMR signal (described in section 1.2.3).

In the rotating frame, the evolution of the net magnetization 3D-vector in the presence of external magnetic fields and relaxation processes (described in section 1.2.5) is given by the following set of relationships known as the Bloch equations[9]:

$$\begin{aligned}
\frac{dM_x}{dt} &= \gamma M_y(B_0 - \omega/\gamma) - \frac{M_x}{T_2} \\
\frac{dM_y}{dt} &= \gamma M_z B_1 - \gamma M_x(B_0 - \omega/\gamma) - \frac{M_y}{T_2} \\
\frac{dM_z}{dt} &= -\gamma M_y B_1 - \frac{(M_z - M_0)}{T_1}
\end{aligned}$$

Here, M_x, M_y, and M_z are the orthogonal components of the net magnetization 3D vector, B_0 is the external magnetic field strength along the z-axis, B_1 is the amplitude of the oscillating RF-field applied along the x-axis and ω is the oscillation frequency of the RF-field.

1.2.7 Relaxometry and introductory spin manipulation

As mentioned in previous sections, the NMR signal amplitude depends on the B_0-field strength, the sample temperature and the flip angle of the B_1-pulse. All of these parameters, except for sample temperature, have magnitudes which are directly related to the experiment design and which cannot be used for sample characterization. The NMR frequency spectrum can be obtained by means of Fourier transformation of the measured NMR signal[8] and can be used to characterize the sample. In addition, the relaxation time constants T_1, T_2 and T_2^* vary with different aspects of the sample composition and can therefore be of value. Relaxometry is the measurement of such NMR relaxation time constants and generally involves spin manipulation schemes, also called **pulse sequences**, other than the FID experiment. This section describes the basic principles of relaxometry methods for measurement of T_1, T_2^* and T_2 time constants and associated pulse sequences.

In general, multiple NMR experiments are performed, each with different timing settings resulting in different NMR signal amplitudes due to the relaxation effect of interest. The signal measurements are compared to a signal model which is known to be accurate for the performed NMR experiment and which includes the time constant of interest as an unknown parameter. Finally, the unknown parameters of the signal model are estimated by nonlinear least squares regression to the measured signal points. This methodology is common to measurements of all three time constants.

The number of signal measurements used in regression analysis must, as an absolute minimum, equal the number of unknown parameters. When this is the case, the signal model will find parameters to perfectly fit the data which makes the measurement extremely sensitive to noise. By increasing the number of signal measurements, robustness to noise is gradually improved. In practice, around 8-15 signal measurements are commonly used for signal models with 2-3 unknown parameters in relaxometry.

Measurement of the T_1 time constant

The T_1 relaxation time can be measured by perturbing the magnetization with a preparation B_1-pulse, measure the NMR signal by applying an additional excitation B_1-pulse after a time interval of undisturbed longitudinal relaxation, and repeating the experiment using different time intervals between magnetization preparation and measurement. In theory, arbitrary flip angles can be used for both magnetization preparation and excitation. In practice, however, it is advantageous to use a preparation pulse which perturbs M_z as far away from the equilibrium magnetization M_0 as possible in order to maximize the dynamic range of the measurement. Further, an excitation pulse resulting in the maximum NMR signal amplitude should be used to reduce the effect of noise on the measurement. Both of these criteria are satisfied by using a 180° preparation pulse followed by a 90° excitation pulse, an experiment called **inversion-recovery**. Longitudinal relaxation over time for inversion-recovery can be described as:

$$M_z(t) = M_0 - (M_0 - (-M_0))e^{-t/T_1} = M_0(1 - 2e^{-t/T_1})$$

Here, t is the time between the end of the 180° preparation pulse and the start of the excitation pulse, also called inversion time (TI), and $M_z(t)$ is the measured signal. M_0 and T_1 are the unknown parameters which are estimated by the fitting algorithm. The longitudinal magnetization has been perturbed to opposite polarity compared to thermal equilibrium by the inversion preparation pulse. For an unbiased T_1 measurement, the time interval between repeated experiments, called the repetition time (TR) has to be long enough to allow for near complete longitudinal recovery. This makes T_1 measurements by inversion-recovery time consuming.

Another commonly used method to measure T1 is the **saturation-recovery** experiment:

$$M_z(t) = M_0 - (M_0 - (0))e^{-t/T_1} = M_0(1 - e^{-t/T_1})$$

In this experiment, A 90° preparation pulse converts the entire longitudinal magnetization to the xy-plane, resulting in nulling of the longitudinal magnetization ($M_z(0) = 0$). t is now the time between the end of the 90° preparation pulse and the start of the excitation pulse, also called saturation time (TS). Ideal saturation recovery measurements does not require complete longitudinal recovery between repeated experiments, thereby improving measurement efficiency. However, only half of the dynamic range is obtained compared to inversion-recovery, which reduces measurement precision.

In practice, a generalized signal model which supports preparation pulses with arbitrary flip angle (α) and takes potential B_1-pulse imperfections into account, is most commonly used for both inversion-recovery and saturation-recovery experiments:

$$M_z(t) = M_0 - (M_0 - (cos(\alpha)M0))e^{-t/T_1} = M_0(1-(1-cos(\alpha))e^{-t/T_1}) = M_0(1-Ae^{-t/T_1})$$

Here, either α or A is used as an additional free parameter determined by the fitting algorithm. Increasing the number of free parameters from 2 to 3 results in improved accuracy at the cost of reduced precision.

Saturation/inversion times in use for a T1-measurement generally includes long times corresponding to near complete longitudinal recovery which mainly define the unknown parameter M_0; short times close to the end of the preparation pulse which mainly define the unknown parameter A or α; and a range of times in between which mainly define the unknown parameter T_1.

Measurement of the T_2^* time constant

T_2^* can be measured from repeated FID experiments with time delays (*t*) between the end of the B_1-pulse and signal measurement according to:

$$M_{xy}(t) = M_{xy}(0)e^{-t/T_2^*}$$

Here, the unknown parameters are $M_{xy}(0)$ and T_2^*. For an unbiased T_2^* measurement, the time interval between repeated experiments, the repetition time (TR) needs to be long enough to allow for complete longitudinal recovery. However, a B_1 excitation pulse with a flip angle lower than 90° can be used without invalidating the signal model. A low flip angle reduces the time needed for the longitudinal magnetization to reach a certain percentage of M_0 compared to the time needed for a 90° flip angle, and the repetition time can therefore be reduced. However, the gain in measurement efficiency comes with reduced precision since lower flip angles result in lower NMR signal amplitudes.

The spin echo and measurement of the T_2 time constant

Inhomogeneous regions of the static B_0 magnetic field over the sample volume will give rise to a distribution of spin Larmor frequencies surrounding the on-resonance frequency. Such a distribution of off-resonance frequencies will lead to loss of phase coherence in the xy-plane and as a result, rapid decay of transverse magnetization.

Since both off-resonance precession and transverse relaxation contribute to the free induction decay (FID), the T_2 time constant describing transverse relaxation alone cannot be measured from the FID signal.

The loss of phase coherence due to off-resonance is reversible, which was first shown by Hahn[11]. When a B_1-pulse with flip angle 180° is applied at a time τ after an initial 90° B_1-pulse, an echo signal is generated at time 2τ after the end of the first pulse (shown in figure 1.4). This echo signal is called spin echo and its origin can be explained using the 3D-vector representation of the net magnetization by Bloch[9] (section 1.2.6). Of note, the first 90° B_1-pulse is usually called excitation pulse and the 180° pulse in a spin echo is called refocusing pulse.

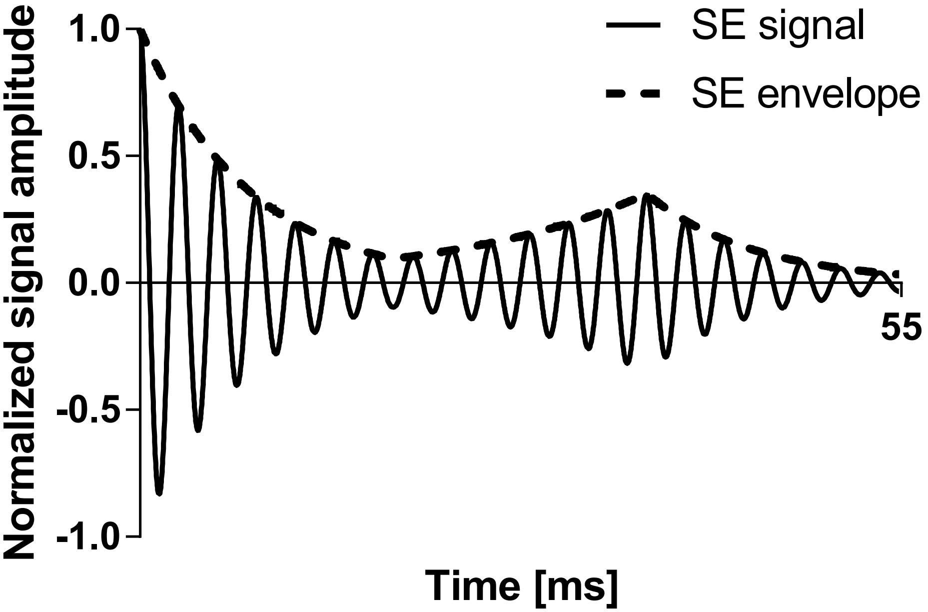

Figure 1.4 The real component of an NMR complex signal (solid line) together with its envelope (dashed lines) in a spin echo experiment (SE), in the presence of an inhomogeneous static magnetic field. The signal is continuously attenuated by irreversible transverse relaxation (T_2 relaxation) and the echo signal is therefore slightly asymmetric. The signal oscillation frequency equals the Larmor frequency but it has been reduced in this figure for better visualization.

The 90° excitation B_1-pulse converts the entire magnetization vector to transverse magnetization in the xy-plane. Since the net transverse magnetization is comprised of spin orientations precessing at different frequencies due to off-resonance, spin orientations will start to disperse/dephase. At time τ the 180° refocusing B_1-pulse is applied and rotates the net magnetization, including the dephased spin orientations, by 180°. Since the net magnetization vector was parallel to the xy-plane before the refocusing pulse was applied, the magnetization vector will still be parallel to the xy-plane after the 180° rotation which was induced by the refocusing pulse. However, the orientation of the net magnetization vector in the xy-plane, its phase, will be shifted into an adjacent quadrant of the unit circle such that, for example a magnetization vector with phase 45° before the refocusing pulse has phase 135° after refocusing. The dephased spin orientations contained in the net magnetization vector will start to rephase after the refocusing pulse. Since the distribution of off-resonance frequencies in the sample hasn't changed during the time course of the experiment, a rephased echo signal will appear at time τ after the refocusing pulse, corresponding to 2τ after the first 90° excitation pulse. This time point is called the echo time (TE).

In a spin echo experiment, the NMR signal amplitude at time point 2τ will not be attenuated by off-resonance, but will be effected by transverse relaxation. Therefore, the T_2 time constant can be measured by repeating the spin echo experiment using different τ times according to:

$$M_{xy}(2\tau) = M_{xy}(0)e^{-2\tau/T_2} = M_{xy}(0)e^{-TE/T_2}$$

Here, the unknown parameters are $M_{xy}(0)$ and T_2. The echo time (TE) is defined as 2τ for spin echo.

An accelerated version of the original spin echo experiment is the Carr Purcell Meiboom Gill pulse sequence[12] (CPMG), also called multi-echo spin echo, in which several 180° refocusing pulses are applied in succession following the first 90° excitation pulse. This pulse sequence produces multiple spin echoes after a single excitation pulse. Refocusing pulses are phase shifted 90° compared to the first excitation pulse in order to reduce the accumulation of small errors in flip angle. For example, the pulse scheme 90°_x, 180°_y, 180°_y may be used to generate two spin echoes after a single excitation pulse. In theory, T_2 can be measured from a single CPMG experiment without repetitions. If a constant time delay (2τ) between adjacent 180° refocusing pulses is used, the echo amplitudes are given by:

$$M_{xy}(2n\tau) = M_{xy}(0)e^{-2n\tau/T_2} = M_{xy}(0)e^{-TE(n)/T_2}$$

Here, n is the current echo number in the refocusing pulse train.

1.2.8 Steady state free precession (SSFP)

The efficiency of NMR experiments is limited by the need to wait for regrowth of longitudinal magnetization between signal measurements. For FID experiments, a lower flip angle can be used to reduce the repetition time (TR) but this results in low signal amplitudes. An alternative is to allow the magnetization to reach a dynamic equilibrium by continuously applying B_1-pulses in close succession with a constant repetition time. TR is kept short relative to transverse relaxation such that transverse magnetization is maintained. Therefore, the signal at dynamic equilibrium, also called the steady state, depends on both T_1 and T_2 relaxation. This experiment was first suggested by Carr[13] and is called steady state free precession (SSFP). The B_1 phase is often shifted 180° between excitations (e.g. 90_x, 90_{-x},

90_x, etc), resulting in refocusing of dephased spin. This refocusing mechanism creates an echo signal centered at time point $TR/2$ after the end of a B_1 pulse, with an echo amplitude which is attenuated by T_2 and T_1 relaxation rather than T_2^* and T_1 relaxation. However, such refocusing can only be achieved for a limited range of off-resonance frequencies and for a frequency of approximately $\frac{1}{2TR}$ the signal becomes highly attenuated. This effect is known as the SSFP banding artifact in magnetic resonance imaging (MRI). The sensitivity to off-resonance can be reduced by reducing the TR, making SSFP particularly useful for rapid NMR experiments. In addition, high flip angles can be used. The combination of short TR and high flip angles gives SSFP currently unmatched signal amplitude per unit time. The SSFP pulse sequence is extensively used for cardiovascular magnetic resonance imaging at 1.5T. At field strength 3T or higher, the off-resonance sensitivity becomes problematic.

1.2.9 The effect of linear magnetic field gradients

In addition to inhomogeneity of the static B_0 magnetic field (section 1.2.5), off-resonance frequencies and widening of the NMR frequency spectrum can be induced by a purposely designed variation in magnetic field strength across the sample, along a specific direction. When such a field variation is present, the Larmor frequency will vary across the sample and broadening of the NMR frequency spectrum will occurr. A linearly varying magnetic field, also known as a field gradient, causes the Larmor frequency to vary along the direction of the magnetic field variation according to:

$$\omega(r) = \gamma(B_0 + Gr)$$

Here, r is the coordinate along the direction in which the gradient is applied and G is the gradient amplitude which is commonly measured in millitesla per meter (mT/m). The gradient field is usually designed to be centered around the position in the magnetic field which is calibrated to have a field strength as close as possible to the ideal value B_0. This point is also known as the isocenter of the static magnetic field. The coordinate r is then defined to be negative on one side of the isocenter and positive on the other. For a gradient field centered around the isocenter, the Larmor frequency will equal the center frequency (γB_0) at the isocenter, and it will be lower and higher for negative and positive r coordinates, respectively. Three gradient fields with orthogonal directions can be combined to create a linearly varying magnetic field strength along any direction in space.

By applying a linear magnetic field gradient with strength G across a sample after a B_1 excitation pulse, the FID signal will have an accelerated signal decay and spin orientations will dephase at a faster rate due to the induced variation in Larmor frequency (section 1.2.5) across the sample. The accumulated phase induced by the gradient field for stationary nuclei at a given coordinate depends on the amplitude of the gradient field and the duration for which it is activate, according to:

$$\phi_G(r) = \gamma r \int_0^{\tau_G} G(t)dt$$

Here, $G(t)$ is the gradient amplitude over time, τ_G is the gradient duration and $\phi_G(r)$ is the accumulated phase of spin orientation induced by the gradient field at position r. The time integral of the gradient amplitude ($\int_0^{\tau_G} G(t)dt$) is known as the zeroth order gradient moment.

The dephased spin orientations can be rephased by applying a second gradient pulse with opposite polarity compared to the first gradient pulse. If the zeroth order gradient moment of the second gradient pulse is equal to or larger than that of the first gradient pulse, an NMR signal echo will form which is known as the **gradient recalled echo** (GRE). The maximum amplitude of the gradient recalled echo is found at the time point for which the total zeroth order gradient moment from both gradient pulses is zero. A pair of gradient pulses which have opposite polarities and which are applied in direct succession is called a **bipolar gradient pulse**.

Similar to the multi-echo spin echo technique (described in section 1.2.7), a train of bipolar gradient pulses can be used to generate multiple gradient echoes following a single B_1 excitation pulse. This technique is called the multi-echo gradient recalled echo pulse sequence, or mGRE. The T_2^* time constant can be measured from an mGRE experiment by using the maximum signal amplitude of each gradient echo together with the mono-exponential signal decay model described in section 1.2.7.

Linear magnetic field gradients are applied in several subfields of NMR. For example, magnetic field gradients are used for image formation in magnetic resonance imaging (MRI).

Phase contrast velocity measurements

In the presence of flow, the application of a bipolar gradient pulse with a total zeroth order gradient moment equal to zero will not rephase the spin orientations completely if parts of the flow occur along the magnetic field gradient. In this case, the accumulated phase from a gradient pulse can be described as:

$$\phi_G = \gamma \int_0^{\tau_G} G(t)r(t)dt$$

Here, the time point corresponding to $t = 0$ is immediately before the activation of the gradient pulse, τ_G corresponds to the end of the gradient pulse and the position of spins along the gradient field direction $r(t)$ changes over time. If the flow velocity can be assumed to be constant during the application of the gradient pulse, the spin position along the magnetic field gradient can be described as $r(t) = r(0) + vt$ and the total accumulated phase during the gradient pulse can be approximated to:

$$\phi = \phi_\epsilon + r(0)\gamma \int_0^{\tau_G} G(t)dt + v\gamma \int_0^{\tau_G} G(t)tdt$$

Here, the background phase ϕ_ϵ is the accumulated phase due to effects other than the gradient pulse, for example static magnetic field inhomogeneity, and v is the constant velocity along the gradient direction. The second time integral term ($\int_0^{\tau G} G(t)tdt$) is known as the first order gradient moment. If a bipolar gradient pulse is used, the zeroth order gradient moment ($\int_0^{\tau G} G(t)dt$) equals zero.

Since the phase signal $\phi(r)$ includes a background phase term ϕ_0, the phase signal alone cannot be used to measure velocity. Instead, two measurements (e.g. two FID or two gradient echo experiments) are performed with different first order gradient moments M_1 and M_2, and the phase signals are subtracted:

$$\Delta\phi = v\gamma \int_0^{\tau G} G_1(t)tdt - v\gamma \int_0^{\tau G} G_2(t)tdt = v\gamma(M_1 - M_2) = v\gamma\Delta M$$
$$=> v = \frac{\Delta\phi}{\gamma\Delta M}$$

This technique is known as **phase contrast magnetic resonance** (**PC-MR**) velocity measurements[14]. In practice, first order gradient moments from two bipolar gradient pulses with opposite polarity are often subtracted. The phase difference signal will often contain residual background phase components. Therefore, background phase correction needs to be performed during

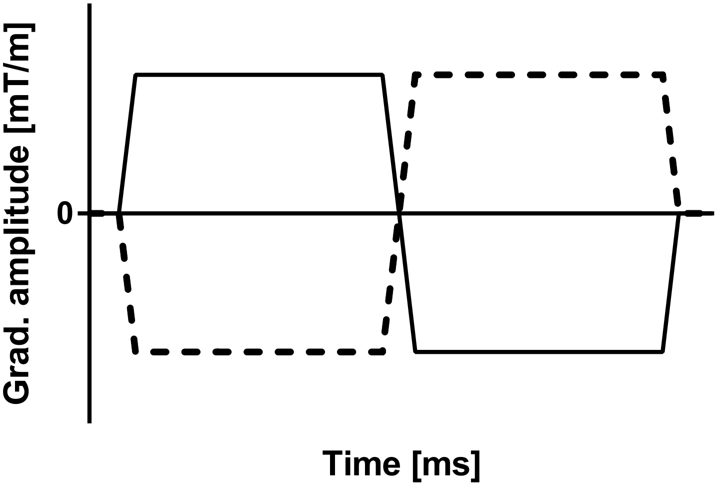

Figure 1.5 This diagram shows two bipolar gradient pulses with opposite polarity (solid and dashed lines) which can be used for PC-MR velocity measurements. Each bipolar gradient pulse is applied in separate NMR measurements performed in close succession. phase signals from both measurements are subtracted to obtain a velocity estimate.

data analysis, described further in section 1.3.2. Figure 1.5 shows an illustration of two bipolar pulses with opposite polarity which can be used for PC-MR velocity measurements.

1.2.10 NMR pulse sequence parameters and signal weighting

Signal averaging of repeated experiments are often used in NMR to reduce the influence of noise. In this setting, different degrees of T_1, T_2 or T_2^* relaxation can be imposed on the NMR signal by changing the pulse sequence parameters in use, also called NMR signal weighting. In previous sections the pulse sequence parameters flip angle (FA), echo time (TE) and repetition time (TR) have been used to obtain NMR signal amplitudes effected by different degrees of T_1, T_2 or T_2^* relaxation. In addition to the already mentioned pulse sequences for relaxometry, T_1 and T_2^* weighting can be achieved by simply repeating a gradient recalled echo experiment, using a B_1-pulse with constant flip angle and phase. A T_1-weighted NMR signal can be generated by using a short echo time (TE) to minimize the effect of T_2^* relaxation and a short repetition time (TR) to introduce partial saturation of the NMR signal due to incomplete longitudinal recovery between B_1-pulses. In this experiment, a strong magnetic field gradient, also known as a crusher gradient, is often used after each NMR measurement to dephase transverse magnetization before the next B_1 excitation pulse.

A T_2^*-weighted NMR signal can be generated by using a long echo time (TE) to induce substantial decay of transverse magnetization due to T_2^* relaxation, and a long repetition time (TR) which enables near complete longitudinal recovery between B_1-pulses, minimizing the effect of T_1 relaxation on the signal. T_2 weighting can be achieved by using the same principles as for T_2^* weighting and replacing the gradient recalled echo with a spin echo experiment. If a short TE is used together with a long TR, relaxation will have limited effect on the NMR signal, which instead will have a spin density weighting, also called proton density (PD) weighting.

1.2.11 Magnetic Resonance Imaging (MRI)

In 1973, Lauterbur published the first image formed from NMR measurements[15], using a method called Zeugmatography. In this experiment, NMR measurements were performed during the application of a linear gradient field across the sample. The frequencies in the NMR spectrum corresponded to a position along the gradient field direction and the NMR spectrum amplitudes represented a projection of the sample spin density along the gradient direction. Several projections at different angles were obtained by rotating the gradient field direction and repeating the NMR measurement. An image was formed by combining the projections at different angles using a backprojection reconstruction algorithm, similar to the Radon transform [16]. In this method, the image resolution depends on the number of, and angular density of, collected image projections and also the NMR frequency bandwidth of the imaged nuclei. This bandwidth increases for increasing inhomogeneity of the static magnetic field and for large decay of transverse magnetization. The method averaged the spin density of a sample along the gradient field rotational axis (perpendicular to the gradient field directions) and therefore assumes that the sample is uniform in this direction. This limitation can be removed by using a combination of three orthogonal gradient fields such that spin density projections can be generated in any direction in space, which enables 3D-imaging.

In 1974, Ernst and colleagues introduced NMR Fourier Zeugmatography[17], also called **Fourier imaging with cartesian sampling**, and is still used in modern MRI methods. Similar to the original Zeugmatography experiment, NMR measurements are performed concurrent with the activation of a linear gradient field (G_x). However, prior to the NMR measurement, and immediately after spin excitation by a B_1-pulse, two gradient pulses are applied in succession (G_z and G_y) which are orthogonal to each other and the gradient pulse (G_x) which is active during NMR measurement. Figure 1.6 illustrates the timing of the B_1-pulse and gradient pulses in the experiment. Variations in spin orientation are thus encoded along all three directions in 3D-space. This experiment is based on the observation that the total accumulated spin phase at position **r** $= (x, y, z)$ from three orthogonal gradient pulses with amplitudes $G_z(t), G_y(t), G_x(t)$ which are applied during separate time intervals, equals the sum of accumulated spin phase from each gradient pulse. The accumulated phase of spin due to the three orthogonal gradient pulses at position (x, y, z) can be described as:

$$\phi_G(x,y,z) = z\gamma\int_0^{t_z} G_z(t)dt + y\gamma\int_{t_z}^{t_y} G_y(t)dt + x\gamma\int_{t_y}^{t_x} G_x(t)dt$$

If the gradient amplitudes are kept constant over time during the experiment this expression can be simplified to:

$$\phi_G(x,y,z) = \gamma(zt_zG_z + y(t_y - t_z)G_y + x(t_x - t_y)G_x) = \gamma(zT_zG_z + yT_yG_y + xT_xG_x)$$

Here, T_z, T_y and T_x are the durations of each gradient pulse. The measured NMR signal in this experiment will contain spin orientations with different phase shifts over the sample volume. A signal phase shift by angle ϕ can be described by a complex number according to Eulers formula ($e^{i\phi} = cos(\phi) + isin(\phi)$). Therefore, the measured NMR signal which contains an ensemble of different phase shifts is proportional to the integration of phase shifts over the sample volume $S(t)$ according to:

$$S(t) = \int\int\int \rho(x,y,z)e^{i(\gamma B_0 t + \phi_\epsilon(x,y,z,t) + \gamma(zT_zG_z + yT_yG_y + x(t - t_y)G_x))}dzdydx$$

Here, $\phi_\epsilon(x, y, z, t)$ is the accumulated phase due to effects other than the gradient pulses and B_0. $\rho(x, y, z)$ is the spin density at coordinate (x, y, z). The signal can be demodulated such that the accumulated spin phase due to the static magnetic field B_0 becomes invisible, which corresponds to observation of the NMR signal in the rotating frame of reference (described in section 1.2.6). Further, if the accumulated phase due to effects other than the gradient pulses and B_0-field is negligible, the expression can be simplified to:

$$S(t) = \int\int\int \rho(x, y, z)e^{i\gamma(zT_zG_z+yT_yG_y+x(t-t_y)G_x)}dzdydx$$
$$=> S(k_z, k_y, k_x) = \int\int\int \rho(x, y, z)e^{i2\pi(zk_z+yk_y+xk_x)}dzdydx$$

Here, a change of variables was performed such that $k_z = \frac{\gamma T_z G_z}{2\pi}$, $k_y = \frac{\gamma T_y G_y}{2\pi}$ and $k_x = \frac{\gamma(t-t_y)G_x}{2\pi}$. The variable S in the new coordinate system, known as k-space, equals the inverse Fourier transform of the spin density $\rho(x, y, z)$, which can be obtained by Fourier transformation:

$$\rho(x, y, z) = \int\int\int S(k_z, k_y, k_x)e^{-i2\pi(zk_z+yk_y+xk_x)}dk_zdk_ydk_x$$

Since the NMR signal in this experiment is approximately proportional to variable S, the Fourier transform of the NMR signal is approximately proportional to the spin density $\rho(x, y, z)$. Using this technique, each MRI image is a two-dimensional frequency spectrum.

In order to form an image, the NMR Fourier experiment needs to be repeated using different values of k_z and k_y, while k_x is sampled continuously since the gradient field along this direction is active during the NMR measurement. The phase steps performed by k_z and k_y are usually called **phase encoding** and the continuous dephasing during the NMR measurement which is performed by k_x is usually called **frequency encoding**. The required number of repeated experiments depends in the prescribed image resolution, or voxel size, and the image field of view (FOV), according to Fourier theory.

The original experiment used an FID pulse sequence together with a frequency encoding gradient pulse with a single polarity. Frequency encoding with a gradient of single polarity causes the NMR signal to dephase rapidly. Instead, a bipolar gradient pulse is commonly used for frequency encoding in order to create a gradient echo signal. Most NMR pulse sequences, for example spin echo or SSFP, can be used together with this imaging method and many currently used MRI techniques are based on NMR Fourier Zeugmatography. However, the method is rather time consuming since the entire volume of the sample is imaged, which is not needed in all applications.

Another method for NMR imaging was proposed by Mansfield and colleagues[18] who used frequency selective RF-pulses together with linear gradient fields to only excite spin within a thin slice of the sample. In one of the proposed techniques the RF-pulse amplitude over time was modulated such that the excitation frequency spectrum was focused within a narrow bandwidth around a center frequency. A linear gradient field was applied at the same time as the RF-pulse which resulted in spin excitation within a thin slice of the sample. This technique is called **slice selection** and the width of the excitation spectrum is called **slice thickness**.

Todays MRI techniques commonly use a combination of slice selection and cartesian sampling. For two-dimensional imaging, a thin slice is excited along one direction and cartesian sampling is performed along the other two orthogonal directions. For 3D imaging, slice selection is commonly used to excite a thick slab of interest and cartesian sampling is performed in all three orthogonal directions in space. The most commonly used method in cardiovascular MRI is two-dimensional imaging with slice selection and cartesian sampling.

The hydrogen nucleus is imaged in most MRI techniques due to its abundance in biological tissue. The gyromagnetic ratio of hydrogen is approximately 42.6 MHz/T, resulting in a Larmor frequency of approximately 64MHz and 128MHz at the clinically used $B0$ field strengths 1.5T and 3T.

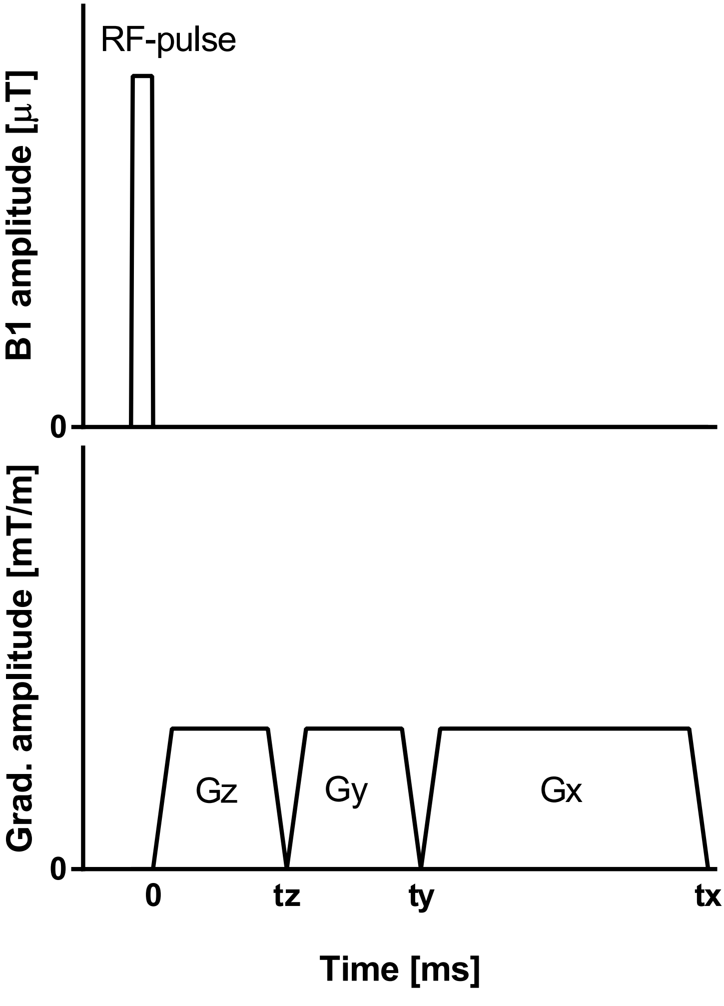

Figure 1.6 Diagram of the original Fourier Zeugmatography experiment by Ernst et al[17], showing the amplitude of the B_1 excitation pulse over time (top) together with the amplitudes of three orthogonal gradient-fields Gz, Gy and Gx over time (bottom). The NMR signal is continuously sampled when the Gx gradient pulse is active. In the original experiment, an FID pulse sequence was used for spin excitation. However, most pulse sequences can be used for Fourier Zeugmatography, which is also known as Fourier imaging with cartesian sampling.

1.3 Cardiovascular magnetic resonance imaging

In cardiovascular MRI, SSFP pulse sequences are commonly used to obtain high image contrast between blood and myocardium, high signal amplitude and efficient imaging. In addition, gradient echo pulse sequences are routinely used for phase contrast blood flow measurements or T_2^* weighted imaging.

Imaging is often performed at a specific time point of the cardiac cycle. For this purpose, the surface electrocardiogram (ECG) is recorded and imaging is triggered at a user-specified delay after the R-wave. The diastasis in mid-diastole is commonly imaged to avoid image artifacts and blurring due to rapid cardiac motion. The image acquisition can be segmented such that only parts of the needed kspace data are acquired in each heart beat. This technique can be used to reduce the imaging duration for each heart beat at the cost of prolonging acquisition.

An alternative is to acquire time resolved cine images of the heart using image gating. In this technique, the ECG-signal is recorded and the same segment of k-space is continuously acquired. Upon detection of an R-wave, a new k-space segment is acquired. The process is repeated over a number of heart beats such that all k-space segments are acquired over a heart beat. Time resolved cine images can then be retrospectively reconstructed by sorting the k-space data such that only data from the same cardiac time phase is combined into an image. In theory, image gating can be used to obtain a time resolution equal to TR.

1.3.1 Cardiac magnetic resonance relaxometry

The basic principles of relaxometry are the same in cardiac applications as for NMR. A set of differently T_1-,T_2- or T_2^*-weighted signals (in this case images) are acquired and the time constant of interest is extracted from nonlinear regression of the signal points using a signal model which includes the time constant as an unknown parameter (section 1.2.7).

Rapid pulse sequences combined with appropriate gating techniques are needed for relaxometry in the heart. Generally, an ECG-trigger is used to ensure that imaging is performed in mid-diastole in order to minimize image artifacts and blurring due to cardiac motion.

In the case of imaging during a single breathhold, total acquisition times need to be approximately less than 16 seconds. Since relaxometry generally involves the acquisition of 8-15 images, single breathhold imaging usually requires single-shot acquisition to be used, in which each contrast prepared image is fully acquired in a single heart beat.

The alternative is to use a respiratory motion navigator which commonly measures diaphragm motion and triggers imaging in end-respiration. With a respiratory motion navigator, single-shot acquisition is no longer needed and only parts of the k-space data used to form an image can be acquired in each heart beat. This improves the time resolution of each image, reducing blurring and artifacts from cardiac motion, but increases the total acquisition time as more heartbeats are needed for the same relaxometry measurement.

For cardiac $T1$-measurements, **saturation-recovery** or **inversion-recovery** based methods are most commonly used[19, 20]. To enable inversion-recovery T_1-measurements within a single breathhold, several images are acquired after each inversion preparation and a correction factor[21] is applied to estimate $T1$. Since imaging is restricted to mid-diastolic time intervals, RF-pulses for imaging are applied in a segmented fashion and not continuously after inversion preparation which was the case for the experiments in which the correction factor was derived[21]. Further, a steady-state free precession (SSFP) imaging pulse sequence is commonly used for cardiac T_1-measurements, which was not used in the original experiments[21]. These differences between inversion-recovery based cardiac T_1-measurements and the originally proposed methodology causes the use of a correction factor to introduce bias in the $T1$-estimate. Saturation-recovery based cardiac T_1-measurements which only acquire one image after each saturation preparation does not have this bias.

Myocardial T_2 measurements can be performed by using a T_2 prepared SSFP pulse sequence. In this pulse sequence, T_2 contrast is generated by a spin echo preparation pulse acting on the entire imaging volume, the transverse magnetization is stored along the longitudinal axis and a mid-diastolic SSFP image is acquired in a single shot. This process is repeated using different spin echo TE, after a user-specified number of recovery heart beats. The recovery heart beats are used to minimize the T_1 weighting of the signal points. Despite using recovery heart beat, images from this pulse sequence will be slightly T_1 weighted due to the SSFP acquisition and the signal model becomes[22]:

$$M_{xy}(TE) = M_{xy}(0)e^{-TE/T_2} + C$$

Here, C is an additional unknown parameter used to enable unbiased T_2 estimation from this pulse sequence.

In the studies presented in this dissertation, invivo cardiac relaxometry is performed using single breathhold imaging only.

1.3.2 2D phase contrast magnetic resonance blood flow quantification

The phase contrast magnetic resonance (PC-MR) technique, which was described in section 1.2.8, can be used to measure velocity and flow in the human body. For this purpose, time-resolved and ECG-gated PC-MR imaging is performed to measure velocities over an average heart beat. Velocities can be measured both parallel or perpendicular to the imaging plane. The flow volume through a blood vessel is measured by using a PC-MR imaging plane oriented along the vessel cross-section, and measuring velocity perpendicular to the imaging plane (parallel to the main blood flow direction). After the vessel of interest has been delineated in all PC-MR images over a heartbeat, the blood flow volume can be calculated as the flow time integral:

$$\int_0^T \bar{v}(t)A(t)dt$$

Here, $\bar{v}(t)$ is the average velocity inside the vessel delineation at time point t of the cardiac cycle, $A(t)$ is the delineation area at t and T is the RR-interval duration.

Correction of background phase residuals in PC-MR images can be performed by finding multiple image regions containing only stationary tissue and fitting the phase spatial variation of such regions to an assumed model. The model which best fit the phase data is then subtracted from the phase difference images before velocities are analyzed. A two dimensional linear polynomial is most commonly applied for background phase correction.

Metric Optimized Gating (MOG) for PC-MR flow measurements

Time resolved PC-MR imaging is usually performed by gating the acquisition with an ECG-recording. Lack of a usable ECG limits the use of fetal PC-MR imaging. To overcome the need for a fetal ECG, Metric Optimized Gating (MOG) [23] was introduced. MOG oversamples each fetal heartbeat such that every k-line acquisition is repeated over at least one fetal RR interval. Retrospective reconstruction is performed by successively discarding a number of k-line repetitions until all data points span over approximately one fetal heartbeat, resulting in time-resolved PC-MR cine images without severe gating artifacts.

An optimization algorithm is used to find the heart rate which results in minimal misgating artifacts. This optimization algorithm uses a 2-parameter piecewise constant heart rate model which assumes that the heart rate during a PC-MR acquisition is changing only once, in the middle of the scan when the central k-space line is acquired. With this heart rate model the optimization algorithm tries to find the two heart rates which results in the maximum time entropy within a user defined region of interest (ROI) in PC-MR images. During this process, the phase difference signal is multiplied with the magnitude signal for noise robustness. This method assumes that misgating results in reduced pulsatility and has been shown to be robust to moderate heart rate variability[23].

Chapter 2

Aims

The aim of the work presented in this dissertation was to develop and evaluate quantitative flow and relaxometry techniques for cardiovascular magnetic resonance imaging with the purpose of enhancing clinical applicability. The specific aims of each study were:

I. To validate a new automatic algorithm for offline T2*
determination for estimation of iron load in the heart and liver.

II. To validate a software for generating T1 and T2 relaxation maps from multiple signal models.

III. To validate a new simulation based post-processing method for improving the accuracy of T1 measurements from the MOLLI pulse sequence based on Bloch simulations of a large spin population with physiologically relevant tissue relaxation constants.

IV. To 1) develop a new vessel delineation algorithm with shape constraints based on manual vessel delineations, 2) validate the method in phantom experiments and 3) compare the method to manual delineation in 2D PC-MR images invivo in the ascending aorta and main pulmonary artery.

V. To 1) validate the previously published method Metric Optimized Gating PC-MR flow measurements for a range of fetal flow velocities using an independent reference standard in phantom experiments; and 2) investigate interobserver variability for fetal flow measurements at an additional imaging center.

Chapter 3

Methods

The protocols and procedures comply with the Declaration of Helsinki, and were approved by the local ethics committees.

3.1 Study population

Collected data did not overlap for any of the presented studies. In **study I**, patients with known or suspected iron load disease (n=23; 15 male; median age 18 years; range 1-69 years) were included and MR images for T2* measurements were acquired as part of routine clinical iron load assessment. In **study II**, One healthy fetus (gestational week 36), one healthy volunteer (female, 15) and one patient with myocarditis (male, 17 years) were included retrospectively. One healthy volunteer (male, 27 years) was included prospectively. In **study III**, healthy volunteers (n=12; 12 male; age 34±12 years) were prospectively included. In **study IV**, a total of 201 human subjects were retrospectively included (50 females; median age 56 years; age range 3-98 years). 18 healthy volunteers and 153 patients with heart failure, defined as having left-ventricular ejection fraction<40%, were included from a previous study of cardiac index[2]. 16 healthy volunteers and 14 patients with atrial septal defects were included from a previous study of atrial septal shunt volumes[24]. In **study V**, healthy fetuses (n=15; gestational week 30-37) were prospectively included.

3.2 Phantom experiments

Phantom experiments were performed to compare measurements designed for invivo use to reference standard measurements. In **studies I-III** pulse sequences and algorithms for invivo relaxometry were evaluated in gel-phantoms while phase contrast flow and velocity measurements were evaluated using a pulsatile flow phantom in **studies IV-V**.

3.2.1 Relaxometry (Studies I-III)

MR relaxometry was performed in gel-phantoms with T1/T2* or T1/T2 values similar to human tissue. In **study I**, twelve phantoms consisting of a mixture of water, agarose, gadolinium (DOTAREM; Guerbet France) and ferumoxsil (LUMIREM; Guerbet, France) were used with T1 range 470-1012ms and T2* range 2.2-40.2ms at 1.5T. Each phantom was scanned separately and was submerged in water during MR imaging to reduce potential susceptibility artifacts.

In **study II**, a Eurospin phantom (Diagnostic Sonar, Livingston, UK) with 12 gel vials were used consisting of a mixture of water, agarose and gadolinium.

In **study III**, two sets of phantoms were scanned: 1) Six vials with a T1 range 210-1520ms and T2 range 44-58ms from the Eurospin phantom which was also scanned in study II; and 2) Six phantoms consisting of a water, agarose and $CuSO_4$ mixture with T1/T2 values similar to pre- and post-contrast myocardium and pre-contrast blood at 1.5T.

Phantoms were placed in the scanner iso-center 2 hours prior to MR imaging to avoid potential T1 drifts during the experiment due to changes in phantom temperature.

3.2.2 Flow quantification (Studies IV-V)

A previously built pulsatile flow phantom[25] consisting of a pulsatile pump, a flow rectifier and a water tank were used for phantom validation in **studies IV-V**. 2D PC-MR flow measurements were compared to timer and beaker flow measurements over a range of flow rates. Timer and beaker flow measurements were performed by measuring the total water volume output from the water tank during 2-4 minutes of continuous pumping and were repeated before and after PC-MR measurements to detect potential flow drifts over time. A timing signal from the servo motor of the pump was forwarded to the pulseoximetry trigger system of the MR scanner to enable retrospective image gating.

In **study IV**, 2D PC-MR flow volume measurements were compared to timer and beaker in flow volume range 12-89ml at 1.5T, and flow volume range 24-89ml at 3T. PC-MR velocity and flow were measured through plastic tubing inside the water tank with inner diameter 26mm.

In **study V**, PC MR flow and velocity measurements using the Metric Optimized Gating method (MOG) were compared to timer and beaker flow and conventionally gated PC-MR velocity measurements at 1.5T. The pulsatile flow phantom setup from study IV was modified to use a pump stroke frequency (145bpm) and flow rates (130-700ml/min) similar to fetal blood flow conditions. The inflow nozzle of the water tank was extended to have a section with inner diameter (6mm) comparable to the fetal descending aorta and umbilical vein during the third trimester.

3.3 Magnetic Resonance Imaging

Images were acquired on MR scanners with field strengths 1.5T and 3T and human subjects were scanned in supine position, the exception being pregnant volunteers in study V, who were scanned in left lateral decubitus position. In **study I**, 1.5T Achieva scanners (Philips Healthcare, Best, The Netherlands) were used at two centers with a 5- or 32-channel phased array cardiac coil (invivo imaging) and a 6-channel SENSE head-coil (phantom imaging). In **Study II** scanners from three different MRI vendors were used: One 1.5T Aera and one 3T Prisma scanner (Siemens Healthcare, Erlangen, Germany) with 60-channel phased array chest coils (invivo imaging) and 20-channel head coils (phantom imaging), one 1.5T Achieva scanner (Philips Healthcare, Best, The Netherlands) with a 32-channel phased array coil and one 3T Discovery 750w scanner (General Electronics, USA) with a GEM flex medium array coil. In **Study III**, imaging was performed on a 1.5T Achieva scanner (Philips Healthcare, Best, The Netherlands) with a 32-channel phased array coil. In **Study IV**, MR images from a 1.5T Magnetom Vision scanner, a 1.5T Aera scanner, a 3T Prisma scanner (Siemens Healthcare, Erlangen, Germany) and a 1.5T Achieva scanner (Philips Healthcare, Best, The Netherlands) were used. In **Study V**, a 1.5T Aera and a 3T Prisma (Siemens Healthcare, Erlangen, Germany) were used with a 16-channel phased array chest coil and one spine imaging coil.

3.3.1 T2* measurements (Study I)

In **study I** T2* measurements were performed both in phantoms and in human subjects. In the invivo study, T2* was measured in the heart and liver of patients with known or suspected iron load disease using multi-echo gradient recalled echo (mGRE) pulse sequences.

For cardiac imaging, a mid-ventricular short-axis slice was acquired at end-diastole within a time window of 110ms per heartbeat. A double-inversion recovery (DIR) prepulse was used to generate black-blood image contrast to reduce blood signal contamination on myocardial T2* measurements and enhance myocardial borders. Parallel imaging factor 2 (SENSE) was used to enable image acquisition within a single breathhold and SPIR fat suppression was applied to reduce the impact of fat on the measurement. The pulse sequence used voxel size 2x2x10mm^3, Flip angle 20°, TR 26ms and TE [2.5, 5.0, 7.5, 10.0, 12.5, 15.0, 17.5, 20.0, 22.5, 25.0] ms.

For liver imaging, a midhepatic transversal slice was acquired during free breathing and using a mGRE pulse sequence with SPIR fat suppression, voxel size 3x3x10mm^3, Flip angle 20°, TR 17ms and TE [1.2, 2.7, 4.2, 5.7, 7.2, 8.7, 10.2, 11.7, 13.2, 14.7]ms.

T2* was measured in phantoms using mGRE pulse sequences similar to the sequences used for invivo imaging. In addition, T2* reference standard measurements were performed in phantoms with a single-echo gradient recalled echo pulse sequence for which TR was set to 6xT1 to enable near complete longitudinal relaxation between excitation rf-pulses, a voxel size 1.96x2x10mm^3, Flip angle 50°, and TE [1.34, 2, 3, 5, 7.5, 10, 12.5, 15, 20, 30, 40, 50, 75, 100, 150, 200, 300]ms.

For all mGRE sequences, T2* maps were automatically generated on the scanner by the Maximum Likelihood Estimation (MLE) algorithm [26].

For offline T2* measurements using the introduced ADAPTS method, regions of interest were manually drawn within the mid-ventricular septum and in a homogenous area of liver parenchyma in T2* weighted images.

3.3.2 T1 measurements (Studies I-III)

The MOdified Look Locker Inversion-recovery pulse sequence (MOLLI) was used to measure T1 in phantoms (Studies I-III) and to measure myocardial T1 in human subjects (Studies II and III). Cardiac MOLLI T1 measurements were performed in short-axis and long-axis imaging planes. MOLLI schemes 5b(3b)3b and 4b(1b)3b(1b)2b were applied in studies I-III for T1 measurements in estimated intervals T1<500ms and T1>500ms, respectively. In study III, one additional MOLLI scheme (5b(0b)3b) without recovery RR-intervals between inversion pulses was acquired.

In addition to MOLLI, T1 reference standard measurements by an inversion-recovery single-echo spin echo pulse sequence with the TR set to 10s were performed in phantoms in studies II-III. In the phantom validation of study II, T1 was also measured by two versions of a single-shot bSSFP pulse sequence, one version using a saturation prepulse and one version using an inversion prepulse. Parameters for the bSSFP pulse sequence were voxel size 1.9x1.9x6mm^3, Flip angle 35°, TE/TR 1.1/2.4ms and time delay between prepulses 40s. For each T1 measurement, the Inversion-recovery bSSFP pulse sequence used 16 T1-weighted images with inversion time range 150-6300ms and one image without contrast preparation. the saturation-recovery bSSFP pulse sequence used 18 T1-weighted images with saturation time range 150-8000ms and one image without contrast preparation.

In study II, T1 was calculated from mono-exponential nonlinear least squares fitting to the measured signal points with three unknown parameters and using the signal model $S(t) = A - Be^{-t/T1}$ where A, B, and T1 are the unknown parameters to be determined and t is the time delay between the end of each prepulse and the following signal measurement.

For the MOLLI pulse sequence, the Look Locker correction[21], $T1 = T1^{*}(B/A - 1)$, was applied after mono-exponential fitting in order to estimate T1.

In study III, T1 was calculated from MOLLI data using both the introduced SQUAREMR method and the conventional mono-exponential fitting method with Look Locker correction described above.

3.3.3 T2 measurements (Studies II-III)

T2 measurements were performed in phantoms and in human subjects in studies II-III. In study II, invivo T2 measurements were performed in the knee of one healthy volunteer using a multi-echo spin echo pulse sequence with voxel size 0.6x0.6x4mm^3, excitation flip angle 90°, refocusing flip angle 180°, TR 1500ms and TE [9, 18, 27, 36, 45, 54, 63, 72, 81, 90, 99, 108, 117, 126, 135, 144]ms. In study III, myocardial T2 measurements were performed using the MOLLI sequence together with SQUAREMR post-processing.

In phantoms, T2 was measured by a single-echo spin echo pulse sequence (Studies II-II), a bSSFP pulse sequence with a T2 contrast preparation pulse (Studies II-III) and MOLLI (Study III). The spin echo pulse sequence was chosen as the T2 reference standard measurement in phantom experiments using a TR of 10s to allow for complete longitudinal relaxation between excitation rf-pulses, voxel size 1.9x1.9x8mm^3, excitation flip angle 90°, refocusing flip angle 180° and TE [6, 12, 20, 30, 40, 50, 70, 90, 120, 140, 180, 300, 400, 600, 1000]ms.

For both spin echo sequences in use T2 was calculated from mono-exponential nonlinear least squares fitting to the measured signal points. The signal model $S(t) = Ae^{-TE/T2}$ with two unknown parameters A and T2, was used for single-echo spin echo data. For multi-echo spin echo data, the signal model $S(t) = Ae^{-TE/T2} + B$ with the three unknown parameters A, B and T2 was applied to reduce T2 bias due to stimulated echoes. For both signal models, TE is the echo time in use.

Parameters for the single-shot bSSFP pulse sequence were voxel size 1.9x1.9x8mm^3, flip angle 35° TE/TR 1.1/2.4ms. The T2 contrast preparation pulse consisted of two excitation pulses with 90° flip angles (flip-down and flip-up) and one refocusing pulse with a 180° flip angle to generate T2 image contrast[27]. Single-shot image acquisition was performed immediately after the T2 preparation pulse. The sequence block consisting of one T2-preparation and one image acquisition was repeated 36 times using different TE for the T2-preparation pulse with TE increment 5ms and range 25-200ms. In order to reduce T2 bias due to T1 effects from the bSSFP acquisition[22], T2 calculation in data from the bSSFP pulse sequence was performed using the same mono-exponential signal model with three unknown parameters as were used for multi-echo spin echo data ($S(t) = Ae^{-TE/T2} + B$).

In study III, MOLLI T2-measurements in phantoms were performed by using SQUAREMR post-processing, described in section 3.5.

3.3.4 PC-MR Flow quantification (Studies VI-V)

Two-dimensional Phase Contrast Magnetic Resonance (2D PC-MR) was used to measure velocity and flow in studies IV-V. Velocity was measured through the selected imaging plane in both studies and PC-MR acquisitions were gated to either measured (PC-MR) or simulated (MOG PC-MR) ECG-signals to enable cine imaging over a heartbeat.

In **study IV**, flow was measured in the ascending aorta (n=171) and the main pulmonary artery of human subjects, using a transversal image orientation and a double oblique image orientation, respectively. PC-MR data were collected using both prospectively gated (n=23 subjects) and retrospectively gated pulse sequences during free breathing and breath-holds (n=18 healthy volunteers).

Flow analysis was performed from time-resolved semi-automatic and manual delineations in the vessel of interest and the net flow volume was calculated as the flow time integral (Figure 3.1). Two different background phase correction techniques were applied for each vendor: 1) Linear background correction in Segment v2.0 R5390 was performed for data from Siemens scanners and 2) Automatic Local Phase Correction built into the scanner was performed during image reconstruction for data from the Philips scanner.

In **study V**, flow was measured by Metric Optimized Gating (MOG) PC-MR in the fetal descending aorta (DAo) and umbilical vein (UV) of fifteen healthy fetuses during maternal breathholds. Image gating was performed using a simulated ECG with 525ms long RR-intervals to oversample the true fetal RR-interval. Fetal RR-intervals were measured by cardiotocography at rest 5 min before the MRI scan in eight subjects, showing maximum RR-intervals with median 444ms (range 413-461ms), resulting in oversampling of 14-27% for MOG PC-MR.

In the phantom experiment of study V, conventionally gated PC-MR data was also acquired in order to validate MOG PC-MR velocity profiles over a beat.

Velocity profiles and flow were quantified from time-resolved manual delineations in study V. In the phantom validation, Regions of interest from conventionally gated PC-MR data were copied to MOG PC-MR images to exclude delineation variability as a confounding factor. In order to reduce PC-MR flow variability due to manual delineations, the phantom nozzle area was measured independently by a 3D-bSSFP sequence at 3T for improved resolution.

3.3.5 Velocity to Noise Ratio in PC-MR data (Study V)

In study V, PC-MR Velocity to Noise Ratio (VNR) was measured in the phantom experiment and was estimated in the fetal descending aorta (DAo) and umbilical vein (UV). VNR was calculated as the peak velocity over a beat divided by the noise standard deviation in phase images. In the phantom experiment, peak velocities were measured in phase images from conventionally gated PC-MR and the noise standard deviation was calculated from the same image region as were used for velocity measurements, in a separate PC-MR acquisition with the water pump turned off.

For fetal imaging, noise standard deviations in the DAo and UV were estimated from a noise prescan which was integrated in the PC-MR acquisition, combined with a previously published algorithm[28]. The noise prescan data from all receive channels were used to estimate the noise covariance matrix. Synthetic normally distributed noise was then generated and synthetic noise for each receive channel were correlated by Cholesky decomposition of the noise covariance matrix. The synthetic noise was added to the k-space PC-MR data which were reconstructed to create a replica of the PC-MR phase images with added noise. This process was repeated to create 128 phase images with added noise and the pixelwise noise standard deviation was calculated. The mean noise standard deviation was finally calculated as the ROI pixel average within the vessel of interest.

As velocities in the fetal DAo and UV were measured using the MOG method, independent peak velocity measurements were not available and VNR in the DAo and UV could not be directly determined. VNR was instead estimated using peak velocity measurements in the corresponding vessels from a previos [29], in which fetal PC-MR was gated using a doppler ultrasound device.

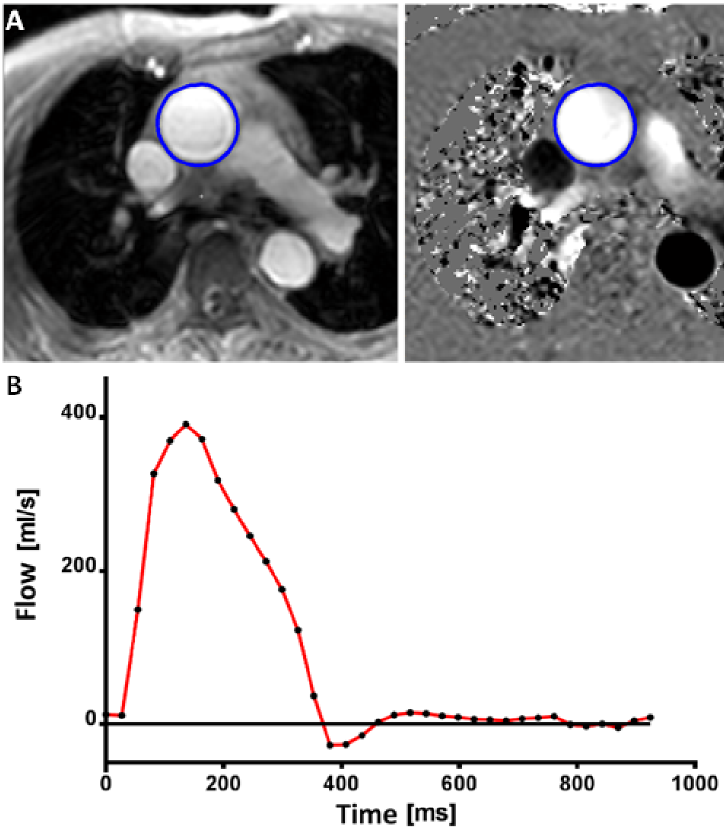

Figure 3.1 Example of a 2D PC-MR flow volume measurement. Top panel (A) shows delineations (blue) of the ascending aorta in a magnitude image in transversal slice orientation (left) and the corresponding phase image (right) in early ventricular systole. The lower panel shows measured flow over time from vessel delineations at all time points of the cardiac cycle. Flow volume is calculated from time integration of this curve.

3.4 Numerical simulations

In **study I**, numerical simulations of T2* measurements were performed to evaluate accuracy and precision of the new T2* algorithm and two previously introduced algorithms[30, 31] for comparison. Mono-exponential T2* decay on the real and imagingary component of a complex signal was generated and zero-mean normally distributed noise were added. The magnitude signal used for T2* measurements was calculated as $M = \sqrt{Im^2 + Re^2}$ where M, Im and Re denotes the magnitude signal, the real part and the imaginary part of the complex signal. Simulated magnitude signals were sampled using two different sets of echo times (TE) with ranges 2.5-25ms and 1-20ms, corresponding to values used in two clinical pulse sequences designed for T2* measurements in the heart and liver at 1.5T. A T2* range of 1-50ms was simulated and simulations were repeated 2000 times. The average T2* error (bias) and 95% confidence intervals were calculated for each T2* algorithm in order to evaluate accuracy and precision. A signal to noise ratio (SNR), defined here as the noise-free magnitude signal at TE=0ms divided by the noise standard deviation, of 15 was used in this simulation study.

In **study III**, simulations of the Bloch equations were used together with the new SQUAREMR method in order to improve T1 accuracy of the MOLLI pulse sequence. Spins with different T1 and T2 values were simulated for T1 range 200-1900ms and T2 range 20-400ms in steps of 1ms, except for spins with T1<T2 which were not simulated.

Simulations of the Bloch equations[9] were performed using the MR physics simulator MRISIMUL by Xanthis et al[32], a MR physics simulator designed for efficient parallel computing on graphical processing units (GPUs). Bloch simulations used a time step of 5μs and RF-pulse slice profiles were taken into account by simulating typically $20 - 100$ spins with the same T1 and T2 values across the slice thickness.

For each MOLLI T1 measurement a total of typically 532 000−63 400 000 simulations of the pulse sequence were performed for a spin population with typically 25 000−628 000 unique T1/T2 combinations. MRSIMUL made it possible to perform all simulations needed for a T1 measurement, including the entire population of spins, on a single server style computer (CPU: $2x$hexa-core 2.3 GHz; RAM: 32GB; GPU: $4x$Nvidia Tesla cards with 6GB GDDR5 memory) without simplifying the MRI physics model.

3.5 Algorithm design and implementation

Algorithms presented in this chapter were implemented in Matlab (Mathworks, Natick, MA, USA), except for the optimization routine used for T1- and T2-map generation in **study III**, which was implemented in the C programming language.

Study I. The new algorithm for ADAPTive T2* estimation from combined Signal models (ADAPTS) is initialized by a manual delineation of the region of interest (ROI) in T2*-

weighted echo-time images, and the ROI pixel average is used for curve fitting. As a first step, T2* is estimated using a mono-exponential signal model with three unknown parameters:

$$S(TE) = PDe^{-TE/T2^*} + C$$

Here, the unknown parameters proton density PD, $T2^*$ and noise-floor C are found from the measured signal S at echo-times TE. This signal model reduces T2* bias from noise in low SNR conditions and for T2* values close to the minimum TE. However, the addition of a third parameter results in lower precision compared to a 2-parameter signal model, which can be used in data with high SNR. The initial T2* estimate is therefore only used to discard images with echo-times longer than a multiple $P1$ of T2* and T2* is re-estimated from remaining echo-time images using a 2-parameter mono-exponential model, similar to the automatic truncation algorithm by He et al [33]:

$$S(TE) = PDe^{-TE/T2^*}$$

The new T2* estimate is only used as final estimate if the number of included images is larger than or equal to parameter $P2$. This check is performed to avoid extensive data truncation, which may lead to unnecessary loss of precision. If the number of images is less than $P2$, T2* is re-estimated again, this time using a previously published 3-parameter noise-correction algorithmFeng et al. [30]:

$$S^2(TE) = PD^2e^{-2TE/T2^*} + 2L\sigma^2$$

Here, σ denotes the noise standard deviation and L the number of receiver coils in use. As previously proposed[30], the right term $2L\sigma^2$ is estimated as one unknown parameter, resulting in a 3-parameter signal model. The purpose of using different signal models and number of included data points in ADAPTS for different signal conditions is to enable robust T2* measurements with high accuracy and precision over a wide T2* interval. Of note, all signal models in use by ADAPTS have been published previously. However, the proposed combination scheme is novel. Algorithm parameters $P1 = 4.5$ and $P2 = 9$ were determined from optimization using data from phantom experiments. The final parameter values were chosen to minimize bias and maximize precision for ADAPTS T2* measurements in two pulse sequences designed for cardiac and liver imaging.

Study II. The software tool for offline T1/T2 measurements was designed to support commonly used mono-exponential signal models with two and three unknown parameters. T1 and T2 curve fitting was performed using the Nelder Mead Simplex nonlinear minimization algorithm [34] which was implemented in the C programming language to reduce computation times.

Study III. The SQUAREMR method was used together with Bloch simulations (described in section 3.4) to improve T1 accuracy of the MOLLI pulse sequence. SQUAREMR compares the signal intensity of each pixel in the acquired inversion-recovery images from a MOLLI T1 measurement with Bloch simulations of the same pulse sequence with identical acquisition parameters for every simulated T1/T2 combination. The simulated T1/T2 pair which best fit the measured signal points, in terms of minimal least squares error, is used as the final T1/T2 estimate.

Study IV. The main aim of the new semi-automatic delineation algorithm for PC-MR images was to provide high delineation accuracy by using multiple refinement steps and high delineation robustness by using shape constrained reconstruction. An overview of the delineation algorithm is shown in figure 3.3. The algorithm is initialized by a manual delineation in one time point of the PC-MR cine image series. Rigid motion-tracking of the vessel of interest is then performed to translate the delineation over time. Interleaved active contour deformations in PC-MR magnitude images and shape constrained reconstruction are used to refine the delineations in each time point.

Delineation refinement is initialized at a time point containing high velocity. Phase images are labeled as either 1) high velocity time point, or 2) low velocity time point by the K-means clustering algorithm[35] and if the manual delineation time point is labeled as high velocity, it is used to initialize delineation refinement. Otherwise, the time point corresponding to maximum velocity is used to initialize delineation refinement.

The algorithm continues with refining remaining time points, first in the high-velocity class and then in the low-velocity class. For each time point, the previously processed delineation from its nearest neighbor is used as starting point. Active contour deformations in PC-MR magnitude images were guided by edge feature images.

After delineation refinement, delineations from high-velocity time points are further processed using active contour deformations in PC-MR phase images in order to increase the inclusion of relevant blood flow. Active contour deformations in PC-MR phase images were guided by filtered and normalized velocity images.

Shape constrained reconstruction was performed by replacing a delineation with a linear combination of typical vessel shape profiles. Vessel shape profiles where extracted from a dataset of 30 manual vessel delineations in time-resolved PC-MR images, 20 delineations of the ascending aorta and 10 delineations of the main pulmonary artery.

The manual delineations where parametrized by resampling (x,y) coordinates into radial distances and resampling the number of time points of each dataset to 20 linearly spaced time points over the cardiac cycle. Principal component analysis (PCA) was performed on the resampled delineations to extract a subset of eigenvectors responsible for 75% of the total variance. The found eigenvectors represent typical vessel shapes in the dataset. A linear combination of eigenvectors can be used to approximate a manual vessel delineation.

Thus, the combination of typical vessel shape profiles used for shape constrained reconstruction were the linear combination of eigenvectors which best approximated the refined delineations, in terms of minimal least squares error.

Algorithm parameters where optimized separately for the ascending aorta and the pulmonary artery, using the same datasets of 30 manual delineations as were used for shape constrained reconstruction.

Study V. No algorithm development was performed in this study.

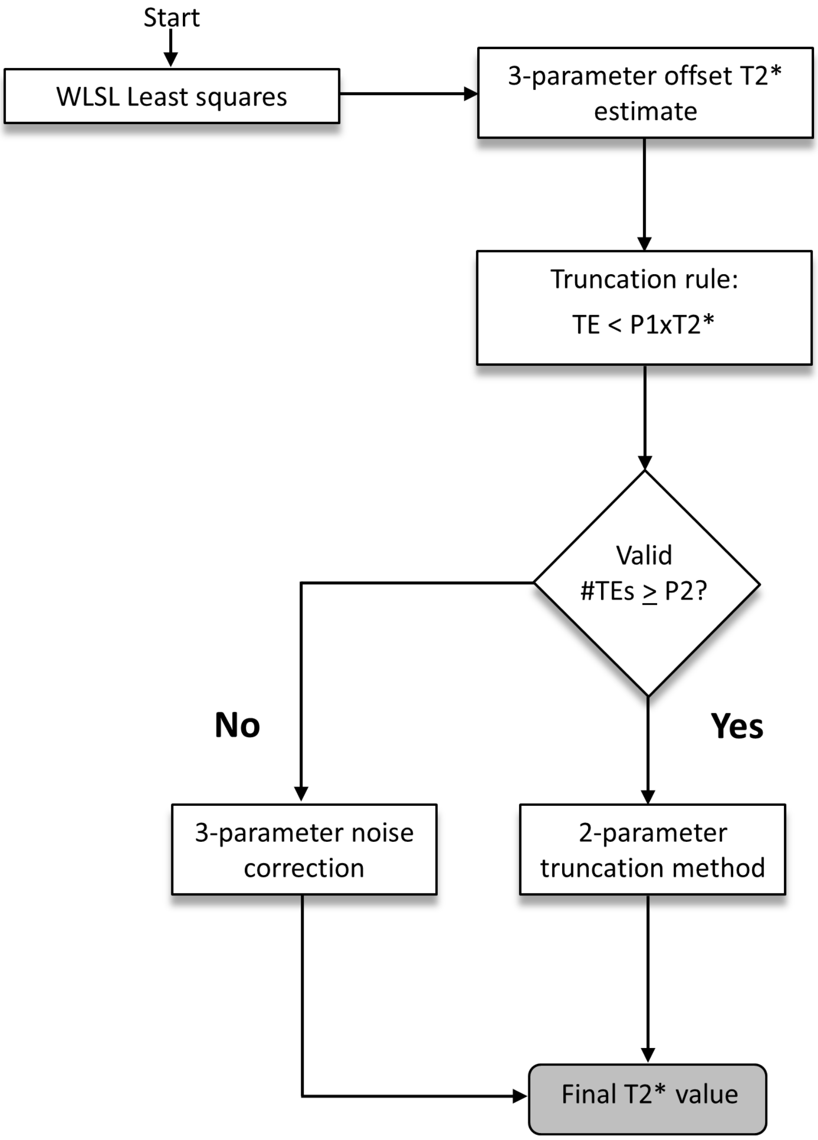

Figure 3.2 Flow chart of the new T2* algorithm from **study I**.

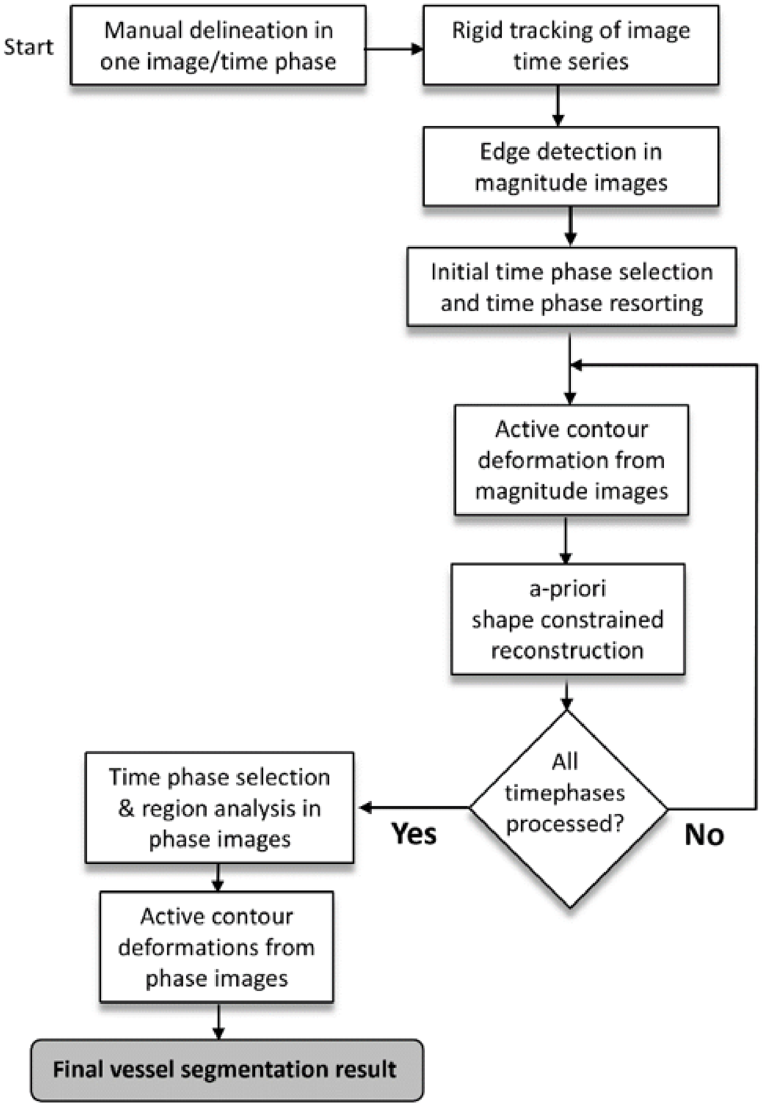

Figure 3.3 Flow chart of the new semi-automatic vessel delineation method from **study IV**.

3.6 Image analysis

Image delineations and measurements were performed in the medical image analysis software Segment v2.0[36], except for MOG processing which were performed using the MOG-Public Software v2.7 (https://github.com/MetricOptimizedGating/MOG-Public).

3.7 Statistical Analysis

Numbers are expressed as mean ± standard deviation (SD), unless stated otherwise. Bland-Altman and Modified Bland-Altman analysis[37] were used to determine bias and variability between two methods, defined as the mean difference ±1.96 SD. For Modified Bland-Altman analysis, error percentages were calculated as differences between two measurements divided by the reference standard measurement and for Bland-Altman analysis, error percentages were calculated as difference between two measurements divided by the average of both measurements. Coefficient of Variation (CV) were computed as the sample standard deviation of differences between measurements divided by their sample mean. Accuracy was determined from the bias of a method compared to a reference standard measurement and 95% confidence intervals (CI) were used to measure precision. In **study III**, a student's two tailed t-test was used to compare paired data. **Study IV** used the Dice coefficient to measure delineation overlap between manual delineations and the new semi-automatic delineation algorithm.

Chapter 4

Results and Comments

4.1 A new T2* algorithm for cardiac and liver iron load determination (Study I)

Patients suffering from iron load disease are at risk of developing organ failure due to iron overload. Iron chelate therapy has been shown to reduce chronic iron overload and improve the prognosis of iron load disease [38]. However, iron chelate therapy is toxic and have been associated with renal failure[39] which warrants careful treatment planning and monitoring of iron load.

Noninvasive T2* measurements by MRI is the current reference standard for assessing iron load in different organs and the technique has been validated to biopsies in the heart and liver [40, 41, 42, 43, 44, 45]. Different algorithms are currently used for determining T2* from MRI images, each with its own advantages and disadvantages at different T2* intervals. In mild to normal iron levels the T2* value is relatively long (T2*>20ms in the heart at 1.5T [40]) and conventional mono-exponential algorithms with only two parameters results in accurate and precise T2* estimation.

In severe iron load the T2* value is short, leading to low signal to noise ratio (SNR) and just a few images with a signal intensity above the noise floor. In this setting, conventional 2-parameter mono-exponential algorithms have been shown to result in overestimation of T2* [46] and are therefore not suitable. Instead, 3-parameter exponential algorithms with noise correction [30] or 2-parameter mono-exponential truncation algorithms which discard images with signal intensity below the noise floor [33] can be used to obtain accurate T2* estimates.

Compared to conventional 2-parameter mono-exponential algorithms, noise correction and truncation algorithms have increased complexity, resulting in lower precision. These algorithms are therefore not desired in cases where the conventional mono-exponential algorithm is accurate.

We aimed to develop and validate a new T2* algorithm called ADAPTS which automatically selects algorithm complexity in order to obtain accurate results in severe iron load and precise measurements in moderate to normal iron load.

We demonstrated algorithm behavior in numerical simulations using echo times from two multi-echo pulse sequences designed for invivo T2* measurements in the heart and liver. Our simulations confirmed that ADAPTS results in high T2* accuracy at short T2* values, similar to noise correction methods, and high precision at long T2* values, similar to the mono-exponential 2-parameter algorithm (Figure 4.1).

Validation in gel phantoms for similar multi-echo pulse sequences as were used for numerical simulations showed good agreement with a previously validated noise correction algorithm available on the scanner (MLE) and also with measurements from our reference standard single-echo pulse sequence (Figures 4.2-4.3). For both the new algorithm (ADAPTS) and the MLE algorithm, the largest T2* differences compared to our reference standard sequence were obtained for long T2* values where T2*>30ms. Since errors for long T2* values were obtained using both algorithms, and the errors could not be reproduced when ADAPTS was applied to data from the single-echo reference standard pulse sequence, we believe that T2* errors at T2*>30ms originated from the multi-echo sequence parameter configuration rather than the T2* algorithms in use. Invivo T2* measurements in the heart and liver of 23 patients with known or suspected iron load disease showed low interobserver variability of the ADAPTS algorithm, similar to the previously validated MLE algorithm (Figure 4.4).

Our findings suggests that the proposed automatic algorithm (ADAPTS) can provide robust T2* measurements in the heart and liver over the range of clinically relevant T2* values in the offline setting.

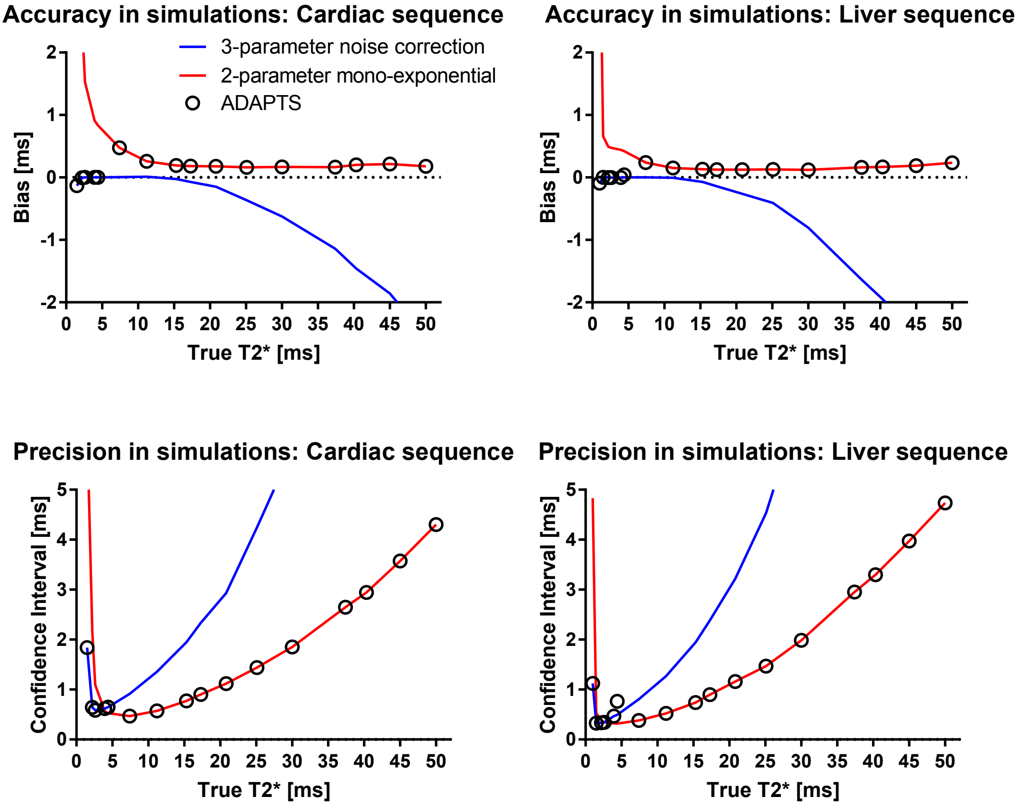

Figure 4.1 Accuracy (top row) and precision (bottom row) of three T2* algorithms were evaluated in numerical simulations using echo times from two clinical T2* sequences for cardiac (left column) and liver (right column) imaging. A mono-exponential algorithm (red solid lines) resulted in increased T2* bias and reduced precision for short T2* values, while a noise correction algorithm (blue solid lines) resulted in increased T2* bias and reduced precision for long T2* values. The introduced ADAPTS algorithm (open circles) switched behavior between a noise correction and a mono-exponential algorithm, which resulted in low bias over the simulated T2* interval.

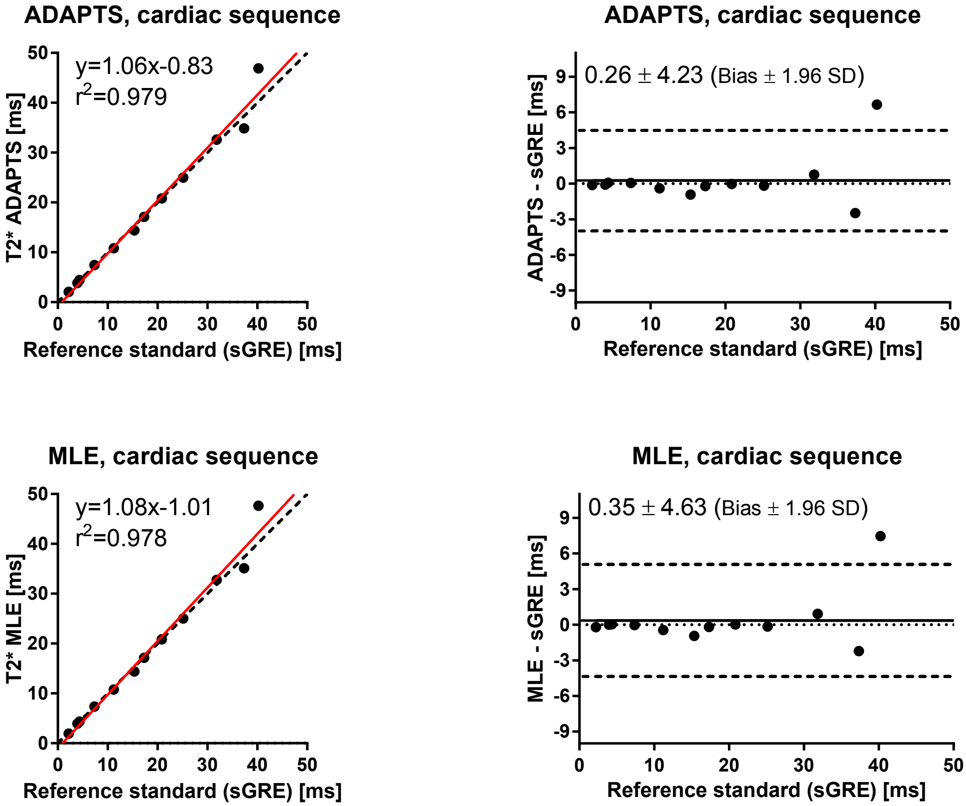

Figure 4.2 Phantom validation of the new ADAPTS (top row) and the MLE (bottom row) T2* algorithms using a multi-echo gre pulse sequence designed for cardiac imaging. Scatter plots (left) show T2* values from multi-echo measurements (y-axes), T2* values from the single-echo reference standard measurement (x-axes), line of identity (dashed lines) and linear regression lines (red solid lines). Modified Bland-Altman plots (right) show T2* differences between multi-echo and single-echo data (y-axes), T2* from single echo reference standard measurements (x-axis), bias (solid lines) and bias±1.96 SD (dashed lines). Both T2* algorithms resulted in small errors compared to the reference standard except for measurements in phantoms with T2*>35ms, likely due to the multi-echo pulse sequence configuration.

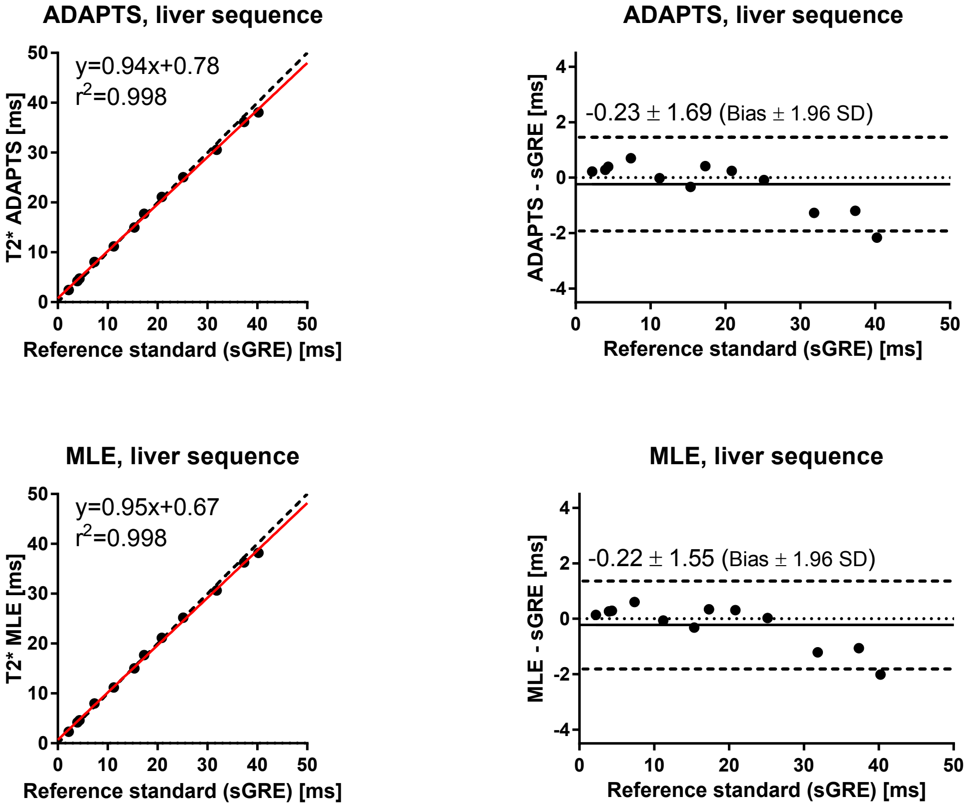

Figure 4.3 Phantom validation of the new ADAPTS (top row) and the MLE (bottom row) T2* algorithms using a multi-echo gre pulse sequence designed for liver imaging. Scatter plots (left) show T2* values from multi-echo measurements (y-axes), T2* values from the single-echo reference standard measurement (x-axes), line of identity (dashed lines) and linear regression lines (red solid lines). Modified Bland-Altman plots (right) show T2* differences between multi-echo and single-echo data (y-axes), T2* from single echo reference standard measurements (x-axis), bias (solid lines) and bias±1.96 SD (dashed lines). Both T2* algorithms resulted in small errors compared to the reference standard except for measurements in phantoms with T2*>30ms, likely due to the multi-echo pulse sequence configuration.

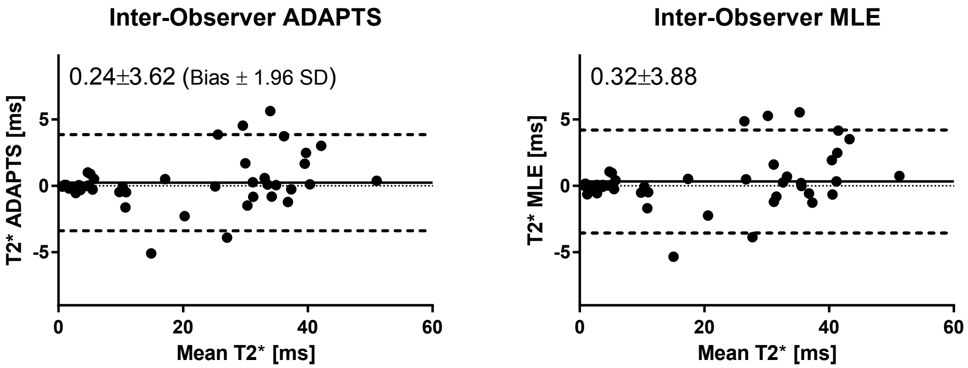

Figure 4.4 Bland-Altman plots showing T2* interobserver variability of the new ADAPTS algorithm (left) and the MLE algorithm (right). Bias and bias±1.96 SD are shown as solid and dashed lines, respectively. The two T2* algorithms had similar interobserver variability.

4.2 Validation of T1 and T2 algorithms from a vendor independent software (Study II)

Quantification of the MR relaxation time constants T1 and T2 is increasingly utilized in medical imaging research and clinical practice. For example, T1 measurements before and after administration of a gadolinium based contrast agent enables determination of myocardial extracellular volume [47], while T2 measurements can be used to detect edema in acute myocardial infarction [48]. Software tools for offline T1 and T2 measurements are needed for standardized data analysis in multi-vendor studies and in the clinical setting. A previous open-source software for T1 and T2 analysis exist which is designed to be used for research [49]. We aimed to create and validate a software for generating T1 and T2 relaxation maps from multiple signal models to be used in research and in clinical practice.

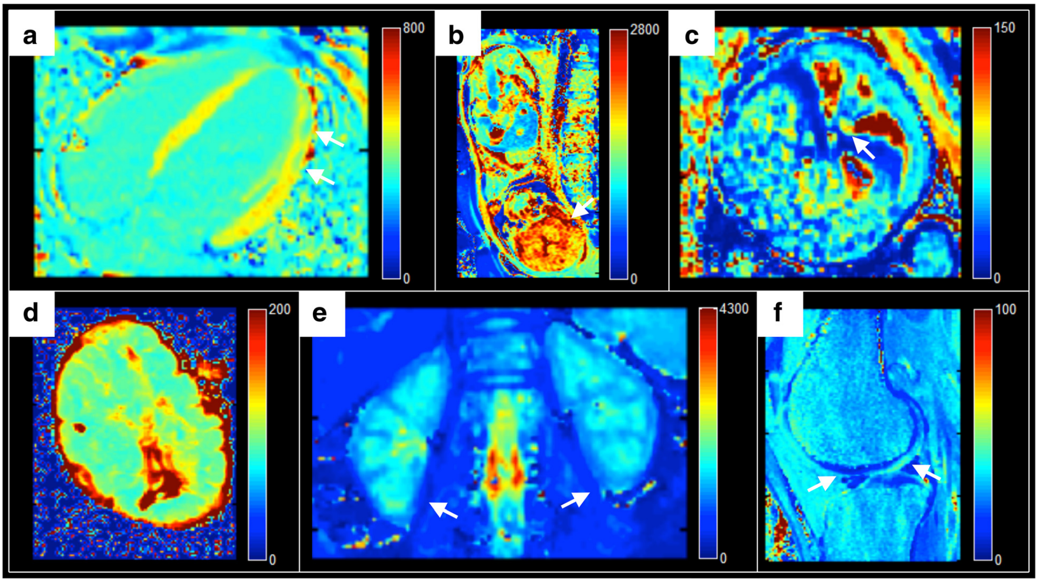

Figure 4.5 Invivo and exvivo T1 and T2 maps generated by the new software tool using images from three different MRI vendors. Arrows point to findings or anatomical structures. **a)** MOLLI T1-map of the cardiac 4-chamber view acquired after gd-contrast administration in a patient with myocarditis (1.5T Siemens); **b)** T1-map of a healthy fetal brain from an inversion-recovery bSSFP pulse sequence (1.5T Siemens); **c)** T2-map of the fetal descending aorta from a T2-prepared bSSFP pulse sequence (1.5T Siemens); **d)** exvivo T1-map of a healthy placenta from an inversion-recovery bSSFP pulse sequence (3T Siemens); **e)** MOLLI T1-map of the kidneys in a healthy volunteer (1.5T Philips); **f)** T2-map of knee cartilage in a healthy volunteer using a multi-echo spin echo pulse sequence (3T GE).

The new T1/T2 analysis software was able to generate T1 and T2 maps using images from three MRI vendors (Siemens, Philips and GE), shown in figure 4.5.

Phantom validation using pulse sequences designed for invivo measurements resulted in low bias and variability, except for MOLLI T1-measurements in phantoms with T2<60ms, similar to findings from a previous study [50] (Figure 4.6).

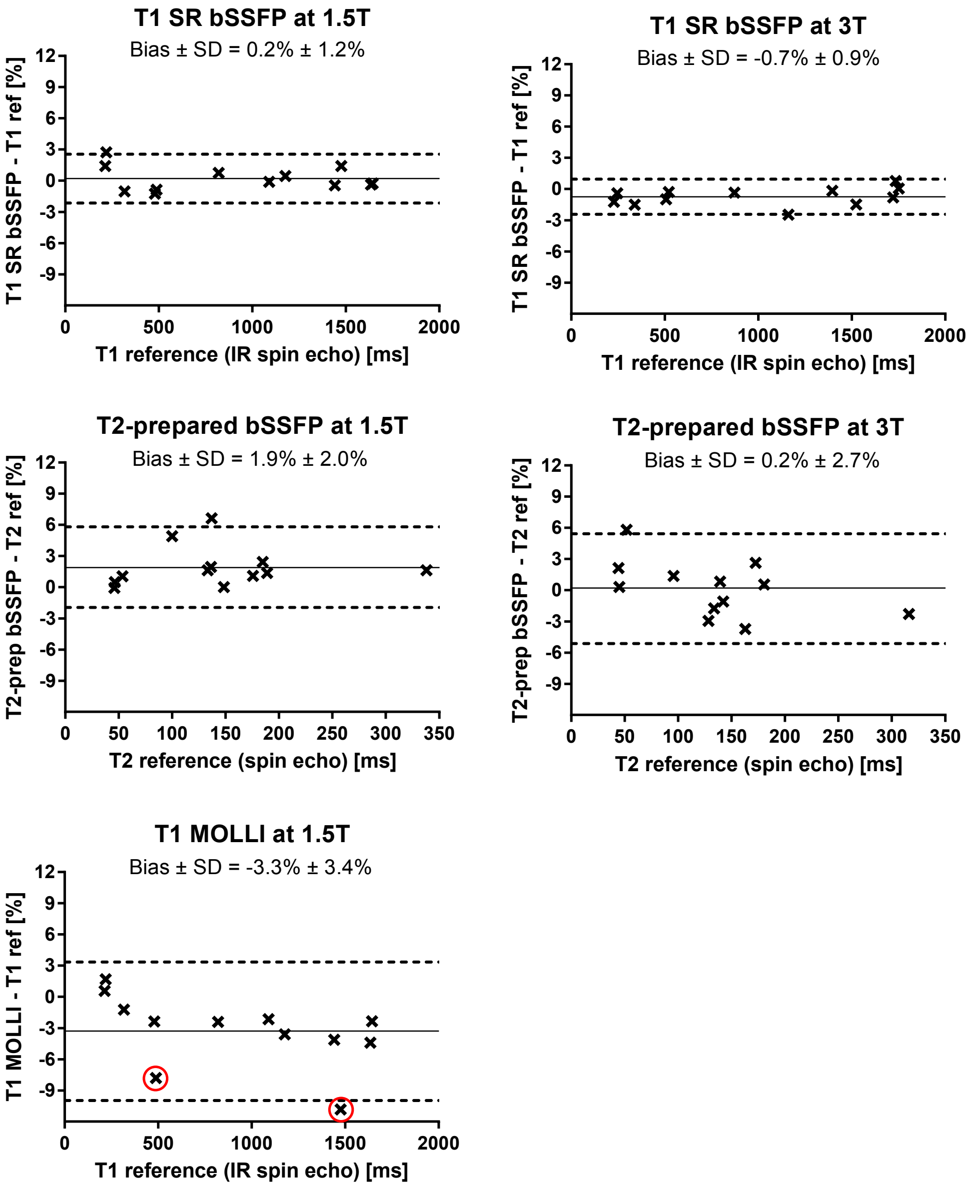

Figure 4.6 Modified Bland-Altman plots from the T1 and T2 phantom validation at 1.5T (left) and 3T (right), showing bias as solid lines and bias±1.96 SD as dashed lines. Top panels: T1 measurements using a saturation recovery free-breathing bSSFP pulse sequence; Middle panels: T2 measurements using a T2-prepared free-breathing bSSFP pulse sequence; Bottom panel: T1 measurements using a MOLLI breathhold pulse sequence. Low bias and variability were found for the evaluated T1 and T2 pulse sequences, except for MOLLI T1 measurements in phantoms with T2<60ms (encircled in red). bSSFP=balanced steady-state free precession; MOLLI=Modified Look-Locker inversion-recovery; SR=Saturation-recovery.

4.3 Validation of SQUAREMR, a new method for accurate T1 estimation using Bloch simulations of a large spin population (Study III)

Methods for determining MR relaxation time constants using Bloch simulations together with specific pulse sequence designs have been successfully applied invivo and is increasingly used in the MR research community[51]. For such applications, novel pulse sequences have so far been used which often require state of the art MR scanner performance. We hypothesized that Bloch simulations could be used to improve T1-accuracy for already existing pulse sequences. We therefore developed an algorithm (SQUAREMR) which can estimate T1 values when combined with a Bloch simulation framework[32], and applied it to data from three schemes of the widely used MOLLI T1-mapping pulse sequence [19] (5(3p)3, 4(1p)3(1p)2 and 5(0p)3).

Validation at 1.5T in one gel-phantom set with T1/T2 values similar to myocardium and blood, and in one gel-phantom set with T2<60ms and a range of T1 values (range 200-1600ms) resulted in improved T1 accuracy for all three schemes of the MOLLI pulse sequence using SQUAREMR processing compared to using conventional mono-exponential fitting with Look Locker correction (Figure 4.7). The largest improvement in T1 accuracy was found for the MOLLI 5(0p)3 pulse sequence without pause RR-intervals between inversions. MOLLI T1-values from SQUAREMR processing had lower bias, and were constantly larger, than MOLLI T1-values from conventional processing with Look-Locker correction.

Myocardial T1 measurements at 1.5T, in twelve human volunteers, resulted in larger T1-values ($p<0.001$, $n=12$) for SQUAREMR processing ($T1=1117\pm25.6$ms) compared to conventional processing with Look-Locker correction ($T1=1025\pm22.9$ms) using MOLLI 5(3p)3, which was consistent with our findings from the phantom validation.

Our study indicates that the new SQUAREMR post-processing method can be used with already available pulse sequences to improve the accuracy of MR relaxometry, both prospectively from newly acquired MR data and retrospectively from previously collected MR data.

Future work is needed to investigate sensitivity of the method to confounding factors such as B0 and B1 variations over the image field of view or magnetization transfer effects for different tissue types.

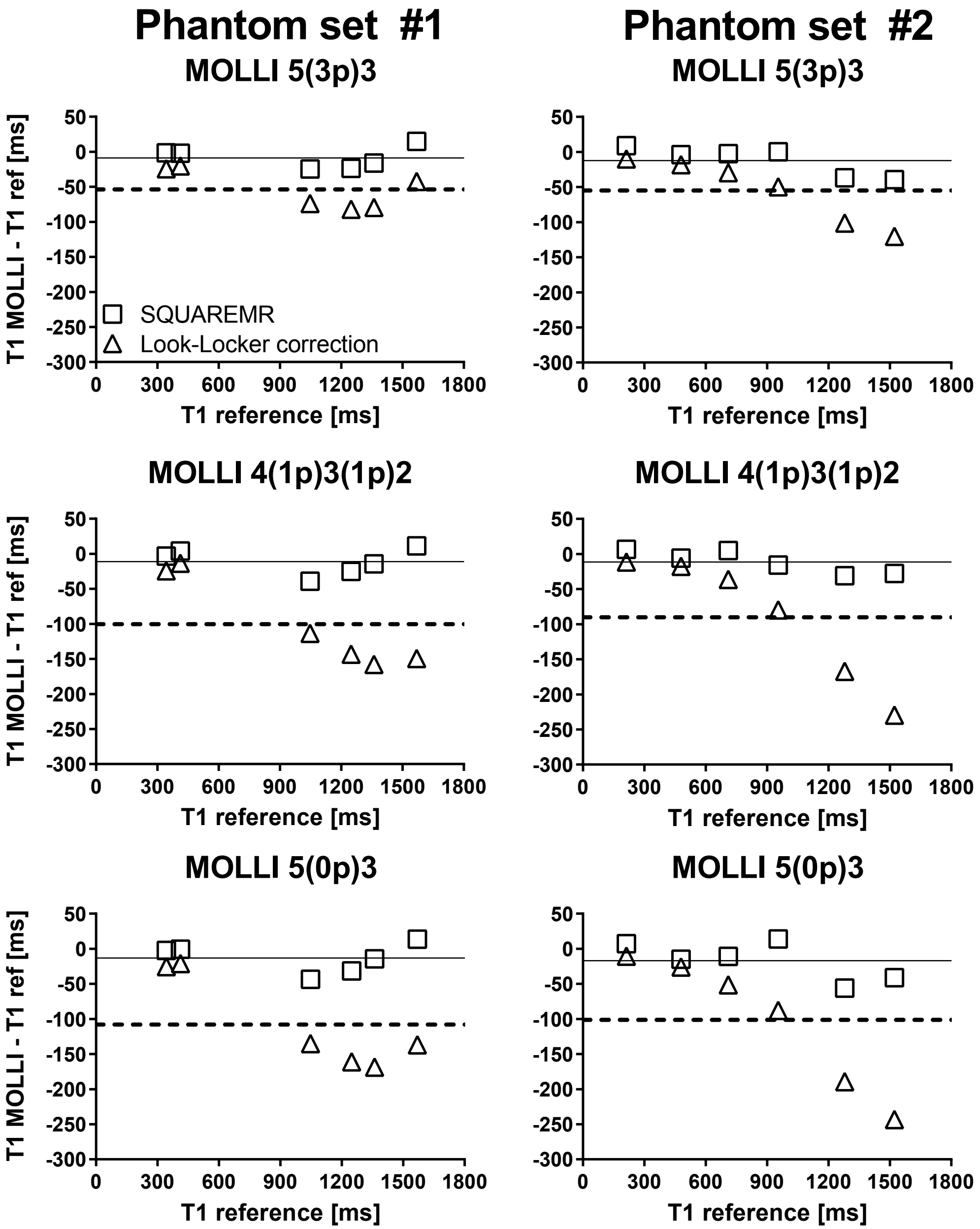

Figure 4.7 Modified Bland-Altman plots from one phantom set with T1/T2 values similar to myocardium and blood (left), and one phantom set with T2<60ms (right). T1 measurements from three MOLLI schemes (rows) using either conventional Look-Locker correction (triangles) or the new SQUAREMR method (squares) were compared to inversion-recovery spin echo reference standard measurements. For both phantom sets and all three MOLLI schemes, T1 bias from SQUAREMR (solid lines) was smaller than T1 bias from Look-Locker correction (dashed lines).

4.4 A new vessel delineation algorithm for 2D PC-MR images (Study IV)

Flow measurements from 2D PC-MR images require accurate time-resolved vessel delineations over the cardiac cycle. Previous semi-automatic delineation algorithms have reduced the required user input and total time of analysis. However, the need for manual corrections remain.

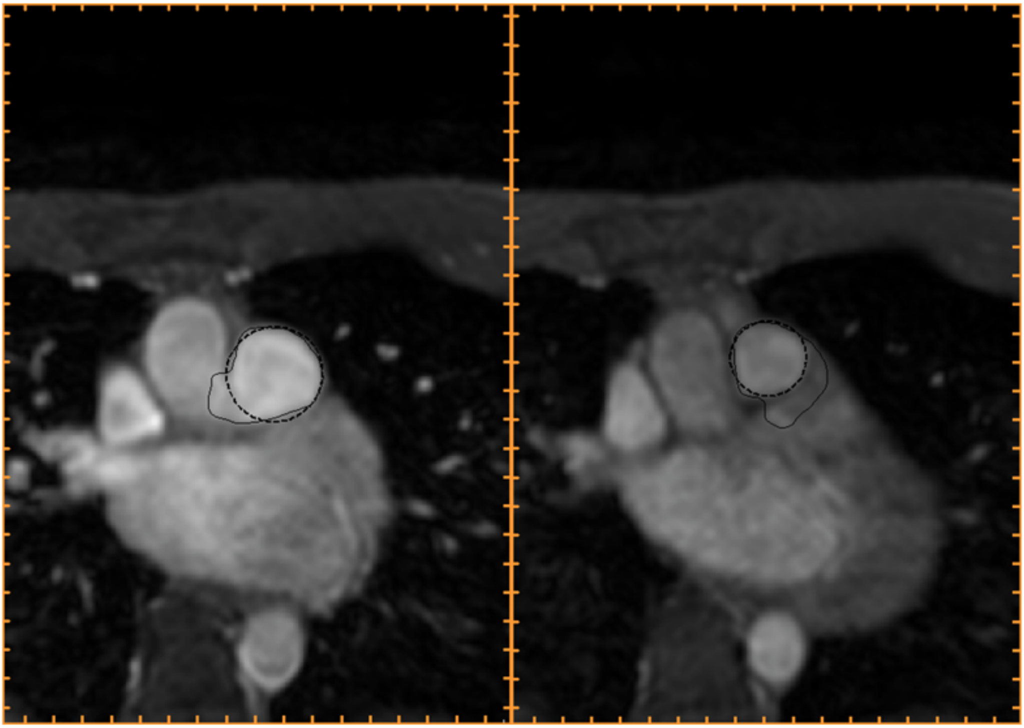

Figure 4.9 Example of semi-automatic delineations in PC-MR magnitude images of the main pulmonary artery during ventricular systole (left) and diastole (right). Delineations from the algorithm with new vessel shape constraints (dashed lines) showed improved robustness compared to delineations from another semi-automatic algorithm without the new shape constraints (solid lines), which erroneously included tissue adjacent to the pulmonary artery.

We hypothesized that shape constraints based on a data set of manual delineations would improve robustness of vessel delineation algorithms which, to our knowledge, have not been implemented previously for 2D PC-MR images. Therefore, we developed a new semi-automatic 2D PC-MR vessel delineation algorithm with shape constraints based on manual vessel delineations, validated the algorithm in phantom experiments and compared the algorithm to manual vessel delineation in the ascending aorta and main pulmonary artery of human subjects. Figure 4.9 shows an example of semi-automatic delineation of the main pulmonary artery demonstrating improved robustness for the new algorithm compared to a previously published algorithm [36].

Validation of 2D PC-MR flow measurements at 1.5T and 3T using a pulsatile flow phantom (figure 4.10) resulted in good agreement with timer and beaker flow measurements for manual delineation. 2D PC-MR flow measurements using the new semi-automatic delineation algorithm resulted in good agreement with timer and beaker flow at 1.5T and underestimated flow at 3T. A larger degree of PC-MR image artifacts were observed at 3T compared to 1.5T data, which may explain the observed flow underestimation, indicating sensitivity to image quality of the new algorithm.

in-vivo 2D PC-MR flow measurements in the ascending aorta (n=134) and main pulmonary artery (n=30) of human subjects, using both manual delineation and the new delineation algorithm initialized at 20% of the RR-interval are shown in figure 4.11. Modified Bland-Altman analysis using manual delineation as reference standard resulted in low bias and variability for the new algorithm (figure 4.11, bottom row), demonstrating possibility for clinical use in both vessels.

Figure 4.12 shows how delineation performance vary when the semi-automatic algorithm is initialized at different RR-interval time points for the ascending aorta and main pulmonary artery. The algorithm was robust to different initialization time points for the ascending aorta, while delineation quality was sensitive to the initialization time point for the main pulmonary artery. A larger variation of vessel diameter over the cardiac cycle was observed for the main pulmonary artery compared to corresponding measurements for the ascending aorta which may explain the sensitivity to the initialization time point for the main pulmonary artery. Of note, the observed difference in vessel diameter variation between the two vessels is most likely not due to differences in actual vessel anatomy but rather explained by the need for double-oblique positioning of the pulmonary artery imaging plane. Therefore, finding the true cross-section of the main pulmonary artery may have been more user dependent during the MRI scan compared to the ascending aorta.

By initializing the semi-automatic algorithm in the main pulmonary artery at time points between 15-35% of the RR-interval, high delineation quality was obtained, similar to the performance found for the ascending aorta. Since 15-35% of the RR-interval was associated with well defined image contrast between the main pulmonary artery and its surroundings, initializing the algorithm in this interval with a manual delineation will most likely not be a major challenge in the majority of cases.

PC-MR flow inter-observer variability was reduced using the semi-automatic algorithm compared to manual delineation in 30 human subjects (Figure 4.13), which combined with the found low bias and variability of measured flow volumes warrants the use of the new delineation algorithm for invivo flow and shunt volume quantification.

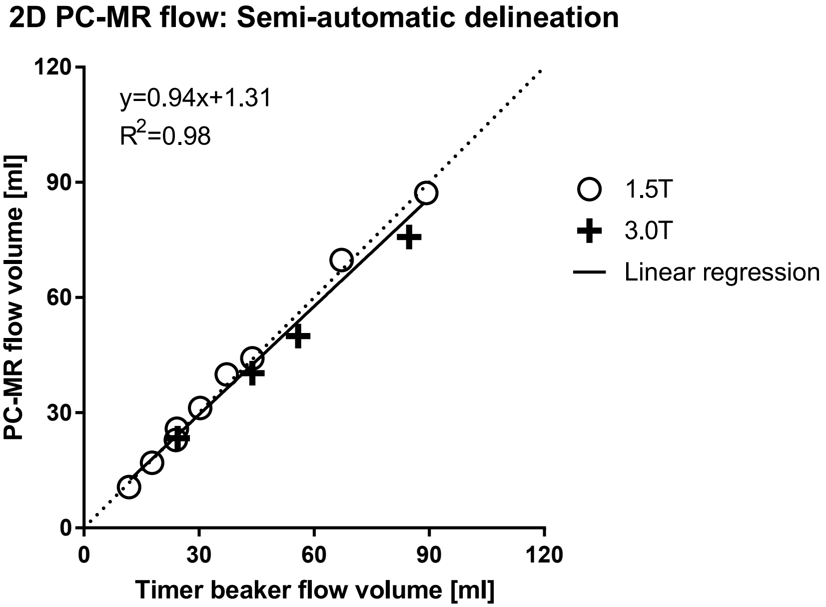

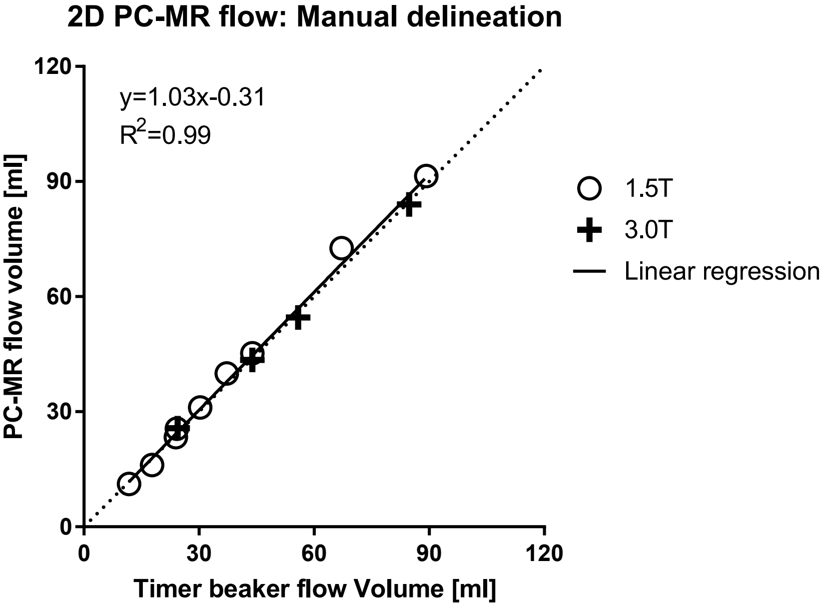

Figure 4.10 Phantom validation of 2D PC-MR flow volume measurements for pulsatile flow at 1.5T (circles) and 3T (crosses). PC-MR measurements using the new semi-automatic delineation algorithm (top) were in good agreement with timer and beaker measurements at 1.5T, and underestimated flow volumes at 3T. PC-MR measurements using manual delineation (bottom) were in good agreement with timer and beaker at both 1.5T and 3T.

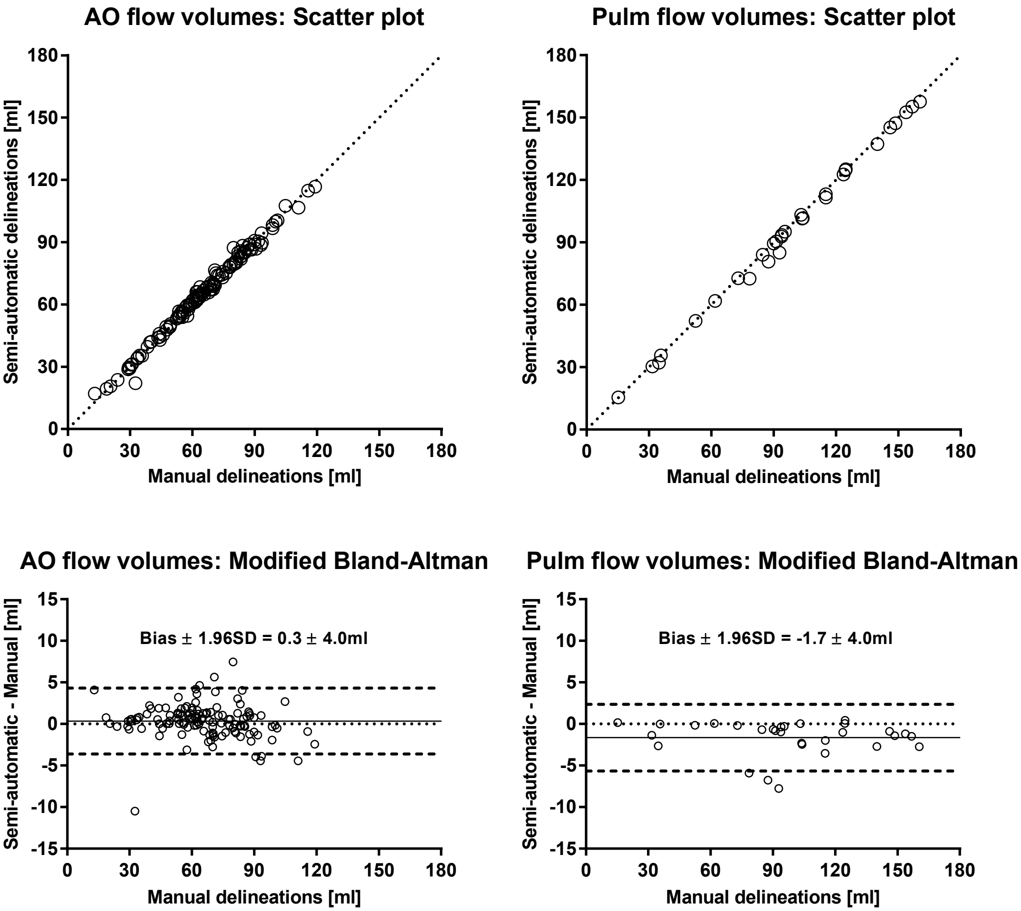

AO flow volumes: Scatter plot

Pulm flow volumes: Scatter plot

AO flow volumes: Modified Bland-Altman

Pulm flow volumes: Modified Bland-Altman

Figure 4.11 Invivo 2D PC-MR flow volume measurements in the ascending aorta (left; n=134) and the main pulmonary artery (right; n=30). Scatter plots (top) show PC-MR flow volume measurements using the semi-automatic algorithm initialized at 20% of the RR-interval (y-axes) and manual delineations (x-axes) together with lines of identity (dotted lines). Flow volumes from the two methods were similar. Modified Bland-Altman plots (bottom) show bias as solid lines, bias±1.96 SD as dashed lines and zero difference as dotted lines. Delineations from the semi-automatic algorithm resulted in low bias and variability compared to manual delineations for both vessels.

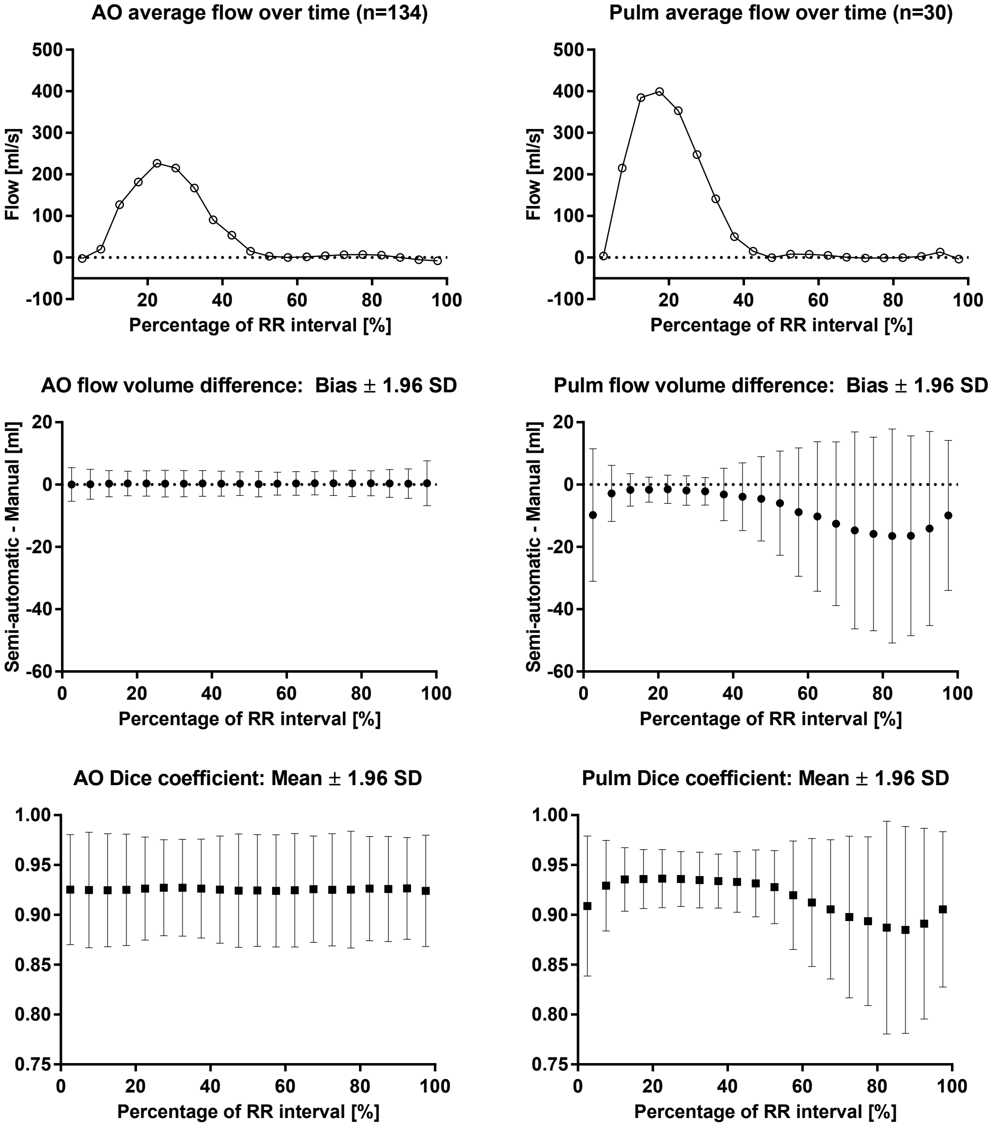

Figure 4.12 Semi-automatic delineation performance was largely unchanged for the ascending aorta (left) and varied for the main pulmonary artery (right) when the algorithm was initialized at different time points of the RR-interval. Top panels show average flow profiles over the RR-interval from manual delineations for both vessels. Middle panels show flow volume bias and limits of agreement (filled circles and error bars) of semi-automatic vs manual delineations. Bottom panels show average Dice coefficients and 1.96 SD (filled squares and error bars). For the main pulmonary artery, delineation quality was sensitive to the initialization time point of the semi-automatic algorithm. However, when the algorithm was initialized at 15-35% of the RR-interval, delineation quality was similar to the ascending aorta in terms of flow volume bias, flow volume variability and Dice coefficient.

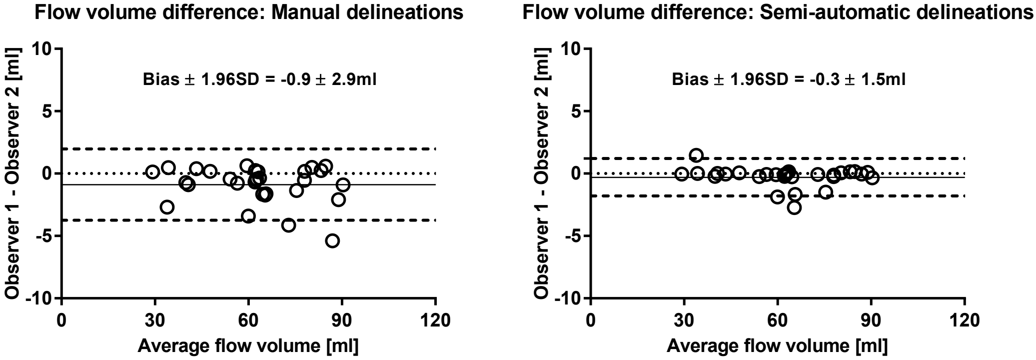

Figure 4.13 Bland-Altman plots showing interobserver variability of invivo PC-MR flow volume measurements in 30 human subjects using manual delineations (left) and the new semi-automatic algorithm (right). Interobserver bias (solid lines) and variability (dashed lines) were reduced by using the semi-automatic algorithm compared to using manual delineations.

4.5 Validation of Metric Optimized Gating Phase Contrast flow measurements for fetal imaging (Study V)

Non-invasive flow and blood velocity measurements in the fetal cardiovascular system by MRI is a promising alternative to doppler ultrasound for diagnosing disease such as congenital heart defects and intra-uterine growth restriction. Conventional phase contrast magnetic resonance (PC-MR) flow measurements require an ECG-recording during the MRI acquisition for image gating. The lack of a usable ECG by surface electrodes for fetal imaging creates the need for alternative image gating approaches such as Metric Optimized Gating (MOG) [23].

MOG PC-MR flow measurements have demonstrated reproducibility at 1.5T and 3T[52] and low inter-observer variability for fetal imaging [53, 54] in studies from one research center. However, validation has not been performed for a range of flow rates or using a reference standard measurement other than PC-MR. We therefore aimed to 1) validate MOG PC-MR flow measurements using an independent flow reference standard (timer and beaker) at a heart-rate (145bpm), a vessel diameter (6mm) and a range of flow rates (120-700ml/min) similar to fetal conditions in a phantom experiment and 2) investigate intra- and interobserver variability for fetal flow measurements at an additional imaging center.

In a pulsatile flow phantom experiment, MOG PC-MR velocity profiles closely resembled PC-MR with conventional image gating (Figure 4.14, top row), except for cases with low VNR ($VNR \leq 3.7$) in which MOG PC-MR resulted in near constant velocity profiles over the RR-interval (Figure 4.14, bottom row). Low VNR coincided with low timer and beaker flow and high VNR coincided with high flow. At high VNR ($VNR \geq 5.0$) MOG PC-MR resulted in underestimation of peak velocity.

MOG PC-MR flow measurements had low bias and high variability compared to timer and beaker flow (Figure 4.15). Underestimation of flow occurred at high flow values due to MOG PC-MR underestimation of peak velocity. Overestimation of flow occurred at low flow values due to near constant MOG PC-MR velocity profiles over the RR-interval which originated from MOG misgating at low VNR ($VNR \leq 3.7$).

For fetal imaging, flow volumes and interobserver variability in the fetal UV and DAo (Figure 4.16) were comparable to previously reported values [53]. Pulsatile flow was found for DAo but not for UV after MOG reconstruction in all subjects. Intra- and interobserver CV for Dao were 6% and 19% and for UV 10% and 17%.

Estimated VNR regimes for MOG PC-MR measurements in the fetal DAo and UV were similar to VNR values found in the phantom validation. VNR values associated with successful MOG reconstruction in the phantom were similar to estimated VNR in the fetal DAo (VNR=8.0), while VNR values associated with MOG misgating in the phantom were similar to estimated VNR in the UV (VNR=1.6).

The found VNR sensitivity of MOG PC-MR and the estimated VNR difference between the fetal DAo and UV warrants sequence parameter optimization to individual fetal vessels for accurate MOG PC-MR velocity and flow measurements.

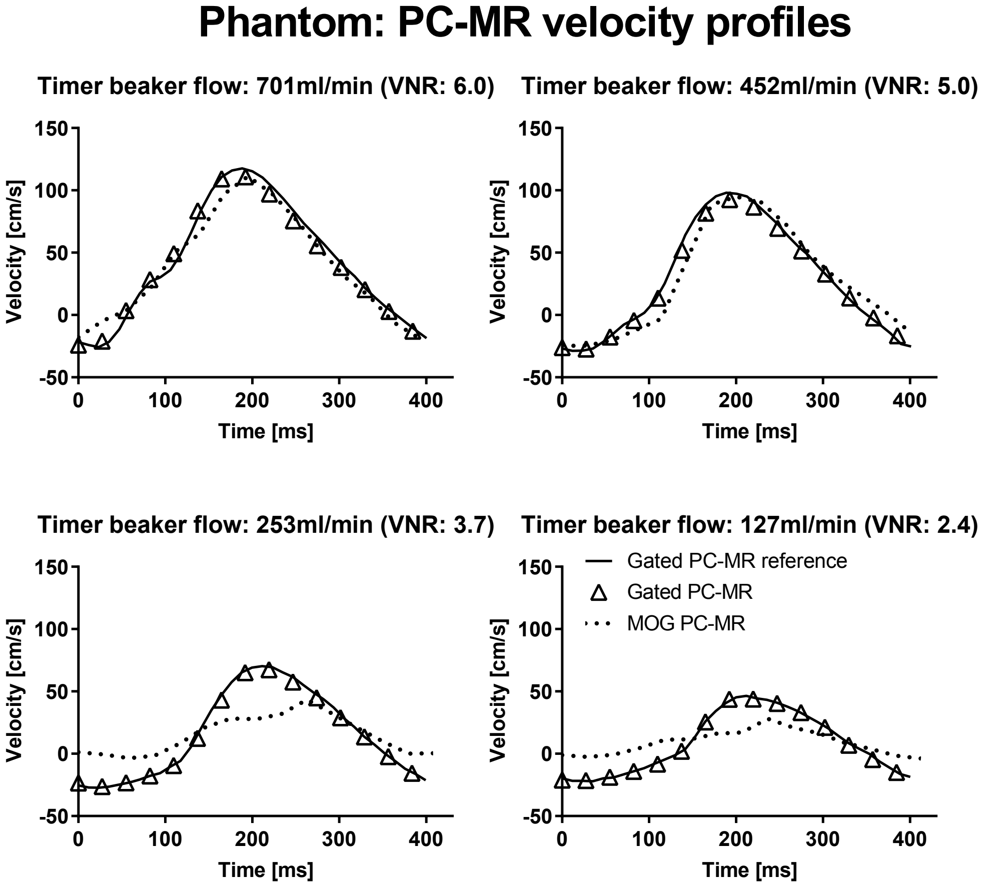

Figure 4.14 Phantom validation of MOG PC-MR velocity profiles. Top panels: At high flow (VNR$\geq$5.0), MOG PC-MR velocity profiles (dotted lines) were in good agreement with a conventionally gated PC-MR pulse sequence with similar acquisition parameters as MOG (triangles) but underestimated peak velocity compared to a conventionally gated PC-MR pulse sequence with improved spatial and temporal resolution (solid lines). Bottom panels: At low flow (VNR$\leq$3.7), MOG PC-MR underestimated peak velocity compared to both conventionally gated PC-MR pulse sequences and MOG PC-MR velocity profiles approximated near constant velocity over the RR-interval due to MOG misgating.

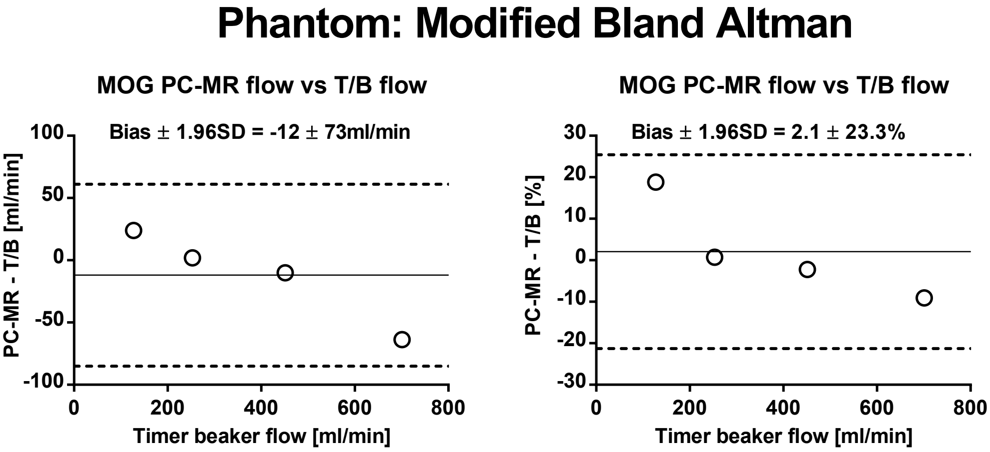

Figure 4.15 Phantom validation of MOG PC-MR flow measurements compared to timer and beaker flow. Modified Bland-Altman analysis resulted in low bias (solid lines) and high variability (dashed lines) for MOG PC-MR, both when using errors in absolute flow (left) and when using errors in percentage (right). MOG PC-MR overestimated flow at low timer and beaker flow values due to MOG misgating and underestimated flow at high flow values due to underestimation of peak velocity.

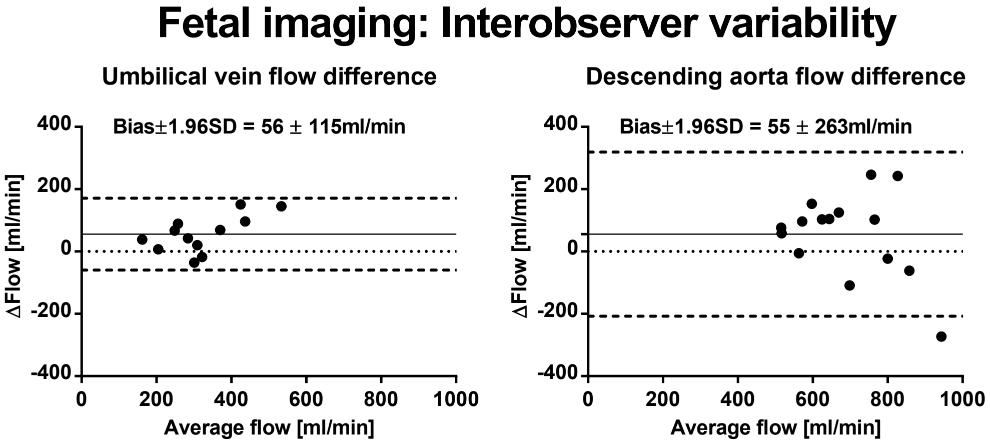

Figure 4.16 Bland-Altman plots of interobserver variability for MOG PC-MR flow measurements in the umbilical vein (left) and the fetal descending aorta (right). Solid lines show bias and dashed lines show bias±1.96 SD.

Chapter 5

Conclusions

In the presented studies, different methods for MRI relaxometry and PC-MR flow quantification were evaluated with a focus on cardiovascular applications. The conclusion for each study was:

I. For two invivo T2* sequences the new algorithm for offline T2* calculation gave rise to low bias and variability in phantoms over the range of clinically relevant T2* values. Low intra- and interobserver variability in patients with known or suspected iron load disease were found, similar to a previously validated T2* algorithm which was available on the MR-scanner.

II. The new software tool for offline T1 and T2 calculation resulted in low bias and variability in phantoms compared to reference standard spin echo pulse sequences and similar bias compared to findings in previous studies were found for pulse sequences designed for invivo imaging. Applicability of the software was demonstrated for images from three MRI vendors.

III. Results from phantom experiments suggest that the new SQUAREMR post-processing method can be used to improve T1 accuracy of the MOLLI pulse sequence. Consistently higher pre-contrast myocardial MOLLI T1 estimates were obtained using SQUAREMR compared to conventional mono-exponential fitting with Look-Locker correction in human volunteers.

IV. The new algorithm for semi-automatic vessel delineation in 2D PC-MR images resulted in low bias and variability when compared to manual delineations in a phantom experiment and in invivo measurements.

V. Phantom validation showed good agreement between MOG and conventionally gated PC-MR except for cases with low VNR, which resulted in MOG misgating and underestimated peak velocities, warranting optimization of PC-MR pulse sequence parameters to individual fetal vessels. Interobserver variability for the fetal descending aorta and umbilical vein were comparable to previously reported values.

Bibliography

[1] E. Widmaier, H. Raff, and K. Strang. *Vander's Human Physiology, Twelfth Edition*. McGraw-Hill, 2011.

[2] M. Carlsson, R. Andersson, K.M. Bloch, K Steding-Ehrenborg, H. Mosén, F. Stahlberg, B. Ekmehag, and H. Arheden. Cardiac output and cardiac index measured with cardiovascular magnetic resonance in healthy subjects, elite athletes and patients with congestive heart failure. *J Cardiovasc Magn Reson*, 14, 2012.

[3] K. Steding-Ehrenborg, M. Carlsson, S Stephensen, and H Arheden. Atrial aspiration from pulmonary and caval veins is caused by ventricular contraction and secures 70independent of resting heart rate and heart size. *Clin Physiol Funct Imaging*, 33, 2013.

[4] C. Chung, M. Karamanoglu, and J.S. Kovacs. Duration of diastole and its phases as a function of heart rate during supine bicycle exercise. *Am J Physiol Heart Circ Physiol*, 287, 2004.

[5] I.I. Rabi. Space Quantization in a Gyrating Magnetic Field. *Phys. Rev.*, 51, 1937.

[6] P. Zeeman. The effect of Magnetization on the Nature of Light Emmitted by a Substance. *Nature*, 55, 1897.

[7] E.L. Hahn. Nuclear Induction Due to Free Larmor Precession. *Phys. Rev.*, 77, 1949.

[8] R.R. Ernst and W.A. Anderson. Application of Fourier Transform Spectroscopy to Magnetic Resonance. *Review of Scientific Instruments*, 37, 1966.

[9] F. Bloch. Nuclear Induction. *Phys. Rev.*, 70, 1946.

[10] P.T. Callaghan. *Principles of Nuclear Magnetic Resonance Microscopy*. Oxford University Press, 1993.

[11] E.L. Hahn. Spin Echoes. *Phys. Rev.*, 80, 1950.

[12] S. Meiboom and D. Gill. Modified Spin-Echo Method for Measuring Nuclear Relaxation Times. *Review of Scientific Instruments*, 29, 1958.

[13] H.Y. Carr. Steady-State Free Precession in Nuclear Magnetic Resonance. *Phys. Rev.*, 112, 1958.

[14] D.J. Bryant, J.A. Payne, D.N. Firmin, and D.B. Longmore. Measurement of Flow with NMR imaging Using a Gradient Pulse and Phase Difference Technique. *J Comput Assist Tomogr*, 8, 1984.

[15] P.C. Lauterbur. Image Formation by Induced Local Interactions: Examples Employing Nuclear Magnetic Resonance. *Nature*, 242, 1973.

[16] J. Radon. Uber die bestimmung von funktionen durch ihre integralwerte langs gewisser mannigfaltigkeiten. *Ber. Verh. Sachs. Akad. Wiss.*, 69, 1917.

[17] A. Kumar, D. Welti, and R.R. Ernst. NMR Fourier Zeugmatography. *Journal of Magnetic Resonance*, 18, 1975.

[18] A.N Garroway, P.K. Grannell, and P. Mansfield. Image Formation in NMR by a selective irradiative process. *J. Phys. C: Solid State Phys.*, 7, 1974.

[19] D.R. Messroghli, A. Radjenovic, D.M. Kozerke, S. Higgins, M.U. Sivananthan, and J.P. Ridgeway. Modiefied Look-Locker inversion recovery (MOLLI) for high-resolution T1 mapping of the heart. *Magn Reson Med*, 52, 2004.

[20] K. Chow, J.A. Flewitt, J.D. Green, J.J. Pagano, M.G. Friedrich, and R.B. Thompson. Saturation recovery single-shot acquisition (SASHA) for myocardial T(1) mapping. *Magn Reson Med*, 71, 2014.

[21] R. Deichmann and A. Haase. Quantification of T1 values by SNAPSHOT-FLASH NMR Imaging. *J Magn Reson*, 612, 1992.

[22] M. Akcakaya, A.B. Tamer, S. Weingärtner, S. Roujol, S. Berg, and R. Nezafat. Improved quantitative myocardial T2 mapping: Impact of the fitting model. *Magn Reson Med*, 2014. doi: 10.1002/mrm.25377.

[23] M.S. Jansz, M. Seed, J.F. van Ameron, D. Wong, L. Grosse-Wortmann, S.J. Yoo, and C.K. Macgowan. Metric optimized gating for fetal cardiac MRI. *Magn Reson Med*, 2010, 2010.

[24] S.S. Stephensen, K. Steding-Ehrenborg, U. Thilen, J. Holm, P. Hochbergs, and H. Arheden. Changes in blood volume shunting in patients with atrial septal defects: assessment of heart function with cardiovascular magnetic resonance during dobutamine stress. *Eur. H. J. Cardiovasc. Im.*, 2016. doi: 10.1093/ehjci/jew176.

[25] J. Töger, S. Bidhult, J. Revstedt, M. Carlsson, H. Arheden, and E. Heiberg. Independent validation of four-dimensional flow MR velocities and vortex ring volume using

particle imaging velocimetry and planar laser-Induced fluorescence. *Magn Reson Med*, 3, 2015.

[26] J. Sijbers, A.J. Dekker, E. Raman, and D. Van Dyck. Parameter estimation from magnitude MR images. *Int J Imaging Syst Technol*, 10, 1999.

[27] J.H. Brittain, B.S. Hu, G.A. Wright, C.H. Meyer, A. Macovski, and D.G. Nishimura. Coronary angiography with magnetization-prepared T2 contrast. *Magn Reson Med*, 33, 1995.

[28] P.M. Robson, A.K. Grant, A.J. Madhuranthakam, R. Lattanzi, D.K. Sodickson, and C.A. McKenzie. Universal Approach to Quantification of SNR and g-Factor for parallel MRI. *15th Annual Meeting of ISMRM*, Berlin, Germany 15, 2007.

[29] E. Hedström, K. Steding-Ehrenborg, S. Bidhult, C. Ruprecht, F. Kording, and A.H. Aletras. Quantitative phase-contrast CMR of blood flow in fetal vessels gated by Doppler ultrasound: Comparison with metric optimized gating. *27th Annual Meeting of ISMRM*, Paris, France 15, 2018.

[30] Y. Feng, T. He, Gatehouse P.D., X. Li, A.M. Harith, D.J. Pennel, W. Chen, and D.N. Firmin. Improved MRI R2 * relaxometry of iron-loaded liver with noise correction. *Magn Reson Med*, 70, 2013.

[31] J.M. Bonny, M. Zanca, J.Y. Boire, and A. Veyre. T2 maximum likelihood estimation from multiple spin-echo magnitude images. *Magn Reson Med*, 36, 1996.

[32] C.G. Xanthis, I. Venetis, A.V. Chalkias, and A.H. Aletras. MRISIMUL: A GPU-Based Parallel Approach to MRI Simulations. *IEEE TRANSACTIONS ON MEDICAL IMAGING*, 33, 2014.

[33] T. He, J. Zhang, J.P. Carpenter, Y. Feng, G.C. Smith, D.J. Pennel, and D.N. Firmin. Automated truncation method for myocardial T2* measurement in thalassemia. *J Magn Reson Imaging*, 37, 2013.

[34] J.A. Nelder and R. Mead. A simplex method for function minimization. *Comput J*, 7, 1965.

[35] J.B. MacQueen. Some Methods for classification and Analysis of Multivariate Observations. *5th Berkeley Symp Math Stat Probab*, 1, 1967.

[36] E. Heiberg, J. Sjögren, M. Ugander, M. Carlsson, H. Engblom, and H. Arheden. Design and validation of segment - freely available software for cardiovascular image analysis. *BMC Med Im*, 10, 2010.

[37] J.M. Bland and D.G. Altman. Statistical methods for assessing agreement between two methods of clinical measurement. *Lancet*, 1, 1986.

[38] D.J. Pennel, J.B. Porter, and M.D. et al Cappellini. Deferasirox for up to 3 years leads to continued improvement of myocardial T2* in patients with b-thalassemia major. *Haematologica*, 97, 2012.

[39] E. Even-Or, R. Becker-Cohen, and H. Miskin. Deferasirox treatment may be associated with reversible renal Fanconi syndrome. *Am J Hematol*, 85, 2010.

[40] L.J. Anderson and B. et al Davis. Cardiovascular T2-star (T2*) magnetic resonance for the early diagnosis of myocardial iron overload. *Eur Heart J*, 22, 2001.

[41] J.P. Carpenter, T. He, and P. et al Kirk. On T2* magnetic resonance and cardiac iron. *Circulation*, 123, 2011.

[42] M.A. Tanner, T. He, M.A. Westwood, D.N. Firmin, and D.J. Pennell. Thalassemia International Federation Heart T2* Investigators. Multi-center validation of the transferability of the magnetic resonance T2* technique for the quantification of tissue iron. *Haematologica*, 91, 2006.

[43] M.A. Westwood, L.J. Anderson, D.N. Firmin, P.D. Gatehouse, C.H. Lorenz, B. Wonke, and D.J. Pennell. Interscanner reproducibility of cardiovascular magnetic resonance T2* measurements of tissue iron in thalassemia. *J Magn Reson Imaging*, 18, 2003.

[44] J.C. Wood, M. Otto-Duessel, M. Aguilar, H. Nick, M.D. Nelson, T.D. Coates, H. Pollack, and R. Moats. Cardiac iron determines cardiac T2*, T2, and T1 in the gerbil model of iron cardiomyopathy. *Circulation*, 112, 2005.

[45] J.C. Wood, C. Enriquez, N. Ghugre, J.M. Tyzka, S. Carson, M.D. Nelson, and T.D. Coates. MRI R2 and R2 * mapping accurately estimates hepatic iron concentration in transfusion-dependent thalassemia and sickle cell disease patients. *Blood*, 106, 2005.

[46] N.R. Ghugre, C.M. Enriquez, T.D. Coates, M.D. Nelson, and J.C. Wood. Improved R2* measurements in myocardial iron overload. *JMRI*, 23, 2006.

[47] H. Arheden, M. Saeed, C.B. Higgins, D.W. Gao, J. Bremerich, R. Wyttenbach, M.W. Dae, and M.F. Wendland. Measurement of the distribution volume of gadopentetate dimeglumine at echo-planar MR imaging to quantify myocardial infarction: comparison with 99mTc-DTPA autoradiography in rats. *Radiology*, 211, 1999.

[48] M. Ugandere, P.S. Bagi, A.J. Oki, B. Chen, L.Y. Hsu, and A.H. et al Aletras. Myocardial Edema as Detected by Pre-Contrast T1 and T2 CMR Delineates Area at Risk Associated With Acute Myocardial Infarction. *JCMG*, 5, 2012.

[49] D.R. Messroghli, A. Rudolph, A. Abdel-Aty, R. Wassmuth, T. Kuhne, and R. et al. Dietz. An open-source software tool for the generation of relaxation time maps in magnetic resonance imaging. *BMC Med Im*, 10, 2010.

[50] N.D. Gai, C. Stahning, M. Nacif, and D.A. Bluemke. Modified Look-Locker T1 Evaluation Using Bloch Simulations: Human and Phantom Validation. *Mang Reson Med*, 69, 2013.

[51] D. Ma, V. Gulani, N. Seiberlich, L. Kecheng, J.L. Sunshine, J.L. Duerk, and M.A. Griswold. Magnetic resonance fingerprinting. *Nature*, 495, 2013.

[52] B. Tsai-Goodman, M. Zhu, M. Al-Rujaib, M. Seed, and C. Macgowan. Foetal blood flow measured using phase contrast cardiovascular magnetic resonance–preliminary data comparing 1.5 T with 3.0 T. *J Cardiovasc Magn Reson*, 17, 2015.

[53] M. Prsa, L. Sun, J. van Ameron, S. Yoo, L. Grosse-Wortmann, E. Jaeggi, C. Macgowan, and M. Seed. Reference ranges of blood flow in the major vessels of the normal human fetal circulation at term by phase-contrast magnetic resonance imaging. *Circ Cardiovasc Imaging*, 7, 2014.

[54] M. Seed, J. van Ameron, , S. Yoo, L. Al Nafisi, B. Grosse-Wortmann, E. Jaeggi, M. Jansz, and C. Macgowan. Feasibility of quantification of the 1 distribution of blood flow in the normal human fetal circulation using CMR: a cross-sectional study. *J Cardiovasc Magn Reson*, 14, 2012.

Part II

Research Papers

Paper I: Validation of a new T2* algorithm and its uncertainty value for cardiac and liver iron load determination from MRI magnitude images.

Paper I

Magnetic Resonance in Medicine 75:1717–1729 (2016)

Validation of a New T2* Algorithm and Its Uncertainty Value for Cardiac and Liver Iron Load Determination from MRI Magnitude Images

Sebastian Bidhult,[1,2] Christos G. Xanthis,[1,3] Love Lindau Liljekvist,[1] Gerald Greil,[4,5] Eike Nagel,[4,5] Anthony H. Aletras,[1,6] Einar Heiberg,[1,2] and Erik Hedström[1,4,5,7]*

Purpose: To validate an automatic algorithm for offline T2* measurements, providing robust, vendor-independent T2*, and uncertainty estimates for iron load quantification in the heart and liver using clinically available imaging sequences.
Methods: A T2* region of interest (ROI)-based algorithm was developed for robustness in an offline setting. Phantom imaging was performed on a 1.5 Tesla system, with clinically available multiecho gradient-recalled-echo (GRE) sequences for cardiac and liver imaging. A T2* single-echo GRE sequence was used as reference. Simulations were performed to assess accuracy and precision from 2000 measurements. Inter- and intraobserver variability was obtained in a patient study (n = 23).
Results: Simulations: Accuracy, in terms of the mean differences between the proposed method and true T2* ranged from 0–0.73 ms. Precision, in terms of confidence intervals of repeated measurements, was 0.06–4.74 ms showing agreement between the proposed uncertainty estimate and simulations. Phantom study: Bias and variability were 0.26 ± 4.23 ms (cardiac sequence) and −0.23 ± 1.69 ms (liver sequence). Patient study: Intraobserver variability was similar for experienced and inexperienced observers (0.03 ± 1.44 ms versus 0.16 ± 2.33 ms). Interobserver variability was 1.0 ± 3.77 ms for the heart and −0.52 ± 2.75 ms for the liver.
Conclusion: The proposed algorithm was shown to provide robust T2* measurements and uncertainty estimates over the range of clinically relevant T2* values. **Magn Reson Med 75:1717–1729, 2016. © 2015 The Authors. Magnetic Resonance in Medicine published by Wiley Periodicals, Inc. on behalf of International Society for Magnetic Resonance.**

Key words: MRI relaxometry; iron-load; offline image processing; validation; uncertainty estimation

INTRODUCTION

Organ failure caused by iron overload is a major cause of death in patients with iron load disease. Accurate quantification of organ iron load has been shown useful in tailoring the therapy for such patients (1). MR imaging is used as the current reference standard to assess iron load in different organs. It is noninvasive, has documented high reliability and has been validated to biopsies in the heart and liver (2–7).

Different methods for quantification of iron load by MR T2* are generally used (7–9). T2* measurements can be performed from signal averages in a delineated region of interest (ROI) or on a pixel by pixel basis. Differences between methods are related to what is included in the ROI, the model used for curve fitting and applied echo times (TEs). In the presence of zero-mean Gaussian noise, a standard least-squares (LSQ) estimator is considered optimal (10). However, the non-Gaussian noise found in magnitude MR images (11,12) introduces a bias in the T2* measurement which depends on the signal-to-noise ratio (SNR). To reduce impact of noise on T2*, an exponential fit combined with a constant offset (13) and automatic truncation of data points (14) have been proposed. In addition, noise-correction schemes for single-channel coils (15) and root-sum-square (RSS) reconstruction of phased-array coils (16) were recently introduced to further reduce noise-bias.

Validated inline methods may simplify iron load measurements and improves clinical availability. However, robust offline T2* methods may have an important role in multivendor settings. The maximum likelihood estimate (MLE) method (17–19) is currently available for inline processing in some vendors and if the noise statistics are known, it is the optimal estimation method in terms of variance (17). However, noise statistics of an

---

[1] Lund Cardiac MR Group, Department of Clinical Physiology, Clinical Sciences Lund, Lund University, Skåne University Hospital, Lund, Sweden.
[2] Department of Biomedical Engineering, Faculty of Engineering, Lund University, Sweden.
[3] Department of Computer Science and Biomedical Informatics, University of Thessaly, Lamia, Greece.
[4] Division of Imaging Sciences and Biomedical Engineering, King's College London, London, United Kingdom.
[5] BHF Centre of Research Excellence and NIHR Biomedical Research Centre at Guy's and St Thomas' NHS Foundation Trusts and King's College London, London, United Kingdom.
[6] Laboratory of Medical Informatics, School of Medicine, Aristotle University of Thessaloniki, Greece.
[7] Department of Diagnostic Radiology, Clinical Sciences Lund, Lund University, Skåne University Hospital, Lund, Sweden.

Grant sponsor: Swedish Research Council; Grant numbers: 2011-3916, 2012-4944; Grant sponsor: the Wellcome Trust and the Engineering and Physical Sciences Research Council; Grant number: WT 088641/Z/09/Z; Grant sponsor: British Heart Foundation; Grant number: RE/08/03; Grant sponsor: the European Commission; Grant number: FP7-ICT-4485:euHeart.

*Correspondence to: Erik Hedström, M.D., Ph.D., Lund Cardiac MR Group, Departments of Clinical Physiology and Diagnostic Radiology, Lund University, Skåne University Hospital, Lund, Sweden. E-mail: erik.hedstrom@med.lu.se, Twitter: @erikheds

Received 2 November 2014; revised 26 March 2015; accepted 16 April 2015

DOI 10.1002/mrm.25767

Table 1
Overview of Typical Sequence Parameters Used in This Study

Parameter	Clinical T2* (cardiac)	Clinical T2* (liver)	Phantom measurements T2* sGRE (reference)	T2* mGRE (cardiac)	T2* mGRE (liver)	T1 MOLLI
Acquired voxel size [mm]	2 × 2	3 × 3	1.96 × 2.0	1.96 × 2.15	1.96 × 2.0	1.98 × 2.0
Slice thickness [mm]	10	10	8	10	10	10
Matrix size	160	116	112 × 106	112 × 102	112 × 110	116 × 90
FOV [mm]	320 × 320	348 × 348	220 × 212	220 × 220	220 × 220	230 × 180
TEs [ms]	2.5, 5.0, 7.5, 10.0, 12.5, 15.0, 17.5, 20.0, 22.5 and 25.0	1.2, 2.7, 4.2, 5.7, 7.2, 8.7, 10.2, 11.7, 13.2 and 14.7	1.34, 2, 3, 5, 7.5, 10, 12.5, 15, 20, 30, 40, 50, 75, 100, 150, 200, 300	2.5, 5, 7.5, 10, 12.5, 15, 17.5, 20, 22.5 and 25.0	1.3, 3.4, 5.5, 7.6, 9.7, 11.8, 13.9, 16, 18, 20.1	1.11
TR [ms]	26 ms	17 ms	6 × T1	26	38	2.4
Flip Angle	20°	20°	50°	20°	20°	35°
Parallel imaging	Factor 2 (SENSE)	No	No	Factor 2 (SENSE)	No	Factor 2 (SENSE)
Read-out profile	Linear	Linear	Linear	Linear	Linear	Linear
Turbo factor	6	No turbo factor;	No turbo factor;	6	No turbo factor;	48
Preparation pulse:	DIR	SPIR	No preparation	DIR	SPIR	IR
Flow-compensation	On	Off	Off	On	Off	On
T1 mapping scheme:	n/a	n/a	n/a	n/a	n/a	5(3s)3;

image-set is rarely available offline without requiring additional user interactions such as manually defining background regions for noise estimation or specifying image reconstruction technique. Moreover, uncertainty estimates for the obtained T2* value are not provided by current ROI-based methods.

Therefore, the purpose of this study was to introduce and validate an automatic algorithm for offline T2* measurements also providing uncertainty estimates for robust quantification of iron load in the heart and liver, optimized for a wide range of T2* values. The method was validated in numerical simulations, in a phantom study and was applied to cardiac and liver MR imaging in patients with known or suspected iron load disease.

METHODS

Patients were included at two centers. The protocol and procedures comply with the Declaration of Helsinki, and were approved by the local research ethics committees. All studies were performed using 1.5 Tesla (T) Philips Achieva systems (Philips Healthcare, Best, The Netherlands). An overview of typical sequence parameters used in this study is provided in Table 1.

Proposed T2* Analysis Method

We propose a new algorithm for T2* estimation in magnitude MR images called ADAPtive T2* estimation from combined Signal models (ADAPTS). It is a ROI-based algorithm adapting the curve-fitting approach to balance accuracy and precision. All image processing including the proposed algorithm was developed using MATLAB (v8.1.0.604, Mathworks) and was implemented in the medical image analysis software *Segment* (20), freely available for research purposes.

An overview of the algorithm is provided in Figure 1. In all steps, the ROI average is used for curve-fitting to increase SNR. The only manual interaction required is the delineation of a ROI. The first T2* estimate is a three-parameter offset model (13), initialized by the weighted least-squares on signal logarithm method (WLSL) (10). The signal model is shown in Eq. [1]:

$$S(TE) = PD{*}e^{-TE/T2^*} + C. \qquad [1]$$

The signal S depends on the TE, the proton density PD and an offset parameter C which approximates the noise-floor. Compared with a two-parameter monoexponential, shown in Eq. [2], The increased degree of freedom of a three-parameter fit enables closer approximation of the measured signal (13).

$$S(TE) = PD{*}e^{-TE/T2^*}. \qquad [2]$$

This, however, makes three-parameter models inherently sensitive to noise and over fitting to the obtained data points. The estimated offset parameter is used to approximate the noise plateau and instead of reporting the obtained T2* estimate (denoted $\widehat{T2}^*$ in the remainder of this section) as the final T2* value, ADAPTS uses the initial fit for data-truncation. TEs exceeding $P1 * \widehat{T2}^*$, where $P1$ is a nonzero constant, are excluded from the

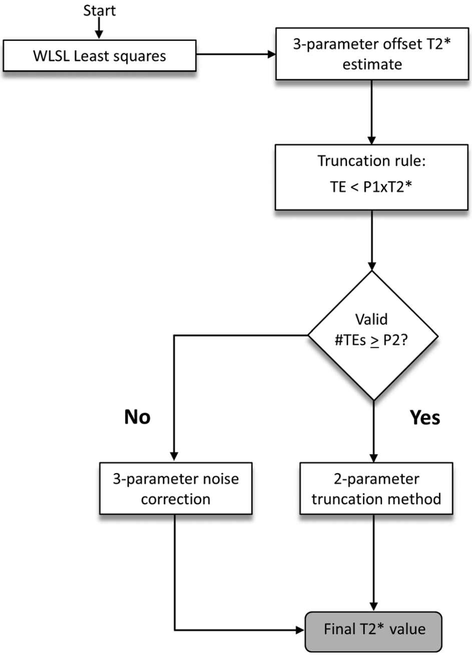

FIG. 1. Overview of the ADAPTS algorithm.

analysis and T2* is re-estimated from a two-parameter monoexponential fit (Eq. [2]) of remaining TE images, similar to the automatic truncation algorithm proposed by He et al (14). To refrain from extensive truncation which may lead to loss of precision, ADAPTS requires a minimum number of available TE images, a second constant *P*2, to proceed with the truncation method. If the number of valid TEs is below *P*2, ADAPTS assumes the number of remaining data points is insufficient for robust T2* estimation and switches to a noise-correction approach, similar to the M2NCM method (Second-Moment Noise-Corrected Model), proposed by Feng et al (16). This method fits the observed signal in all available TE images to the expected value of the noncentral chi distribution in the presence of an underlying monoexponential decay:

$$E\left[M^2\right] = S^2 + 2L\sigma^2. \qquad [3]$$

Here, M denotes the measured signal contaminated with noise, S is the underlying exponential decay (Eq. [2]), σ is the noise standard deviation and L the number of receiver coils in use. As previously proposed (16), the right term of Eq. [3] is estimated as a free parameter, resulting in a three-parameter model. This removes the need for manual noise measurements. The motivation for balancing the amount of included parameters and data points in use by switching between signal models was to enable robust T2* estimation in a wide range of T2* values. The three-parameter noise correction method is specifically designed to reduce noise bias in low SNR conditions and for T2* close to the minimum TE. However, the use of an additional free parameter may degrade precision for regions with high SNR where the noise bias is negligible. In these circumstances, a two-parameter truncation method may result in improved precision. Although the signal models in ADAPTS have all been previously introduced, the proposed combination scheme is novel. All presented curve-fitting methods used the Nelder Mead Simplex algorithm (21) for nonlinear optimization. Values for the constants *P1* and *P2* were optimized in the phantom study and in simulations, described in more detail below.

Estimation of Uncertainty

To estimate uncertainty of the obtained T2* value, T2* was calculated in nonoverlapping, equally sized subregions. From the subregion ensemble of T2* values the 95% confidence interval (CI) size was estimated. The size of the subregions were defined as a fixed percentage of the ROI size to produce a near-constant number of T2* values for each CI estimate. Due to the reduced number of pixels in the subregions compared with the ROI, the standard error of the mean (SEM) will increase for the pixel averages used for subregion T2* estimation. Assuming statistically independent pixels and a linear error propagation from the data-points to the T2* estimate, a correction factor may account for the difference in standard error:

$$SEM_{subroi} = \frac{\sigma}{\sqrt{n}}; \quad SEM_0 = \frac{\sigma}{\sqrt{N}} = \frac{\sqrt{n}}{\sqrt{N}} SEM_{subroi} \qquad [4]$$

$$\hat{\sigma}_{T2^*} = \frac{\sqrt{n}}{\sqrt{N}}\ \hat{\sigma}_{T2^* subrois}. \qquad [5]$$

Here, N denotes the number of independent pixels in the ROI and n denotes the number of independent pixels in a subregion. Although this measure does not directly correspond to the precision of the full-ROI T2* estimate, it serves as an approximation which is further affected by T2* homogeneity and varying noise levels within the ROI. Compared with pixelwise T2* estimates, subregion T2* results in improved precision due to pixel averaging, which more closely resembles the original ROI estimate. ADAPTS reports the T2* 95% CI together with the coefficient of variation (CoV; defined as the standard deviation divided by the ROI T2* value). Based on the obtained CoV estimate the user may be advised to adjust the ROI delineation.

Numerical Simulations

Numerical simulations were performed to assess accuracy and precision of ADAPTS and to evaluate reliability of the uncertainty estimate in relation to known T2* values. RSS reconstruction of 1, 6 and 32 receive-coils was simulated with identical monoexponential T2* decay on the real and imaginary part of a complex signal. Zero-mean Gaussian noise with predefined standard deviation

(SD) σ was added to each channel and the magnitude signal was created by the root sum of squares operation:

$$RSS = \sqrt{\sum_{l=1}^{L} M_l^2} \quad [6]$$

$$M_l = \sqrt{Im_l^2 + Re_l^2} \quad [7]$$

M_l denotes the magnitude signal of receive-channel l, *Im* denotes the imaginary signal component and *Re* the real component. The SNR was defined as S_0/σ, where S_0 is the signal intensity at $TE = 0$. The mean of 40 independent signals was averaged before curve-fitting to simulate ROI-averaging. A T2* range of 1–50 ms for $SNR = 15$ was simulated. TEs corresponding to the clinical T2* cardiac and liver sequences were used with TE ranges of 2.5–25 ms and 1–20 ms, respectively. T2* values below the minimum TE were not simulated for either sequence. This resulted in simulated T2* ranges for cardiac and liver of 2.2–50 ms and 1–50 ms, respectively. Simulations were repeated 2000 times to evaluate accuracy and precision of ADAPTS. From the 2000 repetitions, the mean and 95% CI of the ADAPTS T2* calculation were computed for each simulated T2* value.

In addition to ADAPTS, a two-parameter version of the noise correction method M2NCM was simulated which takes the true noise standard deviation as input. This enabled a comparison with a near-optimal method. The optimized parameters P1 and P2, previously derived from phantom measurements, were refined in simulations and accuracy and precision of ADAPTS was compared with each of the two included signal models (two-parameter automatic truncation and three-parameter noise-correction methods).

Reliability of ADAPTS uncertainty estimate was evaluated by comparing a total of 2000 CI estimates to the CI of the 2000 ADAPTS T2* ROI estimates. This procedure was repeated for multiple subregion sizes and ROI-sizes to optimize the CI estimates. Simulated ROI-sizes and region-sizes was (40, 100, 200, 400) pixels and (4%, 6%, 8%, 10%, 12%, 15%, 20% and 25%, respectively). Simulated ROI-size for evaluating the optimal subregion size was 40 pixels.

Phantom Study

Twelve 300 mL gel-phantoms with T2*/T1 values corresponding to iron overloaded myocardium (22) were used for validation. The phantoms consisted of a mixture of water, agarose, gadolinium (DOTAREM; Guerbet, France) and a SPIO Ferumoxsil contrast agent solution (LUMIREM; Guerbet, France). The concentrations of gadolinium and SPIO contrast-agent were varied to alter T1 and T2* while the agarose concentration was kept constant. Each phantom was scanned separately and was submerged in a water-filled container before imaging to reduce potential susceptibility artifacts.

Phantom Imaging

Phantom imaging was performed using a six-channel SENSE head-coil. Accuracy and precision of ADAPTS were evaluated in two clinically used, single breath-hold, multiecho gradient-recalled echo (mGRE) sequences for heart and liver imaging.

Accuracy of the clinical T2* sequences combined with ADAPTS was evaluated by comparison with a single-echo gradient-recalled echo (sGRE) reference sequence with ($TR > 6\ T_1$) to allow full longitudinal recovery between excitation pulses. T1 was measured in all phantoms with a Modified Look-Locker Inversion-Recovery (MOLLI) sequence using a 5(3s)3 scheme.

Precision was evaluated by calculating CIs in repeated measurements ($n = 120$ repetitions), in three phantoms for each sequence, and with target T2* selected to represent typical values seen in clinical imaging: (4 ms, 10 ms, 20 ms) and (2 ms, 8 ms, 15 ms) for the heart and liver sequences. All repetitions for a single phantom were performed in the same session, in direct sequence with a minimum pause of 7 s between repetitions. In addition, the repeated measurements were used to validate the proposed ADAPTS uncertainty estimate by direct comparison with the CIs obtained from the 120 repetitions, and the effect of varying the ADAPTS parameters $P1$ and $P2$ was evaluated in all combinations of a set of parameter values, specified in Figure 4. In total, 104 parameter configurations were evaluated and final values of parameters were chosen to maximize precision and minimize bias between ADAPTS and an inline MLE method. The sGRE method was not provided as reference in the parameter optimization to be able to use it for independent validation of accuracy for the chosen parameter set.

The sGRE reference sequence used a flip angle of 50° and typical TEs = (1.34 ms, 2 ms, 3 ms, 5 ms, 7.5 ms, 10 ms, 12.5 ms, 15 ms, 20 ms, 30 ms, 40 ms, 50 ms, 75 ms, 100 ms, 150 ms, 200 ms, 300 ms). The mGRE sequence for liver imaging used a flip angle of 20°, a repetition time of 38 ms, and TE = (1.3, 3.4, 5.5, 7.6, 9.7, 11.8, 13.9, 16, 18, 20.1 ms) and the mGRE sequence for cardiac imaging used a black blood DIR preparation scheme, a parallel imaging factor of 2 (SENSE), a flip angle of 20°, a repetition time of 26 ms and TEs = (2.5, 5, 7.5, 10, 12.5, 15, 17.5, 20, 22.5, and 25.0 ms). The MOLLI sequence used a repetition time TR/TE of 2.4/1.11 ms, and a flip angle of 35°. The shim volume was placed equivalently for all sequences in all phantoms and a simulated electrocardiogram was generated with a constant heart rate of 60 bpm. Further sequence details are found in Table 1.

Phantom Data Analysis

T1 in each phantom was measured from the provided inline T1 maps of MOLLI within a 3.1 cm^2 ROI. T2* from the sGRE sequence was determined from the acquired magnitude images, by a two-parameter monoexponential fit of the pixel-mean using a near-identical ROI compared to the one used for T1 measurements (ROI position was approximated due to subtle differences in resolution). The Nelder Mead Simplex algorithm (21) was used for nonlinear optimization and the initial starting values were obtained from the WLSL method (10). T2* from the two mGRE sequences were determined from the same 3.1 cm^2 ROI using inline MLE maps (18,23) and ADAPTS. The number of pixels within the ROIs for T2* estimation in phantoms was similar to

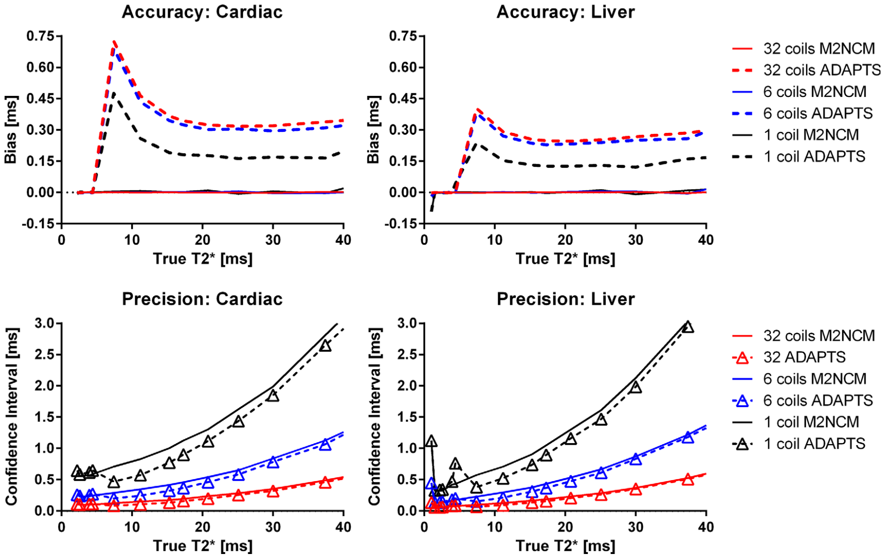

FIG. 2. Accuracy and precision in numerical simulations. Solid lines indicate the M2NCM method and dashed lines show ADAPTS. Number of simulated coils are color-coded. The upper panels show Accuracy in terms of mean differences between true T2* values, shown on the x-axes. The lower panels show CIs from all simulation experiments (2000 repetitions), for each simulated T2* value. Within the clinically relevant range, the proposed method results in high accuracy and precision. The gradual decrease in precision with increasing T2* is most likely attributed to lack of available data-points above 25 ms and 20 ms for cardiac and liver TEs, respectively, and is also seen in the near-optimal noise-corrected method. Simulated ROI size was 40 pixels.

the typical number of pixels in ROIs for heart and liver in the patient study.

Patient Study

Twenty-three patients (15 male; median age, 18 years; range, 1–69 years) with known or suspected iron load disease were included in this study. Written consent was given by the patients or, in case of minors, their guardians. MR images for determination of T2* values were collected as part of routine clinical iron load assessment.

Patient Imaging

For patient imaging, clinical mGRE sequences were used with a 5- or 32-channel cardiac coil in two centers. Two similar sequences were used, one optimized for cardiac and one for liver imaging (Table 1). The two sequences differed in initial TE (2.5 ms versus 1.2 ms), and TE increment (2.5 ms versus 1.5 ms). Both sequences used the generally available SPIR fat suppression and minor parameter changes were allowed to adapt for patient heart rate and field of view (FOV). Fat suppression was applied to avoid impact of fat on T2* quantification, especially in the liver, since previous work has indicated improved precision using fat suppression in mGRE imaging (24).

To assess cardiac iron a mid-ventricular slice was acquired using the clinical cardiac sequence. A black-blood double-inversion recovery (DIR) prepulse was used to decrease measurement error induced by blood contamination, and to enhance myocardial borders (25). Images were acquired within a single breath-hold using parallel imaging factor 2 (SENSE) to improve image resolution. Acquisition was carried out at end-diastole within a time window of approximately 110 ms per heartbeat. To assess liver iron, a midhepatic transversal slice was acquired using the clinical liver sequence.

Online reconstruction of T2* maps from an inline MLE method (18,23) was automatically performed for comparison with inter- and intraobserver variability of ADAPTS. Furthermore, T2* determined from ADAPTS and MLE in patients were directly compared as a proxy to the reference standard sGRE sequence, based on the results from the phantom validation.

Patient Data Analysis

Data were anonymized and randomized for blinded analysis. The ROIs were manually drawn at two occasions, by two observers (14 years and no previous MR experience, respectively) for analysis of intra- and interobserver variability, also accounting for user experience.

The ROIs were drawn in the acquired images for evaluation of T2* in full thickness myocardial septum and in a homogenous area of the liver parenchyma, anteriorly if not prevented by vessels or susceptibility artifacts. These exact ROIs were copied to the inline-constructed MLE T2* map to avoid measurement differences related to ROI delineation. The MLE image was reconstructed from the

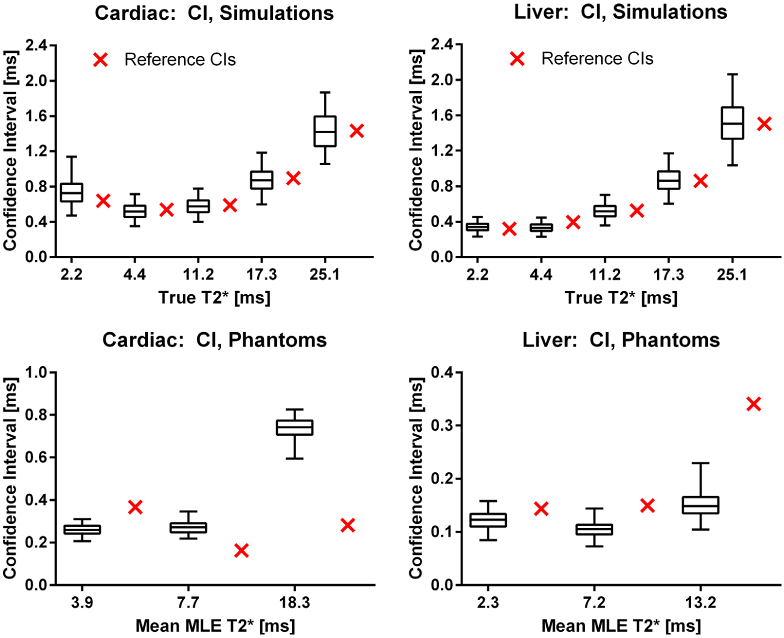

FIG. 3. Box-whiskers plots of the ADAPTS uncertainty estimate validation in simulations (top row) and repeated phantom measurements (bottom row). Simulations: 2.5% (bottom whiskers) and 97.5% (top whiskers) confidence limits from 2000 ADAPTS CI estimates in numerical simulations compared with the CIs obtained from the 2000 repetitions, shown as crosses directly to the right of each corresponding CI estimate. Boxes indicate first and third quartiles of the CI estimates and the horizontal line splitting the boxes shows the median. Note that the CI references (crosses outside boxes) all lie well within the confidence limits of the ADAPTS CI estimates for the simulated T2* values. Simulated ROI size was 40 pixels. Phantom study: 2.5% (bottom whiskers) and 97.5% (top whiskers) confidence limits from 120 ADAPTS CI estimations in repeated phantom scans, compared with the CIs calculated over all 120 repetitions (crosses directly to the right of the corresponding CI estimates). Limited overestimation and underestimation of CIs are observed.

very same acquisition as the ADAPTS analysis. To assure adequate ROI placement for both ADAPTS and MLE the curve fit using ADAPTS was visually inspected and the ROI redrawn in case of obvious incorrect placement. Software advice based on CoV for re-evaluation of delineation was also considered. Motion correction was not performed in the current study, as motion between images acquired within the same breath-hold was not detected.

Statistics

Statistical analyses were performed in MATLAB (v8.1.0.604, Mathworks). By default, statistical measures for the patient study were obtained from the experienced observer. Bias and variability are presented as mean ± 1.96 SD and median (range) was used where appropriate. Bland-Altman analysis (26) was used to compare methods and to analyze intraobserver and inter-observer variability in the patient study. Accuracy was defined as the obtained bias compared with a reference standard and the 95% CI was used to measure precision. In this study, CI is reported as the size of the 95% CI. A *P*-value < 0.001 was used to define statistical significance.

RESULTS

Numerical Simulations

Results from the simulation study are shown in Figures 2–4. Accuracy and precision for ADAPTS and the two-parameter M2NCM method is found in Figure 2. The mean differences between ADAPTS and true T2* for TEs corresponding to the cardiac and liver clinical sequences ranged from 0 to 0.73 ms and 0 to 0.40 ms. In both cases, the largest mean difference was found in the 32-coil simulation. Precision in terms of the 95% CI ranged from 0.08–4.30 ms for the cardiac TEs and 0.06–4.74 ms for the liver TEs. Mean differences for the two-parameter M2NCM method ranged from 0 to 0.04 ms for the cardiac and 0 to 0.10 ms for the liver TEs. For M2NCM, the maximum mean difference was found for the single-coil simulation. CIs were 0.05–1.97 ms and 0.02–2.27 ms for the cardiac and liver sequences. An increase in bias was observed for the ADAPTS method when the number of simulated coils increased. Precision was improved when the number of simulated coils were increased. Supporting Figure S1, which is available online, shows bias and CIs of the optimized parameters

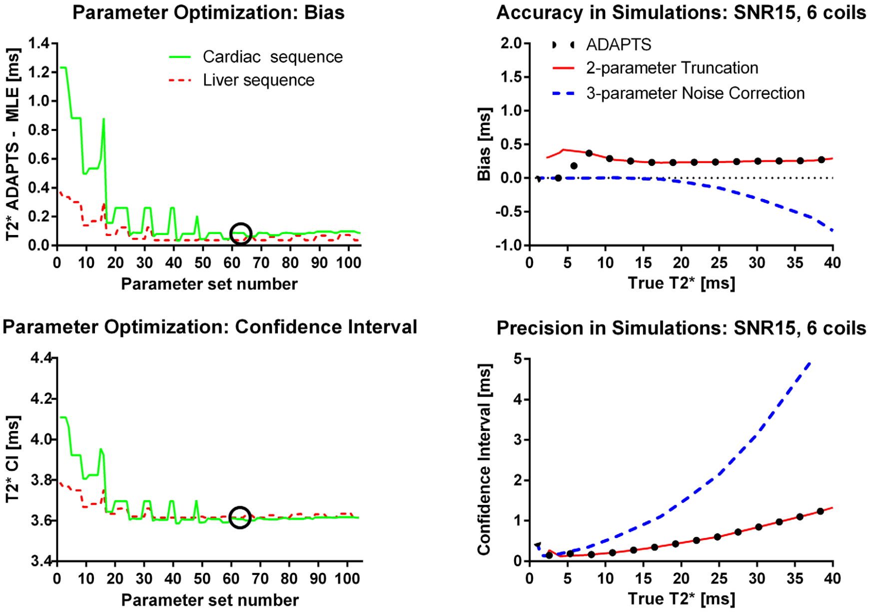

P1 values	1.0 T2* 6.0 T2*	1.5 T2* 6.5 T2*	2.0 T2* 7.0 T2*	2.5 T2*	3.0 T2*	3.5 T2*	4.0 T2*	**4.5 T2***	5.0 T2*	5.5 T2*
P2 values	3	4	5	6	7	8	**9**	10		

FIG. 4. Parameter optimization from phantoms (left column and bottom table) and simulated optimal parameters of the ADAPTS method for the liver sequence TEs (right column). Parameter optimization: Top row shows how varying ADAPTS two parameters impacts bias, defined here as the mean difference between ADAPTS and the inline MLE method. Bottom row shows precision, measured as the CI size of 120 phantom measurements over different parameter values, together with the list of evaluated parameters. In both top and bottom rows, solid lines indicate measurements performed for the cardiac sequence and phantoms and the dashed lines indicate measurements from the liver sequence and phantoms. Circles show the selected parameter set used in the remaining parts of this study. The results indicate a robustness to variations in parameters above a threshold of approximately $P1>3$. Right column compares accuracy and precision of the optimized ADAPTS method with the two included signal models (truncation and noise-correction) individually in simulations. The solid lines indicates the two-parameter truncation method, the dashed line shows the three-parameter noise correction method and the dotted line shows ADAPTS using the optimized parameter values. The optimized ADAPTS method balances low bias with maintained precision over the simulated T2* range. The shown simulations use TEs from the liver sequence, a SNR of 15, a ROI-size of 40 and uses RSS reconstruction with six receive-coils. The list of evaluated parameter values (bottom table) indicates the selected values of P1 and P2 with an underlined bold font.

P1 and P2 in simulations. P2 = 9 was selected as optimal parameter value. A comparison of accuracy and precision for ADAPTS and the two implemented signal models for the liver sequence TEs is shown in Figure 4. The two-parameter truncation method resulted in a limited but constant overestimation of T2* over the simulated range, while bias was minimal for the noise correction method for T2* below 20 ms. For T2* values above the maximum TE, an increasing underestimation was observed for the noise correction method.

The simulation results for ADAPTS uncertainty estimates are shown in Figure 3. Four percent was selected as the optimal subregion size, resulting in a mean bias and CI of 0.02 ms and 0.30 ms for all simulated ROI-sizes. For all simulated T2* values, and TEs, the CI reference standard lies within the 2.5% and 97.5% confidence limits of the 2000 uncertainty estimates and the largest observed mean bias between the CI estimate and the CI reference was 0.10 ms. Supporting Figures S2 and S3 shows bias and CIs of the uncertainty estimate over varying ROI- and subregion-sizes. A consistent improvement in precision (CI) was observed when decreasing the subregion size.

Phantom Study

The T2* and T1 ranges of the 12 phantoms were 2.20–40.24 ms and 470–1012 ms according to the T2* reference standard (sGRE) and MOLLI T1. T1 values are in the range of myocardial tissue. T2* of the six phantoms

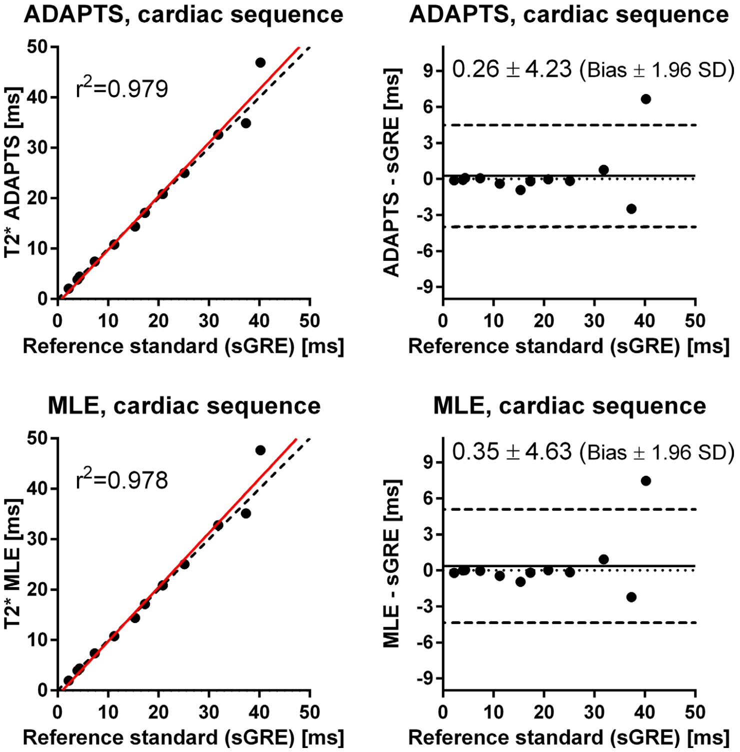

FIG. 5. Scatter plots (left) and difference plots (right) of T2* by ADAPTS (top) and MLE (bottom) using the clinical cardiac sequence, compared with the T2* reference standard (sGRE) in phantoms. Scatter plots: solid lines indicate linear regression and dashed lines represent identity lines. Difference plots: Solid lines indicate bias and dashed lines represent bias ± 1.96 SD. T2* values by ADAPTS and MLE using the clinical cardiac mGRE sequence agree well with the reference standard sGRE over a wide range of T2* values.

used to evaluate precision was 2.3, 3.9, 7.2, 7.7, 13.2, and 18.3 ms, obtained from the inline MLE method. The results from the phantom validation of ADAPTS uncertainty estimates for both clinical sequences are shown in Figure 3 (bottom row). The maximum observed difference between ADAPTS uncertainty estimate and the reference CI (from 120 repetitions) was limited to 0.58 ms for the cardiac sequence, and 0.27 ms for the liver sequence.

The results from the parameter optimization of ADAPTS are shown in Figure 4. The selected parameter set was number 63 (P1 = 4.5 and P2 = 9), where precision in terms of the range of obtained CIs was 0.49–1.36 ms and 0.29–1.60 ms for the six phantoms used for precision evaluation for the cardiac and liver sequences, respectively. The ADAPTS and MLE results from the phantom validation of accuracy for both the cardiac and liver sequences are shown in Figures 5 and 6. For the cardiac sequence, bias and variability (expressed as limits of agreement) for ADAPTS was 0.26 ± 4.23 ms, while MLE resulted in a bias and variability of 0.35 ± 4.63 ms. The liver sequence resulted in ADAPTS having bias and variability of −0.23 ± 1.69 ms, while bias and variability for the MLE was −0.22 ± 1.55 ms. The number of pixels within the drawn ROIs ranged from 194 to 200 pixels.

Patient Study

All images and reconstructed T2* maps were of adequate quality for determination of T2* in both heart and liver. In one patient, however, the cardiac image quality was visually suboptimal due to breathing artifacts, albeit adequate for analysis, and was, therefore, included in further analysis. In this patient we also found the largest intraobserver difference of 3.96 ms (11%). The range of cardiac and liver T2* was 9.6–51.2 ms and 0.6–25.0 ms, respectively, using the ADAPTS method. The range of obtained uncertainty estimates for the ADAPTS method, expressed as coefficient of variation (the estimated standard deviation divided by the ROI T2* value), was 0.05–0.46 for cardiac and 0.01–0.27 for liver measurements. The number of pixels within the drawn ROI:s ranged from 53–561 pixels for liver images and 44–358 pixels for heart images.

T2 by the ADAPTS and MLE Methods*

The ADAPTS and the MLE methods showed good agreement determining T2*, resulting in a bias and variability with limits of agreement of −1.28 ± 2.19 ms for the cardiac sequence; −0.13 ± 0.38 ms for the liver sequence and −0.71 ± 1.94 ms for the cardiac and liver sequences

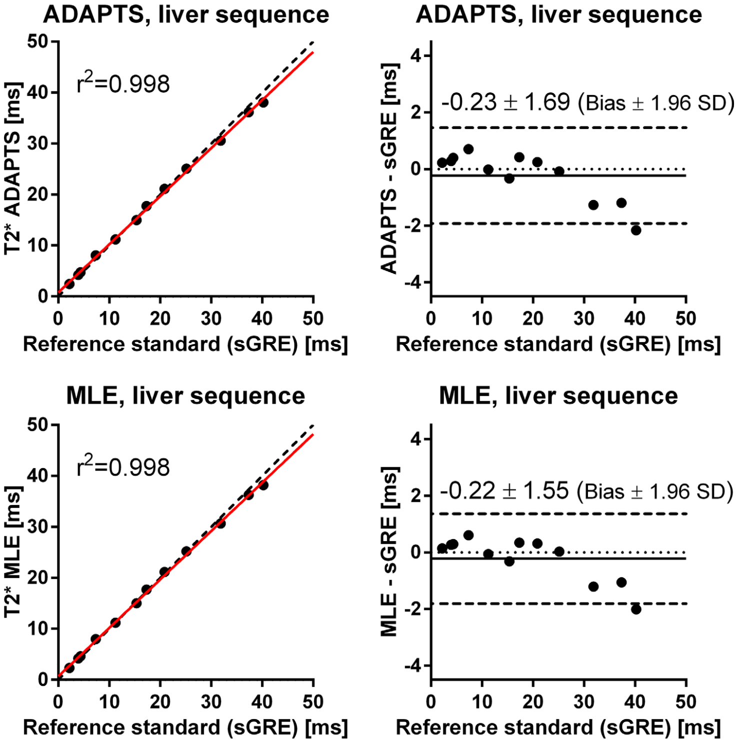

FIG. 6. Scatter plots (left) and difference plots (right) of T2* by ADAPTS (top) and MLE (bottom) using the clinical liver sequence compared with the T2* reference standard sGRE in phantoms. Scatter plots: solid lines indicate linear regression and dashed lines represent identity lines. Difference plots: Solid lines indicate bias and dashed lines represent bias ± 1.96 SD. T2* values by ADAPTS and MLE using the clinical liver mGRE sequence agree well with the reference standard sGRE over a wide range of T2* values.

combined (Fig. 7). T2* measured by the ADAPTS method ranged from 0.60–51.2 ms, while the MLE method ranged from 0.7−51.5 ms. A subtle trend toward higher T2* values was found for the MLE method compared with the ADAPTS method (Fig. 7) resulting in a statistically significant linear-regression slope ($P < 0.0001$ for the null-hypothesis). However, poor goodness of fit was found ($r^2 = 0.43$).

Intraobserver Variability

Low intraobserver variability was found for T2* determination by the experienced observer using both ADAPTS (0.12 ± 1.92 ms for the cardiac sequence, −0.06 ± 0.63 ms for the liver sequence and 0.03 ± 1.44 ms for both sequences combined; Figure 8, top left panel) and the MLE (0.20 ± 2.39 ms for the cardiac sequence, −0.12 ± 0.65 ms for the liver sequence and 0.04 ± 1.74 ms for both sequences combined; Figure 8, top right panel). Intraobserver variability was low also for the inexperienced observer using ADAPTS (0.01 ± 2.63 ms for the cardiac sequence, 0.31 ± 1.94 ms for the liver sequence and 0.16 ± 2.33 ms for both sequences combined; Figure 8, bottom left panel) and MLE (0.06 ± 2.66 ms for the cardiac sequence, 0.30 ± 1.85 ms for the liver sequence and 0.18 ± 2.25 ms for both sequences combined; Figure 8, bottom right panel) methods.

Interobserver Variability

Interobserver variability was low for both methods. Good agreement was found for both ADAPTS (limits of agreement of 1.0 ± 3.77 ms for the cardiac sequence, −0.52 ± 2.75 ms for the liver sequence and 0.24 ± 3.62 ms for both sequences combined; Figure 9, left panel) and MLE (limits of agreement of 1.17 ± 4.16 ms for the cardiac sequence, −0.53 ± 2.90 ms for the liver sequence and 0.32 ± 3.88 ms for both sequences combined; Figure 9, right panel).

DISCUSSION

This study shows that the proposed automatic ADAPTS method provides accurate and precise determination of T2* in heart and liver for iron-load quantification in a wide and clinically relevant range for use in an offline setting. The ADAPTS method provides uncertainty estimates of the calculated T2* value, which is of importance to assess the reported T2* validity, especially in follow-up studies and for titrating treatment. The process of dividing pixels within the ROI into subregions to estimate uncertainty is not unique for ADAPTS and can be applied to most other T2* algorithms. However, validation both numerically and experimentally of such uncertainty measurements are crucial for clinical utility.

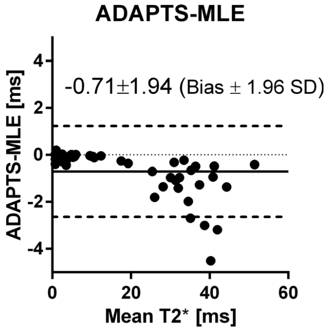

FIG. 7. Bland-Altman analysis of ADAPTS and MLE in patients measured by the experienced user. Good agreement was found.

T2* determination by MRI is commonly used to estimate iron load in patients and has been shown to provide good interscanner and interobserver reproducibility (4,5). The requirement for manual interaction in some of the current analysis methods adds a subjective factor which, although often clinically insignificant in myocardial T2* measurements (27), may present challenges in liver T2* determination (9,19,28). Iron overload is usually first found in the liver (29). Therefore, accurate early determination of liver iron load and treatment thereof may prevent accumulation of iron throughout the body and thus avert organ failure (30–32).

However, extremely low T2* values related to severe iron load of the liver may give few usable data points from the acquired images, due to current limitations in hardware to further reduce TE. This may lead to incorrect iron-load assessment and possibly erroneous follow-up of chelation therapy.

The automatic MLE method has been compared with other available methods for iron-load determination, showing good agreement but also superiority for lower T2* values found in severe liver iron overload (19). By removing the need for manual curve-fitting interaction, the MLE method decreases user dependency. Using the MLE method thereby allowed us to test ADAPTS's validity in patients with reduced user bias. We found that ADAPTS reports accurate T2* values with inter- and intraobserver variability comparable to the MLE method, and thereby can be reliably used, strengthened by phantom validation with the sGRE reference standard. In addition, ADAPTS was shown to have similar precision as a near-optimal, noise correction method in numerical simulations. Although ADAPTS resulted in increased bias, the two-parameter M2NCM used the true noise standard deviation generally unavailable to offline estimation methods. Compared with a single simulated receive-coil, bias was increased for 6 and 32 coils in

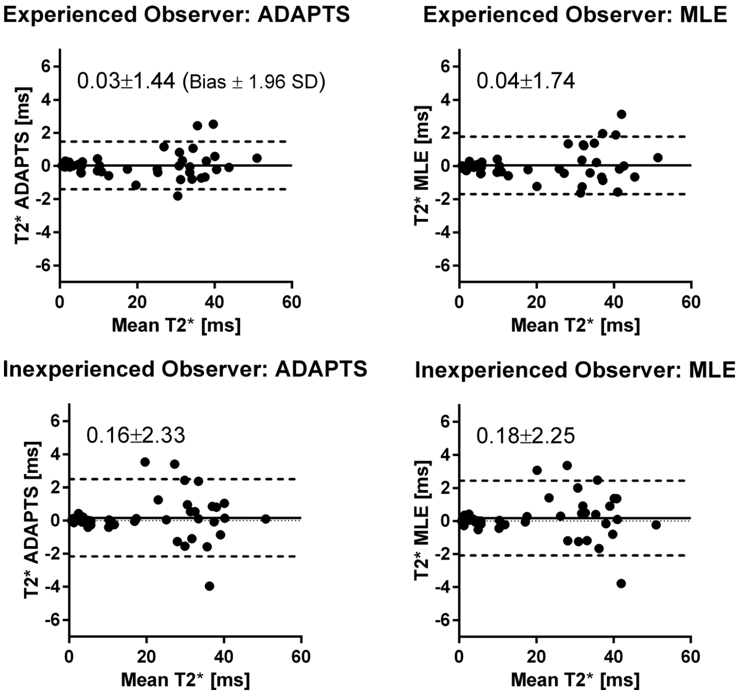

FIG. 8. Bland-Altman analyses of intraobserver variability for the experienced user for ADAPTS (top left) and MLE (top right). Corresponding analyses for the inexperienced user (bottom row). Good agreement was found between all measurements.

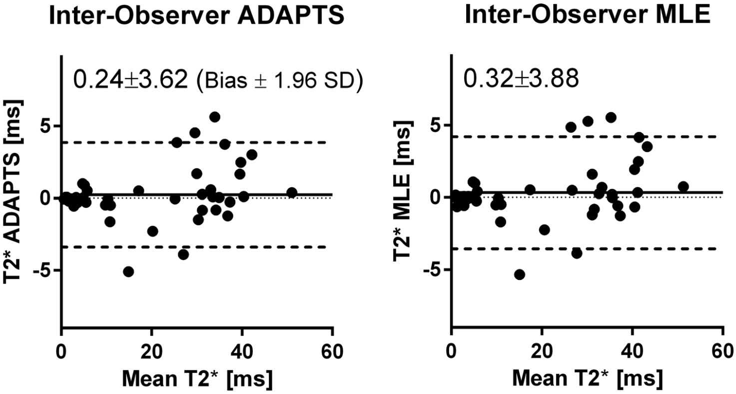

FIG. 9. Bland-Altman analysis of interobserver variability using the ADAPTS method (left panel) and MLE (right panel). Good agreement was found between the experienced and inexperienced observer.

simulations. The observed increase in bias agrees with the expected increase in noise bias for the noncentral chi distribution present in the simulated RSS reconstruction (12). This indicates that a slight sensitivity to noise-bias remains for ADAPTS. However, the observed bias were limited and converged when the number of coils increased from 6 to 32. An increase in precision for both T2* methods was observed when the number of coils increased. The gain in SNR associated with increasing the number of coils in RSS reconstruction may explain this (33).

The T2* uncertainty estimate gives the user possibility to evaluate the precision of measurement and helps determine whether changes in iron load levels have actually occurred between scans. This is especially important in high liver iron load which has a very steep T2* curve and where individual data points may have a large impact on reported T2* values.

Over- and underestimation of the reference T2* CI was observed in phantoms. This behavior was not seen in the numerical simulations where the proposed uncertainty estimate followed the reference CIs with low bias. The images acquired in the phantom experiments may include some degree of noise correlations between receive-channels or adjacent pixels which could partly explain the discrepancy. Furthermore, the uncertainty estimate is sensitive to spatial variations in SNR and T2*. This, however, may aid the user in ROI adjustments by reporting elevated uncertainty in ROIs containing unwanted, heterogeneous T2* regions and noise levels.

Noteworthy, with decrease in iron load a statistically significant trend toward higher T2* values was found in patients for the MLE method compared with the ADAPTS. It remains to study why this happens, and more importantly the clinical significance of these differences. A retrospective study in a large population with biopsy samples available may help shed light on clinical significance and impact of cutoff values for severity of iron load.

Subtle differences were found between ADAPTS and MLE for intra- and interobserver variability. The sample size was, however, too small for deductions of increased performance in regards to user-dependency. One major difference between MLE and ADAPTS is the pixelwise fit performed by the MLE. This may, in part, explain some of the observed discrepancies. Previous studies have shown decreased performance of other pixelwise methods (27,34,35), however, investigating the extent to which these findings are valid for the MLE method is beyond the scope of this study. Bias between observers and intraobserver variability for the inexperienced observer using the ADAPTS method were lower than previously published data (36). This implies that ADAPTS may be straight-forward to start using in centers with low experience of iron load analyses, which may increase availability of iron load determination using MR imaging, in turn leading to enhanced patient care and further decrease of mortality (37).

Limitations

A single-slice approach was applied for patient imaging as this is clinical routine at one of the including centers. The algorithm is, however, not restricted to single-slice acquisition and can be extended to multislice analysis where needed.

Simulations of spatially varying noise were not performed. Future simulation studies using advanced MRI pulse-sequence simulations (38) may provide improvements in this regard.

CONCLUSIONS

ADAPTS is a validated automatic algorithm for T2* determination providing accurate iron load measurements over a wide range of clinically relevant T2* values for the heart and liver. Uncertainty estimates of the reported T2* allows more reliable determination of changes in iron load at follow-up. To allow practical utility of the method the software is freely available for research purposes. Phantom data will be made available upon request for algorithm benchmarking.

ACKNOWLEDGMENTS

Einar Heiberg is the founder of Medviso AB, producing medical image analysis software. All other authors declare no conflict of interest. This study was funded by the Swedish Heart-Lung Foundation; the Medical Faculty of Lund University, Sweden; Skane University Hospital Lund, Sweden; the Swedish Societies of Medicine, Radiology and Cardiology, Sweden; Region of Scania, Sweden; Swedish Research Council. The Division of Imaging Sciences receives support as the Centre of Excellence in Medical Engineering (funded by the Wellcome Trust and the Engineering and Physical Sciences Research Council) as well as the British Heart Foundation Centre of Excellence (British Heart Foundation award). This work was also supported by the European Commission. The authors acknowledge financial support from the Department of Health by means of the National Institute for Health Research comprehensive Biomedical Research Centre award to Guy's and St. Thomas' National Health Service Foundation Trust in partnership with King's College London and King's College Hospital National Health Service Foundation Trust.

REFERENCES

1. Pennell DJ, Porter JB, Cappellini MD, et al. Deferasirox for up to 3 years leads to continued improvement of myocardial T2* in patients with β-thalassemia major. Haematologica 2012;97:842–848.
2. Anderson LJ, Holden S, Davis B, et al. Cardiovascular T2-star (T2*) magnetic resonance for the early diagnosis of myocardial iron overload. Eur Heart J 2001;22:2171–2179.
3. Carpenter J-P, He T, Kirk P, et al. On T2* magnetic resonance and cardiac iron. Circulation 2011;123:1519–1528.
4. Tanner MA, He T, Westwood MA, Firmin DN, Pennell DJ; Thalassemia International Federation Heart T2* Investigators. Multi-center validation of the transferability of the magnetic resonance T2* technique for the quantification of tissue iron. Haematologica 2006;91: 1388–1391.
5. Westwood MA, Anderson LJ, Firmin DN, Gatehouse PD, Lorenz CH, Wonke B, Pennell DJ. Interscanner reproducibility of cardiovascular magnetic resonance T2* measurements of tissue iron in thalassemia. J Magn Reson Imaging 2003;18:616–620.
6. Wood JC, Otto-Duessel M, Aguilar M, Nick H, Nelson MD, Coates TD, Pollack H, Moats R. Cardiac iron determines cardiac T2*, T2, and T1 in the gerbil model of iron cardiomyopathy. Circulation 2005;112: 535–543.
7. Wood JC, Enriquez C, Ghugre N, Tyzka JM, Carson S, Nelson MD, Coates TD. MRI R2 and R2 * mapping accurately estimates hepatic iron concentration in transfusion-dependent thalassemia and sickle cell disease patients. Blood 2005;106:1460–1465.
8. He T, Gatehouse PD, Kirk P, Mohiaddin RH, Pennell DJ, Firmin DN. Myocardial T*2 measurement in iron-overloaded thalassemia: an ex vivo study to investigate optimal methods of quantification. Magn Reson Med 2008;60:350–356.
9. Meloni A, Rienhoff HY, Jones A, Pepe A, Lombardi M, Wood JC. The use of appropriate calibration curves corrects for systematic differences in liver R2* values measured using different software packages. Br J Haematol 2013;161:888–891.
10. Bonny JM, Zanca M, Boire JY, Veyre A. T2 maximum likelihood estimation from multiple spin-echo magnitude images. Magn Reson Med 1996;36:287–293.
11. Henkelman RM. Measurement of signal intensities in the presence of noise in MR images. Med Phys 1985;12:232–233.
12. Constantinides CD, Atalar E, Mcveigh ER. Signal-to-noise measurements in magnitude images from NMR phased arrays. Magn Reson Med 1997;38:852–857.
13. Ghugre NR, Enriquez CM, Coates TD, Nelson MD, Wood JC. Improved R2* measurements in myocardial iron overload. JMRI 2006;23:9–16.
14. He T, Zhang J, Carpenter J-P, Feng Y, Smith GC, Pennell DJ, Firmin DN. Automated truncation method for myocardial T2* measurement in thalassemia. J Magn Reson Imaging 2013;37:479–483.
15. Raya JG, Dietrich O, Horng A, Weber J, Reiser MF, Glaser C. T2 measurement in articular cartilage: impact of the fitting method on accuracy and precision at low SNR. Magn Reson Med 2010;63:181–93.
16. Feng Y, He T, Gatehouse PD, Li X, Harith Alam M, Pennell DJ, Chen W, Firmin DN. Improved MRI R2 * relaxometry of iron-loaded liver with noise correction. Magn Reson Med 2013;70:1765–1774.
17. Sijbers J, den Dekker AJ, Raman E, Van Dyck D. Parameter estimation from magnitude MR images. Int J Imaging Syst Technol 1999;10:109–114.
18. Sénégás J, Knopp T, Dahnke H. Dealing with spatially varying noise in T2* mapping with SENSE. In Proceedings of the 15th Annual Meeting of ISMRM, Berlin, Germany, 2007. Abstract 1782.
19. Yokoo T, Yuan Q, Senegas J, Wiethoff A, Pedrosa IM. Rician-noise based R2* estimation for severe hepatic iron overload: simulation, phantom, and early clinical experience. In Proceedings of the 22nd Annual Meeting of ISMRM, Milan, Italy, 2014. Abstract 144.
20. Heiberg E, Sjögren J, Ugander M, Carlsson M, Engblom H, Arheden H. Design and validation of segment - freely available software for cardiovascular image analysis. BMC Med Imaging 2010;10:1–13.
21. Nelder JA, Mead R. A simplex method for function minimization. Comput J 1965;7:308–313.
22. Feng Y, He T, Carpenter J-P, Jabbour A, Alam MH, Gatehouse PD, Greiser A, Messroghli D, Firmin DN, Pennell DJ. In vivo comparison of myocardial T1 with T2 and T2* in thalassaemia major. J Magn Reson Imaging 2013;38:588–593.
23. Bos C, Duijndam A, Sénégas J. Reference phantom validation of T2-mapping: maximum likelihood estimation of T2 from magnitude phased-array multi-echo data. In Proceedings of the 17th Annual Meeting of ISMRM, Honolulu, Hawaii, USA, 2009. Abstract 4526.
24. Sanches-Rocha L, Serpa B, Figueiredo E, Hamerschlak N, Baroni R. Comparison between multi-echo T2* with and without fat saturation pulse for quantification of liver iron overload. Magn Reson Imaging 2013;31:1704–1708.
25. He T, Gatehouse PD, Kirk P, Tanner MA, Smith GC, Keegan J, Mohiaddin RH, Pennell DJ, Firmin DN. Black-blood T2* technique for myocardial iron measurement in thalassemia. J Magn Reson Imaging 2007;25:1205–1209.
26. Bland JM, Altman DG. Statistical methods for assessing agreement between two methods of clinical measurement. Lancet 1986;1:307–310.
27. Meloni A, Rienhoff HY, Jones A, Pepe A, Lombardi M, Wood JC. Cardiac R2* values are independent of the image analysis approach employed. Magn Reson Med 2014;72:485–491.
28. Hernando D, Levin YS, Sirlin CB, Reeder SB. Quantification of liver iron with MRI: state of the art and remaining challenges. J Magn Reson Imaging 2014;40:1003–1021.
29. Batts KP. Iron overload syndromes and the liver. Mod Pathol 2007; 20(Suppl. 1):S31–S39.
30. Anderson LJ, Wonke B, Prescott E, Holden S, Malcolm Walker J, Pennell DJ. Comparison of effects of oral deferiprone and subcutaneous desferrioxamine on myocardial iron concentrations and ventricular function in beta-thalassaemia. Lancet 2002;360:516–520.
31. Brittenham GM, Griffith PM, Nienhuis AW, McLaren CE, Young NS, Tucker EE, Allen CJ, Farrell DE, Harris JW. Efficacy of deferoxamine in preventing complications of iron overload in patients with thalassemia major. N Engl J Med 1994;331:567–573.
32. Gabutti V, Piga A. Results of long-term iron-chelating therapy. Acta Haematol 1996;95:26–36.
33. Roemer PB, Edelstein WA, Hayes CE. The NMR phased array. Magn Reson Med 1990;16:192–225.
34. Marro K, Otto R, Kolokythas O, Shimamura A, Sanders JE, Mcdonald GB, Friedman SD. A simulation-based comparison of two methods for determining relaxation rates from relaxometry images. Magn Reson Imaging 2011;29:497–506.
35. Feng Y, He T, Feng M, Carpenter J-P, Greiser A, Xin X, Chen W, Pennell DJ, Yang G-Z, Firmin DN. Improved pixel-by-pixel MRI R2* relaxometry by nonlocal means. Magn Reson Med 2014;72:260–268.
36. Paper S, Triadyaksa P, Handayani A, Willems T, Oudkerk M, Sijens PE. Inter-observer reproducibility improvement of myocardial iron T2 * calculation using CNR-optimised composite image. In Proceedings of the Annual Meeting of ECR, Vienna, Austria, 2014.

37. Modell B, Khan M, Darlison M, Westwood MA, Ingram D, Pennell DJ. Improved survival of thalassaemia major in the UK and relation to T2* cardiovascular magnetic resonance. J Cardiovasc Magn Reson 2008;10:42.
38. Xanthis CG, Venetis IE, Chalkias a V, Aletras AH. MRISIMUL: a GPU-based parallel approach to MRI simulations. IEEE Trans Med Imaging 2014;33:607–617.

SUPPORTING INFORMATION

Additional Supporting Information may be found in the online version of this article.

Figure S1. Parameter optimization from simulations. Two near-optimal values of P1 was simulated over the entire range of P2 values. Left column shows Confidence intervals (Top) and mean bias (bottom) for the simulated parameter values for the cardiac sequence TEs and the right column shows the corresponding plots for the liver sequence TEs. In all graphs, the solid lines and dashed lines represent simulations using one and six coils, respectively. The line marked with triangles indicates 32 simulated coils. The dotted vertical line shows the selected parameter set, corresponding to P1 = 4.5 and P2 = 9. A P1 value was selected by mainly considering stability, as shown in Figure 4.

Figure S2. Optimization of the uncertainty estimate in simulations with relative subregion sizes of 4–10%. Top row shows confidence intervals of the uncertainty estimates in simulations and the impact of varying simulated ROI-size and subregion size percentages. Bottom row shows Mean bias of CI estimates with the left and right column showing the results from the cardiac and liver sequence TEs, respectively. Decreasing subregion percentages and increasing the ROI size improve precision of CI estimates. For the liver sequence TEs, bias is consistently decreased when the subregion size is reduced. The observed behavior is also seen in Supporting Figure S3.

Figure S3. Optimization of the uncertainty estimate in simulations with relative subregions sizes of 12–25%. Top row shows confidence intervals of the uncertainty estimates in simulations and the impact of varying simulated ROI-size and subregion size percentages. Bottom row shows Mean bias of CI estimates with the left and right column showing the results from the cardiac and liver sequence TEs, respectively. Decreasing subregion percentages and increasing the ROI size improve accuracy and precision of CI estimates. The order of accuracy and precision among simulated subregion sizes is preserved over the evaluated ROI-size interval. This may suggest that the relative percentages used to define the subregion size is robust to changes in ROI size. The observed behavior is also seen in Supporting Figure S2.

Paper II: Validation of T1 and T2 algorithms for quantitative MRI: Performance by a vendor-independent software.

Paper II

Bidhult *et al. BMC Medical Imaging* (2016) 16:46
DOI 10.1186/s12880-016-0148-6

BMC Medical Imaging

SOFTWARE Open Access

Validation of T1 and T2 algorithms for quantitative MRI: performance by a vendor-independent software

Sebastian Bidhult[1,2], George Kantasis[1,3], Anthony H. Aletras[1,3], Håkan Arheden[1], Einar Heiberg[1,2] and Erik Hedström[1,4*]

Abstract

Background: Determination of the relaxation time constants T1 and T2 with quantitative magnetic resonance imaging is increasingly used for both research and clinical practice. Recently, groups have been formed within the Society of Cardiovascular Magnetic Resonance to address issues with relaxometry. However, so far they have avoided specific recommendations on methodology due to lack of consensus and current evolving research. Standardised widely available software may simplify this process.
The purpose of the current study was to develop and validate vendor-independent T1 and T2 mapping modules and implement those in the versatile and widespread software Segment, freely available for research and FDA approved for clinical applications.

Results: The T1 and T2 mapping modules were developed and validated in phantoms at 1.5 T and 3 T with reference standard values calculated from reference pulse sequences using the Nelder-Mead Simplex optimisation method. The proposed modules support current commonly available MRI pulse sequences and both 2- and 3-parameter curve fitting. Images acquired in patients using three major vendors showed vendor-independence. Bias and variability showed high agreement with T1 and T2 reference standards for T1 (range 214–1752 ms) and T2 (range 45–338 ms), respectively.

Conclusions: The developed and validated T1 and T2 mapping and quantification modules generated relaxation maps from current commonly used MRI sequences and multiple signal models. Patient applications showed usability for three major vendors.

Keywords: T1, T2, Mapping, Quantitative magnetic resonance imaging

Background

Quantitative magnetic resonance imaging (MRI) is increasingly used for several different applications in both research and clinical practice. For cardiac MRI, T1 quantification enables measurement of myocardial extracellular volume [1–3], whereas T2 mapping detects oedema in acute myocardial infarction [4]. The Society of Cardiovascular Magnetic Resonance (SCMR) has also recently formed groups and provides general recommendations on use of mapping for research and clinical applications [5, 6]. However, specific recommendations have been avoided so far due to lack of consensus and current evolving research [6]. The Society is thus awaiting this field to develop so that guidelines can be properly formulated. Standardised software may simplify and speed up this process.

Further, cancer imaging has benefited from T1 to T2 mapping for determining early tumour progression in brain [7], and provides improved discrimination between benign and malign findings in suspected prostate cancer [8]. Also, oxygen saturation in blood has been accurately measured noninvasively by T2 mapping in children with complex congenital heart disease, yielding an opportunity

---

* Correspondence: erik.hedstrom@med.lu.se
[1] Department of Clinical Sciences Lund, Clinical Physiology, Lund University, Skane University Hospital, Lund, Sweden
[4] Department of Clinical Sciences Lund, Diagnostic Radiology, Lund University, Skane University Hospital, Lund, Sweden
Full list of author information is available at the end of the article

Table 1 Supported sequences and signal fitting models

	Supported signal models	
Supported sequences	3-parameter fit model	2-parameter fit model
T1 spin-echo IR (magnitude images)	$S(t) = \lvert A\ (1 - B\ \exp(-t/T1))\rvert$	$S(t) = \lvert A\ (1 - 2\ \exp(-t/T1))\rvert$
T1 PSIR	$S(t) = A\ (1 - B\ \exp(-t/T1))$	$S(t) = A\ (1 - 2\ \exp(-t/T1))$
T1 saturation recovery balanced SSFP	$S(t) = A\ (1 - B\ \exp(-t/T1))$	$S(t) = A\ (1 - \exp(-t/T1))$
T1 MOLLI/T1 Look-Locker correction (magnitude images)	$S(t) = \lvert A\ (1 - B\ \exp(-t/T1^*))\rvert$; $T1 = T1^*\ (B - 1)$	n/a
T1 MOLLI/T1 Look-Locker correction (PSIR images)	$S(t) = A\ (1 - B\ \exp(-t/T1^*))$; $T1 = T1^*\ (B - 1)$	n/a
T2 spin echo (multi-echo and single-echo)	$S(t) = A\ \exp(-t/T2) + B$; $B > 0$	$S(t) = A\ \exp(-t/T2)$
T2-prepared balanced SSFP	$S(t) = A\ \exp(-t/T2) + B$; $B > 0$	$S(t) = A\ \exp(-t/T2)$

IR inversion recovery, *PSIR* phase sensitive inversion recovery, *MOLLI* modified Look-Locker inversion recovery, *SSFP* steady-state free precession

to potentially avoid cardiac catheterisation for follow-up studies in children [9].

Different numerical algorithms can be used to compute T1 and T2 relaxation maps and therefore inline map generation may vary between MRI vendors. Also, most inline systems do not present the curve fit, which, if visualised, can be used as a marker of accuracy. Moreover, the algorithms used are not openly documented. A previous open-source software overcame these limitations, but is only to be used for research [10]. Last but not least, current available software is generally limited in signal models and fitting options.

The purpose of this study was to develop, validate and openly document T1 and T2 relaxation map modules with multiple signal models, test those in images acquired using three major vendors, and implement the validated modules in freely available software for research [11].

Implementation

The T1 and T2 mapping modules were developed and validated in phantoms with reference standard T1 and T2 values calculated from reference spin echo (SE) pulse sequences using the Nelder-Mead Simplex optimisation method available in Matlab (Math Works, Natick, MA; 2014a). The proposed modules support current commonly available MRI pulse sequences and both 2- and 3-parameter curve fitting (Table 1).

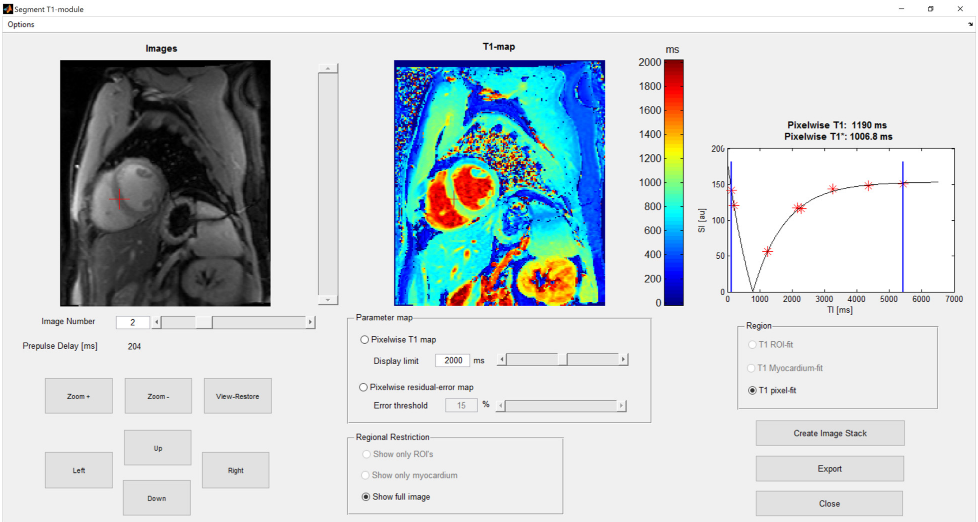

Image Number 2

Prepulse Delay [ms] 204

○ Pixelwise T1 map

Display limit 2000 ms

○ Pixelwise residual-error map

Error threshold 15 %

○ Show only ROI's

○ Show only myocardium

● Show full image

Pixelwise T1: 1190 ms

Pixelwise T1*: 1006.8 ms

○ T1 ROI-fit

○ T1 Myocardium-fit

● T1 pixel-fit

Fig. 1 The image shows the graphical user interface of the T1 mapping module (the T2 mapping module shares the design). An example of a cardiac pre-contrast MOLLI T1 map at 1.5 T in a healthy volunteer is shown. Both pixel-wise mapping, for the whole image and ROI-based, and ROI-based global mean mapping are available. The residuals of the curve fit for both T1 and T2 mapping can be visualised, indicating areas within the image that have a higher deviation from the curve and thus less accurate T1 and T2 values

The T1 mapping module graphical user interface is shown in Fig. 1 (the T2 mapping module shares the design). Both ROI-based global mean mapping and pixelwise mapping for the whole image and ROI-based are available. Further, the residuals of the curve fit for both T1 and T2 mapping can be visualised, indicating areas within the image that have a higher deviation from the curve and thus less accurate T1 and T2 values.

The validated modules were finally implemented in the software Segment, freely available for research (http://www.medviso.com) [11].

Since Segment already includes a validated module for T2* mapping and quantification [12], this topic was not covered in the current study.

Phantom setup and imaging

A Eurospin (Diagnostic Sonar, Livingston, UK) phantom encompassing 12 gadolinium/agarose gel phantoms was used for validation of the proposed modules. The phantoms were scanned at both 1.5 T and 3 T (Siemens Aera and Prisma, Erlangen, Germany). Single-echo spin-echo sequences were used for acquiring the reference T1 and T2 values. Pulse sequence parameters are presented in Table 2. The magnetization was allowed to fully recover between spin radiofrequency excitations.

Commonly available T1 and T2 mapping sequences were used to acquire images of the phantom, and the proposed modules were applied to generate T1 and T2 relaxation constant maps. The sequences were based on a free-breathing single-shot balanced steady-state free precession (bSSFP) sequence.

T1 mapping

Pixelwise T1 estimates were initialized using a lookup-table search performed in two steps in a T1 interval of 0–4000 ms. First, a step of 50 ms between lookup-table entries was applied for high performance. Thereafter, to find the optimal value, a second search was performed using a 5 ms difference between lookup-table entries within 100 ms of the entry found in the first step. In these two steps, depending on the pulse sequence, ideal inversion/saturation efficiency was assumed and each pixel was normalized with the maximum absolute value within its time-series. The T1 lookup-table entry resulting in the minimum sum of absolute error was chosen as the initial T1 value.

Table 2 Typical MRI sequence parameters

	TE (ms)	TR (ms)/delay between contrast preparations pulses	FA (°)	FOV (mm)	Matrix	Preparation pulse delays (ms)	iPAT/SENSE factor	Receiver BW (kHz)	ACQ time (hh:mm:ss)
T1 spin-echo IR (magnitude images)	5.8	10,000/10,000	90	241 × 241	128 × 128	[21, 60, 100, 200, 300, 500, 660, 900, 1050, 1300, 1600, 2000, 2250, 2500, 3000, 3500, 4300]	off	64	06:45:20
T1 PSIR	1.11	2.4/40,000	35	360 × 270	192 × 144	[150, 300, 400, 500, 700, 900, 1100, 1300, 1800, 2000, 2500, 3000, 3700, 4300, 5000, 6300] + 1 reference image without IR-preparation	2	208.32	00:11:20
T1 saturation recovery balanced SSFP	1.11	2.4/40,000	35	360 × 270	192 × 144	[150, 300, 400, 500, 700, 900, 1100, 1300, 1800, 2000, 2500, 3000, 3700, 4300, 5000, 5600, 6300, 8000] + 1 reference image without SR preparation	2	208.32	00:12:40
T1 MOLLI/T1 Look-Locker correction (magnitude and PSIR images)	1.1	2.4/7920	35	360 × 270	192 × 144	[130, 210, 1130, 1210, 2130, 2210, 3130, 4130]	2	208.32	00:00:11
T2 spin echo (single-echo)	[6, 12, 20, 30, 40, 50, 70, 90, 120, 140, 180, 300, 400, 600, 1000]	10,000/10,000	90	241 × 241	128 × 128	n/a	off	64	05:20:00
T2 spin echo (multi-echo)	[9, 18, 27, 36, 45, 54, 63, 72, 81, 90, 99, 108, 117, 126, 135, 144]	1500/n/a	90	160 × 160	256 × 256	n/a	off	62.5	00:06:24
T2-prepared balanced SSFP	1.11	2.4/20,000	35	360 × 270	192 × 144	T2p range = 25 – 200; ΔT2p = 5;	2	208.32	00:12:20

IR inversion recovery, *PSIR* phase sensitive inversion recovery, *MOLLI* modified Look-Locker inversion recovery, *SSFP* steady-state free precession

Following T1 initialization, pixel T1 values were refined using a C implementation of the Nelder-Mead Simplex nonlinear optimisation algorithm [13]. Convergence was assumed when the maximum T1 absolute difference between two simplexes was less than 0.10 ms. The C implementation was performed to reduce computation times and was thus not used for calculating the ROI-based global mean where instead the pre-implemented Matlab fminsearch method [14] was sufficient.

For T1 reference values, an inversion recovery (IR) single-echo spin echo sequence was used with a short echo time and long repetition time (Table 2). Two variations of the free-breathing bSSFP sequence were used for T1 mapping; one based on SR and one based on IR preparation pulses respectively applied before imaging readout. At 1.5 T, T1 was also estimated using a breath-hold MOLLI sequence with pre- and post-contrast cardiac configurations (5(3b)3 and 4(1b)3(1b)2) for analysis of phantoms with $T1 > 600$ ms and $T1 < 600$ ms, respectively. Since the MOLLI acquisition alters the recovery curve in itself, inducing T1* measurements, the Look-Locker correction from T1* to T1 was performed (Table 1), as previously proposed [15]. Magnitude images were used to estimate T1 from spin echo, SR-bSSFP and MOLLI sequences. For IR-bSSFP, the phase and magnitude images were extracted in order to reconstruct phase-sensitive inversion recovery (PSIR) images, as previously proposed [16].

T2 mapping

The initial T2 estimate was initialized by a weighted 2-parameter linear regression of the signal logarithm [17]. The estimation was repeated for stepwise truncation of the maximum echo time until three data points remained. The T2 estimate resulting in the minimum sum of absolute error over all data points was chosen as the initial T2 estimate.

Following the T2 initialisation, all pixels with T2 values outside the interval $0 < T2 < 400$ ms were excluded from further analysis and the final T2 estimate was refined using the above-mentioned nonlinear optimisation algorithm. Convergence was assumed when the maximum T2 absolute difference between two simplexes was less than 0.10 ms. Pixels that were not refined with nonlinear optimization were set to 0 in the resulting T2 map.

For T2 reference values, a single-echo spin echo sequence was used. The free-breathing bSSFP sequence used T2 preparation pulses for T2 mapping. An SR-prepared image with a short saturation time was used for the T2 calculation in order to improve the 3-parameter curve fit [18]. Magnitude images were used to estimate T2 from both spin echo and bSSFP sequences.

Residual calculation for T1 and T2 mapping

Curve-fit residuals for T1 and T2 mapping were calculated as the average absolute difference between the fitted curve and corresponding pixel values. Residuals were normalised relative to the maximum absolute pixel value within its time-series and reported as a percentage.

Application on human MR images

The developed and validated T1 and T2 mapping modules were applied on images acquired from three major vendors. Standard available sequences were used on Siemens (1.5 T Aera and 3 T Prisma, Erlangen, Germany) with 60-channel phased array coils and a 20-channel head coil; Philips (1.5 T Achieva, Best, the Netherlands) with 32-channel phased array coils; and on GE (3 T Discovery 750w, General Electrics, USA) with a GEM flex medium array coil. The local ethics committee approved the research protocol and all subjects provided written consent.

Table 3 Computational times for pixel-wise mapping in the complete image and in a selected ROI, respectively

	Pixel-wise (complete image)	Pixel-wise (ROI only)
T1 spin-echo IR (magnitude images)	2.5 s (3 parameters, 17 images, 128 × 128 images, 13 435 refined pixels)	0.03 s (3 parameters, 17 images, 200 pixels, 152 refined pixels)
T1 PSIR	11.7 s (3 parameters, 17 images, 192 × 144 matrix, 26 597 refined pixels)	0.15 s (3 parameters, 17 images, 200 pixels, 200 refined pixels)
T1 saturation recovery balanced SSFP	11.2 s (3 parameters, 15 images, 192 × 144 matrix, 26 594 refined pixels)	0.09 s (3 parameters, 15 images, 202 pixels, 202 refined pixels)
T1 MOLLI/T1 Look-Locker correction (magnitude and PSIR images)	6.4 s (3 parameters, 9 images, 192 × 144 matrix, 25 128 refined pixels)	0.05 s (3 parameters, 9 images, 202 pixels, 198 refined pixels)
T2 spin echo (single-echo and multi-echo)	1.12 s (2 parameters, 15 images, 128 × 128 matrix, 9 175 refined pixels)	0.04 s (2 parameters, 15 images, 207 pixels, 160 refined pixels)
T2-prepared balanced SSFP	11.7 s (3 parameters, 37 images, 192 × 144 matrix, 16 322 refined pixels)	0.14 s (3 parameters, 37 images, 207 pixels, 184 refined pixels)

The ROI-based global mean fitting takes less than 2 s for all sequences and is not listed. Performance was tested at a 2.4 GHz, 8 GB RAM, SSD HDD standard laptop running the MS Windows 7 64-bit operating system

IR inversion recovery, *PSIR* phase sensitive inversion recovery, *MOLLI* modified Look-Locker inversion recovery, *SSFP* steady-state free precession

Statistics

Bias and variability were determined using the modified Bland-Altman analysis. The bias and variability percentages were computed as the difference between the proposed method and the reference standard divided with the reference standard values. Values were expressed as mean ± SD and 95 % limits of agreement.

Results

Computational times were generally fast independent of amount of information, i.e. for both full image and ROI-based calculations (Table 3).

The T1 and T2 reference values ranged from 214 to 1643 ms and 46–338 ms for 1.5 T, and 229–1752 ms and 45–316 ms for 3 T, respectively. Phantom validation results are shown for 1.5 T and 3 T (Fig. 2) and corresponding curve fit examples at 1.5 T (Fig. 3). The T1 bias and variability at 1.5 T were 0.8 ± 8 ms (0.2 ± 1.2 %) for SR-bSSFP using the 3-parameter fit, and 24 ± 9 ms (3.5 ± 2.3 %) using the 2-parameter fit. Corresponding bias and variability for PSIR-bSSFP at 1.5 T were 3.2 ± 3.8 ms (0.6 ± 1.0 %) and −31 ± 26 ms (−3.5 ± 2.1 %). For cardiac MOLLI at 1.5 T the bias and variability was −39 ± 45 ms (−3.3 ± 3.4 %). The higher variability for MOLLI was related to low T2, with errors above 5 % originating from phantoms with reference T2 values < 60 ms.

The T1 bias and variability at 3 T were for SR-bSSFP − 6 ± 11 ms (−0.7 ± 0.9 %) when applying a 3-parameter fit, whereas a 2-parameter fit yielded 22 ± 13 ms (2.8 ± 1.6 %). Corresponding bias and variability for PSIR-

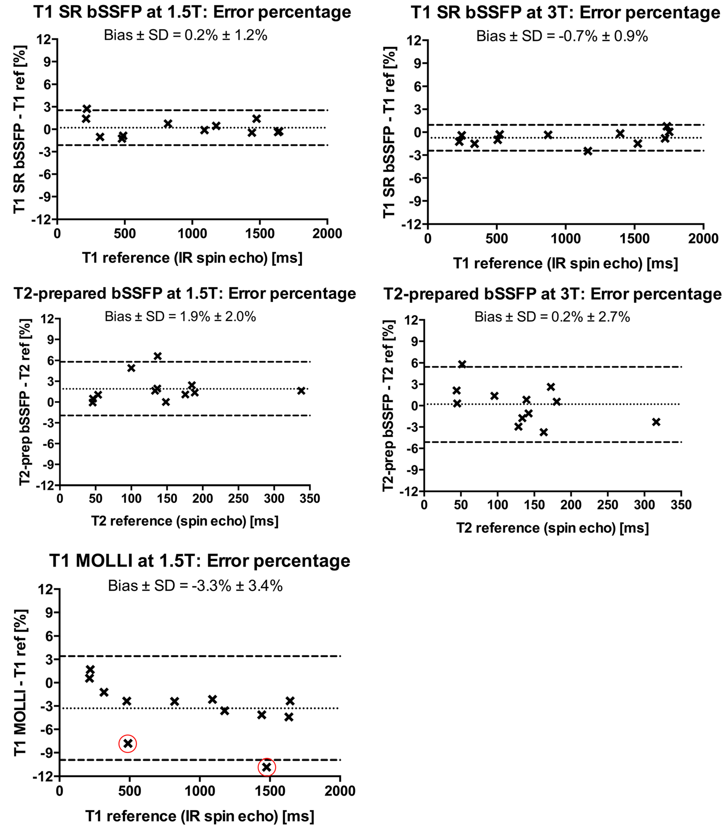

Fig. 2 Modified Bland-Altman analyses of the phantom validation data at 1.5 T (*left column*) and 3 T (*right column*). All curve fits were performed using the 3-parameter fit. The dotted and dashed lines represent bias and 95 % limits of agreement. A generally high agreement was found. The T1 outliers dependent on low T2 (<60 ms) found using the MOLLI sequence at 1.5 T are encircled in *red*. bSSFP = balanced steady-state free precession; MOLLI = modified Look-Locker inversion recovery; SR = saturation recovery; IR = inversion recovery

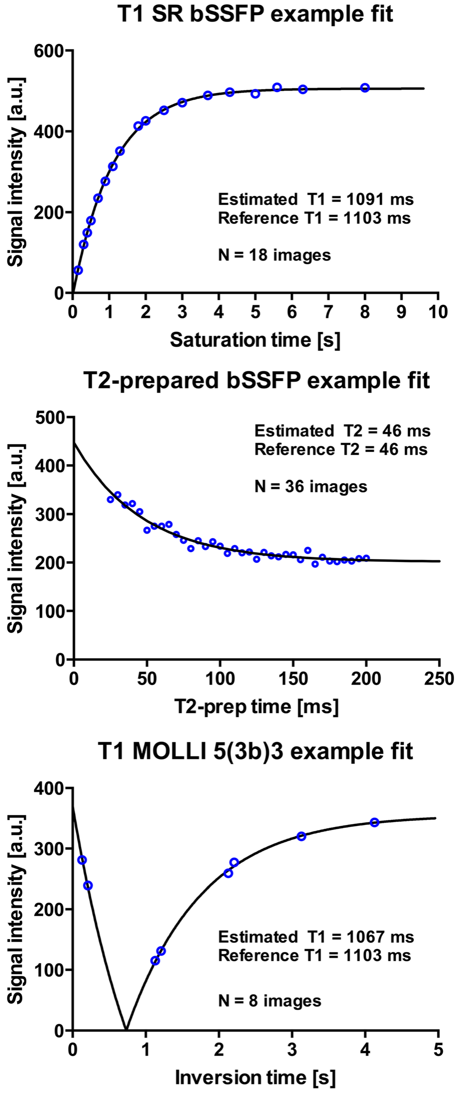

Fig. 3 Example curve fits for T1 and T2 at 1.5 T in two phantoms. The solid lines represent estimated relaxation curves. bSSFP = balanced steady-state free precession; MOLLI = modified Look-Locker inversion recovery; SR = saturation recovery

bSSFP at 3 T were −9 ± 13 ms (−1.1 ± 1.0 %) and −36 ± 33 ms (−3.3 ± 2.1 %).

The T2 bias and variability were 2.8 ± 2.7 ms (1.9 ± 2.0 %) at 1.5 T and −0.7 ± 3.6 ms (0.2 ± 2.7 %) at 3 T using the 3-parameter fit.

Figure 4 shows T1 and T2 maps from human applications for three major vendors.

Discussion

The developed and validated T1 and T2 mapping modules generated maps from commonly used MRI sequences and multiple signal models. Generally low bias and variability were found compared with reference standard measurements in phantoms. Patient applications showed usability for three major vendors. The main software is freely available for research and well documented.

The proposed algorithms showed particularly good agreement with the reference standard for saturation recovery sequences. However, T1 was underestimated by MOLLI when also phantoms with low T2 values (<60 ms) were included. This is similar to previously published data showing T2 sensitivity for MOLLI T1 mapping, with approximately 5 % error in T1 values for T2 below 30 ms [19]. This underestimation may be corrected for by using recently proposed lookup-table methods [20]. Another explanation for the increased variability using MOLLI compared to saturation recovery may be the reduced number of sampling points used for MOLLI in this study.

The slightly higher, albeit not large, variability shown for the T2 prepared sequence may be explained by limited signal-to-noise ratio. The T2 prepared mapping may be improved by acquiring several data points (echoes), especially late TE images since an offset is known to occur. Another solution is to acquire fewer echoes and instead add a saturation recovery acquisition, as performed in the current study [18]. This solution only adds a single heartbeat to the acquisition time (approximately 1 s) and is therefore applicable in most patients. Preferably, more than 1 saturation recovery acquisition should be added for averaging. This number may on the other hand need to be optimised in the individual case, especially in cardiac disease where the patient may have difficulties extending the duration of the breath hold.

The proposed software modules include both 2- and 3-parameter T1 and T2 fitting. In theory, a reduced number of parameters should result in reduced random errors (i.e. reduced variability) while however also leading to a risk of introducing a bias due to increased sensitivity to measurement imperfections. In cardiac MRI, 3-parameter T1 curve fitting is commonly applied to reduce bias associated with imperfect preparation-pulse efficiency and/or effects from applied readout pulses [21, 22]. The 3-parameter curve fit has also been suggested for cardiac T2 mapping when using the T2-prepared bSSFP sequence [18]. Unbiased 2-parameter fitting for cardiac T1 mapping has recently been proposed [23], which may lead to an increased need for software

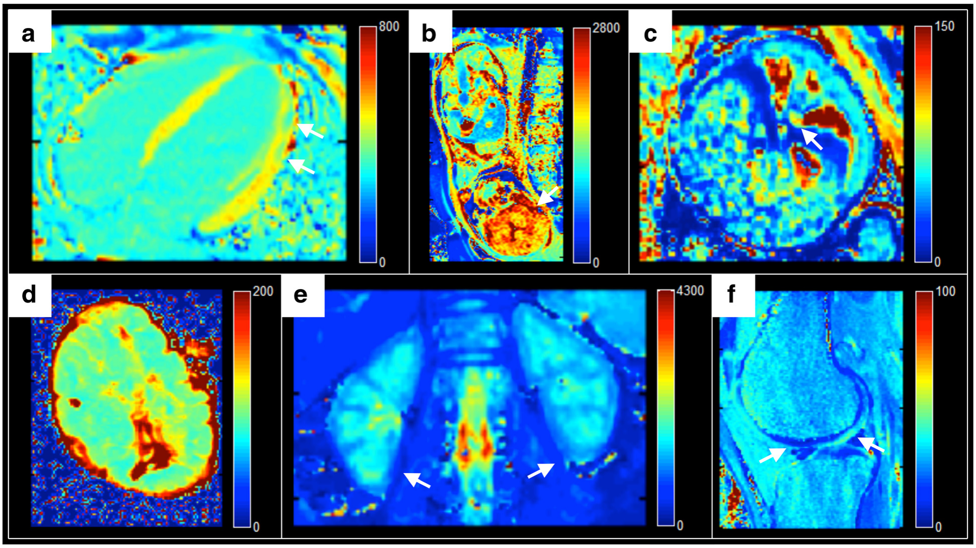

Fig. 4 Application of the proposed T1 and T2 mapping modules on images acquired in humans and ex vivo. Data from 3 major vendors were used for reconstruction of T1 and T2 maps. Arrows point to findings or structures. **a** Siemens Aera 1.5 T myocarditis (T1, MOLLI); **b** Siemens Aera 1.5 T healthy foetal brain (T1, inversion-recovery bSSFP); **c** Siemens Aera 1.5 T healthy foetal blood oxygenation in descending aorta (T2, T2-prepared bSSFP); **d** Siemens Prism 3 T ex vivo healthy placenta (T1, inversion-recovery bSSFP); **e** Philips 1.5 T healthy kidney (T1, MOLLI); **f** GE 750w 3 T healthy knee cartilage (T2, multi-echo spin-echo)

supporting 2-parameter T1 mapping in the near future. Clinical validation was not performed as part of the current study, as it is important to first validate algorithms that are to be applied in future in vivo studies. Finally, albeit data from three major vendors were tested, other vendors may use other sequences or reporting of data for fitting, and future studies may benefit from including additional vendors.

Limitations

In the current modules neither rigid nor non-rigid registration has been implemented. These methods may in some cases improve the diagnostic quality and are subject to future improvements and investigations and will be included in future updates of the modules. Further, some MRI vendors use private dicom headers for data needed for T1 and T2 mapping. These headers may change between MRI vendor software updates. Current known private dicom headers have been implemented in the proposed modules and future updates aim to cover these changes.

Conclusions

The developed and validated T1 and T2 mapping modules generated relaxation maps from current commonly used MRI sequences and multiple signal models. Patient applications showed usability for three major vendors. The main software is freely available for research and well documented.

Abbreviations

bSSFP, balanced steady-state free precession; IR, inversion recovery; MOLLI, modified Look-Locker inversion recovery; MRI, magnetic resonance imaging; PSIR, phase-sensitive inversion recovery; SCMR, society of cardiovascular magnetic resonance; SE, spin echo; SR, saturation recovery.

Acknowledgements

We gratefully acknowledge Medical MR physicist Christian Gustafsson, Department of Radiation Physics, Lund University, for assistance acquiring mapping data on the GE scanner.

Funding

Funding was received from: Swedish Research Council (621-2012-4944), Swedish Heart and Lung Foundation, Region of Skåne, Skåne University Hospital in Lund, and as an Excellence Grant from the Greek General Secretariat for Research and Technology.

Availability of data and materials

The project name is Segment and the project home page is http://www.medviso.com. Pre-compiled versions are available for Microsoft Windows. The Matlab source-code version requires Matlab R2014a or later. Segment is freely available for academic investigational research use, provided that relevant original research publications related to the software are cited. For usage of the T1 and T2 modules the current study is the appropriate citation. The software is free for educational purposes. The terms of the licence do not generally include trials paid by pharmaceutical companies. For commercial use, Segment is sold and supported by Medviso

AB, Lund, Sweden. Individuals or organisations are not allowed to compile software products derived from Segment that are to be sold commercially or shipped together with other commercial products without the express written permission of Medviso AB.
Phantom data sets and anonymous subject data sets can be made available on request.

Authors' contributions
SB performed most of the programming, made substantial contributions to conception and design, acquired, analysed and interpreted data and drafted the manuscript. GK made substantial contributions to conception and design, acquired data, and revised the manuscript for important intellectual content. AHA made substantial contributions to conception and design, provided MR physics expertise for validation experiments, and revised the manuscript for important intellectual content. HA and EiH made substantial contributions to conception and design, and revised the manuscript for important intellectual content. ErH made substantial contributions to conception and design, acquired, analysed and interpreted data, and drafted the manuscript. All authors read and approved the final manuscript.

Competing interests
The authors declare that they have no competing interests, with the following exception. Dr. Einar Heiberg founded the company Medviso AB, Lund, Sweden, and is the major shareholder of said company, selling the FDA-approved software version of Segment for commercial use.

Consent for publication
Consent to publish individual images was signed as part of ethical written consent.

Ethics approval and consent to participate
The Lund Regional ethics committee approved the study and all subjects provided written consent.

Author details
[1]Department of Clinical Sciences Lund, Clinical Physiology, Lund University, Skane University Hospital, Lund, Sweden. [2]Department of Biomedical Engineering, Faculty of Engineering, Lund University, Lund, Sweden. [3]Laboratory of Medical Informatics, School of Medicine, Aristotle University of Thessaloniki, Thessaloniki, Greece. [4]Department of Clinical Sciences Lund, Diagnostic Radiology, Lund University, Skane University Hospital, Lund, Sweden.

Received: 16 December 2015 Accepted: 28 July 2016

References

1. Arheden H, Saeed M, Higgins CB, Gao DW, Bremerich J, Wyttenbach R, et al. Measurement of the distribution volume of gadopentetate dimeglumine at echo-planar MR imaging to quantify myocardial infarction: comparison with 99mTc-DTPA autoradiography in rats. Radiology. 1999;211:698–708.
2. Ugander M, Oki AJ, Hsu LY, Kellman P, Greiser A, Aletras AH, et al. Extracellular volume imaging by magnetic resonance imaging provides insights into overt and sub-clinical myocardial pathology. Eur Heart J. 2012; 33:1268–78.
3. Kellman P, Hansen MS. T1-mapping in the heart: accuracy and precision. J Cardiovasc Magn Reson. 2014;16:1–20.
4. Ugander M, Bagi PS, Oki AJ, Chen B, Hsu LY, Aletras AH, et al. Myocardial Edema as Detected by Pre-Contrast T1 and T2 CMR Delineates Area at Risk Associated With Acute Myocardial Infarction. JCMG Elsevier Inc. 2012;5:596–603.
5. Moon JC, Messroghli DR, Kellman P, Piechnik SK, Robson MD, Ugander M, et al. Myocardial T1 mapping and extracellular volume quantification: a Society for Cardiovascular Magnetic Resonance (SCMR) and CMR Working Group of the European Society of Cardiology consensus statement. J Cardiovasc Magn Reson. 2013;15:1.
6. Schulz-Menger J, Bluemke DA, Bremerich J, Flamm SD, Fogel MA, Friedrich MG, et al. Standardized image interpretation and post processing in cardiovascular magnetic resonance: Society for Cardiovascular Magnetic Resonance (SCMR) Board of Trustees Task Force on Standardized Post Processing. J Cardiovasc Magn Reson. 2013;15:1.
7. Lescher S, Jurcoane A, Veit A, Bähr O, Deichmann R, Hattingen E. Quantitative T1 and T2 mapping in recurrent glioblastomas under bevacizumab: earlier detection of tumor progression compared to conventional MRI. Neuroradiology. 2014;57:11–20.
8. Yamauchi FI, Penzkofer T, Fedorov A, Fennessy FM, Chu R, Maier SE, et al. Prostate cancer discrimination in the peripheral zone with a reduced field-of-view T2-mapping MRI sequence. Magn Reson Imaging Elsevier Inc. 2015; 33:525–30.
9. Nield LE, Qi X-LL, Valsangiacomo ER, Macgowan CK, Wright GA, Hornberger LK, et al. In vivo MRI measurement of blood oxygen saturation in children with congenital heart disease. Pediatr Radiol. 2005;35:179–85.
10. Messroghli DR, Rudolph A, Abdel-Aty H, Wassmuth R, Kühne T, Dietz R, et al. An open-source software tool for the generation of relaxation time maps in magnetic resonance imaging. BMC Med Imaging BioMed Central Ltd. 2010;10:16–8.
11. Heiberg E, Sjögren J, Ugander M, Carlsson M, Engblom H, Arheden H. Design and validation of Segment—freely available software for cardiovascular image analysis. BMC Med Imaging BioMed Central Ltd. 2010;10:1.
12. Bidhult SL, Xanthis CG, Liljekvist LL, Greil GF, Nagel E, Aletras AH, et al. A new validated T2* analysis method with certainty estimates for cardiac and liver iron load determination. J Cardiovasc Magn Reson BioMed Central Ltd. 2015;17:P52.
13. Nelder JA, Mead R. A Simplex Method for Function Minimization. Comput J Oxford University Press. 1965;7:308–13.
14. Lagarias JC, Reeds JA, Wright MH, Wright PE. Convergence properties of the Nelder–Mead simplex method in low dimensions. SIAM J Optim. 1998;9: 112–47.
15. Deichmann R, Haase A. Quantification of T 1 values by SNAPSHOT-FLASH NMR imaging. J Magn Reson (1969). 1992;96:608–12.
16. Xue H, Greiser A, Zuehlsdorff S, Jolly M-P, Guehring J, Arai AE, et al. Phase-sensitive inversion recovery for myocardial T1 mapping with motion correction and parametric fitting. Magn Reson Med Wiley Subscription Services, Inc, A Wiley Company. 2013;69:1408–20.
17. Bonny JM, Zanca M, Boire JY, Veyre A. T2 maximum likelihood estimation from multiple spin-echo magnitude images. Magn Reson Med. 1996;36:287–93.
18. Akçakaya M, Basha TA, Weingärtner S, Roujol S, Berg S, Nezafat R. Improved quantitative myocardial T 2mapping: Impact of the fitting model. Magn Reson Med. 2014;74:93–105.
19. Gai ND, Stehning C, Nacif M, Bluemke DA. Modified Look-Locker T1 evaluation using Bloch simulations: human and phantom validation. Magn Reson Med Wiley Subscription Services, Inc, A Wiley Company. 2013;69:329–36.
20. Xanthis CG, Bidhult S, Kantasis G, Heiberg E, Arheden H, Aletras AH. Parallel simulations for QUAntifying RElaxation magnetic resonance constants (SQUAREMR): an example towards accurate MOLLI T1 measurements. J Cardiovasc Magn Reson. 2015;17:104.
21. Messroghli DR, Radjenovic A, Kozerke S, Higgins DM, Sivananthan MU, Ridgway JP. Modified Look-Locker inversion recovery (MOLLI) for high-resolutionT1 mapping of the heart. Magn Reson Med. 2004;52:141–6.
22. Chow K, Flewitt JA, Green JD, Pagano JJ, Friedrich MG, Thompson RB. Saturation recovery single-shot acquisition (SASHA) for myocardial T1mapping. Magn Reson Med. 2013;71:2082–95.
23. Kellman P, Xue H, Chow K, Spottiswoode BS, Arai AE, Thompson RB. Optimized saturation recovery protocols for T1-mapping in the heart: influence of sampling strategies on precision. J Cardiovasc Magn Reson. 2014;16:55.

Paper III: Parallel simulations for QUAntifying RElaxation magnetic resonance constants (SQUAREMR): an example towards accurate MOLLI T1 measurements.

Paper III

Xanthis *et al. Journal of Cardiovascular Magnetic Resonance* (2015) 17:104
DOI 10.1186/s12968-015-0206-1

Journal of Cardiovascular Magnetic Resonance

RESEARCH **Open Access**

Parallel simulations for QUAntifying RElaxation magnetic resonance constants (SQUAREMR): an example towards accurate MOLLI T1 measurements

Christos G. Xanthis[1,2], Sebastian Bidhult[1], George Kantasis[3], Einar Heiberg[1,4,5], Håkan Arheden[1] and Anthony H. Aletras[1,3*]

Abstract

Background: T1 mapping is widely used today in CMR, however, it underestimates true T1 values and its measurement error is influenced by several acquisition parameters. The purpose of this study was the extraction of accurate T1 data through the utilization of comprehensive, parallel Simulations for QUAntifying RElaxation Magnetic Resonance constants (SQUAREMR) of the MOLLI pulse sequence on a large population of spins with physiologically relevant tissue relaxation constants.

Methods: A CMR protocol consisting of different MOLLI schemes was performed on phantoms and healthy human volunteers. For every MOLLI experiment, the identical pulse sequence was simulated for a large range of physiological combinations of relaxation constants, resulting in a database of all possible outcomes. The unknown relaxation constants were then determined by finding the simulated signals in the database that produced the least squared difference to the measured signal intensities.

Results: SQUAREMR demonstrated improvement of accuracy in phantom studies and consistent mean T1 values and consistent variance across the different MOLLI schemes in humans. This was true even for tissues with long T1s and MOLLI schemes with no pause between modified-Look-Locker experiments.

Conclusions: SQUAREMR enables quantification of T1 data obtained by existing clinical pulse sequences. SQUAREMR allows for correction of quantitative CMR data that have already been acquired whereas it is expected that SQUAREMR may improve data consistency and advance quantitative MR across imaging centers, vendors and experimental configurations. While this study is focused on a MOLLI-based T1-mapping technique, it could however be extended in other types of quantitative MRI throughout the body.

Keywords: Magnetic resonance imaging, Mapping, MOLLI, Simulations, Relaxometry

Background

In the field of cardiovascular magnetic resonance (CMR) T1 mapping, quantitative measures of myocardial and blood T1 enabled the calculation of important myocardial biomarkers, such as extracellular volume (ECV) fraction and native T1 in the myocardium [1, 2]. Recent advances in T1 mapping include various new techniques such as Modified Look-Locker inversion recovery (MOLLI), Saturation recovery single-shot acquisition (SASHA), AIR, SAPPHIRE and Shortened MOLLI (ShMOLLI) [3–7]. Moreover, there have been significant efforts towards understanding how accuracy, precision and reproducibility of these methods are affected by acquisition and post-processing parameters [8–11].

While T1 mapping has the potential to improve patient diagnosis, the challenge remains in acquiring reliable data in terms of accuracy and precision.

---

* Correspondence: aletras@hotmail.com
[1] Cardiac MR Group, Department of Clinical Physiology and Nuclear Medicine, Skåne University Hospital Lund, Lund University, Lund, Sweden
[3] Laboratory of Computing and Medical Informatics, School of Medicine, Faculty of Health Sciences, Aristotle University of Thessaloniki, Thessaloniki, Greece
Full list of author information is available at the end of the article

Different T1 mapping methods and parameter sets should yield similar results for a specific tissue type. However, the complex nature of the underlying physics involved and the multitude of parameters that affect image acquisition and post-processing do not allow for consistent reference T1 values of normal myocardium and blood across all methods. Examples of this inconsistency include recent studies on cardiac T1 mapping, which have reported different ranges of T1 values for normal myocardium and blood depending on the methods being used [3, 6, 11–13].

More recently, a single vendor, multicenter clinical study [14] demonstrated reproducibility of myocardial T1 values and provided data from healthy myocardium. Interestingly, the reported T1 values in the literature covers a large range depending on the methods [8]. The T1 mapping technique (MOLLI) and the acquisition parameter set used in the aforementioned multicenter study are listed [14] as limiting factors in terms of accuracy when compared to other setups (different T1 mapping techniques, acquisition scheme, flip angle etc.) [8, 10].

The development of new CMR techniques for obtaining quantitative information usually involves a two-step process: acquisition of images from the MRI scanner with a custom designed pulse sequence and post-processing of the acquired images through a data fitting procedure with closed form equations. Recently, a novel approach to collect and process images for extracting quantitative data from MRI experiments was proposed [15]. This new approach relies on making pseudorandom measurements and comparing the rapidly acquired data against a large dictionary of Bloch simulations. When the matching dictionary entry is found then the tissue constants are known since each of the entries was created based on specific tissue constants. This approach is new in quantitative MRI but requires a uniquely designed pulse sequence with a continuous variation of the acquisition parameters throughout the data collection.

In the past, CMR simulations have been used within a limited scope. Simulations have been used to identify the effect of various acquisition parameters on measurement accuracy and precision [10, 16] and to produce T1-maps through an inverse problem solving fitting procedure [17]. However, in order for the simulator to be executed within a reasonable amount of time, several assumptions and compromises on pulse sequence design had to be made (such as the addition of a crusher to reduce T2-dependency). For the same reason some realistic aspects of the experiment (such as excitation slice profile) had not been incorporated.

In this study, we propose Simulations for QUAntifying RElaxation Magnetic Resonance constants (SQUAREMR), a new method for extracting quantitative tissue MR data from clinical pulse sequences with the aid of comprehensive, parallel MRI simulations of the Bloch equations. The specific aim was to utilize realistic simulations of MOLLI on a large population of spins so as to compute all possible outcomes of this pulse sequence for a range of physiologically relevant tissue relaxation constants. We hypothesized that quantitative CMR acquired with MOLLI can be improved by comparing the signals acquired from the MRI scanner to the entire pool of possible outcomes that are produced by these simulations for different tissue types. While this study is focused on a MOLLI-based T1 mapping technique, it could however be extended in other types of quantitative MRI throughout the body.

Methods

MOLLI theory and pitfalls

Figure 1 demonstrates a basic MOLLI pulse sequence scheme [5], where two inversion-recovery-prepared modified-Look-Locker experiments are separated by a pause, which is usually defined in terms of a number of heart cycles. In short, each modified-Look-Locker experiment consists of ECG-triggered single-shot acquisitions performed at end-diastole of consecutive heart beats. Each single-shot acquisition consists of a ramp up preparation (a startup sequence where the flip angle is increased linearly) followed by a balanced steady-state free precession (bSSFP) readout. For every modified-Look-Locker experiment, the effective inversion times (TIs) of the single-shot images are defined by the time measured between the end of the inversion recovery (IR) radiofrequency pulse and the center of k-space of each bSSFP readout within the same modified-Look-Locker experiment. At the end of the MOLLI experiment, the acquired images undergo exponential fitting on a pixel-by-pixel basis in order to estimate T1.

In MOLLI T1 mapping, the bSSFP readouts that follow the IR pulse perturb the relaxation process itself and do not allow for an ideal exponential recovery that is based solely on the equilibrium magnetization (M0) and the relaxation constant T1. As a result, the true recovery follows an apparent relaxation constant T1* which is always shorter than the true relaxation constant T1. MOLLI reconstruction compensates for this apparent relaxation by means of a 3-parameter exponential signal model and the “Look-Locker” correction factor [5]. However, the “Look-Locker” correction factor has been derived based on a Fast Low Angle Shot (FLASH) readout [18] and is used for the bSSFP readout since a simple closed form expression does not exist for the actual MOLLI pulse sequence. Although it has been shown that the FLASH-based correction factor is reasonably effective under specific conditions [10], it does lead to inaccuracies in T1 maps.

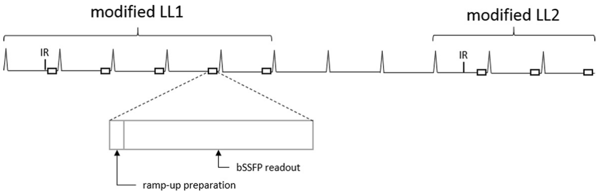

Fig. 1 MOLLI acquisition scheme 5(3p)3. Illustration of a MOLLI pulse sequence scheme consisting of two successive ECG-triggered modified-Look-Locker experiments (modified LL1 and modified LL2) with five and three single-shot readouts respectively. A pause of three heart beats has been retained between the two modified-Look-Locker experiments. Each single-shot acquisition consists of a ramp up preparation followed by a balanced steady-state free precession (bSSFP) readout

SQUAREMR overview

The basic concept of this study is based on the premise that the signals obtained from the simulation of a clinical pulse sequence on simulated tissue with specific relaxation constants (T1, T2) would be identical to the measured signals acquired from the MRI scanner by applying the same pulse sequence on real tissue with the same relaxation constants (T1, T2). Therefore, for the same pulse sequence, obtaining identical simulated and measured signals would ideally indicate that the tissue constants were identical in both the simulation and the MRI scanner. Using a closed form expression of the clinical pulse sequence was not necessary but instead the identical pulse sequence was simulated and was applied on a computer model of spins. The solutions of the Bloch equations provided the temporal evolution of each spin magnetization vector under the influence of the RF pulses and magnetic field gradients of the pulse sequence.

A basic block diagram of SQUAREMR is shown in Fig. 2. In a conventional manner (dashed lines), the patient is scanned in an MRI scanner by applying a user-selected acquisition parameter set. Then, the MRI signals, acquired from the MRI scanner, are processed in order to quantify tissue relaxation constants. With SQUAREMR, several steps were added to this workflow (solid lines). The identical acquisition parameter set was used by a parallel simulator to process the entire range of physiological tissue relaxation constants. The noise-free simulated signal was sampled at the exact inversion times (TIs) used in the MRI scanner with MOLLI. Then, a custom database of simulated signals was constructed so as to link each recorded simulated signal to a single pair of T1 and T2 values. Then, for the MOLLI images acquired by the scanner, on a pixel-by-pixel basis, the relaxation times T1 and T2 were estimated by finding the simulated signal in the database that produced the least squared difference to the MOLLI MRI signal within a pixel. In other words, when this least squared difference was identified, the related database entry returned the tissue relaxation constants.

Acquisition parameters

The acquisition parameters described the MOLLI pulse sequence. These included the following parameters: number of inversion-recovery-prepared modified-Look-Locker experiments, number of ECG-triggered single-shot acquisitions per modified-Look-Locker experiment, number of pausing heart cycles between modified-Look-Locker experiments, IR RF pulse duration and shape, TR and TE durations, bSSFP readout RF pulse duration and shape, slice thickness, acquisition scheme, Field-Of-View

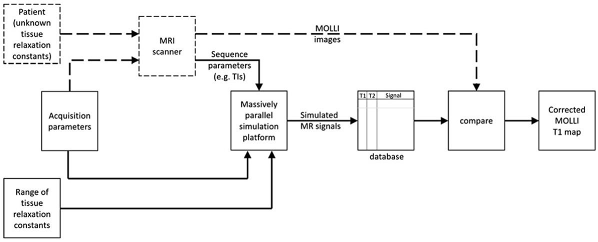

Fig. 2 Block diagram of SQUAREMR. The dashed lines demonstrate the conventional MOLLI workflow whereas solid lines illustrate the workflow steps introduced by SQUAREMR. (HR = heart rate)

(FOV), matrix size, SENSE factor, receiver bandwidth (rBW) and number of startup TRs in the linear flip angle ramp.

In MOLLI, the TIs for a number of the single-shot images depend on the actual heart rate and cannot be known before the pulse sequence execution. Therefore, the simulations were performed after image acquisition.

Parallel simulation platform

A comprehensive MR physics simulator, MRISIMUL, was used [19, 20]. Compared to other previously developed MR simulators, MRISIMUL is neither an image-based simulator that utilizes T1, T2 and PD maps in combination with equations that describe the image intensity [21] nor a kspace-based simulator that utilizes the k-space formalism [22]. MRISIMUL is a simulation platform based on discrete-event Bloch equations applied on anatomical models of spins that incorporates realistic aspects of the MR experiment, makes no assumptions or simplifications for simulating the underlying MR physics and exploits parallel computing based on Graphics Processing Units (GPUs) for high computational performance. The computationally demanding core services (kernel) of MRISIMUL were developed in CUDA-C (NVIDIA, Santa Clara, CA) and distributed in parallel within the graphic processing units (GPUs) whereas the simulation wrapper was developed in MATLAB (The Mathworks Inc., Natick, MA, USA).

For each MOLLI experiment, the identical pulse sequence was simulated on a population of spins for a large range of physiological combinations of T1 and T2. T1 and T2 values of 200–1900 msec and 20–400 msec respectively were simulated with a step of 1 msec. Simulations were not performed for combinations where T2 > T1. To explore faster SQUAREMR execution times, a step of 5 msec was also used. The ranges of T1 and T2 values were chosen based on physiological myocardial and blood values found in the literature [10, 14] with an expanded range based on the characteristics of each experiment. For example, since no gadolinium was administered, very short T1 values below 200 msec were not considered. For each one of the simulations, the MOLLI pulse sequence was applied on a spin with unique characteristics (T1, T2 and position along the slice direction). The simulated MOLLI pulse sequence was based on the pulse sequence run on the MRI scanner. The receiver bandwidth (rBW) of the MRI scanner also defined the temporal step Δt of the simulated pulse sequence. A total of approximately 75,000 to 150,000 time steps were computed for each simulation. The Bloch simulation temporal resolution was 10 μsec and 5 μsec respectively. The bSSFP condition was retained throughout the simulated MOLLI pulse sequence, whereas software crushers [19] were utilized before and after the IR pulse. Also, in order for realistic slice profiles to be incorporated in the simulations, approximately 20 to 100 spins were simulated across the slice thickness. A total of approximately 532,000 to 63,400,000 simulations of the entire imaging pulse sequence were performed. The resulting database consisted of a total of approximately 25,000 to 628,000 entries respectively.

Simulations were performed on a single-node system consisting of a server style computer of 2 hexa-core (Intel E5-2630, 2.30 GHz) processors, 32 GB RAM and four Tesla C2075 GPU cards. Each Tesla C2075 graphics card utilized a total dedicated memory of 6 GB GDDR5 and a total of 448 stream processors.

SQUAREMR performance

To investigate SQUAREMR performance, two sets of pre-Gd MOLLI experiments were performed. For a given experiment, the total SQUAREMR execution time could be reduced by decreasing either the total number of spins within the spin model or the total number of pulse sequence time steps or the T1 map size or a combination of them.

The first set of MOLLI experiments was performed with a simulation temporal step of 10 μsec and an acquisition matrix size of 128x128 whereas the second set of experiments was performed with a simulation temporal step of 5 μsec and an acquisition matrix size of 320x320. To further investigate how spin model size relates to SQUAREMR performance, two different test cases were considered for each set of experiments. For the first test case, a short T1 and T2 sampling step of 1 msec was combined with a large number of 101 spins along slice thickness resulting in a total of approximately 533,000 database entries. For the second test case, a longer T1 and T2 sampling step of 5 msec was combined with a small number of 21 spins along slice thickness resulting in a total of approximately 21,500 database entries. For both test cases, T1 and T2 values of 600–2000 msec and 20–400 msec respectively were simulated.

Phantom setup

Two phantoms of six "tissues", each with its own T1 and T2 values, were used in this study. The phantoms were prepared with varying concentrations of $CuSO_4$ and Agar [23] in order to obtain specific combinations of T1 and T2 values. Agarose powder was weighted and dissolved in distilled water and the proper amount of a 10 mM $CuSO_4$ solution was added. The mixture was heated, poured into containers (one per "tissue") and was left to reach room temperature.

The first phantom consisted of six "tissues" (plastic bottles of 500 ml) with target T1 and T2 values close to real cardiac tissues relaxation constants found in the literature, both with and without gadolinium contrast

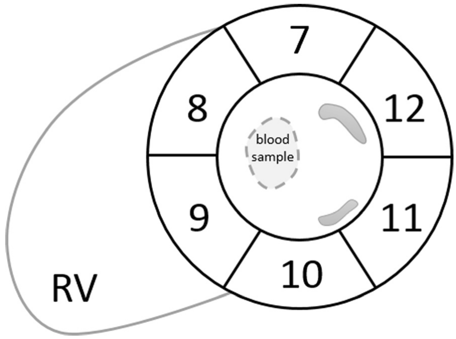

Fig. 3 Myocardial segmentation and blood region of interest in a mid-ventricular short-axis slice. Display of the six myocardial segments [32] and the region of interest within the blood pool from which blood relaxation constants were measured (dashed area)

agent present. The "tissues" used in this set had T1s and T2s of pre-contrast normal myocardium [11, 24], pre-contrast blood [10, 25], pre-contrast edematous myocardium [26], pre-contrast infarcted myocardium [5, 24], post-contrast normal myocardium (2–3 min after gadolinium contrast administration) and post-contrast normal myocardium (13–15 min after contrast administration) [27, 28]. The second phantom set consisted of 6 "tissues" (Eurospin II Test System, Livingston, UK) with T2 values close to T2 of normal myocardium [24] and T1 values covering the range from 200 msec to 1600 msec.

To study the SQUAREMR T2 estimates obtained with the MOLLI sequence a third set of 10 phantoms of varying combinations of T1 and T2 values was scanned with the clinically relevant 5(3p)3 scheme only. The target T1 and T2 values were chosen so as to cover the following four combinations: short T1 and short T2 values; short T1 and long T2 values; long T1 and short T2 values; long T1 and long T2 values.

Relaxation constants reference standard values were measured on a 1.5 T Philips Achieva systems (Philips Healthcare, Best, Netherlands). For T1 measurements Saturation Recovery was used (Tsat = 0.01–15 sec, TR = 10 sec) because it allowed for visual evaluation of the effectiveness of the saturation pulse at the shortest saturation time i.e. for long T1s, the remaining signal was within or uniformly close to the noise floor. For T2 measurements T2p-SSFP was used for faster data acquisition since it has been validated in the past as a reference standard against slow spin-echo experiments [29].

Healthy volunteer population

Twelve (12) healthy volunteers with no medical history (12 men, age 34 ± 12 years) were studied. Eight out of twelve were studied with the clinically relevant 5(3p)3 scheme only. The study was approved by the local ethics committee and all subjects provided written consent (The regional ethics committee, Lund, Sweden. Ethics application number: 541/2004).

CMR protocol

CMR studies were performed on a 1.5 T Philips Achieva scanner (Philips Healthcare, Best, Netherlands) equipped with a 32-channel receiver coil and advanced research packages for cardiac applications. The CMR protocol included a series of MOLLI pulse sequences with different acquisition schemes:

1. 5(3p)3 (clinical MOLLI pulse sequence for pre-contrast myocardial T1 mapping) [9, 10]
2. 4(1p)3(1p)2 (clinical MOLLI pulse sequence for post-contrast myocardial T1 mapping) [10]
3. 5(0p)3 (custom MOLLI pulse sequence for shorter myocardial T1 mapping acquisition)

where p stands for heartbeats pauses between modified-Look-Locker experiments (Fig. 1).

All MOLLI pulse sequences shared the following parameters: the IR pulse was a hyperbolic secant adiabatic pulse [30] with 4.74 msec duration, whereas the bSSFP readout used a 490 μsec sinc shaped RF pulse with 6 mm slice thickness and 35° excitation flip angle, rBW 200 kHz (1612.9 Hz/pixel), field-of-view (FOV) 272 mm×272 mm,

Table 1 Reference T1 and T2 values of the "tissues" in the myocardium phantom

Tissue type	T1 [ms]	T1 StDev [ms]	T2 [ms]	T2 StDev [ms]	CuSO4 [g/L]	Agarose [g/L]
Normal myocardium (pre-contrast)	1048	12	50	2	0,12	17.80
Blood (pre-contrast)	1570	20	196	11	0,07	4.00
Edema (pre-contrast)	1249	15	62	3	0,09	14.67
Infarct (pre-contrast)	1361	21	64	3	0,07	14.51
Normal myocardium (post-contrast 2–3 min)	344	6	52	4	0,2	20.00
Normal myocardium (post-contrast 13–15 min)	413	12	50	3	0,5	17.51

T1 and T2 values were measured with Saturation Recovery and T2p-SSFP respectively on a 1.5 T Philips Achieva systems (Philips Healthcare, Best, Netherlands)

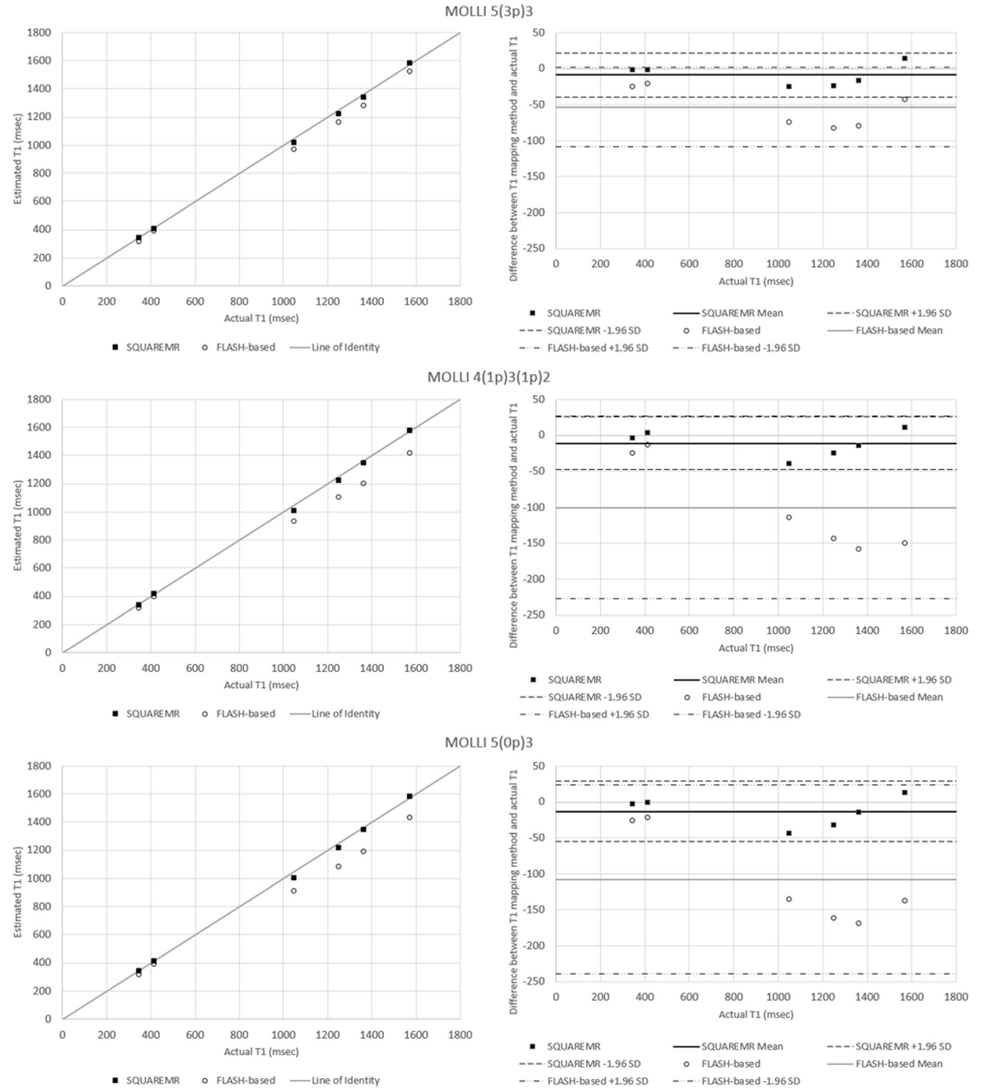

MOLLI 5(3p)3

MOLLI 4(1p)3(1p)2

MOLLI 5(0p)3

Fig. 4 Comparison between SQUAREMR and conventional MOLLI post-processing (FLASH-based) for the myocardial phantom set. Each row of plots represents a separate MOLLI acquisition scheme. The left column shows the deviation of the measured T1 values of the phantoms with SQUAREMR (black *rectangles*) and with conventional (i.e. FLASH-based Look Locker correction factor) MOLLI post-processing (*open circles*) from the line of identity (*gray line*). The right column shows the corresponding modified Bland Altman plots for both methods (solid horizontal lines represent the means, dashed horizontal lines represent the 95 % confidence limits). Compared to conventional MOLLI post-processing, SQUAREMR presented high accuracy and a similar behavior across the different MOLLI schemes

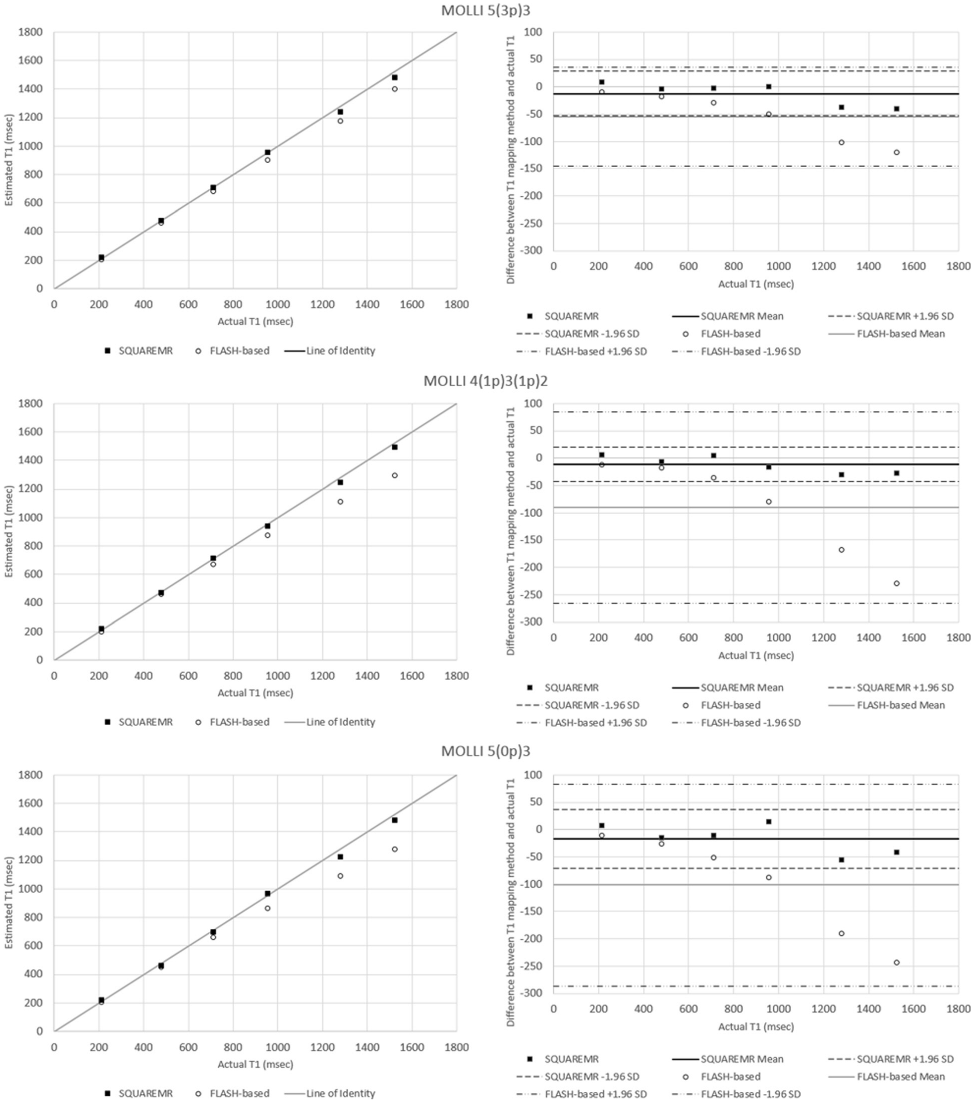

Fig. 5 Comparison between SQUAREMR and conventional MOLLI post-processing (FLASH-based) for the Eurospin II phantom set. Each row of plots represents a separate MOLLI acquisition scheme. The left column shows the deviation of the measured T1 values of the phantoms with SQUAREMR (*black rectangles*) and with conventional (i.e. FLASH-based Look Locker correction factor) MOLLI post-processing (*open circles*) from the line of identity (*gray line*). The right column shows the corresponding modified Bland Altman plots for both methods (solid horizontal lines represent the means, dashed horizontal lines represent the 95 % confidence limits). Compared to conventional MOLLI post-processing, SQUAREMR presented high accuracy and a similar behavior across the different MOLLI schemes

acquisition matrix 124×124, linear k-space trajectory and SENSE acceleration factor of 2 (actual number of phase encoding steps was 65). A linear ramp up preparation of 10 pulses was used to reach steady state prior to the bSSFP readout.

In phantom studies TR was set to 2.54 msec and TE to 1.27 msec. MOLLI schemes 1 and three used initial TIs equal to 114 msec and 350 msec whereas MOLLI scheme 2 used initial TIs equal to 114 msec, 232 msec and 350 msec (initial TI increment of 118 msec). For phantoms, a 6-channel head coil was used along with a simulated ECG (60 beats per minute). A coronal single slice was acquired for the myocardial phantom whereas an axial single slice was acquired for the Eurospin II phantom.

In healthy volunteer studies the TR was 3 msec and the TE 1.5 msec. MOLLI schemes 1 and 3 used initial TIs of 134 msec and 350 msec whereas MOLLI scheme 2 used initial TIs of 134 msec, 242 msec and 350 msec (initial TI increment of 108 msec). The CMR protocol was applied in a single mid-ventricular short axis slice with a 32-channel receiver coil.

The term “initial TI” was defined as the first TI measured between the end of the adiabatic inversion pulse and the center of k-space of the first single-shot bSSFP readout that followed within the same modified-Look-Locker experiment. The TIs between the inversion pulse and the center of the other bSSFP readouts within the same modified-Look-Locker experiment were determined by the initial TI and the duration of the cardiac cycles preceding each readout.

Image analysis

Parameter mapping with SQUAREMR was performed using the GPU-framework of MATLAB (The Mathworks Inc., Natick, MA, USA) on a single GPU whereas MOLLI T1 values were measured from the MOLLI magnitude images using conventional MOLLI post-processing (i.e. with a FLASH-based Look Locker correction factor [5, 18]) with a 3-parameter fit [5, 10]. In-vivo myocardial segmentation was implemented manually [31]. For phantom studies, relaxation constants were measured by placing a rectangular region of interest (ROI) in the center of each phantom and estimated T1 values were reported. For the third set of phantoms, which was intended for studying the T2 estimates, both T1 and T2 values were reported. In healthy volunteer studies, left-ventricular (LV) myocardium was segmented in 6 areas in the mid-ventricular

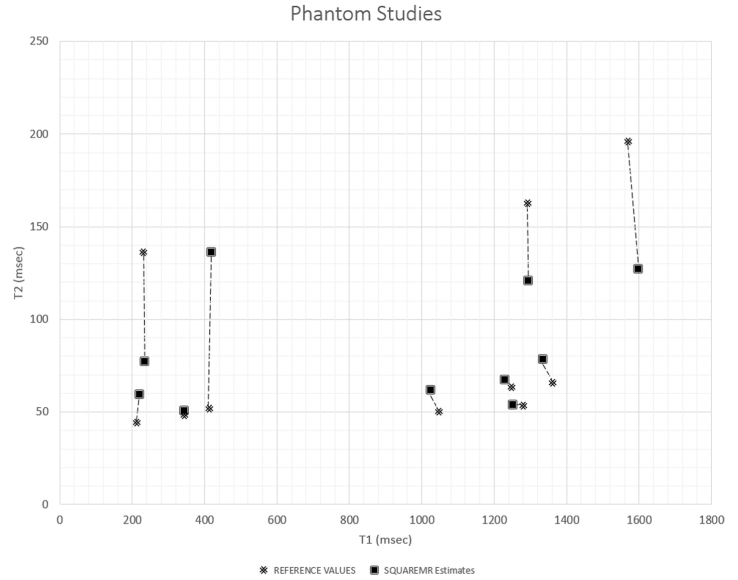

Fig. 6 SQUAREMR T1 and T2 estimates of ten phantoms in comparison to their reference T1 and T2 values for a clinically relevant 5(3p)3 MOLLI acquisition scheme. In black rectangles are the T1 and T2 values given by SQUAREMR whereas in black x are the corresponding relaxation constants reference standard values. SQUAREMR demonstrated a small T1 estimation error for all T1 and T2 combinations. The T2 estimation error was small only for phantoms with long T1 and short T2 values. For samples with other T1 and T2 combinations, SQUAREMR demonstrated a larger error in estimating T2 with the MOLLI pulse sequence

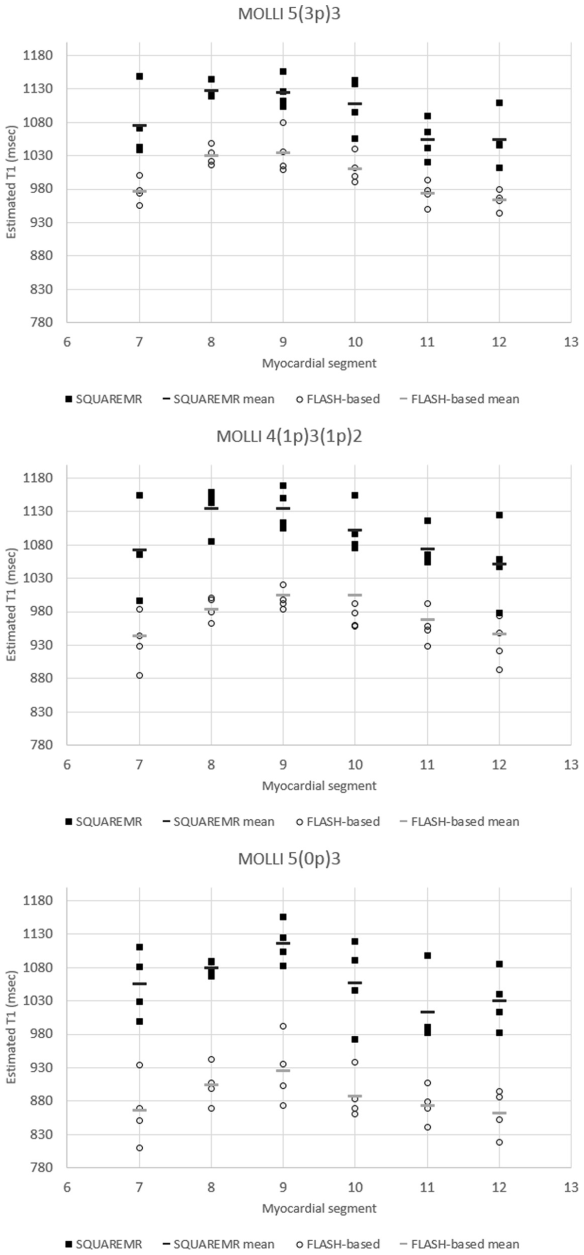

Fig. 7 (See legend on next page.)

(See figure on previous page.)
Fig. 7 Myocardial T1 values measured from the six myocardial segments (7 to 12). Myocardial T1 values were measured in the mid-ventricular short-axis slices for three different MOLLI acquisition schemes. In black rectangles are the T1 values given by SQUAREMR whereas in black circles are the corresponding T1 values given by the conventional MOLLI post-processing (FLASH-based). In solid black and gray short lines are the mean segmental T1 values for SQUAREMR and conventional MOLLI post-processing respectively. Data were extracted from the four volunteers that were examined additionally with 4(1p)3(1p)2 and 5(0p)3

short axis (SAX) slice [32] and relaxation times were measured for each segment separately but also for the entire LV myocardium. Blood T1 and T2 values were measured from an ROI placed within the LV blood pool (Fig. 3). Myocardium and blood ROIs were drawn so as to avoid signal contamination from adjacent tissues. All values in this study are reported as mean ± standard deviation (SD). For phantom studies, modified Bland-Altman plots [33] were used to demonstrate the agreement of the two methods (SQUAREMR and conventional MOLLI post-processing) with the reference standards.

Statistics

Comparisons were performed with student's two tailed *t*-test for paired data.

Results

Phantom studies

The reference T1 and T2 values of the "tissues" in the first phantom are shown in Table 1. The reference T1 relaxation times of the "tissues" in the second phantom ranged from 212 msec to 1522 msec whereas the reference T2 relaxation times was kept close to that of normal myocardium (52 ± 6 msec).

Results from the first phantom are shown in Fig. 4. For the range of relaxation times corresponding to cardiac tissues (pre- and post- contrast) that were studied, SQUAREMR presented high accuracy and a similar behavior across the different MOLLI schemes. For the first phantom, SQUAREMR demonstrated better accuracy compared to conventional MOLLI post-processing [5(3p)3 scheme bias of 8.8 ± 15.3 msec vs. 53.6 ± 28.2 msec, $p < 0.05$; 4(1p)3(1p)2 scheme bias of 11 ± 18.8 msec vs. 100.2 ± 64.9 msec, $p < 0.05$; 5(0p)3 scheme bias of 13.1 ± 21.1 msec vs. 107.9 ± 66.9 msec, $p < 0.05$; $N = 6$], even in cases of "tissues" with long T1s and MOLLI schemes that do not allow for full relaxation of long T1s prior to the next inversion. Conventional MOLLI post-processing in these cases presented a bias higher than 100 msec for the phantoms with high T1 values.

In the second phantom, which had close to normal myocardium T2s and a range of T1s, SQUAREMR demonstrated better accuracy than conventional MOLLI [5(3p)3 scheme bias of 12.1 ± 20.5 msec vs. 54.7 ± 45.7 msec, $p < 0.05$; 4(1p)3(1p)2 scheme bias of 11.4 ± 16.1 msec vs. 90.2 ± 89.3 msec, $p < 0.05$; 5(0p)3 scheme bias of 16.9 ± 27.2 msec vs. 101.3 ± 94.3 msec, $p < 0.05$; $N = 6$], (Fig. 5). Conventional MOLLI post-processing introduced an increasing error with increasing T1, as has been previously shown in simulation studies [10].

Figure 6 shows the SQUAREMR T1 and T2 estimates in phantoms ($N = 10$) against their reference T1 and reference T2 values. SQUAREMR demonstrated small error (14.3 ± 11.2 msec; $N = 10$) in estimating T1 for all T1 and T2 combinations. The error was also relatively small in estimating T2 (7.2 ± 6 msec; $N = 4$) for phantoms with high T1 and low T2 values. For other T1 and T2 combinations, SQUAREMR yielded larger errors (45.3 ± 31.8 msec; $N = 6$) in estimating T2.

Human studies

Figure 7 shows the segmental T1 values given by SQUAREMR and the conventional MOLLI post-processing for the three different MOLLI schemes. SQUAREMR yielded higher T1 values for all segments compared to the conventional MOLLI post-processing, for all three MOLLI schemes. With the MOLLI scheme 5(3p)3, which is being used clinically for pre-contrast myocardial T1 mapping, the average T1 value per short axis slice was 1025 ± 22.9 msec for conventional MOLLI post-processing and 1117 ± 25.6 msec for SQUAREMR ($p < 0.001$, $N = 12$). The average myocardial T1 value for segment 9 (inferior septal myocardium) was 1053 ± 33 msec for conventional MOLLI post-processing and 1148 ± 38 msec for SQUAREMR ($p < 0.001$, $N = 12$). The average blood T1 values were 1570 ± 52.8 msec and 1634 ± 50 msec respectively ($p < 0.001$, $N = 12$). As other studies have already shown [6, 14], a regional variation of segmental average T1 values was measured whereas the average T1 value of myocardial segment 9 was higher compared to the average T1 value of the entire slice.

Figure 8 shows how the T1 values, resulting from SQUAREMR and from the conventional MOLLI post processing, have been affected by the three different MOLLI schemes. The T1 values were measured over the entire slice, myocardial segment 9 and blood pool. SQUAREMR was well behaved with consistent mean T1 values and consistent variance across the different MOLLI schemes. The conventional MOLLI post-processing overall showed significantly different mean T1 values between schemes [e.g. $p < 0.001$ for myocardial 5(3p)3 vs. 5(0p)3]. Table 2 gives the results presented in Fig. 8 whereas Fig. 9 shows T1 maps from a healthy volunteer derived from the conventional MOLLI post processing (left image) and

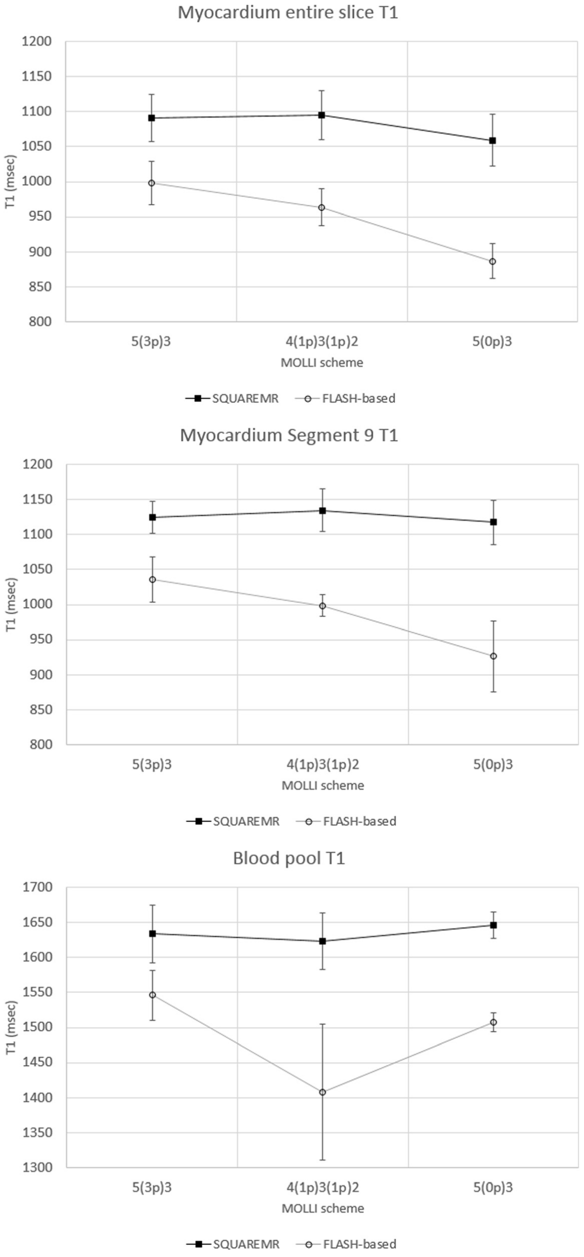

Fig. 8 (See legend on next page.)

(See figure on previous page.)

Fig. 8 Mean T1 values per short axis slice, myocardial segment nine and blood pool. The mean T1 values were measured with SQUAREMR and conventional MOLLI post-processing for three different MOLLI acquisition schemes. In black rectangles are the mean T1 values given by SQUAREMR whereas in black circles are the corresponding mean T1 values given by the conventional MOLLI post-processing (FLASH-based). Error bars depict the standard deviation of the mean for each MOLLI acquisition scheme. Data were extracted from the four volunteers that were examined additionally with 4(1p)3(1p)2 and 5(0p)3

SQUAREMR (right image) for a 5(3p)3 acquisition scheme.

SQUAREMR performance

To illustrate the performance of SQUAREMR, two different sets of pre-Gd MOLLI experiments were examined. The simulation execution times and the database search times for different MOLLI experiment sizes were recorded and are shown in Table 3. It can be seen that the duration of the SQUAREMR processing varied depending on the complexity of the experiment, which can be defined by a number of parameters such as the size of the acquisition matrix, the number of database entries, MOLLI pulse sequence timesteps, etc. The total execution times range from 33 s to 47 min on a server with four Tesla C2075 GPU cards.

Discussion

A new method for improving measurements from clinical pulse sequences in CMR relaxometry was presented. The use of parallel simulations was shown to improve the T1 estimates in MOLLI by comparing the MRI signals acquired from the MRI scanner to the entire pool of physiological simulated signals that were produced by parallel simulations of the identical pulse sequence on a population of spins. While the current study explored the feasibility of obtaining T1 properties from MOLLI images, in principle it could be extended in other areas of quantitative MR.

MOLLI T1 mapping is widely used today; however the correction of the T1 recovery relies on the a FLASH closed form expression [5] only because such an expression does not exist for the actual bSSFP readout that the MOLLI pulse sequence utilizes. Several studies have already shown that MOLLI T1 mapping underestimates true T1 whereas its measurement error is influenced by several acquisition protocol parameters [5, 6, 10, 12, 16]. SQUAREMR does not rely on closed form expressions but rather on an extended simulation of the pulse sequence itself. The basic concept of SQUAREMR was based on the premise that realistic simulations of clinical pulse sequences on tissue models of specific parameters (T1, T2) would result in identical signals to the signals acquired from the MRI scanner after the application of the same pulse sequences on true tissues with the same relaxation properties.

In the current work, a CMR protocol consisting of three different MOLLI pulse sequences was implemented: 5(3p)3, 4(1p)3(1p)2 and 5(0p)3. For every MOLLI experiment, the identical MOLLI pulse sequence was simulated for T1 and T2 ranges of 200 to 1900 msec and of 20 to 400 msec respectively taking into account realistic aspects of the MR experiment, such as realistic excitation slice profiles and heart rate variation in in-vivo studies. For that purpose, MRISIMUL, a GPU-based, MR physics simulator [19, 20] was utilized in this study.

The CMR T1 mapping protocol was applied on three phantom setups and on twelve healthy volunteers. All twelve volunteers and phantom setups were examined with the clinical 5(3p)3 scheme. The actual TI timings were extracted from the scanner data and used for the SQUAREMR simulations allowing for more realistic simulations. Four out of twelve volunteers and two out of three phantom setups were imaged additionally with 4(1p)3(1p)2 and 5(0p)3. Results of the CMR protocol on the phantom setups demonstrated improvement of accuracy and a substantially reduced T1 variability across the different MOLLI schemes. Compared to conventional MOLLI post-processing, SQUAREMR showed improved accuracy even for long T1s with no pause between modified-Look-Locker experiments. The latter

Table 2 Mean T1 values (msec) per slice, myocardial segment 9 and blood pool

	Myocardium entire slice T1				Myocardium segment 9 T1				Blood pool T1			
	MOLLI		SQUAREMR		MOLLI		SQUAREMR		MOLLI		SQUAREMR	
MOLLI scheme	Mean	SD	Mean	SD	Mean	SD	Mean	SD	Mean	SD	Mean	SD
5(3p)3	998	31	1091	34	1035	32	1125	23	1546	36	1633	41
4(1p)3(1p)2	964	26	1095	35	998	16	1135	30	1408	97	1623	40
5(0p)3	887	25	1059	37	926	51	1117	31	1507	13	1646	19

T1 values were measured with SQUAREMR and conventional MOLLI post-processing for three different MOLLI acquisition schemes. Data were extracted from the four volunteers that were examined additionally with 4(1p)3(1p)2 and 5(0p)3

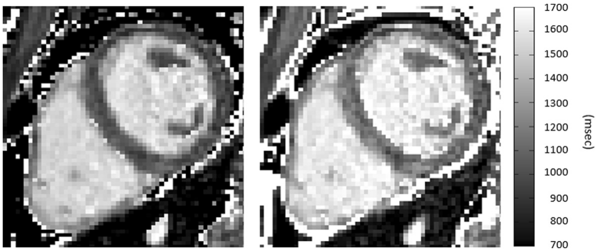

Fig. 9 T1 maps of a healthy volunteer. Left image: Conventional MOLLI map derived from a clinical pulse sequence. Right image: T1 map obtained from MOLLI-based tissue signal intensities using SQUAREMR. (MOLLI acquisition scheme 5(3p)3, rBW = 200 kHz, FOV = 272 mm×272 mm, acquisition matrix = 124×124, SENSE acceleration factor = 2). Grayscale images are presented to avoid exaggerating contrast when crossing different color boundaries, which commonly occurs with color images

demonstrates that the T1 estimates are not dependent on the duration of the delay between successive modified Look-Locker experiments, which in patient scans may change due to heartrate variations.

In order to investigate whether SQUAREMR could also provide T2 estimates from data obtained with a MOLLI pulse sequence, the methodology was applied on phantoms with a range of T1 and T2 values. SQUAREMR showed reasonable T2 values in phantoms with long T1s and short T2s. Larger errors in estimating T2 were observed for the remaining T1 and T2 combinations; however, this was expected for a T1 mapping pulse sequence, such as MOLLI. Previous studies have shown that the MOLLI pulse sequence introduces some T2 modulation on the signal, which is more pronounced for long T1 and short T2 values [10, 34]; therefore, for these values SQUAREMR provided reasonable T2 estimates. For other T1s and T2s, SQUAREMR was unable to provide reasonable T2 estimates since the MOLLI signal simply did not contain this information. The T2 results shown in Fig. 6 indicate that this was not a limitation of SQUAREMR in terms of convergence but rather a limitation imposed by the MOLLI pulse sequence itself which has been designed to mainly modulate the MOLLI signal based on the T1 values of the tissues irrespective of their T2 values.

In in-vivo studies, myocardial and blood T1 values were measured. The average T1 values obtained with the CMR protocol for both the conventional MOLLI post-processing and SQUAREMR are summarized in Table 2 for $N = 4$. SQUAREMR showed substantially elevated T1 values for both myocardium and blood pool when compared to conventional MOLLI post-processing. Conventional MOLLI T1 values in this work were similar to values previously reported in the literature. In particular, the conventional MOLLI scheme 5(3p)3 yielded an average blood T1 value of 1570 ± 52 msec ($N = 12$). Previous studies have reported 1534 msec with MOLLI [27] and 1516 ± 21 msec [13] with saturation recovery FLASH. Also, in this work, the conventional MOLLI T1 value for myocardium (segment 9) of 1053 ± 33 msec ($N = 12$) was similar to that of previous studies with MOLLI (1034 ± 56 msec [35] and 1052 ± 41 msec [11]). On the other hand, SQUAREMR resulted in MOLLI T1 values similar to more accurate CMR T1 mapping techniques. In particular, the average blood T1 value of 1634 ± 50 msec ($N = 12$) was close to that previously reported with SASHA (1639 ± 97 msec [3]). The average T1 value in myocardial segment nine obtained with SQUAREMR MOLLI was 1148 ± 38 msec ($N = 12$) which was close to that previously reported with rapid cardiac gated single-shot IR-FSE sequence (1092 ± 64 msec [8]) and two dimensional SASHA (1105 ± 46 msec [36]).

The application of a parallel realistic simulator in order to correct measured data from the scanner is a new concept. In the past, MR simulations have been used in a limited scope [10, 16, 17] with the exception of

Table 3 SQUAREMR performance for MOLLI experiments with varying complexity

#	Simulation timesteps	Simulation temporal step (μsec)	Database entries	Sampling step (msec)	T1 map size	Spins along slice	Simulation execution (min:sec)	Database search (min:sec)	Total execution time (min:sec)
1	63705	10	533400	1	128x128	101	17 m:47 s	0 m:29 s	18 m:16 s
2	63705	10	21560	5	128x128	21	0 m:9 s	0 m:24 s	0 m:33 s
3	156877	5	533400	1	320x320	101	44 m:27 s	2 m:47 s	47 m:14 s
4	156877	5	21560	5	320x320	21	0 m:22 s	1 m:50s	2 m:12 s

The simulation execution times and the database search times were recorded for the application of SQUAREMR on MOLLI experiment of varying size

MR-fingerprinting [15]. SQUAREMR depends on extended and realistic MR simulations of already available clinical pulse sequences in order to build an extensive database of simulated signals identical (ideally) to the signals obtained from the MR scanner for the same experiment configuration. The utilization of multi-GPU technology along with the technology advancements taking place on the GPU hardware suggest that this method has the potential to become a real-time routine on the MRI scanner in the future.

In this work, some limitations apply. Simulation of magnetization transfer (MT) was not studied although previous simulation studies [10, 37] suggest that MT plays a role in T1 underestimation with MOLLI. However, accurate simulation of MT becomes challenging for the entire range of relaxation times being studied in this work since previous work has shown alteration of MT in disease cases (e.g. myocardial infarction [38]) and among different tissue types (blood vs. myocardium) [10]. Also, blood flow effects were not studied in this work. Simulations assumed a stationary spin model during the application of MOLLI pulse sequence. Although the bSSFP readout is applied during diastasis, when the heart muscle is mostly stationary, blood flow effects may alter the apparent T1 relaxation in the blood pool and, in turn, the T1 estimation [10]. In this implementation, a linear full search of the database was utilized, which limited the performance of SQUAREMR in terms of its execution speed. Non-linear optimization might be way forward but were not tested. In the future, optimization of algorithms for database construction (such as using a variable step for T1 and T2 values, eliminating database T1, T2 pairs not pertaining to a particular MR application, etc.) and database search (such as using data specific schemes) could further improve overall SQUAREMR performance. Despite these limitations, SQUAREMR demonstrated improved T1 accuracy in phantom studies whereas in healthy volunteer studies the reported T1 values of myocardium and blood were close to those acquired with more accurate CMR T1 mapping techniques in the literature. Last but not least, the substantially reduced T1 variability across the different MOLLI schemes with SQUAREMR suggests that myocardial tissue characterization could potentially be achieved within 8 heart beats.

Conclusion

In conclusion, SQUAREMR is a new method that allows for quantification of CMR data with already available clinical pulse sequences and with the aid of comprehensive, parallel MRI simulations. In this study, a MOLLI-based T1 mapping example was investigated demonstrating improvement of accuracy in phantom studies and consistent mean T1 values and consistent variance across the different MOLLI schemes in humans. This was true even for a wide range of T1 values with MOLLI schemes with no pause between modified-Look-Locker experiments, indicating potential value for myocardial tissue characterization within just 8 heart beats.

The methods presented in this study represent a different approach in quantitative CMR with existing clinical pulse sequences. SQUAREMR allows for correction of quantitative CMR data (e.g. MOLLI T1 maps) that have already been acquired by simulating the clinical pulse sequence that was used for the data acquisition. Last, it is expected that in the future SQUAREMR may improve data consistency and advance quantitative MR to become more robust across imaging centers, vendors and experimental configurations and the technique may be extended in other areas of quantitative MR imaging.

Ethics, consent and permissions

The study was approved by the local ethics committee and all subjects provided written consent for publication of this study and accompanying images (The regional ethics committee, Lund, Sweden. Ethics application number: 541/2004).

Competing interests

EH is the founder of Medviso AB, Lund, Sweden, that develops medical image-analysis software. The remaining authors declare that they have no competing interests.

Authors' contributions

CGX and AHA conceived the study, carried out the experiments and study design and drafted and finalized the manuscript. CGX carried out the SQUAREMR development. SB and GK carried out the development of the phantoms. CGX, SB and GK carried out data collection. EH and HA participated in the design of the study. All authors have contributed to final manuscript and approved it.

Acknowledgements

Funding was provided by the Greek General Secretariat for Research and Development via an Excellence grant, by the Swedish Heart and Lung Foundation, the Region of Skåne and by the Medical Faculty at Lund University. We would like to thank Mikael Kanski, MD, PhD for his assistance in acquiring the human volunteer images.

Author details

[1]Cardiac MR Group, Department of Clinical Physiology and Nuclear Medicine, Skåne University Hospital Lund, Lund University, Lund, Sweden. [2]Department of Computer Science and Biomedical Informatics, University of Thessaly, Lamia, Greece. [3]Laboratory of Computing and Medical Informatics, School of Medicine, Faculty of Health Sciences, Aristotle University of Thessaloniki, Thessaloniki, Greece. [4]Department of Biomedical Engineering, Faculty of Engineering, Lund University, Lund, Sweden. [5]Centre of Mathematical Sciences, Faculty of Engineering, Lund University, Lund, Sweden.

Received: 29 June 2015 Accepted: 15 November 2015

References

1. Arheden H, Saeed M, Higgins CB, Gao DW, Bremerich J, Wyttenbach R, et al. Measurement of the distribution volume of gadopentetate dimeglumine at echo-planar MR imaging to quantify myocardial infarction: comparison with 99mTc-DTPA autoradiography in rats. Radiology. 1999;211:698–708.

2. Moon JC, Messroghli DR, Kellman P, Piechnik SK, Robson MD, Ugander M, et al. Myocardial T1 mapping and extracellular volume quantification: a society for cardiovascular magnetic resonance (SCMR) and CMR working group of the european society of cardiology consensus statement. J cardiovasc magn reson: off J Soc Cardiovasc Magn Reson. 2013;15:92.
3. Chow K, Flewitt JA, Green JD, Pagano JJ, Friedrich MG, Thompson RB. Saturation recovery single-shot acquisition (SASHA) for myocardial T(1) mapping. Magn Reson Med. 2014;71:2082–95.
4. Fitts M, Breton E, Kholmovski EG, Dosdall DJ, Vijayakumar S, Hong KP, et al. Arrhythmia insensitive rapid cardiac T1 mapping pulse sequence. Magn Reson Med. 2013;70:1274–82.
5. Messroghli DR, Radjenovic A, Kozerke S, Higgins DM, Sivananthan MU, Ridgway JP. Modified Look-Locker inversion recovery (MOLLI) for high-resolution T1 mapping of the heart. Magn Reson Med. 2004;52:141–6.
6. Piechnik SK, Ferreira VM, Dall'Armellina E, Cochlin LE, Greiser A, Neubauer S, et al. Shortened modified look-locker inversion recovery (ShMOLLI) for clinical myocardial T1-mapping at 1.5 and 3 T within a 9 heartbeat breathhold. J cardiovasc magn reson: off J Soc Cardiovasc Magn Reson. 2010;12:69.
7. Weingärtner S, Akçakaya M, Basha T, Kissinger KV, Goddu B, Berg S, et al. Combined saturation/inversion recovery sequences for improved evaluation of scar and diffuse fibrosis in patients with arrhythmia or heart rate variability. Magn Reson Med. 2014;71:1024–34.
8. Cooper MA, Nguyen TD, Spincemaille P, Prince MR, Weinsaft JW, Wang Y. How accurate is MOLLI T1 mapping in vivo? Validation by spin echo methods. PloS one. 2014;9:e107327.
9. Higgins D, Moon J. Review of T1 mapping methods: comparative effectiveness including reproducibility issues. Curr Cardiovasc Imaging Rep. 2014;7:1–10.
10. Kellman P, Hansen MS. T1-mapping in the heart: accuracy and precision. J cardiovasc magn reson: off J Soc Cardiovasc Magn Reson. 2014;16:2.
11. Roujol S, Weingartner S, Foppa M, Chow K, Kawaji K, Ngo LH, et al. Accuracy, precision, and reproducibility of four T1 mapping sequences: a head-to-head comparison of MOLLI, ShMOLLI, SASHA, and SAPPHIRE. Radiology. 2014;272:683–9.
12. Messroghli DR, Greiser A, Frohlich M, Dietz R, Schulz-Menger J. Optimization and validation of a fully-integrated pulse sequence for modified look-locker inversion-recovery (MOLLI) T1 mapping of the heart. JMRI. 2007;26:1081–6.
13. Wacker CM, Bock M, Hartlep AW, Beck G, van Kaick G, Ertl G, et al. Changes in myocardial oxygenation and perfusion under pharmacological stress with dipyridamole: assessment using T*2 and T1 measurements. Magn Reson Med. 1999;41:686–95.
14. Dabir D, Child N, Kalra A, Rogers T, Gebker R, Jabbour A, et al. Reference values for healthy human myocardium using a T1 mapping methodology: results from the International T1 Multicenter cardiovascular magnetic resonance study. J cardiovasc magn reson: off J Soc Cardiovasc Magn Reson. 2014;16:69.
15. Ma D, Gulani V, Seiberlich N, Liu K, Sunshine JL, Duerk JL, et al. Magnetic resonance fingerprinting. Nature. 2013;495:187–92.
16. Gai ND, Stehning C, Nacif M, Bluemke DA. Modified look-locker T1 evaluation using Bloch simulations: human and phantom validation. Magn Reson Med. 2013;69:329–36.
17. Ramanan V, Ghugre NR, Cunningham CH, Stainsby JA, Connelly KA, Leber A, et al. Relaxometry using sequence SimuLation (RUSSL): application to myocardial T1-mapping using MOLLI. Salt Lake City, UT, USA: ISMRM 21th Annual Meeting; 2013.
18. Deichmann R, Haase A. Quantification of T1 values by SNAPSHOT-FLASH NMR imaging. J Magn Reson. 1969;1992(96):608–12.
19. Xanthis CG, Venetis IE, Aletras AH. High performance MRI simulations of motion on multi-GPU systems. J cardiovasc magn reson: off J Soc Cardiovasc Magn Reson. 2014;16:48.
20. Xanthis CG, Venetis IE, Chalkias AV, Aletras AH. MRISIMUL a GPU-based parallel approach to MRI simulations. IEEE Trans Med Imaging. 2014;3:607–17.
21. Wissmann L, Santelli C, Segars WP, Kozerke S. MRXCAT: realistic numerical phantoms for cardiovascular magnetic resonance. J cardiovasc magn reson: off J Soc Cardiovasc Magn Reson. 2014;16:63.
22. Petersson JS, Christoffersson JO, Golman K. MRI simulation using the k-space formalism. Magn Reson Imaging. 1993;11:557–68.
23. Mitchell MD, Kundel HL, Axel L, Joseph PM. Agarose as a tissue equivalent phantom material for NMR imaging. Magn Reson Imaging. 1986;4:263–6.
24. Verhaert D, Thavendiranathan P, Giri S, Mihai G, Rajagopalan S, Simonetti OP, et al. Direct T2 quantification of myocardial edema in acute ischemic injury. J Am Coll Cardiol Img. 2011;4:269–78.
25. Kellman P, Wilson JR, Xue H, Ugander M, Arai AE. Extracellular volume fraction mapping in the myocardium, part 1: evaluation of an automated method. J cardiovasc magn reson: off J Soc Cardiovasc Magn Reson. 2012;14:63.
26. Kellman P, Xue H, Chow K, Spottiswoode BS, Arai AE, Thompson RB. Optimized saturation recovery protocols for T1-mapping in the heart: influence of sampling strategies on precision. J cardiovasc magn reson: off J Soc Cardiovasc Magn Reson. 2014;16:55.
27. Schelbert EB, Testa SM, Meier CG, Ceyrolles WJ, Levenson JE, Blair AJ, et al. Myocardial extravascular extracellular volume fraction measurement by gadolinium cardiovascular magnetic resonance in humans: slow infusion versus bolus. J cardiovasc magn reson: off J Soc Cardiovasc Magn Reson. 2011;13:16.
28. Ugander M, Oki AJ, Hsu LY, Kellman P, Greiser A, Aletras AH, et al. Extracellular volume imaging by magnetic resonance imaging provides insights into overt and sub-clinical myocardial pathology. Eur Heart J. 2012;33:1268–78.
29. Akcakaya M, Basha TA, Weingartner S, Roujol S, Berg S, Nezafat R. Improved quantitative myocardial T2 mapping: Impact of the fitting model. Magn Reson Med. 2015;74(1):93–105.
30. De Graaf RA, Nicolay K. Adiabatic rf pulses: Applications to in vivo NMR. Concepts Magn Reson. 1997;9:247–68.
31. Heiberg E, Sjogren J, Ugander M, Carlsson M, Engblom H, Arheden H. Design and validation of Segment–freely available software for cardiovascular image analysis. BMC Med Imaging. 2010;10:1.
32. Cerqueira MD, Weissman NJ, Dilsizian V, Jacobs AK, Kaul S, Laskey WK, et al. Standardized myocardial segmentation and nomenclature for tomographic imaging of the heart. A statement for healthcare professionals from the cardiac imaging committee of the council on clinical cardiology of the American heart association. Int J Cardiovasc Imaging. 2002;18:539–42.
33. Bland JM, Altman DG. Statistical methods for assessing agreement between two methods of clinical measurement. Lancet. 1986;1:307–10.
34. Kellman P, Herzka DA, Hansen MS. Adiabatic inversion pulses for myocardial T1 mapping. Magn Reson Med. 2014;71:1428–34.
35. Nacif MS, Turkbey EB, Gai N, Nazarian S, van der Geest RJ, Noureldin RA, et al. Myocardial T1 mapping with MRI: comparison of look-locker and MOLLI sequences. J Magn Reson Imaging. 2011;34:1367–73.
36. Henningsson M, Botnar R, Voigt T. 3D saturation recovery imaging for free breathing myocardial T1 mapping. J Cardiovasc Magn Reson. 2013;15:P44.
37. Robson MD, Piechnik SK, Tunnicliffe EM, Neubauer S. T1 measurements in the human myocardium: the effects of magnetization transfer on the SASHA and MOLLI sequences. Magn Reson Med. 2013;70:664–70.
38. Weber OM, Speier P, Scheffler K, Bieri O. Assessment of magnetization transfer effects in myocardial tissue using balanced steady-state free precession (bSSFP) cine MRI. Magn Reson Med. 2009;62:699–705.

Paper IV: Validation of a new vessel segmentation algorithm with data driven shape constraints for robust noninvasive blood flow quantification from phase contrast magnetic resonance images.

Paper IV

Validation of a new vessel segmentation algorithm with data driven shape constraints for robust non-invasive blood flow quantification from phase contrast magnetic resonance images

Sebastian Bidhult[1,2], Erik Hedström[1,3], Marcus Carlsson[1], Johannes Töger[4], Katarina Steding-Ehrenborg[1, 5], Håkan Arheden[1], Anthony Aletras[1,6], Einar Heiberg[1,2]

Affiliations

[1]Lund University, Department of Clinical Sciences Lund, Clinical Physiology, Skane University Hospital, Lund, Sweden

[2]Lund University, Department of Biomedical Engineering, Faculty of Engineering, Lund, Sweden

[3]Lund University, Department of Clinical Sciences Lund, Diagnostic Radiology, Skane University Hospital, Lund, Sweden

[4]Lund University, Department of Diagnostic Radiology, Faculty of Medicine and National 7T Facility, Lund Bioimaging Center, Lund, Sweden

[5]Lund University, Department of Health Sciences, Physiotherapy, Lund, Sweden

[6]School of Medicine, Aristotle University of Thessaloniki, Laboratory of Computing, Medical Informatics ad Biomedical – Imaging Technologies, Thessaloniki, Greece

Word count: 3530

Corresponding author:

Einar Heiberg
Department of Clinical Physiology
Lund University,
SE-221 00, Lund
Sweden
einar.heiberg@med.lu.se
+46-76-1836442

Summary (Clinical Phys Funct Im instructions: Maximum 250 words, no abbreviations, no references)

Summary

Blood flow measurements from two-dimensional phase contrast magnetic resonance images require accurate time-resolved vessel segmentation over the cardiac cycle. Current semi-automatic segmentation methods often involve time consuming manual correction, relying on user experience for accurate results. The purpose of this study was to develop a vessel segmentation algorithm with shape constraints based on manual vessel delineations for robust segmentation of the ascending aorta and pulmonary artery, to evaluate the method in healthy volunteers and patients with heart failure and congenital heart disease, and to validate the proposed method against timer beaker flow measurements in a pulsatile flow phantom experiment.

Algorithm shape constraints were extracted from manual delineations of the ascending aorta and pulmonary artery (n=30 human subjects including both patients and healthy volunteers) and were included into an active contour, semi-automatic segmentation method requiring manual delineation in one image.

Phantom validation showed good agreement between the proposed method and timer beaker flow volumes. Flow volume bias and variability (bias±1.96SD) for the proposed algorithm vs. manual delineation were 0.3±4ml in the ascending aorta (n=134 subjects; 7 healthy volunteers; 127 heart failure patients) and -1.7±4 ml in the pulmonary artery (n=30; 16 healthy volunteers; 14 patients with Tetralogy of Fallot). Inter-observer flow volume bias and variability (bias±1.96SD) were lower for the proposed semi-automatic method (-0.3±1.5ml) compared to manual delineations (-0.9±2.9ml). In conclusion, the proposed semi-automatic vessel segmentation algorithm enables efficient analysis of flow and shunt volumes in the aorta and pulmonary artery.

Keywords: PC-MRI, Vessel segmentation, Aorta, Pulmonary artery, Shape regularization, Validation

Background

Phase-Contrast Magnetic Resonance (PC-MR) enables non-invasive quantification of blood flow[1] and is widely used to characterize cardiovascular disease[2] in the clinical setting. The technique currently serves as reference standard for non-invasive quantification of cardiac output (CO) and measurement of the left and right stroke volume ratio (Qp/Qs) used to detect and quantify shunt volumes [3].

PC-MR blood flow measurements require delineation of the vessel of interest over the cardiac cycle. Manual delineation in PC-MR images is time consuming, warranting robust automatic or semi-automatic segmentation algorithms. Previous vessel segmentation algorithms have effectively reduced the required time of analysis and improvements have been made in edge detection performance [4], pixelwise detection of the vessel lumen [5], the amount of required user input [6] and active contour tracking [7–9] have been applied to improve segmentation robustness. However, the need for manual corrections remain.

For two-dimensional PC-MR techniques, image contrast varies over the cardiac cycle. Time phases during ventricular systole which commonly contain high blood flow velocities tends to have greater image contrast between arteries and surrounding tissue compared to time phases during ventricular diastole. Therefore, segmentation algorithms often solely rely on built-in vessel shape constraints during diastolic time phases for accurate results. Previous methods have used shape constraints based on either fixed curvature and elasticity criteria within the segmentation model[7, 8] or shape templates from previously completed segmentations in adjacent time phases[9].

We hypothesized that shape constraints based on a data set of manually delineated PC-MR images can improve robustness of semi-automatic vessel segmentation methods. Therefore, the purpose of this study was to 1) develop a vessel segmentation algorithm with shape constraints based on manual vessel delineations, 2) validate the method in phantom experiments and 3) compare the method to manual delineation in 2D PC-MR images invivo in the ascending aorta and main pulmonary artery.

Methods

The study was approved by the Regional Ethical Review Board in Lund. The study population consisted of 201 human subjects in total (50 females; median age 56 years; age range 3-98 years). Two-dimensional PC-MR data of the ascending aorta from 18 healthy volunteers and 153 patients with heart-failure (defined as ejection fraction below 40%) were retrospectively included from a previous study of cardiac index[10]. Two-dimensional PC-MR data of the pulmonary artery from 16 healthy volunteers and 14 patients with atrial septal defects were also included from a previous study of atrial septal shunt volumes[11]. Vessel shape constraints and optimized algorithm parameters were extracted from 30 data sets, 20 from the ascending aorta group and 10 from the pulmonary artery group. Remaining data sets were used for algorithm evaluation.

Imaging data

The proposed segmentation algorithm was trained and evaluated for use in two-dimensional PC-MR human data from two 1.5T MR-scanner models: Magnetom Vision (Siemens; Erlangen; Germany) and Achieva (Philips; Best; The Netherlands). Validation of measured flow volumes was performed in a pulsatile flow phantom[12] using two scanners: One 1.5 T scanner (Aera, Siemens, Erlangen, Germany) and one 3T scanner (Prisma, Siemens, Erlangen, Germany). Flow measurements of the ascending aorta were collected in a transversal slice orientation (Figure 1A) and measurements of the pulmonary artery were collected in a double oblique orientation, both according to clinical routine. Typical sequence parameters for 2D PC-MRI pulse sequences are shown in Table 1. 2D PC-MRI data was collected using both prospectively gated (n=23 subjects) and retrospectively gated sequences during free-breathing and breath-holds (n=18 healthy volunteers). For patients with suspected valve insufficiency, prospective gating was performed over 2 RR-intervals to cover the entire cardiac cycle (n=10 subjects). Two different background phase correction techniques were applied for each vendor: 1) Linear background correction in Segment v2.0 R5390 was performed for data from Siemens scanners and 2) Automatic Local Phase Correction built into the scanner was performed during image reconstruction for data from the Philips scanner. For blood volume quantification, the vessel of interest was delineated in all cardiac time phases and the net blood flow volume was calculated as the blood flow time integral. A blood flow over time plot is shown in Figure 1B.

Extracting vessel shape profiles

Shape profiles were extracted from the training set (n=30 subjects) by parameterization of shape changes over the cardiac cycle from manual vessel delineations of the ascending aorta. In short, Principal Component Analysis (PCA)[13] was applied to compress manual delineation data such that typical shape profiles were extracted (implementation details are found in **Appendix A**). An example of the effect of such shape constraints is shown in Figure 2, demonstrating improved segmentation accuracy compared to shape constraints from optimized elasticity/curvature active contour parameters.

Algorithm overview

The proposed method for semi-automatic vessel segmentation is based on a modified active contour scheme constrained by the vessel shape constraints described above. A flow chart of the method is shown in Figure 3. The algorithm is initialized by selecting a vessel of interest from a manual delineation in one time phase of the image series. The manual delineation is then subjected to rigid motion tracking and the time series is divided into two parts by the K-means clustering algorithm using 2 classes[14] from the mean phase signal inside the time tracked manual delineation. The time series interval corresponding to large mean phase signal were set as potential candidates for initialization of the time resolved vessel segmentation. The manually delineated time phase was selected as starting point of the segmentation if this frame was included in the large mean phase class. If this was not the case, the time phase corresponding to the maximum mean phase signal was selected as starting point. The algorithm started to process the time interval associated with high velocity (as determined by the K-means classification), continued with time phases following the high velocity interval and completed the segmentation by processing the time interval before the high velocity interval. Processing of one time phase consisted of edge guided active contour deformations derived from the corresponding magnitude image, and subsequent shape constrained reconstruction. All images except the initialization time phase were initialized as the shape constrained segmentation result from its previously processed neighbor. Following time resolved vessel segmentation from magnitude images, active contour deformations from phase images were performed at selected time phases in order to increase the inclusion of relevant blood flow velocity. The main motivation behind the proposed segmentation scheme was to balance robustness and flexibility such that erroneous segmentation expansions into adjacent anatomy and image artifacts are avoided while a high degree of segmentation accuracy is obtained. Further algorithm implementation details are found in **Appendix B**.

Parameter optimization

Optimization of the segmentation method was performed in order to find a set of algorithm parameters resulting in a high degree of segmentation accuracy and robustness. Segmentation performance was evaluated by calculating the Dice overlap coefficient[15] between the proposed method and manual delineations from an expert reader, serving as the reference standard. A large mean and a small standard deviation of the Dice coefficient were considered indicators of high segmentation accuracy and robustness, respectively. All numerical optimizations were performed within the training set and the evaluated parameter combinations are summarized in Table 2. Active contour deformations using magnitude and phase images were optimized separately.

Phantom measurements

In order to validate PC-MRI flow measurements with a reference standard largely independent of user experience, flow volume measurements were performed in a custom made flow phantom[12] consisting of a pulsatile pump and a flow rectifier connected to plastic tubing inside a water tank. 2D PC-MRI flow volume measurements were compared to timer and beaker flow volumes which were obtained by measuring the total water volume output from the water tank during 2-4 minutes (depending on pump setting) of continuous pumping while accounting for the time between pump trigger signals. Phantom experiments were performed at varying pump stroke volumes and at two field strengths: 1.5T (Aera; Siemens, Erlangen, Germany) and 3T (Prisma; Siemens, Erlangen, Germany). The MR scanners were connected to the phantom pump trigger signal in order to enable gating of the MRI acquisition. 2D PC-MRI images were acquired in a transversal imaging plane through plastic tubing (26mm inner diameter) inside the water tank, with a velocity measurement direction perpendicular to the imaging plane. Regions of interest were drawn manually or by using the proposed semi-automatic segmentation method. Sequence parameters for sequences in use are shown in Table 1.

Statistical analysis

For invivo data, the proposed semi-automatic segmentation method was compared to manual delineations in the test set containing time resolved delineations of the ascending aorta in 134 human subjects and delineations of the pulmonary artery in 30 human subjects. The Dice overlap coefficient was used to measure segmentation overlap with manual delineations and blood flow volumes were compared using modified Bland-Altman analysis[16] with manual delineations serving as reference standard. Bias and variability between two methods were defined as mean±1.96 SD. The performance evaluation was repeated for two versions of the algorithm where the segmentation result was extracted before and after phase deformations, respectively. In this comparison, the RR-interval time phase of manual initializations was set to 20% of the RR-interval for all data sets. The performance impact of changing time phase of the manual initialization was evaluated by repeating the test set comparison for initialization in 20 equidistant time phases over the RR-interval. Inter-observer variability of manual delineations and the proposed semi-automatic method was determined from two expert readers in a randomly sampled subgroup of the ascending aorta test set (n = 30).

Results

Optimal parameter values from numerical optimization in the training set (n=30 human subjects) are shown in Table 2 (right column). Phantom timer beaker measurements resulted in a flow volume range of 11.8-89.3 ml (1.5T) and 24.4-89.8 ml (3T). Good agreement between timer beaker and 2D PC-MRI flow volume measurements was found at both field strengths (Figure 4). The proposed semi-automatic method resulted in modest underestimation of flow volumes at 3T with a bias and variability of XX±YY ml which was not found at 1.5T (bias±variability = ZZ±WW ml). Manual delineations showed good agreement at both 1.5T and 3T (XX±YY ml and ZZ±WW ml). A larger degree of image artifacts were observed at 3T compared to 1.5T data.

The change in segmentation performance with added processing blocks for the ascending aorta and the main pulmonary artery are shown in Figure 5. In the ascending aorta, activating additional algorithm blocks resulted in consistently reduced flow volume variability. In the pulmonary artery, magnitude deformations with shape constraints resulted in improvements in terms of flow volume bias, flow volume variability and mean Dice coefficient. However, phase deformations in the segmentation algorithm gave rise to reduced performance in the pulmonary artery.

Semi-automatic segmentations in images from free-breathing sequences resulted in good agreement with manual delineations. Semi-automatic measurements in the ascending aorta with algorithm initialization at 20% of the RR interval and using full algorithm functionality (Phase deformations ON in Figure 4) resulted in flow volume bias±1.96 SD of 0.3±4ml or 0.8±9.1% (Figure 6A). Corresponding mean Dice coefficient±1.96 SD were 92.5±5.6% with range 76.8–96.9%. The processing time of the proposed segmentation method ranged from 0.9–3.7seconds.

Results for the pulmonary artery (n=30) semi-automatic segmentation with constant initialization of the algorithm at 20% of the RR interval and using the segmentation algorithm version of preference (Magnitude deformations ON in Figure 5) are shown in Figure 6B. Flow volume bias and variability were -1.7±4 ml or-1.9±5.1% and mean Dice coefficient±1.96 SD were 93.6±3% with range 90.5–96%. The computation time for the pulmonary artery ranged between 1–1.4 seconds.

Flow volume outliers marked in Figure 6 and additional Dice coefficient outliers with Dice overlap below the lower limit of agreement are shown in Web Supplemental Figure 1 for the pulmonary artery and Supplemental Figure 2 and Supplemental Figure 3 for the ascending aorta.

Semi-automatic segmentations of the ascending aorta from Breath-hold acquisitions showed slightly degraded performance compared to corresponding free-breathing data in terms of bias and variability (-3.94±4.90 ml; Figure 7). Slight underestimation of flow volumes and increased variability was observed.

Figure 8 shows changes in flow volume bias and variability, and average Dice coefficients and Dice variability when the proposed semi-automatic method was initialized at different parts of the RR-interval for the ascending aorta and the pulmonary artery. For the ascending aorta (Figure 8A), the proposed segmentation algorithm was robust to changes initialization time point with worst-case absolute flow volume bias and variability of 0.5ml and 7.2ml, obtained with algorithm initialization at 85% and 100% of the RR-interval, respectively. Dice coefficient minimum average value and maximum variability were 92.4% and 5.9%, obtained with algorithm initialization at 100% and 80% of the RR-interval, respectively. Confidence intervals of flow volume differences were maintained below 9.7ml for algorithm initialization within 5-95% of the RR interval. In general, initializing segmentations at the very beginning and end of the RR interval gave rise to slightly reduced performance in terms of flow volume difference limits of agreement.

For the pulmonary artery, segmentation performance was sensitive to the selected RR-interval initialization time point (Figure 8B), resulting in a worst-case absolute flow volume bias and variability of 16.5ml and 34.3ml (at 85% of the RR-interval) and a Dice coefficient minimum average value and maximum variability of 88.5% and 10.7% (at 90% and 85% of the RR-interval). However, initializing segmentations at 15-35% of the RR interval resulted in worst-case absolute flow volume bias and variability limited to 2.2ml and 4.8ml, and Dice coefficient minimum average value and maximum variability within 93.4% and 3.2%. 15-35% of the RR interval corresponded to an expanded vessel radius in the acquired imaging slices for the pulmonary artery and well defined image contrast between the vessel of interest and its surroundings were generally found.

The interobserver variability study in 30 human subjects with semi-automatic segmentations initialized at 20% of the RR interval showed a difference in measured flow volumes of -0.9±2.9ml (bias±1.96 SD) for manual delineations and -0.3±1.5ml (mean±1.96 SD) for semi-automatic segmentations (Figure 9). Interobserver mean Dice coefficient±1.96 SD and range were 94.7±3.7% (range 87.9-96.9%) and 99.1±2.4% (range 93.1-99.8) for manual delineations and the proposed segmentation method, respectively. An increased interobserver Dice overlap was found for the proposed segmentation method in 100% of the 30 evaluated subjects compared to manual delineations.

Discussion

Automated vessel segmentation methods for PC-MRI data have the potential of improving efficiency in the clinical setting. Previous semi-automatic algorithms have shown clear improvements in processing speed[4], interobserver variability compared to manual delineations[8] and good agreement in phantom measurements[9]. This study presents an algorithm for semi-automatic segmentation of the ascending aorta and the pulmonary artery in 2D PC-MRI images with implemented shape constraints based on eigenvector decomposition of manual delineation training data.

The proposed method resulted in good agreement with timer and beaker flow volume measurements in a pulsatile flow phantom experiment at two field strengths and a wide range of flow volumes. The observed underestimation of flow volumes at 3T may be attributed to the observed image artifacts in the 3T data, indicating sensitivity to image quality for the proposed semi-automatic method. Good agreement between the proposed method and manual delineation was found for flow measurements in the ascending aorta and the main pulmonary artery, demonstrating possibility for clinical use in both vessels. The underestimation of flow volumes for breath-hold acquisitions may be explained by an overrepresentation of free-breathing data in the training.

Different versions of the proposed algorithm gave rise to maximum segmentation robustness in terms of low flow volume bias, low flow volume variability and Dice overlap. However, due to the large difference in shape variation over the cardiac cycle between the ascending aorta and the main pulmonary artery, alteration of segmentation algorithm parameters is warranted for optimal performance.

Segmentation of the ascending aorta (AO) was shown robust to the RR time point of initialization while segmentations of the pulmonary artery required an initialization time point at 15-35% of the RR interval for satisfactory results. This may be explained by the larger variation of vessel diameter in imaging slices used for pulmonary artery flow volume measurements compared to corresponding measurements for the ascending aorta. Of note, this is not due to differences in actual vessel anatomy but rather explained by the need for double-oblique positioning of the pulmonary artery imaging plane. Therefore, getting the true cross-section of the pulmonary artery is more user dependent during the MRI scan compared to the aorta where a transversal slice at the level of the pulmonary bifurcation results in cross-section of the vessel. Time points at 15-35% of the RR-interval, generally corresponding to near-maximum expansion of the vessel diameter, usually feature modest vessel shape and size variations in comparison to the rapid diameter expansion found in the beginning of the RR interval and can be reflected in finer detail at a given temporal resolution. The found sensitivity to initialization time point of the proposed method may indicate an underlying sensitivity to temporal resolution for vessels with large shape and size variations over the RR interval. However, since the optimal initialization time points for pulmonary artery segmentation was associated with large vessel diameters and well defined image contrast between the vessel of interest and its surroundings, manual delineation in this time interval will most likely not be a major challenge in the majority of cases.

Outliers in the validation study revealed slight sensitivity to abnormal anatomy, resulting in reduced segmentation quality and inability of the algorithm to reproduce rapid shape variations. Future work should be focused on limiting such behavior which may be reduced by adapting edge detection and deformation parameters to the pixel size, temporal resolution, expected rate of in-plane vessel motion and vessel diameter, or by introducing additional region analysis forces to aid the tracking of rapid in-plane motion. However, despite current limitations, obtained flow volume limits of agreement from both vessel types were small in relation to reported flow volume errors caused by potential background velocity offset errors[17]. A reduction in inter observer variability was found for the proposed semi-automatic method compared to manual delineations in 30 subjects, which combined with the limited variability of measured flow volumes warrants the use of the proposed segmentation method for flow and shunt volume quantification. Manual user input is still required for initialization of the proposed segmentation method. Recent developments in the field have resulted in methods for automatic identification of the ascending and descending aorta in 2D PC-MRI images, assuming a strictly circular vessel lumen[18]. Methods with added shape flexibility and time resolved segmentation algorithms, as proposed in the current study, may facilitate fully automatic 2D PC-MRI flow volume measurements independent of user experience in the clinical setting in the near future.

Conclusion

Semi-automatic segmentation methods for the ascending aorta and the pulmonary artery were developed and showed good agreement with manual delineations from expert readers in terms of flow volume bias, flow volume variability and Dice coefficient overlap with reduced inter observer variability, enabling efficient and robust flow and shunt volume quantification in the clinical setting.

Limitations

The proposed segmentation method was mainly validated using manual delineations as reference standard, a measure highly dependent on user experience. An extensive validation in a phantom experiment using a fully independent gold standard and featuring large shape variations which was shown difficult for the proposed method may enable further development of segmentation robustness. Impact of the composition of selected training data on segmentation performance was not explored. The selection of training data and adjustment of the amount of training data compression may alter segmentation performance and may limit adequate segmentation for pathology types not included in the training set. The segmentation method was evaluated in segmented MRI data only and have not been validated for use with real time PC-MRI data. Sequence parameters was not matched between in-vivo experiments and phantom validation.

Competing interests

Einar Heiberg is a major shareholder of Medviso AB, which produces cardiovascular imaging software. No funding has been received from any non public funding source. No other authors have any competing interests to disclose

Author's Contributions

SB contributed to the design of the study, developed and implemented the algorithms, analyzed and interpreted results, and drafted the manuscript. EHed contributed to the design of the study and to the automatic algorithm and performed manual delineations of the pulmonary data, MC contributed to the design of the study and performed manual delineations in all patients. JT acquired the phantom data and contributed to the design of the algorithm. KSE contributed to the design of the study and collected the normal subject's data. HA contributed to the design of the study and assisted in conceiving the study. AA contributed to the design of the study and to the design of automatic algorithm and provided in depth Cardiac MRI knowledge needed for algorithm development. EHei contributed to the design of the automatic algorithm and conceived the study. All authors revised the manuscript for intellectual content, and have read and approved the final version of the manuscript.

Acknowledgements

This study has been funded by the Swedish Research Council (2011-3916, 2012-4944, 2011-4078), the Swedish Heart and Lung Foundation, Swedish Medical Society, the Medical Faculty of Lund University, Sweden, and Region of Scania, Skane University Hospital, Sweden. The authors wish to acknowledge the skillful assistance of Ann-Helen Arvidsson and Christel Carlander in collecting the patient materials.

Tables

Table 1. Typical 2D PC-MRI sequence parameters for in-vivo and phantom data acquisitions

MRI Sequence parameters	In-vivo data (Philips 1.5T) Free-Breathing Retrospective gating	In-vivo data (Philips 1.5T) Breath-hold Retrospective gating	In-vivo data (Siemens 1.5T) Free-Breathing Prospective gating	Phantom data (Siemens 1.5T) Retrospective gating	Phantom data (Siemens 3T) Retrospective gating
Echo time [ms]	5.3	2.3	5	2.66	3.0
Slice thickness [mm]	6	10	8	5	5
Time resolution [ms]	17.3	15.7	30	19.7	21.4
VENC [cm/s]	200	200	250	200	200
Flip Angle [°]	15	15	30	20	20

Table 2. Optimized algorithm parameters

Optimized algorithm parameters	Parameter values: [min, max] Δ = interval spacing Alternatively: [parameter values]	Determined optimum value
Number of iterations (magnitude deformations)	[5, 50]; Δ =5;	10
External edge force constant (magnitude deformations)	[0.5, 10]; Δ = 0.5;	1
External region analysis force constant (magnitude deformations)	To be re-performed before submission	
Number of iterations (phase deformations)	[5, 10, 20, 30, 40];	5
External region analysis force constant (phase deformations)	[3, 15]; Δ = 3;	12
Systolic exclusion percentage γ (phase deformations)	[40%, 90%]; Δ = 10%;	50%
VNR threshold (phase deformations)	[1, 2, 3, 4]	1

Figure Legends

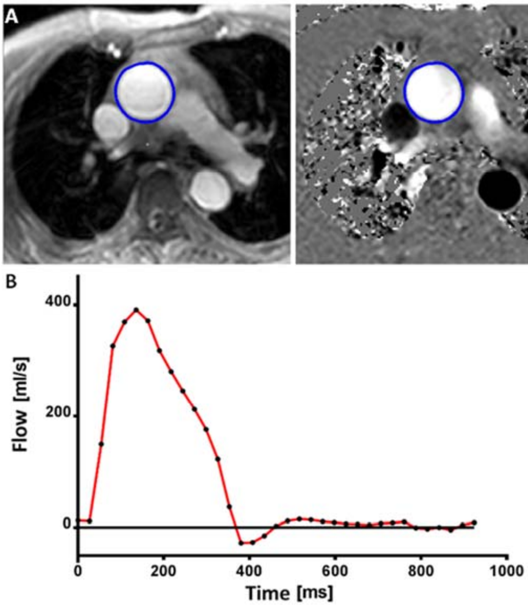

Figure 1. Example of a 2D PC-MRI flow volume measurement. Top panel (A) shows manual delineations (blue) of the ascending aorta in a magnitude image (left) and the corresponding phase image (right) in early systole in a transversal slice orientation. The lower panel (B) shows measured flow (y-axis) over time after manual delineations in all time phases throughout the cardiac cycle. The flow volume is calculated from time integration of this curve.

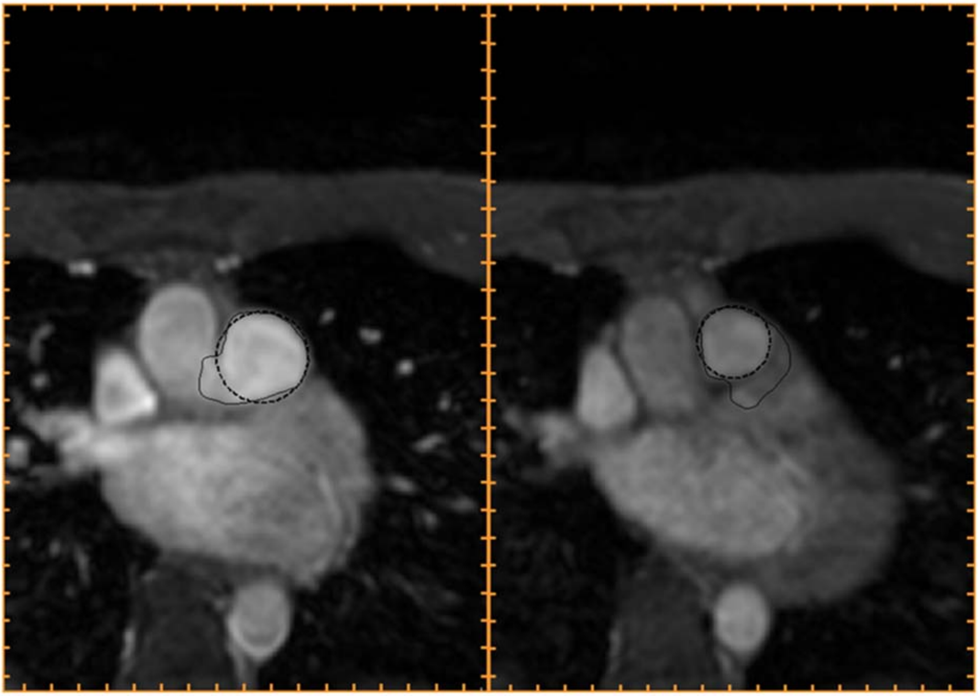

Figure 2. Improvement in segmentation accuracy using the proposed shape constraints. The image shows a double-oblique imaging slice used for flow volume measurements in the pulmonary artery in ventricular systole (left panel) and ventricular diastole (right panel). Semi-automatic inaccurate segmentations using conventional shape constraints are shown as solid black lines and semi-automatic segmentations using the proposed shape constrained reconstruction are shown as dashed black lines.

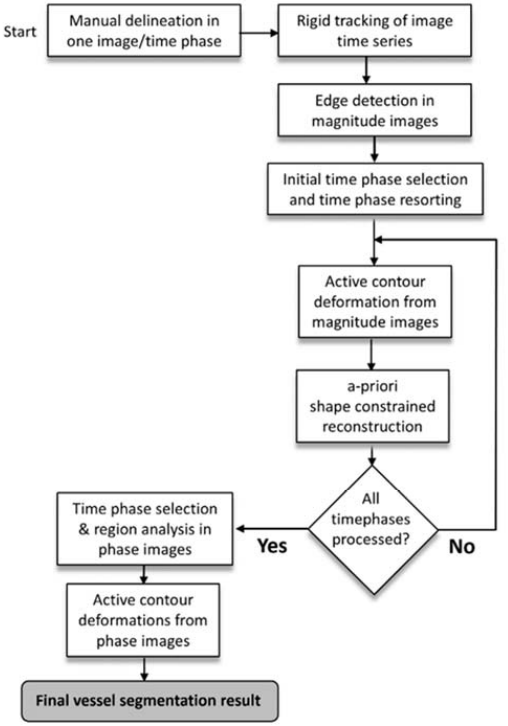

Figure 3. Flow chart of the proposed semi-automatic segmentation method. The method is initialized by a manual delineation in one time point and continues with rigid motion-tracking, interleaved active contour deformations using magnitude images and shape constrained reconstruction and ends with active contour deformations using phase images.

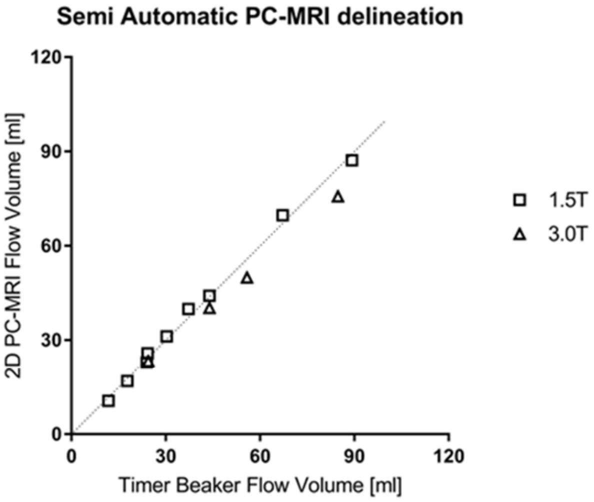

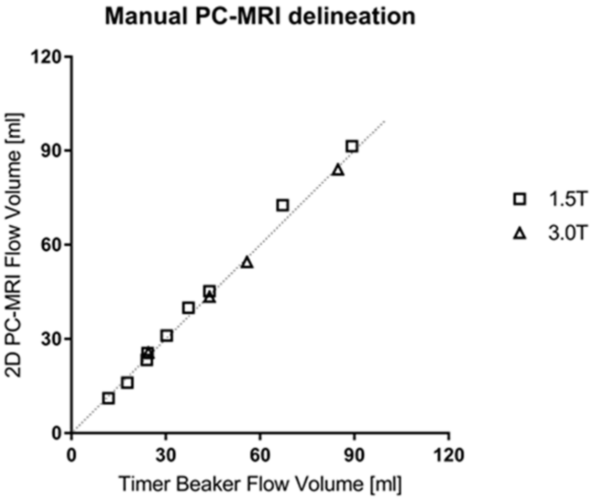

Figure 4. Validation in a pulsatile phantom experiment resulted in close agreement between timer beaker measurements and 2D PC-MRI at 1.5T (squares) and 3T (triangles) and for both semi-automatic (top panel) and manual PC-MRI ROI delineations. The proposed semi-automatic method resulted in modest underestimation of flow volumes at 3T.

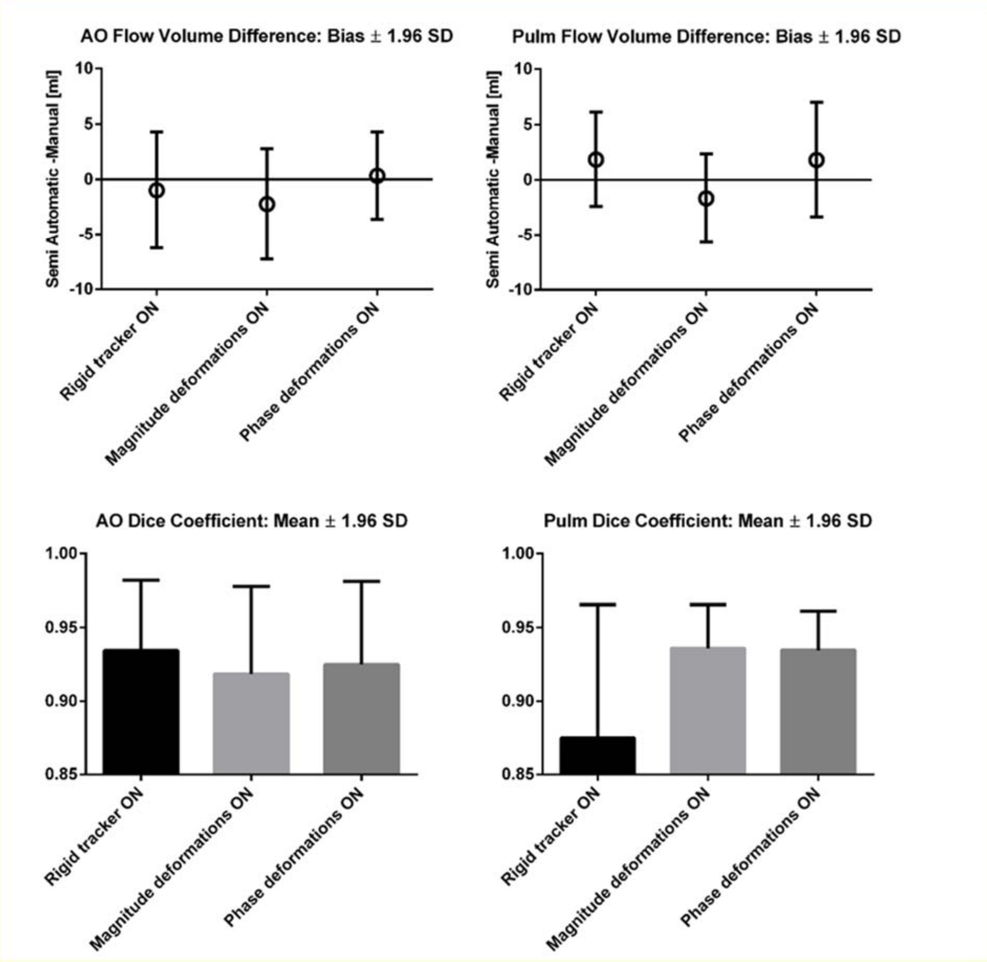

Figure 5. Segmentation performance varies with different algorithm steps turned on/off and the vessel of interest. Top panels: Flow volume bias (open circles) and limits of agreement (error bars) for the semi-automatic method vs manual delineations. Bottom panels: Dice coefficient averages (bars) and standard deviations (error bars). The left panels show results for the ascending aorta (denoted AO) and the right panels show results for the pulmonary artery (denoted Pulm). The algorithm setting with best performance for the ascending aorta and the pulmonary artery was “Phase deformations ON” and “Magnitude deformations ON”, respectively.

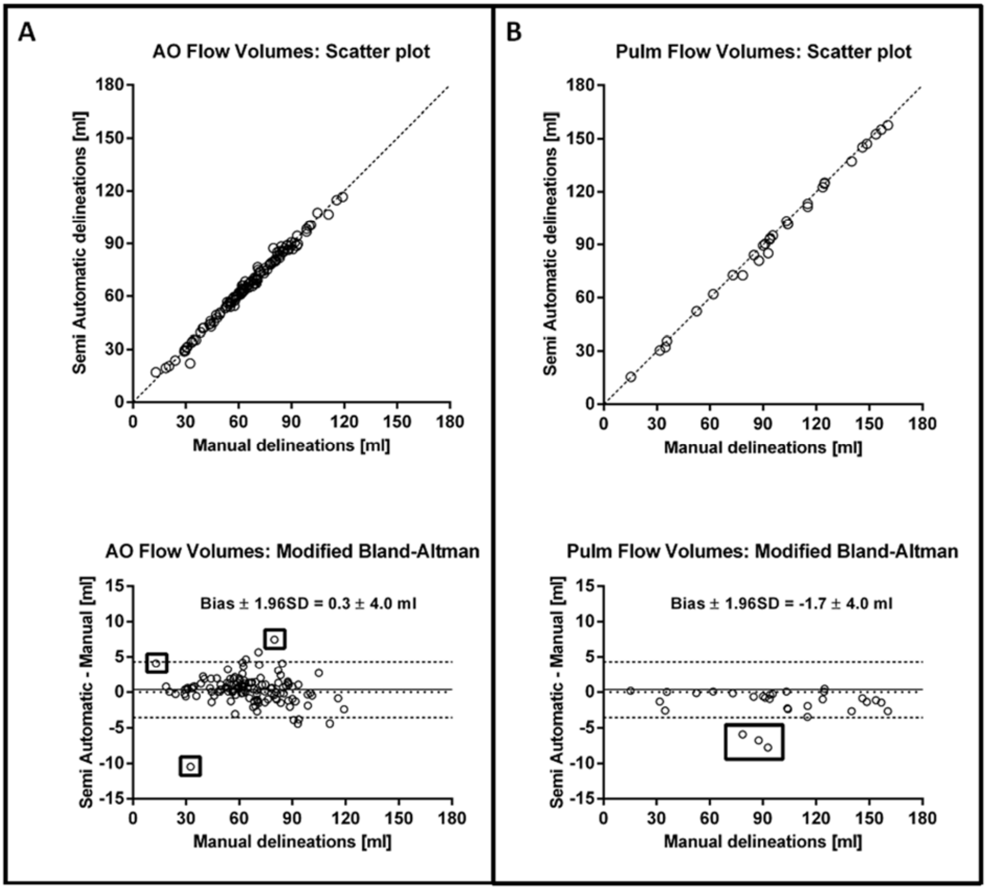

Figure 6. The semi-automatic method results in flow volumes similar to manual delineations in the ascending aorta (n=134; panel A) and in the pulmonary artery (n=30; panel B). Top panels show flow volumes measured from the semi-automatic method (y-axes) and manual delineations (x-axes). The dashed line indicates line of identity. Bottom panels show corresponding modified Bland-Altman analysis flow volume difference (y-axes) over flow volumes from manual delineation (x-axes). The dotted lines indicate zero flow volume difference, the solid lines indicate bias and the dashed lines indicate limits of agreement. Flow volume outliers are enclosed in solid rectangles for both vessel types and are shown in Web Supplemental Figures 1-2. Low bias and variability were found. For the semi-automatic method, manual initialization was performed at 20% of the RR interval and algorithm settings with best performance for the two vessel types were used.

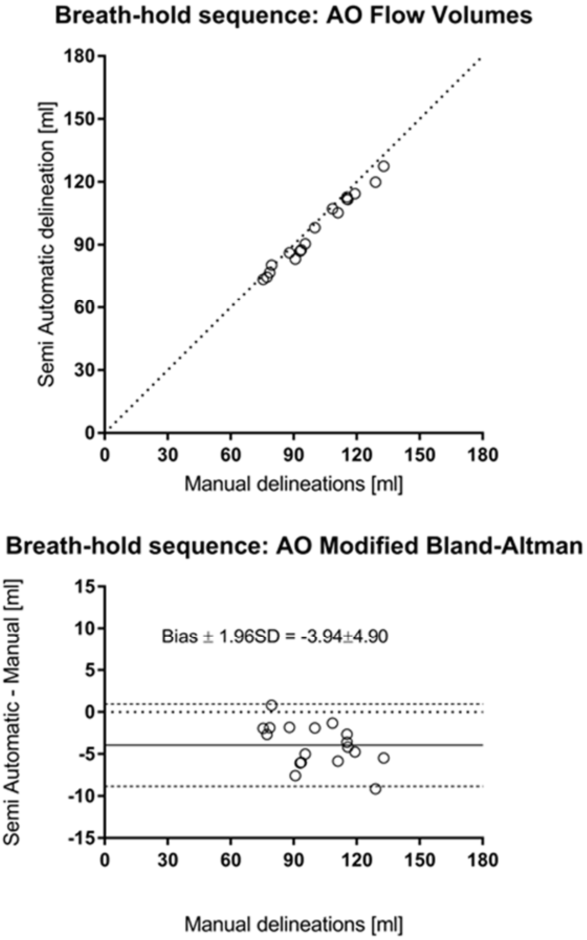

Figure 7. Flow volume comparison between semi-automatic and manual vessel delineations of the ascending aorta in breath-hold PC-MRI data. The proposed semi-automatic method resulted in underestimation of flow volumes in breath-hold acquisitions.

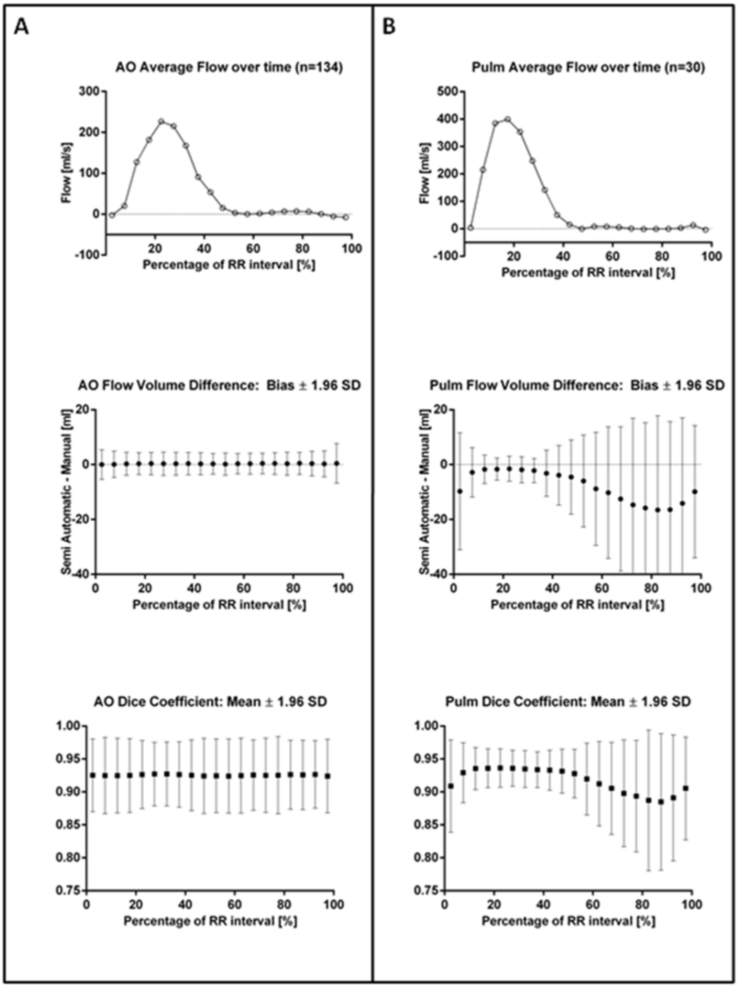

Figure 8. Segmentation performance varies with the time point used for algorithm initialization. Top panels show average flow profiles over the RR-interval from manual delineations for the ascending aorta (n=134; panel A) and the pulmonary artery (n=30; panel B). Middle panels show flow volume bias and limits of agreement (filled circles and error bars) of the semi-automatic method vs. manual delineations. Bottom panels show Dice coefficients and 1.96 SD (filled squares and error bars). The proposed segmentation algorithm was robust to the initialization time point for the ascending aorta. For the pulmonary artery, segmentations were sensitive to the initialization time point. However, when segmentation initializations were confined to 15-35% of the RR-interval, segmentation quality was similar to the ascending aorta in terms of flow volume bias, flow volume variability and Dice coefficient.

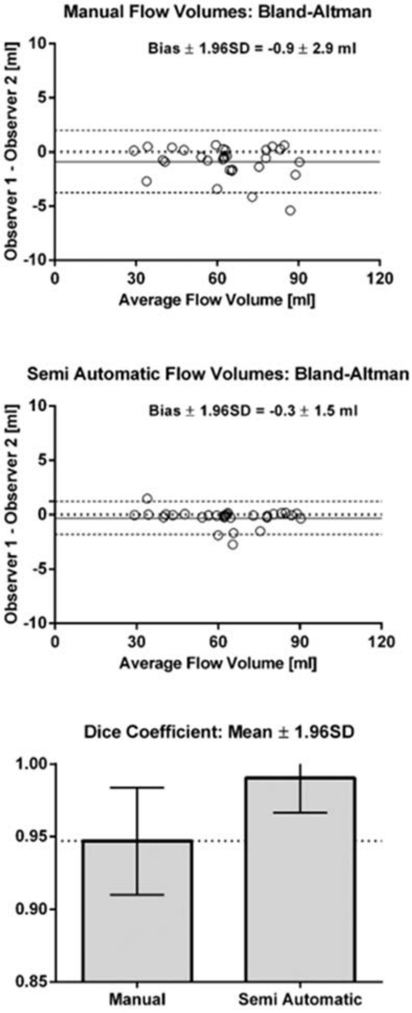

Figure 9. Inter observer variability of flow volume differences and Dice coefficient overlap for manual delineations and the proposed semi-automatic method between two observers. Top panel shows Bland-Altman analysis of flow volume differences between two observers from manual delineations (y-axis) over the average flow volume (x-axis). The dotted line indicates zero flow volume difference, the solid line indicates bias and dashed lines indicate limits of agreement. Middle panel shows corresponding Bland-Altman analysis for two observers using the semi-automatic method. Bottom panel shows Dice overlap coefficient mean value (bars) and standard deviation (error bars) between two observers for manual delineations (left; Dice range 87.9-96.9%) and the semi-automatic method (right; Dice range 93.1-99.8%). The dotted line indicates the mean Dice coefficient value for manual delineations. A clear reduction in inter observer variability for both measured flow volumes and Dice coefficient overlap were observed for the semi-automatic method.

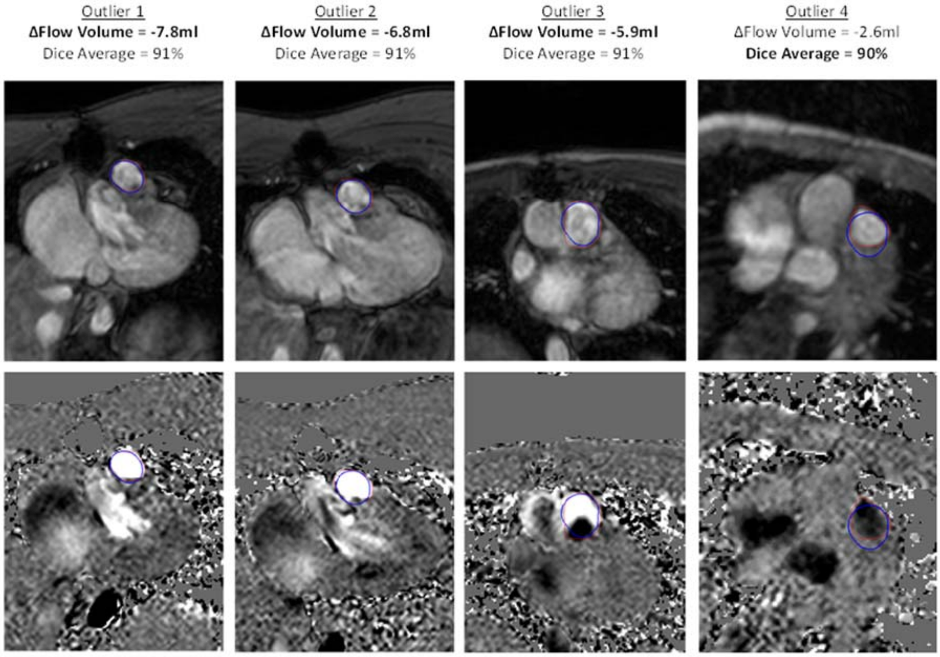

Web Supplemental Figure 1. Outlier datasets with degraded segmentation quality for the pulmonary artery. The image shows three flow volume outliers marked in Figure 5B (outliers 1-3) and one Dice coefficient outlier (outlier 4). Top panels show magnitude images from each outlier dataset with manual (red) and semi-automatic (blue) segmentations at a time point which demonstrates segmentation errors. Bottom panels show corresponding phase images at the same time point. Obtained flow volumes and Dice coefficients outside the limits of agreement are displayed in a bold font. The outliers demonstrate flow volume underestimation during ventricular systole (outliers 1-3) and an overestimation of the vessel area during ventricular diastole (outlier 4).

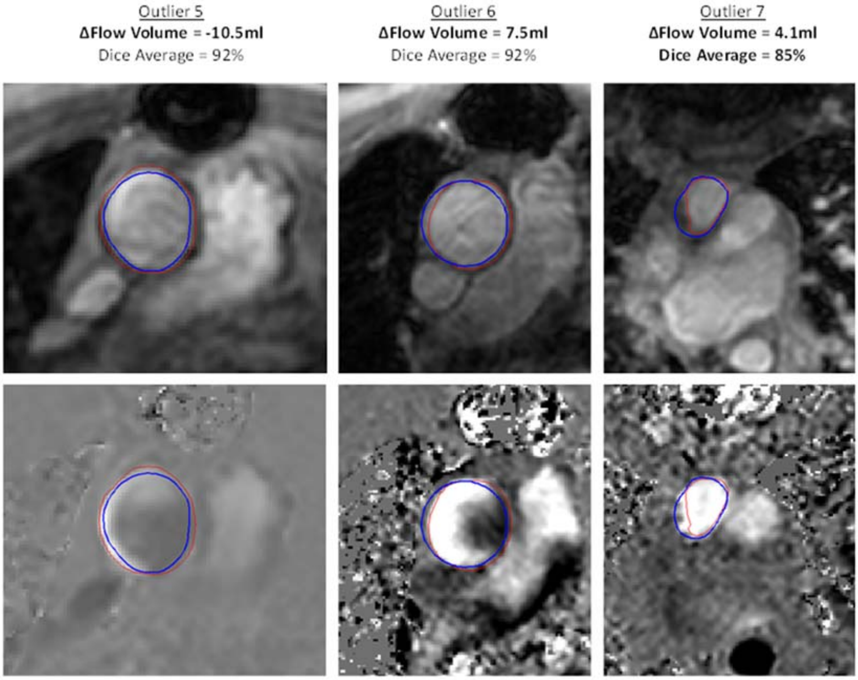

Outlier 5
ΔFlow Volume = -10.5ml
Dice Average = 92%

Outlier 6
ΔFlow Volume = 7.5ml
Dice Average = 92%

Outlier 7
ΔFlow Volume = 4.1ml
Dice Average = 85%

Web Supplemental Figure 2. Outlier datasets with degraded segmentation quality for the ascending aorta. The image shows three flow volume outliers marked in Figure 5A for the ascending aorta. Top panels show magnitude images from each outlier dataset with manual (red) and semi-automatic (blue) segmentations at a time point which demonstrates segmentation errors. Bottom panels show corresponding phase images at the same time point. Obtained flow volumes and Dice coefficients outside the limits of agreement are displayed in a bold font. The outliers demonstrate flow volume underestimation (outlier 5) and overestimation (oultiers 6-7) during ventricular systole.

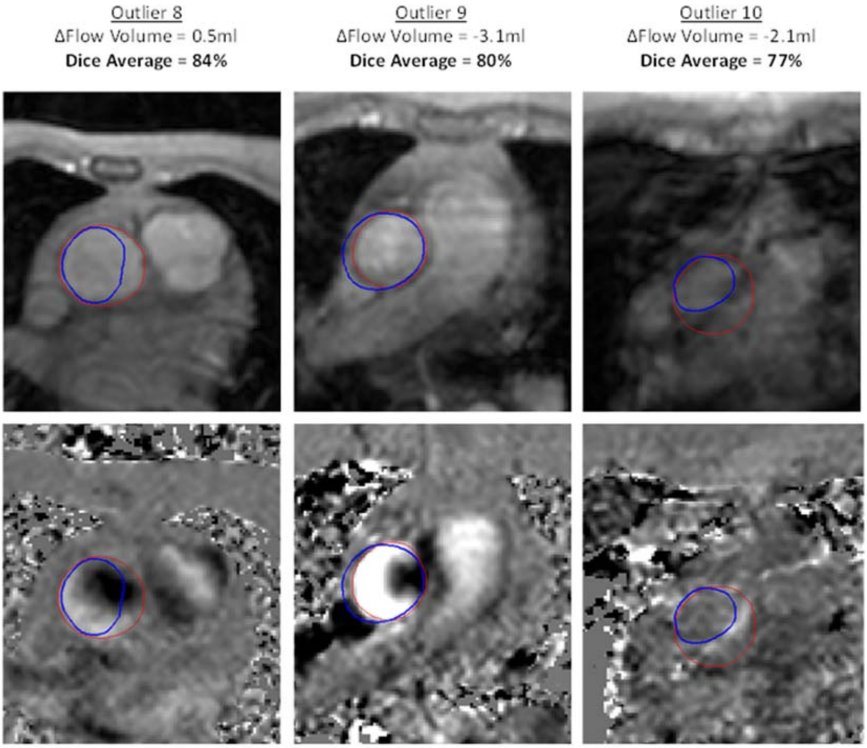

Supplemental Figure 3. Outlier datasets with degraded segmentation quality for the ascending aorta. The image shows three outlier datasets for the ascending aorta with Dice coefficients below the lower limit of agreement. Top panels show magnitude images from each outlier with manual (red) and semi-automatic (blue) segmentations at a time point which demonstrates segmentation errors. Bottom panels show corresponding phase images at the same time point. Obtained flow volumes and Dice coefficients outside the limits of agreement are displayed in a bold font. The outliers demonstrate flow volume underestimation during ventricular systole (outlier 9) and underestimation of the vessel area during ventricular systole and diastole (outlier 8 and 10, respectively).

Appendix A: Details on Extracting shape profiles from the training set

In order to achieve coordinate correspondence, vessel shape changes over the cardiac cycle were parameterized by transforming the manual delineation coordinates into radial distances, sampled at 40 equidistant angles and normalized by the mean radial distance over time. The time resolution was resampled to 20 linearly spaced time phases over a cardiac cycle to ensure equidistant sampling of a cardiac cycle for all datasets. Shape profiles were stored in a matrix R with size 30x800 (i.e. including 30 subjects and 40 delineation nodes in 20 time phases) and decomposition of the data into orthonormal eigenvectors and corresponding eigenvalues was performed using Principal Component Analysis (PCA)[13] of matrix R. This decomposition enables lossless reconstruction of a resampled vessel segmentation dataset from the weighted sum of all eigenvectors, according to equations (1-2):

$$r = m + \sum_{\mathrm{i}=1}^{\mathrm{N}} \mathrm{a_i v_i}; \tag{1}$$

$$a_i = v_i \cdot (r - m)^T = \sum_{j=1}^{N} r(j) v_i(j); \tag{2}$$

Here, ***m*** denotes the dataset mean shape column vector, ***a*i** indicates the eigenvector weight (scalar) for eigenvector ***vi*** (column vector), ***r*** is the fully reconstructed dataset (column vector) and ***N*** is the number of available eigenvectors (scalar). If a shape profile is reconstructed from a subset of eigenvectors the result will be an approximation of the original dataset constrained by shape profiles from the selected eigenvectors. Finding the eigenvector weights $\tilde{a}$ for a subset of eigenvectors from equation (2) can be rewritten as a solution to a linear least squares regression problem:

$$\hat{r} = r - m; \tag{3}$$

$$V_K = [v_1, v_2, \ldots., v_K]; \tag{4}$$

$$\tilde{a} = \underset{a}{argmin} \, \|\hat{r} - V_K a\|_2^2 = (V_K^T V_K)^{-1} V_K^T \hat{r} = I V_K^T \hat{r} = V_K^T \hat{r} \tag{5}$$

Here uppercase letters represent matrices while lower case letters represent column vectors. ***VK*** denotes selected eigenvectors (column vectors) with the ***K*** largest eigenvalues and ***I*** is the identity matrix. This method may be used to apply shape constraints on time resolved vessel segmentations of the ascending aorta. However, due to differences in shape variation and motion profiles over the cardiac cycle between the ascending aorta and the main pulmonary artery in 2D PC-MRI images, the method described above is not suitable for imposing shape constraints on pulmonary artery segmentations. Therefore, the shape constraints were generalized by using only one mid-systolic time phase of the a priori eigenvector data and reconstructing the segmentation of each time phase separately according to equations (6)- through (9):

$$\hat{s}_t = s_t - m_t; \tag{6}$$

$$V_{K,t} = \left[v_{1,t}, v_{2,t}, \dots., v_{K,t}\right]; \tag{7}$$

$$\tilde{a}_t = \underset{a_t}{argmin} \left\| \hat{s}_t - V_{K,t} a_t \right\|_2^2 \tag{8}$$

$$p_t = m_t + V_{K,t} \tilde{a}_t; \tag{9}$$

Here, $\boldsymbol{s_t}$ represents the segmentation result at time phase $\boldsymbol{t}$, $\boldsymbol{m_t}$ represents the mean a priori shape column vector at time phase $\boldsymbol{t}$, $\boldsymbol{V_{K,t}}$ represents the $\boldsymbol{K}$ eigenvectors (column vectors) corresponding to the $\boldsymbol{K}$ largest eigenvalues at time phase $\boldsymbol{t}$, $\boldsymbol{a_t}$ (column vector) represents eigenvector weights for $\boldsymbol{V_{K,t}}$ and $\boldsymbol{p_t}$ represents the shape constrained segmentation result at time phase $\boldsymbol{t}$. The number of eigenvalues in use $\boldsymbol{K}$ was determined from numerical optimization. An estimation of the segmentation mask center of mass was needed to convert segmentation node coordinates into radial distances before imposing shape constraints. In order to approximate the center of mass of a segmentation result containing outlier nodes, all segmentations were eroded before calculating the center of mass.

Appendix B: Algorithm implementation details

Rigid Motion-Tracking in magnitude images

The user-defined delineation was tracked through the image time series by a two-dimensional local cross-correlation algorithm. An analysis window surrounding the manual delineation extracted the magnitude image data from two adjacent time phases. The data was then resampled using bilinear interpolation with a factor of 2 and cross correlation was performed by conjugate multiplication in the Fourier domain. The spatial shift resulting in maximum correlation was chosen as the detected vessel translation between adjacent time phases.

Active contour deformation model

The implemented active contour model is based on the original formulation by Kass et al[19] and was implemented in part in two previous studies[20, 21]. The active contour uses the following energy minimization problem for a given segmentation ***v*(*s*)**:

$$\begin{aligned} \arg\min_{v} E &= \int_0^1 E(v(s))ds \\ &= \int_0^1 (E_{int}(v(s)) + E_{ext}v(s))ds \end{aligned} \tag{10}$$

Here ***v*(*s*)** is represented by a set of equidistantly spaced discrete node points along a closed contour. The internal energy term, E_{int}, imposes shape constraints on the curvature while the external energy term, E_{ext}, enables attraction and repulsion from various image features. A local energy minimum is found by solving the Euler-Lagrange differential equation:

$$0 = \frac{\delta}{\delta s}(\frac{\delta}{\delta v_s}E_{int}) + \frac{\delta}{\delta v_s}E_{ext} = KU + F(U) \tag{11}$$

The two derivative terms represent internal and external forces controlling the segmentation evolution. The equation is converted into a finite difference scheme in the right hand side of equation (11), where ***U*** represents the node point coordinates, the stiffness matrix ***K*** corresponds to internal forces, and ***F(U)*** represents forces associated with external image features at node point coordinates ***U***. The internal force of the proposed method was set to zero and was replaced by the a priori shape constraints described above. The external force for magnitude images was based on edge detection while the external force for phase images was based on regional analysis in order to identify pixels with high velocity-to-noise ratio (VNR). Active contour deformations were performed over an optimized number of iterations.

Edge detection in magnitude images

The edge detection was implemented as four separate edge detectors using the one-dimensional filter kernel [-1 2 -1] at different orientations rotated 45° from each other, creating one horizontal, one vertical and two diagonal filter kernels. Convolution with the filter kernels was preceded by horizontal and vertical smoothing of the magnitude images using the filter kernel [0.25 0.5 0.25]. For each node point, the active contour model used a weighted combination of the two filter directions resulting in the largest and second-largest scalar product with the local delineation normal vector, as previously proposed[20]. Using this method, nodes on the closed curve was attracted to strong image gradients along their local normal vectors.

Region analysis in magnitude images

The external force of active contour deformations in magnitude images were derived from the difference between the magnitude image and the median magnitude value inside the ROI after rigid motion tracking in all timeframes. All pixels deviating from the median ROI value no more than an optimized constant times a robust standard deviation estimate (calculated as 1.4826*Median Absolute Deviation) of pixels inside the ROI were set to not produce any forces on the active contour. Pixels exceeding this threshold were set to produce a local expansion of the active contour while pixels with intensities below the threshold were set to compress the active contour. The threshold constant multiplier was determined from numerical optimization (labelled as External Region analysis force constant (magnitude deformations) in table 2).

Region analysis in phase images

The external force of active contour deformations in phase images was based on regional analysis of phase images containing a high degree of flow content within the segmented contour. A high degree of flow content was defined as pixel values above a set VNR threshold β and images with a high degree of flow content were defined as images with a median estimated VNR inside the vessel delineation larger than β. The pixelwise VNR was defined as $VNR(x,y) = |phase(x,y)|/\sigma_{noise}$ where $|phase(x,y)|$ denotes the normalized absolute pixelwise phase and σ_{noise} denotes the estimated noise standard deviation in the phase images. The noise standard deviation was estimated from pixels within the vessel segmentation in phase images with a low degree of flow content. These images were identified by calculating the average blood flow velocity within the vessel delineation in all time phases, computing the median blood flow velocity over time and excluding the phase image with maximum average flow deviation from the median iteratively. The number of iterations was set to exclude a fix percentage γ of all images. Pixels of the external force map with VNR values below threshold β were set to zero. Remaining pixels were given values $mag(x,y)*phase2\ (x,y)/\sigma_{noise}$ where *phase2(x,y)* was shifted in sign such that positive values corresponded to the main flow direction within the vessel delineation and *mag(x,y)* was the magnitude pixel value which was used to reduce erroneous segmentation expansion from pixels in low signal areas such as lung tissue. Only the connected flow regions with maximum overlap with segmentations were used as non-zero external forces in order to reduce erroneous segmentation expansion due to flow from adjacent vessels. The external force map was normalized to the maximum pixel value in images with a high degree of flow content before active contour deformations. The constants β and γ were determined by parameter optimization.

References

1. Nayler GL, Firmin DN, Longmore DB. Blood flow imaging by cine magnetic resonance. Journal of Computer Assisted Tomography. 1986;10:715–22. doi:10.1097/00004728-198609000-00001.

2. Schulz-Menger J, Bluemke D a., Bremerich J, Flamm SD, Fogel M a., Friedrich MG, et al. Standardized image interpretation and post processing in cardiovascular magnetic resonance: Society for Cardiovascular Magnetic Resonance (SCMR) Board of Trustees Task Force on Standardized Post Processing. JCMR. 2013;15:35. doi:10.1186/1532-429X-15-35.

3. Petersen S, Voigtländer T, Kreitner K, Kalden P, Wittlinger T, Scharhag J, et al. Quantification of shunt volumes in congenital heart diseases using a breath-hold MR phase contrast technique--comparison with oximetry. Int J Cardiovasc Imaging. 2002;18:53–60. http://www.ncbi.nlm.nih.gov/pubmed/12135123.

4. Chwialkowski MP, Ibrahim YM, Li HF, Peshock RM. A method for fully automated quantitative analysis of arterial flow using flow-sensitized MR images. Comput Med Imaging Graph. 1996;20:365–78. doi:10.1016/S0895-6111(96)00010-9.

5. Alperin N, Lee SH. PUBS: Pulsatility-based segmentation of lumens conducting non-steady flow. Magn Reson Med. 2003;49:934–44.

6. Zöllner FG, Ankar Monssen J, Rørvik J, Lundervold A, Schad LR. Blood flow quantification from 2D

phase contrast MRI in renal arteries using an unsupervised data driven approach. Z Med Phys. 2009;19:98–107. doi:10.1016/j.zemedi.2008.10.011.

7. Krug R, Boese JM, Schad LR. Determination of aortic compliance from magnetic resonance images using an automatic active contour model. Phys Med Biol. 2003;48:2391–404.

8. Herment A, Kachenoura N, Lefort M, Bensalah M, Dogui A, Frouin F, et al. Automated segmentation of the aorta from phase contrast MR images: validation against expert tracing in healthy volunteers and in patients with a dilated aorta. JMRI. 2010;31:881–8. doi:10.1002/jmri.22124.

9. Kozerke S, Botnar R, Oyre S, Scheidegger MB, Pedersen EM, Boesiger P. Active Contours in Cine Phase Contrast Flow Measurements. JMRI. 1999;10:41–51.

10. Carlsson M, Andersson R, Bloch K, Steding-Ehrenborg, K Mosén H, Stahlberg F, Ekmehag B, et al. Cardiac output and cardiac index measured with cardiovascular magnetic resonance in healthy subjects, elite athletes and patients with congestive heart failure. J Cardiovasc Magn Reson. 2012;14.

11. Stephensen SS, Steding-Ehrenborg K, Thilén U, Holm J, Hochbergs P, Arheden H, et al. Changes in blood volume shunting in patients with atrial septal defects: assessment of heart function with cardiovascular magnetic resonance during dobutamine stress. Eur Hear J – Cardiovasc Imaging. 2016; February:jew176. doi:10.1093/ehjci/jew176.

12. Töger J, Bidhult S, Revstedt J, Carlsson M, Arheden H, Heiberg E. Independent validation of four-dimensional flow MR velocities and vortex ring volume using particle imaging velocimetry and planar laser-Induced fluorescence. Magn Reson Med. 2015;75:1064–75. http://doi.wiley.com/10.1002/mrm.25683.

13. Pearson K. On lines and planes of closest fit to systems of points in space. Philos Mag. 1901;2:559–72. doi:10.1080/14786440109462720.

14. MacQueen JB. Some Methods for classification and Analysis of Multivariate Observations. 5th Berkeley Symp Math Stat Probab 1967. 1967;1:281–97. doi:citeulike-article-id:6083430.

15. Dice LR. Measures of the amount of ecologic association between species. Ecology. 1945;26:297–302.

16. J. M. B, D. G. A. Statistical methods for assessing agreement between two methods of clinical measurement. Lancet. 1986;1:307–10.

17. Gatehouse P, Rolf M, Graves M, Hofman M, Totman J, Werner B, et al. Flow measurement by cardiovascular magnetic resonance: a multi-centre multi-vendor study of background phase offset errors that can compromise the accuracy of derived regurgitant or shunt flow measurements. J Cardiovasc Magn Reson. 2010;12.

18. Goel A, McColl R, King KS, Whittemore A, Peshock RM. Fully automated tool to identify the aorta and compute flow using phase-contrast MRI: Validation and application in a large population based study. JMRI. 2014;40:221–8. doi:10.1002/jmri.24338.

19. Kass M, Witkin A, Terzopoulos D. Snakes: Active contour models. International Journal of Computer Vision. 1988;1:321–31.

20. Heiberg E, Wigström L, Carlsson M, Bolger a. F, Karlsson M. Time resolved three-dimensional automated segmentation of the left ventricle. Comput Cardiol. 2005;32:599–602.

21. Tufvesson J, Hedström E, Steding-ehrenborg K, Carlsson M, Arheden H, Heiberg E. Validation and Development of a New Automatic Algorithm for Time-Resolved Segmentation of the Left Ventricle in Magnetic Resonance Imaging. Biomed Res Int. 2015;2015.

Paper V: Independent validation of Metric Optimized Gating for fetal cardiovascular phase contrast flow imaging.

Paper V

Independent validation of Metric Optimized Gating for fetal cardiovascular phase-contrast flow imaging

Sebastian Bidhult MSc[1,2], Johannes Töger PhD[1], Einar Heiberg PhD[1,2], Marcus Carlsson MD PhD[1], Håkan Arheden MD PhD[1], Anthony H. Aletras PhD[1,3], Erik Hedström MD PhD[1,4]

Affiliations

[1]Lund University, Skane University Hospital, Department of Clinical Sciences Lund, Clinical Physiology, Lund, Sweden
[2]Lund University, Department of Biomedical Engineering, Faculty of Engineering, Lund, Sweden
[3]Laboratory of Computing, Medical Informatics and Biomedical – Imaging Technologies, School of Medicine, Aristotle University of Thessaloniki, Greece
[4]Lund University, Skane University Hospital, Department of Clinical Sciences Lund, Diagnostic Radiology, Lund, Sweden

Word count: 2777/2800

Corresponding author: Erik Hedström, Department of Clinical Sciences Lund, Lund University, SE-221 00, Lund, Sweden, Tel:+46-709948667

Acknowledgements:
Grant Support: Swedish Heart and Lung Foundation, Swedish Research Council, the Medical Faculty at Lund University, and Region of Skåne, the Greek General Secretariat for Research and Development via an Excellence grant.

Running Title: MOG PC-MR validation for fetal blood flow.

Abstract

Purpose

1) To validate Metric Optimized Gating Phase-Contrast Magnetic Resonance (MOG PC-MR) flow measurements for a range of fetal flow velocities in phantom experiments. 2) To investigate intra- and interobserver variability for fetal flow measurements at an imaging center other than the original site.

Methods

MOG PC-MR was compared to timer/beaker measurements in a pulsatile flow phantom using a heart rate (~145bpm), nozzle diameter (~6mm) and flow range (~130–700ml/min) similar to fetal imaging. Fifteen healthy fetuses were included for intra- and interobserver variability in the fetal descending aorta (DAo) and umbilical vein (UV).

Results

Phantom MOG PC-MR flow bias and variability was 2±23%. Accuracy of MOG PC-MR was degraded for flow profiles with low velocity to noise ratio (VNR). Intra- and interobserver coefficients of variation were 6% and 19% respectively for fetal DAo and 10% and 17% for the UV.

Conclusion

Phantom validation showed good agreement between MOG and conventionally gated PC-MR except for cases with low VNR, which resulted in MOG misgating and underestimated peak velocities, warranting optimization of sequence parameters to individual fetal vessels. Inter- and intra-observer variability for fetal MOG PC-MR imaging were comparable to previously reported values.

Keywords: PC-MR validation, fetal MRI, Metric optimized gating

Introduction

Non-invasive measurement of blood flow in the fetal cardiovascular system may increase our knowledge of fetal cardiovascular physiology and aid in the diagnosis of diseases such as congenital heart disease and intra-uterine growth restriction. Currently, the most commonly applied method for fetal blood flow measurements is pulsed Doppler ultrasound[1,2]. The technique is widely available, safe, relatively inexpensive and has demonstrated fair reproducibility[3]. Despite numerous advantages, flow measurements by pulsed Doppler ultrasound have inherent limitations, including sensitivity to the angle between the Doppler beam and the blood flow direction and assumptions of vessel shape and velocity profile shape across the vessel lumen are required[4].

Magnetic Resonance Imaging (MRI), a non-ionizing imaging modality considered safe for fetal applications[5–9], is a viable alternative for non-invasive flow quantification by utilizing phase contrast (PC-MR) which has been validated extensively in large vessels[10–15] and to some extent in small vessels[16–19], including validation in coronary vessels and phantoms similar in size to the fetal aorta and umbilical vein[19,20]. Lack of a usable ECG by surface electrodes for fetal imaging makes fetal blood flow measurements by phase contrast MR (PC-MR) particularly challenging.

To overcome the need for a fetal ECG, Jansz et al introduced Metric Optimized Gating (MOG)[21] which has demonstrated reproducibility at 1.5T and 3T[22] and low inter-observer variability for fetal applications[23,24] but validation and variability results published are from a single research center. Validation at multiple sites is crucial for wider application. Further, phantom validation of MOG PC-MR has not been performed for a range of flow velocities and sensitivity to varying signal conditions is unclear. We hypothesized that the accuracy of velocity profiles from MOG PC-MR is more sensitive to varying signal conditions than conventionally gated PC-MR.

Therefore, the aims were to 1) validate MOG PC-MR flow measurements for a range of fetal flow velocities using an independent reference standard in phantom experiments; and 2) investigate intra- and interobserver variability for fetal flow measurements at an additional imaging center.

Materials and Methods

The study was approved by the Regional Ethical Review Board in Lund, Sweden and complies with the Declaration of Helsinki. Written informed consent was obtained from all study subjects and MR imaging was performed at a 1.5T scanner (Aera, Siemens Healthcare, Erlangen, Germany) using one 16-channel phased-array chest coil and one spine imaging coil. Image processing and measurements, except for MOG reconstruction, were performed in the medical image analysis software Segment v2.0[25].

Phantom validation

Phantom experiments were performed to validate MOG PC-MR against an independent flow reference standard using a heart rate (~145bpm), a vessel diameter (~6mm) and flow (~130-700ml/min) similar to fetal conditions. A pulsatile flow phantom[26] consisting of a servo motor driven pump and a flow rectifier connected to a water tank was extended with an outflow nozzle submerged in water with an inner diameter (6mm) comparable to the umbilical vein and fetal descending aorta during the third trimester[27,28]. The pump frequency was set to 145bpm and a trigger signal was forwarded to the MR system for conventional image gating. 2D PC-MR images were acquired in a transversal plane perpendicular to the nozzle tube. Three gradient recalled echo PC-MR sequences were evaluated: One MOG PC-MR sequence (Table 1, column 2), and two versions of a conventionally gated PC-MR sequence (Table 1, columns 3 & 4).

The two conventionally gated acquisitions differed in sequence parameters in order to have one set of parameters similar to the MOG PC-MR sequence (Table 1, column 3; Gated PC-MR matched) and one set of parameters with improved temporal and spatial resolution, to be used as reference standard measurement for velocity (Table 1, column 4; Gated PC-MR velocity reference standard). MOG PC-MR was compared to the gated PC-MR matched sequence in order to exclude differences in sequence parameter settings as a confounding factor.

Gating of the MOG PC-MR sequence was performed using a simulated ECG signal with a constant 525ms RR-interval in order to oversample the true RR-interval of the pump (~414ms), as previously described[21]. MOG reconstruction was performed using the MOG-Public Software v2.7(https://github.com/MetricOptimizedGating/MOG-Public). A square region of interest (ROI) 11 pixels wide was placed over the phantom outflow nozzle, also covering areas with stationary water, and a 2-parameter heart rate model from the original MOG publication[21] was used (c.f. supporting text S1).

Velocity encoding (VENC) was set to 150cm/s for the MOG PC-MR sequence and the gated PC-MR matched sequence while a VENC of either 150cm/s or 80cm/s was used for the gated

PC-MR velocity reference standard sequence, depending on the expected peak velocity. Timer and beaker measurements were performed as an independent flow reference standard before and after PC-MR velocity measurements to detect potential flow drifts over time.

PC-MR velocity profiles and flow were obtained from manual ROI delineation. Regions of interest from the gated PC-MR matched sequence (Table 1, column 3) were copied to MOG PC-MR images to exclude delineation variability as a confounding factor. In order to reduce PC-MR flow variability due to manual delineations, the phantom nozzle area was measured independently by a 3D-bSSFP sequence at 3T for improved resolution (Table 1, column 5). PC-MR max-min velocity over the RR-interval was calculated as the difference between maximum and minimum velocity over a beat. Velocity to noise ratio (VNR) was calculated as peak velocities divided by the noise standard deviation while signal to noise ratio (SNR) was calculated as the average magnitude signal divided by the noise standard deviation. Noise standard deviations were estimated in a separate PC-MR measurement with the pump turned off. To investigate the impact of erroneous gating from MOG on PC-MR velocity measurements, the MOG PC-MR dataset with highest VNR was reconstructed with pre-set erroneous heart rates ranging from 128-164bpm. To investigate the variation of MOG gating due to random noise, numerical experiments were performed (c.f. supporting text S2).

Fetal imaging

Fifteen healthy fetuses (gestational week 30-37) were prospectively included and imaging was performed in the maternal left lateral decubitus position. A 2D PC-MR sequence was used for flow measurements in the fetal descending aorta (DAo) and the intra-abdominal umbilical vein (UV). MOG PC-MR measurements were acquired during maternal breath-holds using a simulated ECG signal as described above. Cardiotocography was performed at rest 5 min before the MRI examination in eight subjects, showing maximum RR intervals of median 444ms (range 413-461ms), resulting in oversampling of 14-27% for MOG PC-MR. Background phase correction was performed by subtraction of a first-order polynomial. Two independent experienced observers assessed inter-observer variability. One observer repeated the measurements for intra-observer variability. Noise standard deviations in the UV and DAo were estimated by using a noise prescan which was integrated in the PC-MR acquisition, with a previously validated algorithm[29].

Statistical analysis

Bias and variability of PC-MR measurements were determined using modified Bland-Altman analysis[30] with error percentages calculated as differences between two measurements divided by the reference standard measurement. Coefficient of Variation (CV) for intra- and interobserver variability were computed as the sample standard deviation of differences between measurements divided by their sample mean.

Results

Phantom validation

Timer and beaker flow measurements ranged between 127-701ml/min. The maximum difference in timer and beaker flow before and after PC-MR measurements was less than 13.1ml/min (1.86%), indicating stability of the flow reference standard measurement and low pump stroke volume variation.

Gated PC-MR velocity reference standard measurements

The maximum flow difference between the gated PC-MR velocity reference standard sequence and timer and beaker was 9.6ml/min (2.9%), suggesting good agreement between gated PC-MR flow and timer and beaker flow. Max-min velocities for all pump programs ranged between 68-143cm/s.

Gated PC-MR matched sequence measurements

Maximum flow differences compared to timer and beaker increased using the gated PC-MR sequence with sequence parameters similar to the MOG acquisition (-23.9ml/min and -6.6%). Max-min velocity bias and variability compared to the gated PC-MR velocity reference standard sequence was -4±2cm/s (-3.7±1.1%), indicating good agreement with the velocity reference standard.

MOG PC-MR measurements

Estimated pump frequency from MOG reconstructions ranged from 130-150 bpm and resulted in error ranges -16 to -2.3 bpm compared to the true pump frequency (Table 2, row 3-4).

Velocity profiles from MOG PC-MR and gated PC-MR sequences are shown in Figure 1. MOG PC-MR velocity profiles closely resembled gated PC-MR velocity profiles except for the two pump settings with low flow and velocity. At all pump settings, MOG PC-MR underestimated max-min velocity compared to the gated PC-MR sequence with similar acquisition settings, with bias and variability -23±42cm/s (-27.5±53.0%). Figure 2 shows a comparison between PC-MR and timer and beaker flow. MOG PC-MR overestimated flow at the pump setting with minimum timer & beaker flow (18.8%) and underestimated flow at the pump setting with maximum timer &

beaker flow (-9.1%). Maximum difference in flow between MOG PC-MR and timer and beaker was -63.8ml/min (18.8%), shown in Table 2, row 3-4.

Low errors in estimated pump frequency and max-min velocity from MOG were found for the two pump settings (Table 2 row 2-3) with VNR between 5-6. For the two remaining pump settings (Table 2 row 4-5) with lower VNR 2.4–3.7), errors in estimated pump frequency and max-min velocity increased.

To investigate the underlying cause of the two outlier cases (Table 2, row 4-5), new MOG reconstructions were performed using different reconstruction settings for increased noise robustness. A constant heart rate was assumed, with a search step of 2 bpm and the MOG ROI width was reduced from 11 to 3 pixels, covering only the phantom outflow nozzle. The new MOG reconstructed velocity profiles are shown in Supporting Figure S1. For the pump program with timer and beaker flow 253ml/min the new reconstruction matched the reference velocity profile. The pump frequency error was reduced from -16bpm to -5.8bpm, and max-min velocity error was reduced from -51.9% to -5.4%. For the pump program with timer and beaker flow 127ml/min, the new MOG reconstruction did not resemble the reference velocity profile and the max-min velocity error from MOG remained large (-46.8%). Supporting animations S1-S6 show PC-MR images after MOG reconstruction at all pump settings.

Figure 3 shows the relationship between errors in MOG heart rate estimation and errors in MOG PC-MR max-min velocity, indicating that a MOG heart rate error less than approximately 3bpm was required to achieve a max-min velocity error lower than 30%. Results from numerical experiments are shown in Supporting text S2 and Supporting table S1.

Fetal imaging

Supporting figure S2 shows an example of a fetal MOG PC-MR flow measurement. One umbilical vein case was excluded due to major fetal movement. For interobserver variability, two other umbilical vein cases were not delineated by observer two due to challenging image quality and were excluded from interobserver analysis. Diameters for the fetal descending aorta and umbilical vein ranged between 5-8mm and 5-9mm. Pulsatility was shown for DAo but not for UV after MOG reconstruction in all subjects. Flow ranged between 546-948ml/min in DAo and 181-606ml/min in the UV. Intra- and interobserver variability were for DAo 7±83ml/min (bias±1.96SD) and 55±263ml/min, and for UV 9±70 ml/min and 56±115ml/min, respectively (Supporting figure S3). Intra- and interobserver CV for Dao were 6% and 19% and for UV 10%

and 17%. Noise standard deviations were for DAo 7.5±3.1cm/s (mean±SD) and for UV 9.6±3.4cm/s.

Discussion

This study presents phantom validation of the Metric Optimized Gating (MOG) method for a range of flow values similar to the fetal descending aorta and umbilical vein, together with inter and intra-observer variability for fetal MOG PC-MR measurements. Low bias was found for MOG PC-MR flow measurements in phantom experiments, although velocities were underestimated for low VNR. Inter and intra-observer variability for MOG PC-MR imaging in vivo were comparable to previously reported values[23].

Our phantom validation adds data compared to previous MOG validation studies[21,24] in two specific areas. First, phantom experiments in the current study included timer and beaker flow measurements as reference standard. Second, the flow phantom setup in the current study enabled validation for a range of flow velocities, a pump frequency and a nozzle inner diameter similar to fetal vessels.

In the phantom experiment MOG PC-MR underestimated flow at high flow values and overestimated flow at low flow values compared to timer and beaker. MOG PC-MR flow underestimation at high flow probably originates from the observed underestimation of velocity peaks. The MOG PC-MR flow overestimation at low flow on the other hand, may be caused by reduced flow pulsatility due to MOG misgating, leading to near constant and positive velocity over the RR-interval.

Erroneous MOG PC-MR velocity profiles at low flow and velocity can likely be attributed to either limited VNR or the specific MOG reconstruction settings in use. The MOG reconstruction errors found at pump settings with low velocity partly originated from MOG reconstruction parameter settings since accurate velocity profiles were obtained at one of the outlier cases after re-tuning of MOG reconstruction settings. The initially selected 11 pixels wide ROI was larger than the tubing diameter, covering both areas with stationary and flowing water. The increased MOG accuracy using a reduced ROI for reconstruction is likely related to exclusion of regions containing stationary water, enhancing the pulsatile flow component in the ROI average. Of note, the performed tuning of reconstruction settings in the phantom validation is not a feasible option for in-vivo fetal applications since the assumption of a constant heart rate is not realistic for fetal imaging. Numerical experiments demonstrated that VNR levels similar to that found for the two MOG outlier cases gave rise to errors in estimated heart rate in the same range as for errors observed in the phantom study, which is in line with our hypothesis.

Residual background phase error was likely not a major confounding factor in the phantom experiment since low bias and variability was found between timer and beaker flow and gated PC-MR flow.

The finding that MOG PC-MR is more sensitive to VNR compared to conventionally gated PC-MR should not discourage the use of MOG PC-MR in fetal MRI, but rather warrants optimization of sequence parameters to each fetal vessel of interest. Further work is needed to determine which specific sequence parameter optimization is best suited for improving MOG reconstruction robustness.

For fetal imaging, flow volumes and intra- and interobserver variability in the fetal UV and DAo were comparable to previously reported values[23]. For analysis of MOG reconstructed PC-MR images the main source of variability is likely attributed to differences in vessel delineation. The interobserver variability, being slightly higher than intraobserver variability, indicates that delineation of fetal quantitative flow images poses additional challenges compared to corresponding analysis in children and adults. This may in part be related to lower image quality due to limited spatial resolution but also due to fetal movement and residual gating error after MOG reconstruction.

Velocity-to-noise regimes for in-vivo fetal MOG PC-MR measurements were further analyzed as phantom validation showed MOG misgating at low VNR. As velocities were measured by the investigated MOG method in this study, VNR in DAo and UV could not be directly determined. However, noise standard deviations were estimated in acquired images without MOG processing from the current data set, and combined with peak velocities in the corresponding vessels assessed in a previous study[31], in which fetal PC-MR was gated using a doppler ultrasound device. The VNR regimes for the fetal DAo and UV was thus estimated to 8.0 and 1.6, respectively. These values are similar to VNR regimes in the current phantom validation, which resulted in both successful (DAo VNR=8.0) and failed (UV VNR=1.6) MOG reconstructions. The estimated VNR difference between DAo and UV further warrants sequence parameter optimization to individual fetal vessels and expected velocities for accurate MOG PC-MR.

Limitations

Phantom studies did not include heart rate variability. However, this has been evaluated previously[21].

The present study did not investigate the accuracy of background phase correction in fetal imaging, which may be challenging due to lack of stationary tissue adjacent to the vessel of interest. Furthermore, the currently used PC-MR sequences for fetal flow measurements result in approximately 4-5 pixels across the vessel lumen of the intra-abdominal umbilical vein and the fetal descending aorta during the third trimester. Although considered sufficient for accurate PC-MR velocity measurements[16], limited spatial resolution may cause bias in flow measurements due to partial volume effects influencing ROI delineation.
Cardiotocography was not performed in all fetuses. However, the simulated RR-interval of 525ms used for MOG PC-MR corresponds to a fetal heart rate of 115bpm, which is lower than expected in healthy fetuses.

Conclusion

Phantom validation showed good agreement between MOG and conventionally gated PC-MR except for cases with low VNR, which resulted in MOG misgating and underestimated peak velocities, warranting optimization of sequence parameters to individual fetal vessels. Inter- and intra-observer variability for fetal MOG PC-MR imaging were comparable to previously reported values.

References

1. Gill RW. Pulsed Doppler with B-mode imaging for quantitative blood flow measurement. Ultrasound in Medicine & Biology. 1979;5(3):223–235.

2. Eik-Nes SH, Brubakk AO, Ulstein M. Measurement of human fetal blood flow. British medical journal. 1980;280(6210):283–4.

3. Thuring A, Laurini R, Maršál K. Uterine venous blood flow in normal and complicated pregnancies: A methodological study. Ultrasound Obstet Gynecol. 2010;35:462–467.

4. Gill RW. Measurment of blood flow by US: Accuracy and sources of error. Ultrasound Med Biol. 1985;I(4):625–641.

5. Baker P, Johnson I, Harvey P, Gowland P, Mansfield P. A three-year follow-up of children imaged in utero with echo-planar magnetic resonance. Am J Obstet Gynecol. 1994;170(1):32–33.

6. Myers C, Duncan K, Gowland P, Johnson I, Baker P. Failure to detect intrauterine growth restriction following in utero exposure to MRI. Br J Radiol. 1998;71(845):549–551.

7. Schenck J. Safety of strong, static magnetic fields. J Magn Reson Imaging. 2000;12(1):2–19.

8. Clements H, Duncan K, Fielding K, Gowland P, Johnson I, Baker P. Infants exposed to MRI in utero have a normal paediatric assessment at 9 months of age. Br J Radiol. 2000;73(866):190–194.

9. Kok R, de Vries M, Heerschap A, van den Berg P. Absence of harmful effects of magnetic resonance exposure at 1.5 T in utero during the third trimester of pregnancy: a follow-up study. Magn Reson Imaging. 2004;22(6):851–854.

10. Beerbaum P, Körperich H, Gieseke J, Barth P, Peuster M, Meyer H. Blood Flow Quantification in Adults by Phase-Contrast MRI Combined with Sense - A Validation Study. J Cardiovasc Magn Reson. 2005;7(2):361–369.

11. Lotz J, Döker R, Noeske R, Schuttert M, Felix R, Galanski M, Gutberlet M, Meyer GP. In vitro validation of phase-contrast flow measurements at 3 T in comparison to 1.5 T: Precision, accuracy, and signal-to-noise ratios. J Magn Reson Imaging. 2005;21:604–610.

12. Gatehouse P, Rolf M, Graves M, Hofman M, Totman J, Werner B, Quest R, Liu Y, von Spiczak J, Dieringer M, et al. Flow measurement by cardiovascular magnetic resonance: a multi-centre multi-vendor study of background phase offset errors that can compromise the accuracy of derived regurgitant or shunt flow measurements. J Cardiovasc Magn Reson. 2010;12(5). doi:10.1186/1532-429X-12-5

13. Arheden H, Holmqvist C, Thilen U, Hanseus K, Björkhem G, Pahlm O, Laurin S, Ståhlberg

F. Left-to-right cardiac shunts: comparison of measurements obtained with MR velocity mapping and with radionuclide angiography. Radiology. 1999;211(2):453–458.

14. Carlsson M, Andersson R, Bloch K, Steding-Ehrenborg, K Mosén H, Stahlberg F, Ekmehag B, Arheden H. Cardiac output and cardiac index measured with cardiovascular magnetic resonance in healthy subjects, elite athletes and patients with congestive heart failure. J Cardiovasc Magn Reson. 2012;14(51). doi:10.1186/1532-429X-14-51

15. Rolf M, Hofman M, Gatehouse, PD Markenroth-Bloch, K Heymans M, Ebbers T, Graves M, Totman J, Werner B, van Rossum A, Kilner P, Heethaar R. Sequence optimization to reduce velocity offsets in cardiovascular magnetic resonance volume flow quantification--a multi-vendor study. J Cardiovasc Magn Reson. 2011;13(18). doi:10.1186/1532-429X-13-18

16. Arheden H, Saeed M, Törnqvist E, Lund G, Wendland M, Higgins C, Ståhlberg F. Accuracy of segmented MR velocity mapping to measure small vessel pulsatile flow in a phantom simulating cardiac motion. J Magn Reson Imaging. 2001;13(5):722–728.

17. Keegan J, Firmin D, Gatehouse P, Longmore D. The application of breath hold phase velocity mapping techniques to the measurement of coronary artery blood flow velocity: phantom data and initial in vivo results. Magn Reson Med. 1994;31(5):526–536.

18. Hofman M, Visser F, van Rossum A, Vink Q, Sprenger M, Westerhof N. In vivo validation of magnetic resonance blood volume flow measurements with limited spatial resolution in small vessels. Magn Reson Med. 1995;33(6):778–784.

19. Lund G, Wendland M, Shimakawa A, Arheden H, Ståhlberg F, Higgins C, Saeed M. Coronary sinus flow measurement by means of velocity-encoded cine MR imaging: validation by using flow probes in dogs. Radiology. 2000;217(2):487–493.

20. Bloch K, Carlsson M, Arheden H, Ståhlberg F. Quantifying coronary sinus flow and global LV perfusion at 3T. BMC Med Imaging. 2009;9(9).

21. Jansz M, Seed M, van Amerom J, Wong D, Grosse-Wortmann L, Yoo S, Macgowan C. Metric optimized gating for fetal cardiac MRI. Magn Reson Med. 2010;64(5):1304–1314.

22. Tsai-Goodman B, Zhu M, Al-Rujaib M, Seed M, Macgowan C. Foetal blood flow measured using phase contrast cardiovascular magnetic resonance--preliminary data comparing 1.5 T with 3.0 T. J Cardiovasc Magn Reson. 2015;17(30). doi:10.1186/s12968-015-0132-2

23. Prsa M, Sun L, van Amerom J, Yoo S, Grosse-Wortmann L, Jaeggi E, Macgowan C, Seed M. Reference ranges of blood flow in the major vessels of the normal human fetal circulation at term by phase-contrast magnetic resonance imaging. Circ Cardiovasc Imaging. 2014;7(4):663–670.

24. Seed M, van Amerom J, Yoo S, Al Nafisi B, Grosse-Wortmann L, Jaeggi E, Jansz M,

Macgowan C. Feasibility of quantification of the distribution of blood flow in the normal human fetal circulation using CMR: a cross-sectional study. J Cardiovasc Magn Reson. 2012;14(79). doi:10.1186/1532-429X-14-79

25. Heiberg E, Sjögren J, Ugander M, Carlsson M, Engblom H, Arheden H. Design and validation of Segment--freely available software for cardiovascular image analysis. BMC Med Imaging. 2010;11(10).

26. Töger J, Bidhult S, Revstedt J, Carlsson M, Arheden H, Heiberg E. Independent validation of four-dimensional flow MR velocities and vortex ring volume using particle imaging velocimetry and planar laser-Induced fluorescence. Magn Reson Med. 2015;75(3):1064–1075.

27. Tonge H, Struijk P, Wladimiroff J. Blood flow measurements in the fetal descending aorta: technique and clinics. Clin Cardiol. 1984;7(6):323–329.

28. Mahony B, McGahan J, Nyberg D, Reisner D. Varix of the fetal intra-abdominal umbilical vein: comparison with normal. J Ultrasound Med. 1992;11(2):73–76.

29. Robson PM, Grant AK, Madhuranthakam AJ, Lattanzi R, Sodickson DK, McKenzie CA. Universal Approach to Quantification of SNR and g-Factor for parallel MRI. 15th Annual Meeting of ISMRM, Berlin, Germany. 2007;15:1747.

30. Bland J, Altman D. Statistical methods for assessing agreement between two methods of clinical measurement. Lancet. 1986;1(8476):307–310.

31. Hedström E, Steding-ehrenborg K, Bidhult S, Ruprecht C, Kording F, Aletras AH. Quantitative phase-contrast CMR of blood flow in fetal vessels gated by Doppler ultrasound : Comparison with metric optimized gating. 27th Annual Meeting of ISMRM, Paris, France. 2018;27:2944.

Table captions

Table 1. MRI sequence parameters in use.

MRI sequence parameters	Phantom imaging: MOG PC-MR	Phantom imaging: Gated PC-MR matched	Phantom imaging: Gated PC-MR velocity reference standard	Phantom imaging: 3D-bSSFP	Fetal imaging: MOG PC-MR
Flip angle [°]	20	20	20	48	20
TE/TR [ms]	2.8/5.1	2.8/5.1	3.2/5.6	3.5/7.0	2.8/5.1
VENC [cm/s]	150	150	150 or 80	n/a	150
Acquired temporal resolution [ms]	30.5	30.5	11.2	n/a	30.4
Acquired voxel size [mm^3]	1.3x1.3x5	1.3x1.3x5	1.0x1.0x5	0.4x0.4x0.4	1.3x1.3x5
Views per segment	3	3	1	single shot	3
Acquisition time [sec]	29	29	116	638	29

Table 2. MOG PC-MR errors in pump frequency and max-min velocity (columns) for each pump setting sorted according to declining timer & beaker flow (rows). The two pump programs with low timer & beaker flow have larger MOG errors in both pump frequency and max-min velocity compared to the two pump settings with high timer & beaker flow.

	MOG Pump frequency error [bpm]	MOG Max-min velocity error [%]	MOG Max-min velocity error [cm/s]
Pump program #1 Timer & beaker flow: 701ml/min Gated PC-MR VNR: 6.0 Gated PC-MR SNR: 55.2	2.4	-9.8	-14.1
Pump program #2 Timer & beaker flow: 452ml/min Gated PC-MR VNR: 5.0 Gated PC-MR SNR: 53.9	-2.3	-5.6	-7.1
Pump program #3 Timer & beaker flow: 253ml/min Gated PC-MR VNR: 3.7 Gated PC-MR SNR: 53.0	-16.0	-51.9	-50.6
Pump program #4 Timer & beaker flow: 127ml/min Gated PC-MR VNR: 2.4 Gated PC-MR SNR: 47.0	-15.6	-53.4	-36.6

Figure captions

Figure 1.

In the phantom experiment, MOG PC-MR underestimated max-min velocity at pump settings with low flow (bottom panels). The four panels show velocity profiles from the three evaluated PC-MR sequences (Table 1) at four pump settings with different flow. For the two pump settings with largest flow (top panels) MOG PC-MR (dotted lines) and the gated PC-MR sequence with similar acquisition parameters as MOG PC-MR (open triangles) were both in good agreement with the gated PC-MR velocity reference standard sequence (solid lines), while MOG PC-MR underestimated velocity peaks at the two pump settings with low flow (bottom panels).

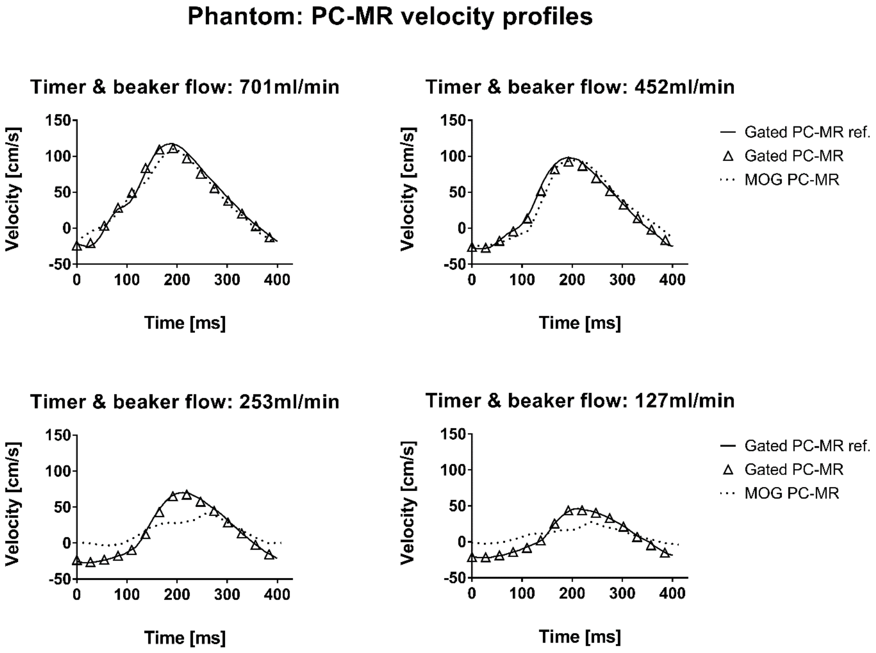

Figure 2.

Metric Optimized Gating PC-MR shows low flow bias and high flow variability (bottom panels). The panels show modified Bland Altman analysis comparing PC-MR flow measurements with timer and beaker (T/B) flow in absolute volumes (left panels) and percentage units (right panels). Open circles indicate individual data points, solid lines indicate bias and dashed lines indicate bias±1.96SD. The gated PC-MR velocity reference standard sequence (top panels) showed good agreement with timer and beaker flow with low bias and variability. The gated PC-MR sequence with similar acquisition parameters as MOG PC-MR (middle panels) also demonstrated low bias and variability, while MOG PC-MR (bottom panels) resulted in increased flow variability compared to both conventionally gated PC-MR sequences (top and middle panels).

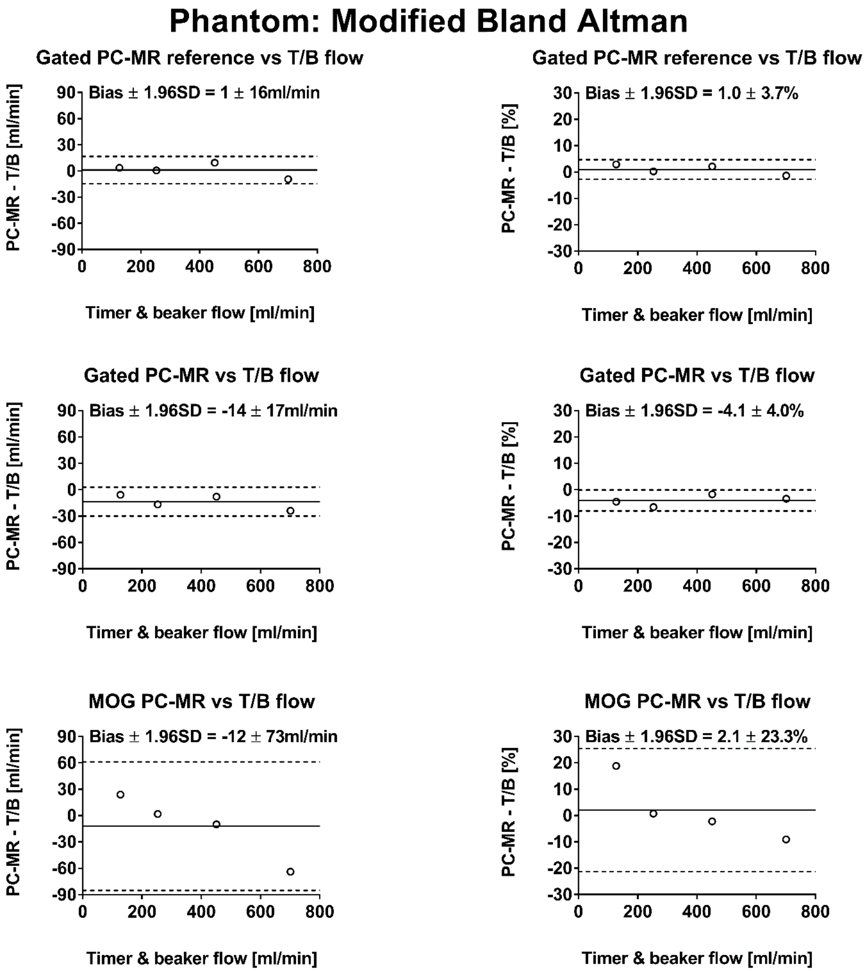

Phantom: Modified Bland Altman

Gated PC-MR reference vs T/B flow

Gated PC-MR reference vs T/B flow

Gated PC-MR vs T/B flow

Gated PC-MR vs T/B flow

MOG PC-MR vs T/B flow

MOG PC-MR vs T/B flow

Figure 3.
In the phantom experiment, MOG PC-MR max-min velocity measurements were sensitive to heart rate errors from MOG reconstruction (x-axis). The y-axis shows the error in max-min velocity from MOG PC-MR compared to gated PC-MR for the pump setting with largest VNR. In the phantom experiment, a heart rate error less than approximately 3bpm was required to achieve a max-min velocity error below 30%.

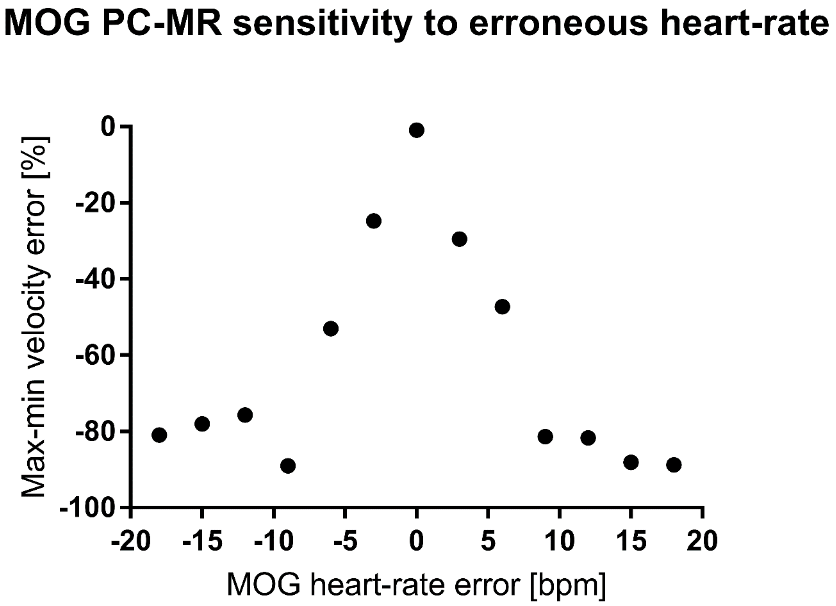

Supporting information legends:

Supporting Figure S1.

In the phantom experiment, re-tuned MOG reconstruction settings resulted in accurate MOG velocity profiles in one out of two outlier cases (top panel). The figure shows Metric Optimized Gating (MOG) velocity profiles for the outlier cases both before (dotted lines) and after (solid lines) re-tuning of MOG reconstruction settings, together with conventionally gated PC-MR velocity profiles (open triangles). The remaining erroneous MOG velocity profiles (bottom panel) are likely caused by limited peak velocity of the underlying flow relative to the PC-MR velocity encoding in use (150cm/s). The re-tuning of MOG parameters was performed to investigate the cause of obtained velocity errors from MOG and is not feasible for in vivo fetal applications.

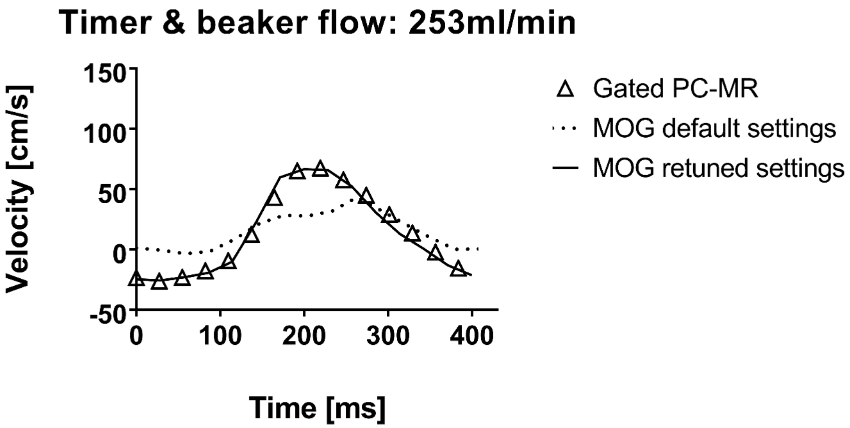
Timer & beaker flow: 253ml/min

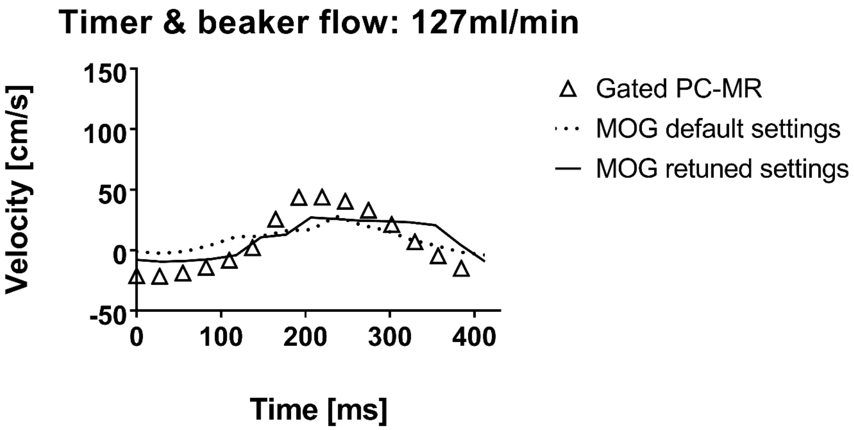
Timer & beaker flow: 127ml/min

Supporting Figure S2.

Magnitude (A and D) and velocity-encoded (B and E) MOG PC-MR images and corresponding typical flow curves (C and F) for the fetal descending aorta (top row) and umbilical vein (bottom row) with the respective vessel delineated in blue.

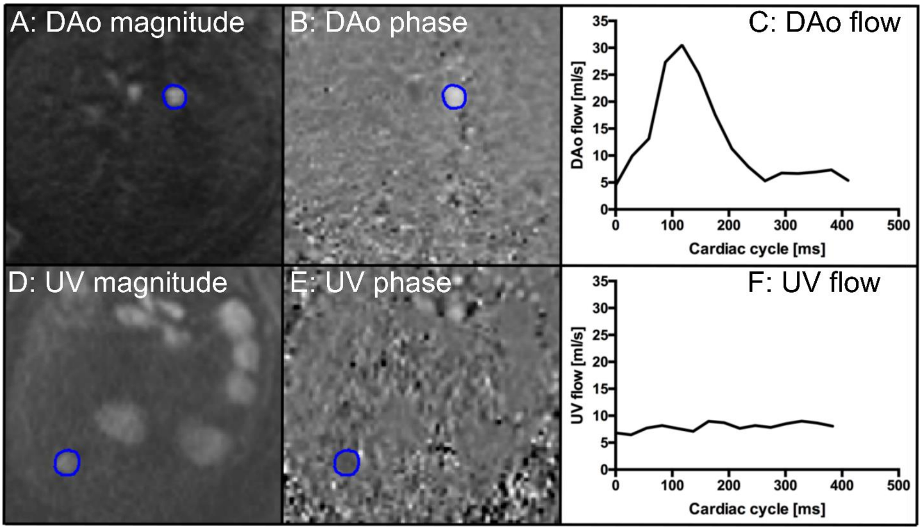

Supporting Figure S3.

Bland-Altman analyses of intra- (left panels) and inter-observer (right panels) variability for flow measurements in the fetal descending aorta (DAo; top panels) and umbilical vein (UV; bottom panels). The dotted lines indicate bias and the solid lines indicate bias±1.96SD.

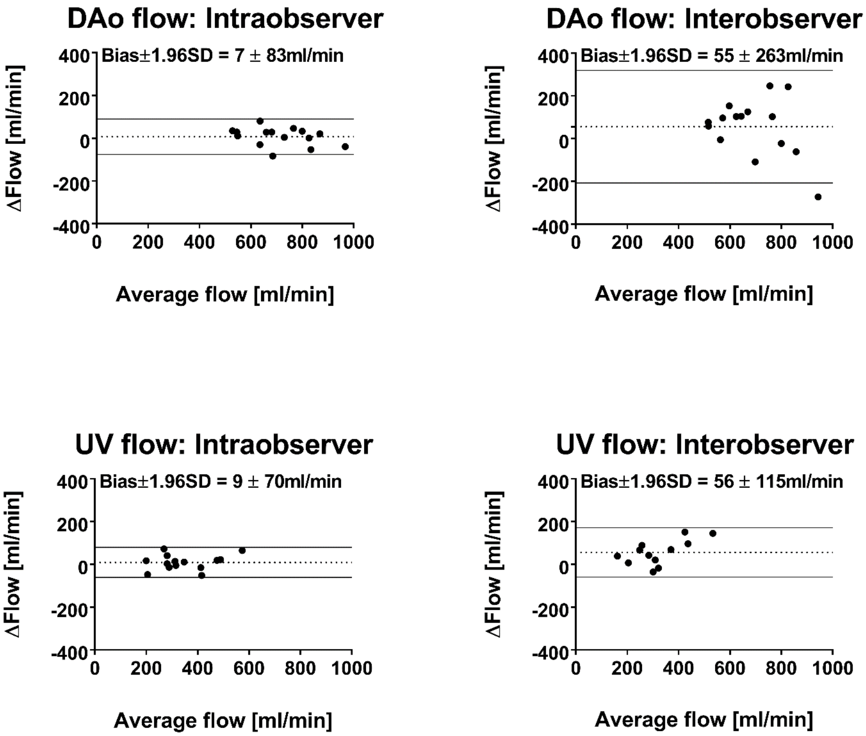

Supporting animation S1-S2.
MOG PC-MR magnitude (left panels) and phase difference (right panels) image time series from pump settings 701ml/min and 452ml/min in the phantom experiment resulted in accurate pulsatile flow and phase difference images without severe misgating artifacts after MOG reconstruction.

Supporting animation S3-S4.
MOG PC-MR magnitude (left panels) and phase difference (right panels) image time series from pump settings 253ml/min and 127ml/min in the phantom experiment resulted in clearly visible misgating artifacts in phase difference images after MOG reconstruction, indicating inaccurate heart rate estimation from MOG.

Supporting animation S5.
With the modified MOG reconstruction settings, MOG PC-MR magnitude (left panels) and phase difference (right panels) image time series from pump setting 253ml/min in the phantom experiment resulted in accurate pulsatile flow and phase difference images without severe misgating artifacts after MOG reconstruction.

Supporting animation S6.
With the modified MOG reconstruction settings, MOG PC-MR magnitude (left panels) and phase difference (right panels) image time series from pump setting 127ml/min in the phantom experiment did not result in accurate pulsatile flow, indicating inaccurate heart rate estimation from MOG. However, only subtle misgating artifacts were visible in phase difference images, indicating that misgating artifacts alone may be insufficient for determining the accuracy of MOG reconstructions.

Supporting text:

Supporting text S1: Description of the MOG optimization algorithm
The optimization algorithm used in Metric Optimized Gating, which was originally proposed by Jansz et al[1], uses a 2-parameter piecewise constant heart rate model which assumes that the heart rate during a PC-MR acquisition is changing once, in the middle of the scan when the central k-space line is acquired. With this heart rate model the optimization algorithm tries to find the two heart rates which results in the maximum time entropy (defined in [1]) within a user defined quadratic 11 pixels wide region of interest (ROI) in PC-MR images where the phase difference signal has been multiplied with the magnitude signal for noise robustness. This method assumes that misgating results in reduced pulsatility and has been shown to be robust to moderate heart rate variability[1].

In the current study, two versions of the MOG algorithm was used: 1) The original algorithm using the 2-parameter piecewise constant heart rate model and a 11 pixels wide ROI covering both the vessel of interest and immediately surrounding stationary regions was applied to all phantom and invivo MOG PC-MR datasets and 2) for two MOG datasets from the phantom study a modified version of the MOG algorithm was also applied using a 1-parameter constant heart rate model and a 3 pixels wide ROI which only covered flow regions within the phantom outflow nozzle in order to improve noise robustness by increasing the maximum time entropy during MOG reconstruction. The purpose of using the modified MOG algorithm was to investigate noise sensitivity of MOG during the phantom experiment. However, the modified algorithm is not suitable for use invivo since the assumption that the fetal heart rate is constant during a PC-MR acquisition is not realistic and the small ROI size in use which is defined in the PC-MR images before gating may miss the vessel of interest completely for vessels with large inplane motion during a fetal heartbeat.

Reference:

1. Jansz M, Seed M, van Amerom J, Wong D, Grosse-Wortmann L, Yoo S, Macgowan C. Metric optimized gating for fetal cardiac MRI. Magn Reson Med. 2010;64(5):1304–1314.

Supporting text S2: Numerical experiments using computer generated noise

Methods:

In order to evaluate the effect of noise on the MOG algorithm in the phantom experiment, computer generated zero mean Gaussian random noise was added to phase difference images from the MOG PC-MR dataset with largest velocity to noise ratio (VNR), corresponding to the pump setting with timer and beaker flow 701ml/min. The standard deviation of computer generated noise was chosen such that the resulting VNR had similar orders of magnitude as VNRs observed in the phantom experiment, ranging from 2-6. For each VNR case the mean and standard deviation of estimated heart rates from MOG was estimated from 500 repetitions. The MOG heart rate estimate from the phantom dataset without added noise was used as ground truth for simulations.

Results:

Supporting Table S1 shows MOG heart rate mean±SD and ranges from numerical experiments at different velocity to noise ratio (VNR; range 2-6). The MOG heart rate errors associated with failed MOG reconstructions in the phantom experiment (-15.6 bpm and -16 bpm) were within the range of heart rate errors found in numerical experiments (-17.5 bpm to 12.5 bpm) at similar VNR, indicating that the two cases for which MOG failed to reconstruct accurate velocity profiles in the phantom experiment may have been caused by insufficient VNR.

Supporting tables:

Supporting Table S1. The variation of estimated MOG heart rate due to noise increased with decreasing velocity to noise in numerical experiments. The observed heart rate errors from MOG associated with inaccurate velocity profiles in the phantom experiment (-16 bpm and -15.6 bpm) were within the range of MOG variation due to noise for simulated VNR 3 (bold), indicating that inaccurate MOG velocity profiles in the phantom experiment may have been caused by insufficient VNR.

Simulated velocity to noise ratio	Variation of estimated MOG heart rate due to noise mean±1.96SD (range) [bpm]
6	-0.4±2.7 (-4.5 to 12.5)
4	-0.6±5.5 (-17.5 to 12.5)
3	-0.3±8.9 **(-17.5 to 12.5)**
2	-1.5±12 (-33.5 to 26.5)